Parametric Modeling of small terminals and Multiband or Ultra wideband Antennas

Muhammad Amir Yousuf

Parametric Modeling of Small Terminals and Multiband or UWB Antennas

Department of Electronic and informatics

Doctoral Dissertation

Presented by:
Muhammad Amir Yousuf

Jury Members

Ala Sharaiha	Reviewer
Cyril Luxey	Reviewer
Alain Sibille	Supervisor
Christophe Roblin	Examiner
Serge Bories	Examiner

Parametric Modeling of Small Terminals and Multiband or UWB Antennas

Department of Electronic and informatics

Doctoral Dissertation

Presented by:
Muhammad Amir Yousuf

Jury Members

Prof.Alain Sibille	ENSTA-ParisTech
Prof. Ala SHARAIHA	Université de Rennes 1,
Prof. Cyril Luxey	Université de Nice-Sophia Antipolis
Prof.Christophe Roblin	ENSTA-ParisTech
Engg.Serge Boris	CEA / Léti

To my Mother

Acknowledgements

First of all, I thank to all mighty ALLAH (S.W.T) without his will nothing is possible. I acknowledge my deepest gratitude and appreciation to my supervisor Professor Christophe Roblin for his guidance and persistent help throughout my doctoral studies. Your professional support helped me to identify and to understand actual research problems and to pursue their solutions. Thanks to my director Professor Alain Sibille for having confidence in me to work in antenna research team at ENSTA-ParisTech. I also pay my respect to Professor Omer Hammami for introducing me to ENSTA-ParisTech.

I am grateful to all members of the jury for taking their time reading this thesis. The excellent appreciation comments from Professor Ala Sharaiha made me confident and the critical analysis of Professor Cyril Luxey help me to increase the readability of the manuscript.

I thank all my colleagues in ENSTA-ParisTech, Telecom-ParisTech and all my friends for their support throughout my journey of PhD. Notably I would like to thank Mr. Amin Mellah who help me understanding the complex phenomenon and Mr. Moussa Sacko who is very supportive in all my small chores. I cannot forget the contribution of Mr. Francesco Guidi for his patience on many difficult occasions. I also appreciate the efforts of Mr. Taj Muhammad Khan, Mr. Abdul Wahab and Mr. Shoaib Naqvi for organizing the refreshments after my PhD defense.

Especial thanks to Lucia Guerri and Adnan Ahmed Dogar for their love and affections that keeps my stress level down during my difficult times. In addition, I would also like to thank to all who pray for me.

Last, but truly not least, I want to thank to my parents. The work done in this thesis is a result of their indirect efforts and sacrifices they have made during whole my life. I also thank my sister for her support throughout my childhood and in my early education. It would have never been possible without their unconditional love, support and understanding.

In the last, I would like to pay all my gratitude to my mother for her brave decision to sent me for engineering college despite the fact that my father did not have money to support my studies, I guess this PhD was started with my mother's decision has ended today. Thanks to my great mother.

ABSTRACT

Since the inception of short range Ultra Wideband (UWB) communication systems the factors like device miniaturization and high speed data rate create big challenges for antenna designers. One way to make the design job easy is to statistically model the variabilities of antenna radiation behavior as a function of its geometry. Such an effort is also useful for the better usage of the communication channel by combining the antenna model with it. This thesis is an attempt towards statistical modeling of UWB antennas. The subject faces two main challenges, the creation of sizeable statistical population of the class of antenna design(s) and modeling of antenna's radiation pattern which is composed of huge number of complex parameters. In this thesis we try to answer the former by proposing a generic design approach for UWB planar antennas and the latter by presenting the use of ultra-compressed parametric modeling technique. The generic design approach is based on trapezoidal shapes and offers great flexibility and versatility in designing various UWB antennas. This approach shows a significant ease in antenna optimization (also for population creation) as it reduces the no. of parameters that controls the antenna geometry without compromising the degree of freedom.

Ultra-compressed parametric modeling is based on two antenna synthesis methods, singularity expansion method (SEM) and Spherical mode expansion method (SMEM) that reduce the required no. of complex parameters for the radiation pattern by 99.9%, making the modeling effort possible. A statistical model of biconical antenna based on ultra-compressed modeling technique has been presented.

Keywords: UWB Antennas, Antenna Statistical Analysis, Antenna Design, Parametric modeling, Multiband antenna, Planar Antennas, Spherical mode expansion method (SMEM), Singularity expansion Method (SEM)

ABSTRACT (Français)

Depuis le lancement systèmes des communications d’ultra large bande (ULB) en courtes distances les facteurs comme la miniaturisation d’appareil et haut débit créer des grands défis pour les concepteurs d'antennes. Une façon de faire le travail de conception facile est du modéliser statistiquement la variabilité de comportement de rayonnement de l'antenne en fonction de sa géométrie. Tel effort est également utile pour la meilleure utilisation du canal de communication si on combine le modèle d'antenne avec ça. Cette thèse est une tentative vers la modélisation statistique des antennes ULB. Le sujet est confronté à deux défis majeurs, la création de la population statistiques considérable d’une classe(s) d'antenne et la modélisation du diagramme de rayonnement de l'antenne qui est composé de grand nombre de paramètres complexes. Dans cette thèse, nous essayons de répondre le premier en proposant une approche de conception générique pour les antennes planaires ULB et le second en présentant l'utilisation de technique l'ultra-compressé de modélisation paramétrique. L'approche de conception générique est basé sur des formes trapézoïdales et offre une grande flexibilité et polyvalence dans la conception des antennes ULB diverses. Cette approche montre une facilité importante dans l'optimisation d'antennes (également pour la création de la population), car elle réduit le nombre de paramètres qui contrôle la géométrie de l'antenne, sans compromettre le degré de liberté.

Ultra-compressé modélisation paramétrique est basée sur deux méthodes de synthèse d'antenne, la méthode d'expansion singularité (SEM) et sphériques méthode d'expansion de mode (SMEM) qui permettent de réduire le nombre de paramètres complexes requis pour le diagramme de rayonnement de 99,9%, permettant à l'effort de modélisation possibles. Un modèle statistique de l'antenne biconique basé sur cette technique a été présenté.

Mots clé : Antennes ultra large bande, Analyse statistique, Conception d’antennes, Modélisation paramétrique, Antenne Multi bande, Antennes planaires, Méthode de développement en Mode sphérique, Méthode du développement en singularités

x

RESUME (Français)

Dans les systèmes de communications radio récents ou émergents, l’étude des petites antennes et des petits terminaux devient déterminante. Il faut aujourd’hui l’aborder par une approche fonctionnelle (dans la chaîne de communication) et contextuelle ou in situ. La très grande variabilité des situations incite à aborder cette étude selon une approche statistique. En science, nous avons connu pendant plus de deux siècles que les phénomènes qui sont difficiles à prédire à partir des lois déterministes peuvent être prédits à partir de la théorie des probabilités avec un certain niveau d'incertitude acceptable. La modélisation statistique des antennes est basée sur cette reconnaissance très générale. Bien qu'il soit très rare d'utiliser des méthodes statistiques et probabilistes dans le domaine des antennes, il n'y a aucune raison fondamentale pour laquelle il devrait être prohibé.

Bien que l'histoire de la modélisation statistique des antennes soit vieille de plusieurs décennies, il a surtout été appliqué dans le domaine des processus de fabrication d'antennes. Un certain nombre d'articles ont été publiés dans ce contexte, la plupart d'entre eux sont principalement consacrées à l'étude du diagramme de rayonnement moyenne et le gain moyen. L'approche adoptée dans ce dernier est généralement basée sur la modélisation statistique de la tolérance qui est permis dans la fabrication des éléments d'antenne.

La représentation et la caractérisation des antennes ULB, multi-bandes ou environnées requiert une quantité de données sensiblement plus importante qu’en bande étroite ou isolées. Une approche prometteuse consiste d’abord à réduire fortement leur volume par une modélisation paramétrique des caractéristiques radioélectriques des antennes, l’objectif final étant l’obtention de modèles statistiques de *classes* d’antennes.

Dans cette thèse, nous nous sommes concentrés sur la modélisation statistique des petites antennes ultra large bande (ULB). Le travail effectué traite de deux questions principales, pré-requis importants pour la modélisation statistiques des antennes: la génération d’ensembles statistiques d’antennes (« réalisations ») suffisamment grands et la modélisation des principales caractéristiques d'une population d’antenne.

Nous avons proposé une approche de conception générique d'antennes planaires ULB comme outil à la fois pratique et efficace de génération de populations d'antennes suffisamment « peuplées ». Les principaux avantages de cette approche sont sa simplicité, sa flexibilité, sa versatilité (c'est-à-dire sa relative « généricité ») et son potentiel de généralisation. Sa flexibilité tient à la nature paramétrique du modèle qui permet des modifications incrémentales ou de grande amplitude. Sa versatilité tient à la grande variété de formes d'antennes accessibles (triangulaire, disque ou crab-claw). Divers monopôles et dipôles planaires ont été conçus par cette approche à titre d'exemples et en vue des analyses statistiques ultérieures.

Au total cinq monopôles (de formes triangulaire, circulaire, en marches d'escalier, en « pince de crabe » et à double alimentation), conçus ainsi sont présentés. Deux dipôles planaires équilibré, de formes triangulaire et elliptique, sont aussi présentés. Toutes ces antennes ont été optimisées —grâce à un algorithme évolutionnaire— selon des critères classiques : la compacité d'une part et l'adaptation d'entrée d'autre part, avec un coefficient de réflexion inférieur à −10 dB sur une bande ULB de [3—11] GHz.

Afin d'illustrer les possibilités de la méthode et de montrer sa versatilité, une conception multi-bande compacte a également été proposée dans le même esprit. Cette antenne opère dans les trois bandes WiFi IEEE 802.11 «a / g / n», «b / g / n» et «y». Une antenne biconique (volumique) a également été conçue selon une approche paramétrique analogue, et optimisée avec un algorithme génétique sous contraintes de bande ULB et de compacité (sphère minimale de rayon sub quart d'onde à la fréquence de coupure basse).

Nous avons aussi proposé une méthode assez générale (relativement systématique) permettant de générer une population d'antennes, à partir d'une conception optimale utilisée comme « générateur », par variations de paramètres géométriques ou physiques (incrémentales ou de grande amplitude) autour des valeurs optimisées. En utilisant cette méthode, les populations statistiques de toutes les antennes mentionnées précédemment ont été générées.

Une analyse statistique de ces antennes a été menée sur deux grandeurs caractéristiques (« observables » ou « variables » statistiques) : le rendement d'adaptation moyen (*MME*) et le maximum (angulaire) du gain réalisé moyenné sur la bande d'adaptation (MRG_{max}). Il a été observé que parmi plusieurs distributions candidates classiques, la loi des valeurs extrêmes généralisée (GEV) constitue un modèle approprié pour ces deux observables.

La caractérisation du rayonnement lointain des antennes ULB, correctement échantillonné, requiert une quantité importante de grandeurs complexes. Ce grand nombre de variables semble difficilement compatible avec une modélisation statistique ; c'est pourquoi il semble préférable dans un premier temps de réduire drastiquement ce nombre au moyen d'une modélisation paramétrique à très forte « réduction d'ordre ». L'association de la méthode des singularités (SEM) et de la méthode de développement en modes sphériques (SMEM) permet d'atteindre des taux de compression extrêmes (supérieurs à 99 %) avec une précision correcte. Ces techniques « d'ultra-compression » ont été utilisées pour modéliser les populations d'antennes évoquées plus haut, l'analyse puis la modélisation statistique portant sur les paramètres du modèle paramétrique à la place des grandeurs radioélectriques «primaires» telles que le champ ou la fonction de transfert. Pour les bicones, la symétrie de révolution permet une représentation à très faible nombre de paramètres.

Enfin, un modèle statistique de bicones a été proposé, avec 14 pôles pour la SEM, et un ordre dominant N = 5 pour la SMEM. Il a été observé que les fréquences naturelles de ce modèle sont définies avec la loi normale alors que la distribution des facteurs d'amortissement peut être modélisée avec la loi des valeurs extrêmes généralisée (GEV). Par ailleurs, les modaux résidus pourraient être raisonnablement bien décrits par une distribution de loi T-Scale. Un modèle pour le pôle fréquences naturelles (f_p) a été proposé et validé par la régénération de paires de pôles.

Le manuscrit est organisé comme suit: le chapitre 2 décrit la conception générique d'antennes planaires ULB. Les diverses conceptions d'antennes monopôles tels que disques, triangulaire, crab-claw etc., sont des variantes de la conception générique et sont décrites dans cette partie. La conception générique de planaire dipôle balancé est également abordée, avec deux exemples commun, triangulaire et disque dipôles balancés. Une version multi-bandes de la conception générique est également étudiée, ainsi que la conception 3D biconique.

Procédures d'optimisation des différentes conceptions, leurs espaces de paramètres et de leurs objectifs sont discutés dans le chapitre 3. La conception optimisée de chaque type d'antenne (classe ou sous-classe) discuté dans le chapitre 2 est ensuite décrite et analysée. La fonction de transfert d'antenne et de ses spécificités sont également abordés dans ce chapitre.

Le chapitre 4 est consacré à la génération d'une population statistique des antennes UWB, avec ses analyses statistiques. Ce concerne les paramètres globaux de radioélectriques, tels que le (MME) et la moyenne maximale du gain réalisé (MRGmax) pour chaque population de l'antenne (class et sous-classe). Modélisation des paramètres globaux radioélectrique est également étudiée dans ce chapitre.

La technique utilisée pour la compression ultra-haute des caractéristiques des données des antennes est expliqué dans le chapitre 5. La méthode d'expansion en mode sphérique (SMEM) et la méthode d'expansion de singularité (SEM) sont présentés avec quelques exemples. Ce chapitre se termine par une explication sur l'efficacité de modélisation des données compressé, basée sur la combinaison des deux méthodes ci-dessus. Le rôle de la symétrie structurelle de l'antenne sur les performances de compression est également discuté.

Enfin, la modélisation de rayonnement en champ lointain de l'antenne biconique en utilisant la technique ultra-compression est résumée dans le chapitre 6.

Contents

Abbreviations and Acronyms

AIR	Antenna Impulse Response
ATF	Antenna Transfer function
BW	Band width
CST MWS	Computer System Technology - Microwave Studio
CEPT	European Conference of Postal and Telecommunications Administration
DAA	Detect and Avoid
ECC	Electronic Communications Committee
EM	Electromagnetic
FCC	Federal Communication Commission
GMP	Generalized Matrix pencil
LDC	Low Duty Cycle
MME	Mean Matching Efficiency
MNP	Monopole
MRG	Mean Realized Gain
PBD	Planar Balanced Dipole
R_{min}	Radius of the minimal sphere around the antenna.
SEM	Singularity Expansion Method
SMEM	Spherical Mode Expansion Method
UWB	Ultra wide band
WiFi	Wireless Fidelity
WPAN	Wireless Personal Area Network

Chapter 1

Introduction

1.1. UWB Technology

“Ultra-wideband technology holds great promise for a vast array of new applications that have the potential to provide significant benefits for public safety, businesses and consumers in a variety of applications such as radar imaging of objects buried under the ground or behind walls and short-range, high-speed data transmission”,[1].

This quote shows the importance of Ultra wideband (UWB) technology as its applications are numerous and diverse. UWB communication is either based on the transmission of very wide band signals in the frequency domain or very short pulses with relatively low energy in the time domain. The short pulses allow very high data rates, for instance, in impulse radio and short ranges due to the low energy. In the near future, the use of this technology in the field of wireless communications and ranging will surely increase, owing to the many advantages offered by the technology. UWB technique has a fine time resolution which indeed makes appropriate for accurate ranging and positioning.

The term ‘ultra-wideband’ usually refers to a technology for which the transmission of information is spread over an extremely large operating bandwidth (BW), and this provides the possibility for these UWB communication systems to be able to coexist with other electronic systems. Though UWB technology has been around for decades, its original applications were mostly in military domains. However, the first Report and Order by the Federal Communications Commission (FCC) authorizing the unlicensed use of UWB on February 14, 2002, gave a huge boost to the research and development efforts of both industry and academia [2]. The intention is to provide an efficient use of limited frequency spectrum, while enabling short-range but high-data-rate wireless personal area network (WPAN) and long-range but low-data-rate wireless connectivity applications. The table below encompasses the frequency bands for possible UWB systems use, as envisioned by the FCC in 2002.

Table 1.1 Frequency ranges for various types of UWB systems under -41.3dBm EIRP emission limits

Applications	Frequency Range (GHz)
Indoor communication systems	3.1-10.6
Ground-penetrating radar, wall imaging	3.1-10.6
Through-wall imaging systems	1.61-10.6
Surveillance systems	1.99-10.6
Medical imaging systems	3.1-10.6
Vehicular radar systems	22-29

1.1.1. UWB bandwidth

According to FCC definition, any signal is called UWB if it has a fractional bandwidth (bw) larger than 0.20, or which occupies a bandwidth (BW) greater than 500 MHz. The fractional bandwidth is defined as the ratio of signal bandwidth to the center frequency f_c:

$$bw = \frac{BW}{f_c} = \frac{(f_h - f_l)}{(f_h + f_l)/2} \quad \text{----------(1.1)}$$

Where, f_h and f_l are the upper and lower transmitted frequencies at –10 dB emission points. The conventional radio signals i.e. narrowband and wideband signals have quite small fractional bandwidths when compared to UWB signals (Fig. 1.1). For example, The UMTS system, which operates around 2 GHz and with 5 MHz BW, has a fractional bandwidth of 0.0025, which is around 80 times smaller than 0.2 according to relation (1.1).

1.1.2. FCC Spectral Mask

The FCC has assigned the effective isotropic radiated power (EIRP) allowed for each frequency band, mentioned in Table 1.1, in order to avoid interference with existing communication systems. This regulation limits various regions of the spectrum to have different power spectral densities (PSD).

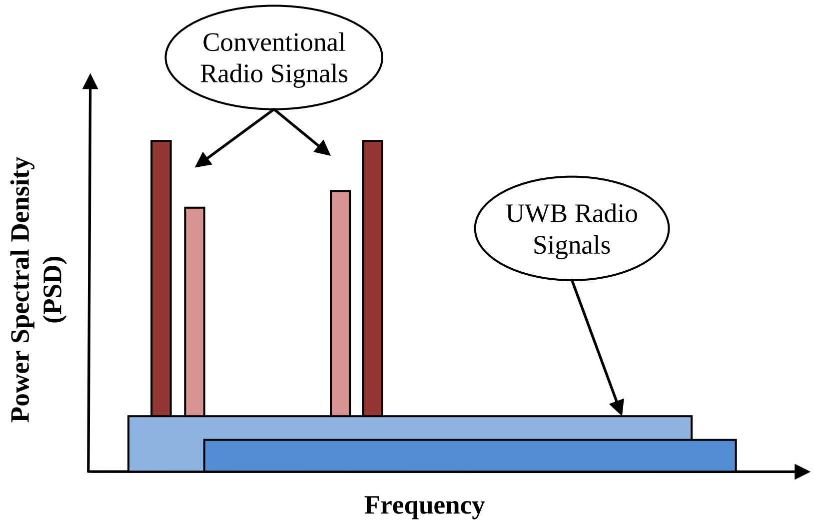

Fig. 1.1 Spectrum of UWB signals versus conventional signals

The EIRP (equivalent isotropically radiated power or Effective isotropic radiated power) is the amount of power radiated by a transmitter, relative to theoretical isotropic antenna or radiator. EIRP refers to the highest signal strength measured in any direction and at any frequency by the UWB device or system. EIRP is used to estimate the service area of the transmitter, and to coordinate various transmitters on the same frequency, so that their coverage areas do not overlap. Fig. 1.2 illustrates the FCC radiation limits for the indoor and outdoor UWB communication systems. The level of –41.3 dBm/MHz in the frequency band of 3.1–10.6 GHz is set to limit interference to existing communication systems and to protect the existing radio services. This level (–41.3 dBm/MHz), is 75 nW/MHz, which is in fact identical to the unintentional radiation level of television sets or monitors [2]. For the indoor and outdoor UWB communications, the FCC radiation limits in the frequency range of [3.1–10.6] GHz are alike. While for the [1.61–3.1] GHz frequency range the outdoor radiation limit is 10 dB lower than the indoor mask. It should be noted that FCC rules confine the outdoor UWB communications to handheld devices with no use of fixed infrastructure.

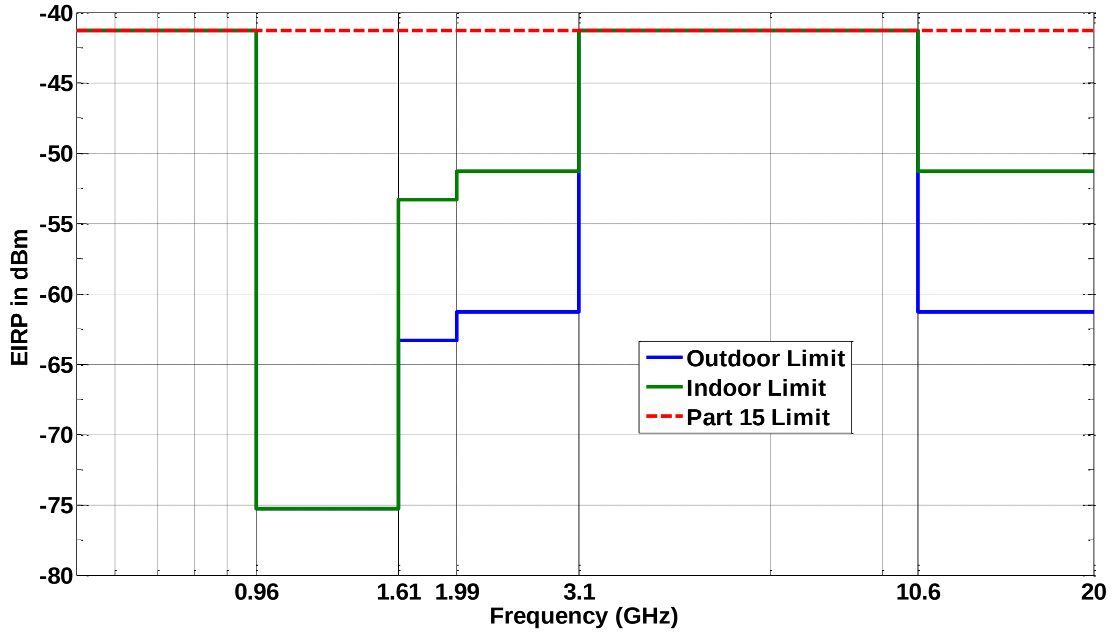

Fig. 1.2 UWB ERIP emission mask authorized by FCC for Indoor and Outdoor communications.

In USA, the UWB band is 3.1—10.6 GHz. However, the European regulations put more severe constraints on the use of UWB technologies than in the USA. Fig. 1.3 depicts the current status of the regulation in Europe. The band for which there is no more restriction than in USA is the 6 to 8.5 GHz band. The band from 3.1 to 4.8 GHz can be used in LDC (Low Duty Cycle) conditions, while the one from 4.2 to 4.8 GHz can be used in Detect and Avoid (DAA) conditions.

1.1.3. UWB signal

UWB pulses are typically narrow time pulses of sub-nanosecond or Pico-second’s order. The fundamental signal that may be used for the UWB transmission is the Gaussian pulse [3] expressed as:

$$G(t)=\frac{A}{\sqrt{2\pi\sigma^2}}e^{\left[\frac{-t^2}{2\sigma^2}\right]} \quad \text{------(1.2)}$$

Where, ‘A’ and ‘σ’ denote the amplitude and spread of the Gaussian pulse, respectively. The Gaussian pulses are frequently used in the UWB systems since they can be easily generated by pulse generators. Usually higher derivatives of Gaussian shape are more popular for the UWB transmission. This is mainly due to the DC value of the Gaussian pulse. As antennas are not efficient at DC, it is preferable to use derivatives of Gaussian shape having smaller DC components.

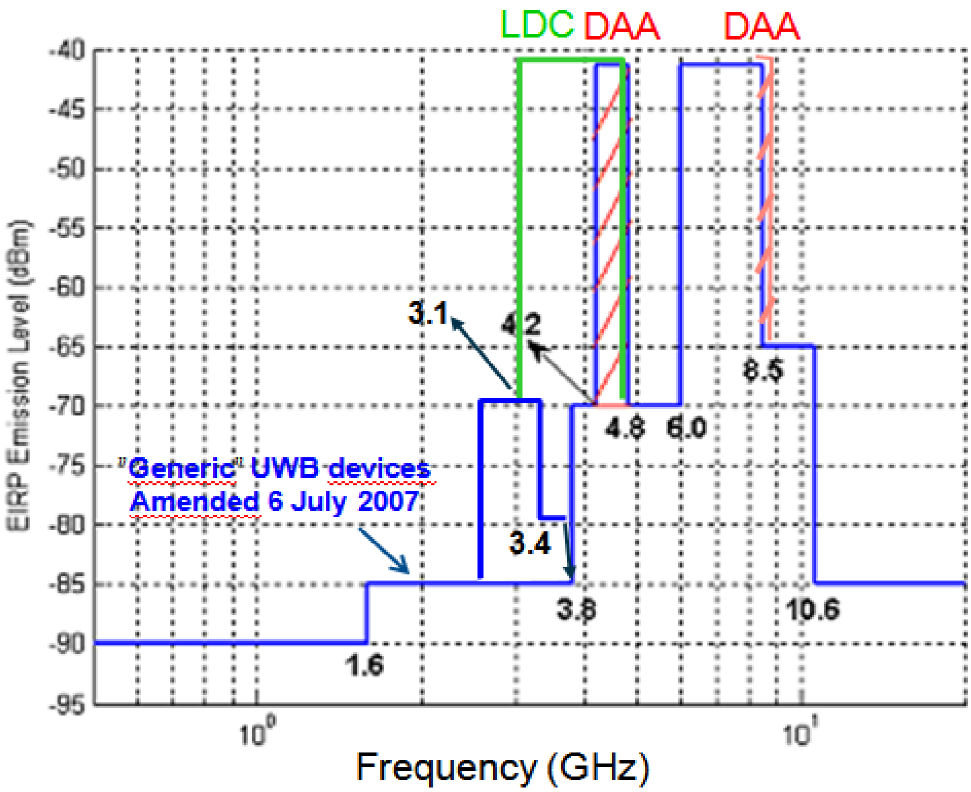

Fig. 1.3 UWB ERIP emission mask in Europe by ECC of CEPT.

The nth derivative of Gaussian pulse can be obtained recursively from the following expression:

$$G^n(t) = \frac{d^n}{dt^n}\left[e^{-t^2/2\sigma^2}\right] \text{---(1.3)}$$

In Fig. 1.4 the first derivative also called Gaussian mono pulse and second derivative also called Gaussian Doublet pulse and their spectrum are shown. It is worth mentioning that due to the properties of transmitter and receiver antennas, which are usually modeled as differentiators, the received pulse is further differentiated by the antennas. The design of these signals for emission control is important. The pulse length, rise time of the leading edge of the pulse, and the pass-band of radiating antenna determine signal bandwidth and spectral shape, while the pulse shape determines its centre frequency. In [6] it has been shown that for indoor communication a fourth order derivative and for outdoor communication a seventh order derivative of Gaussian pulse comply the FCC spectral mask.

Another pulse that is used often with UWB systems is Rayleigh mono-pulse, or first order Rayleigh pulse [4],

$$p(t)=\left[\frac{t^2}{\sigma^2}\right]e^{\left(\frac{-t^2}{2\sigma^2}\right)} \qquad (1.4)$$

The Gaussian and Rayleigh mono-pulses have similar spectral shapes and effective time duration, although they are temporally even and odd respectively. Other UWB signals are Laplacian, and Cubic [4] waveforms, and modified Hermitian monocycles [5]. In all these waveforms the goal is to obtain a nearly flat frequency domain spectrum of the transmitted signal over the bandwidth of the pulse and to avoid a DC component.

1.2. Challenges and Requirements of UWB Antenna design

One of the challenges for the implementation of UWB systems is the development of a suitable or optimal antenna. The UWB system characteristics are heavily dependent on the design of the radiating element. The requirements imposed on UWB antennas, such as the phase linearity and the spectral efficiency, are more demanding than narrow band and broad band antennas. In designing UWB antenna, both the frequency and time-domain responses should be taken into account. In the following, the fundamental requirements for the UWB antennas are discussed briefly. In chapter 3 the parameters for characterizing a UWB antenna will be discussed.

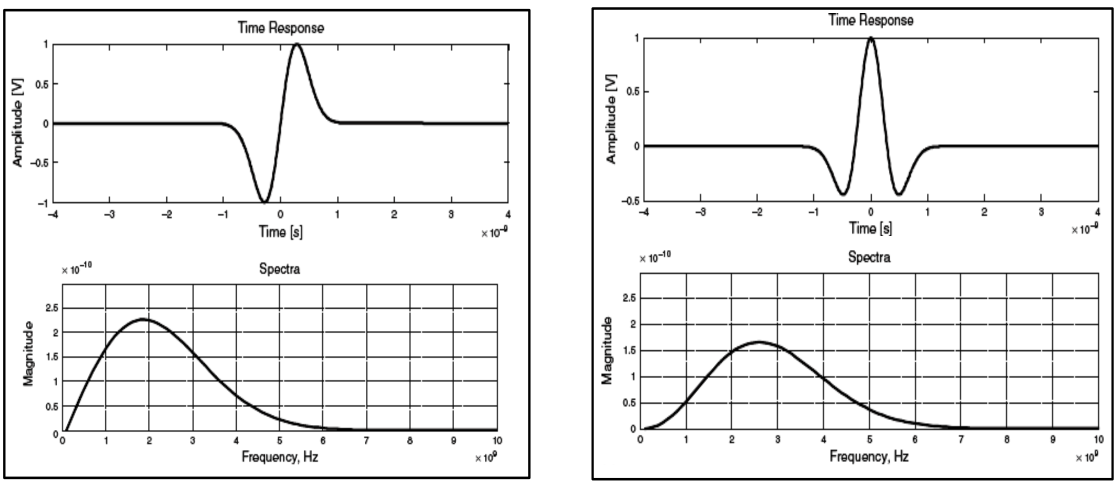

(a) (b)

Fig. 1.4 Gaussian pulses, (a) Mono (b) Doublet (source)

1.2.1. Input Impedance bandwidth

The impedance bandwidth is measured in terms of reflection coefficient or voltage standing wave ratio (VSWR). Usually, the return loss should be less than 0.312 (or −10 dB reflection coefficient) for an antenna to be considered properly matched. An antenna with an impedance bandwidth narrower than the operating bandwidth behaves like a band pass filter and, as a result, modifies the transmitted/received signal. In other words, it reshapes the radiated or received pulses in the time domain.

Small UWB antennas have a small radiation resistance and a large reactance. Consequently, it is difficult to achieve a suitable impedance matching. Therefore, the threshold of −10 dB can be seen as a too strict criterion when enforced over the whole operating bandwidth. Instead a more relaxed −6 dB threshold can also be considered, especially when it is neared over a small bandwidth as compared to the total BW of interest.

1.2.2. Spectral Efficiency

It is a measure of how efficiently a limited frequency spectrum is utilized for information rate. In other words, it evaluates the quality of matching over the frequency band. It is defined [7] as:

$$\eta_{rad}\left(\%\right)=\frac{\int_0^\infty P_t\left(\omega\right)\left(1-\left|S_{11}\left(\omega\right)\right|^2\right)d\omega}{\int_0^\infty P_t\left(\omega\right)d\omega}\times 100\% \text{ --(1.5)}$$

Where, P_t is the power at the antenna terminals. This efficiency is representative of the antenna performance over the whole spectrum. More precisely, the matching efficiency should be multiplied by the radiation efficiency in order to provide a global efficiency integrating all sources of losses. The latter include the conduction and dielectric efficiency, where applicable [8]. If these conductor and dielectric losses are negligible, then total efficiency is given by (1.5).

1.2.3. Signal distortion and dispersion

An antenna introduces a deformation of the output radiated pulse, as compared to the input pulse. Usually, the output pulse is a stretched-out version of the input pulse, owing to the fact that often enough an antenna acts as a mathematical differentiator.

The dispersion is another way to express the fundamental phenomena at the origin of the distortion. It expresses the fact that the delay experienced by the wave in the course of its progression from the input port to the air, is frequency dependent. From the properties of the Fourier transform, this is a cause of distortion. In some cases, it is appropriate to view this phenomenon as a movement of the antenna phase center with frequency. An exemplary case is that of the log-periodic antenna, where this movement can be ascribed to the changing position with frequency of the dipoles exhibiting a strong current. Then, it appears intuitive that we will have a variation of the radiated UWB pulse shape as a function of the look angle. The detrimental character importance of distortion and dispersion in UWB communications at high data rate has been stressed and analyzed in [9]. As a consequence, low distortion and low dispersion are requirements on antennas for such applications.

1.3. Context of the work

The history of UWB antennas goes back to 1898, according to Schantz [10]. Lodge disclosed spherical dipoles, square plate dipoles, biconical dipoles and triangular or “bow-tie” dipoles in his patent [11]. He also introduced the concept of a monopole antenna using the earth as a ground [10]. Since then, many derivatives of these dipole and monopoles, in addition to new designs have been proposed [12].

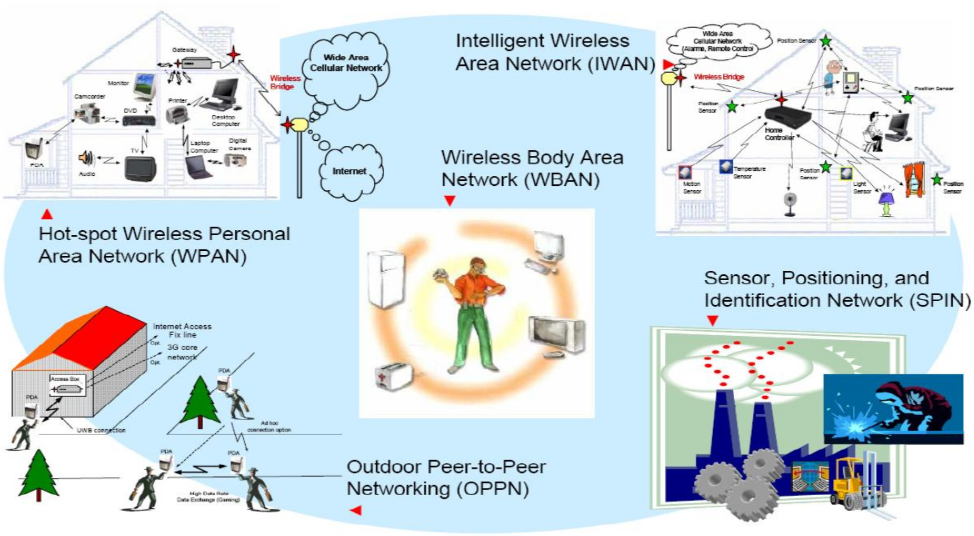

Fig. 1.5 Some application area for small UWB devices [21]

Since the FCC published its regulation decisions, the area that has relatively more interest than others are small UWB communication devices/equipments, some potential application areas being shown in Fig. 1.5. In such devices, the size of the antenna is one of the main concerns, as the overall size of the devices must be small. In this context, the requirements for UWB antenna design are more challenging than ever.

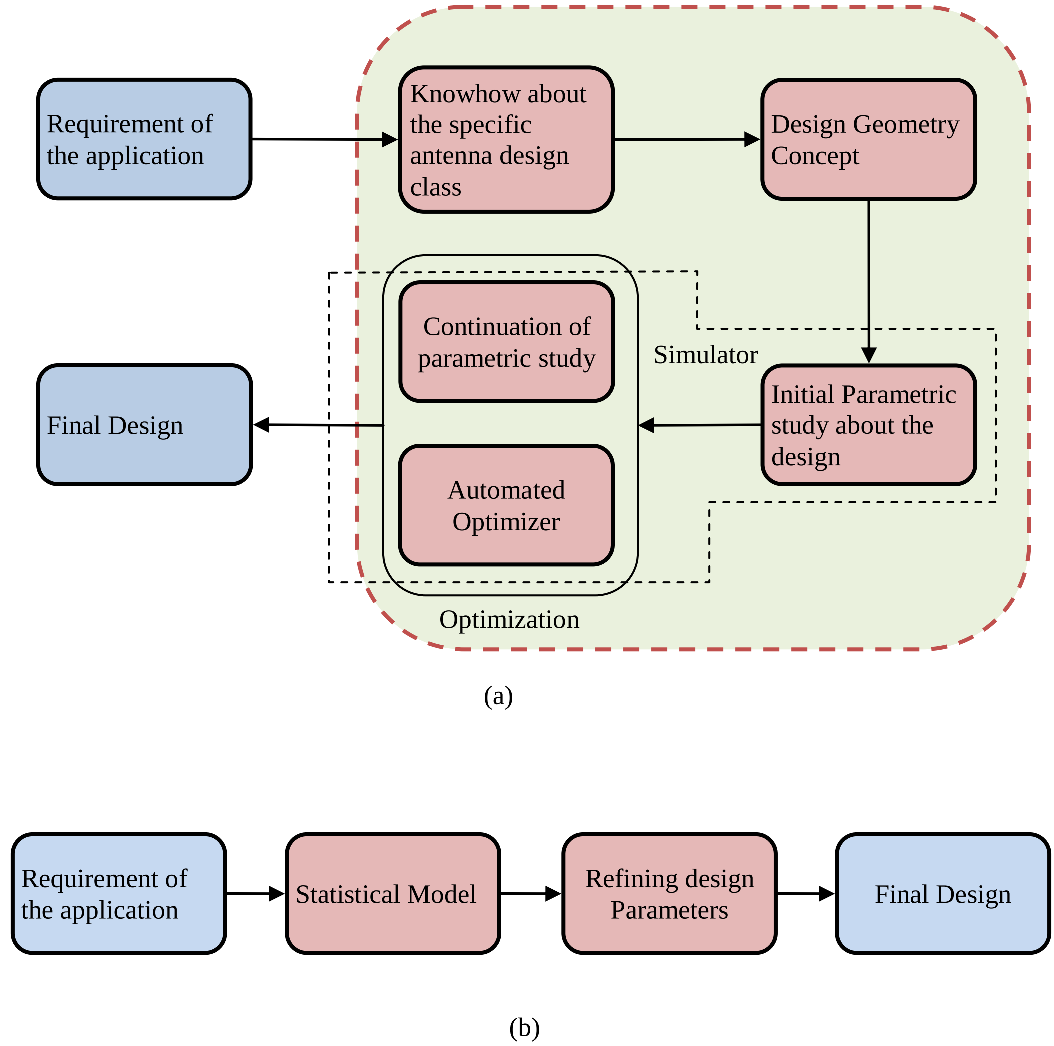

Fig. 1.6 Antenna designing flow (a) A conventional way (b) A statistical Model Approach

Planar monopole antennas are good candidates for use in UWB wireless technology, because of their wide impedance bandwidth and quasi omnidirectional azimuthal radiation pattern. The patch monopoles can be integrated with other components on a printed circuit board, without the need of a back ground plane. This makes the printed antenna technology very cost effective, which is ideally suited for UWB technology-based low-cost systems [13—20]. In these antennas, the coplanar waveguide (CPW) configuration is more suitable than other feeding techniques, as it facilitates the use of an active device placed near the antenna's radiating element. In addition, of course, there is an easy connectivity with other integrated circuits, hybrid or monolithic.

However, in any antenna design endeavor, the aim is to meet the application specific requirements. The possible steps towards this goal can be presented as depicted in Fig. 1.6a. The antenna geometry is among the first considerations of the design engineer, because a number of general constraints point to a limited set of geometries (required form factor for integration into a device, complexity limitations for cost reasons, fabrication simplicity etc.). By chance, there is an enormous amount of literature on antenna design, numerous handbooks and even now libraries of antenna elements or of complete antennas in certain software tools [22]. Nevertheless this literature is help full but not the solution, since the specific requirements are never met by a given antenna. These requirements are typically the operating frequency band, the required maximum gain, the matching efficiency and the size of the antenna. Often enough, antenna designers put forward a design concept that might fulfill the given requirements. The parameters of design geometry are subsequently studied with, usually, an electromagnetic (EM) simulator as a powerful tool in order to determine the deterministic effect of these parameters with respect to the requirements Depending of the complexity of the design and the experience of the engineer, the optimization is performed manually (through a parametric study) or by the use of an automated optimization module, which is nowadays commonly available in many EM simulators. Unfortunately, the complexity of the design may cause the automated optimization to need several passes till the final design is achieved.

The bottom line of the above procedure is the design time required from the start to the final design. This time may go from days to months, depending on the antenna complexity and the difficulty of the requirements, which is in a "time to market" competitive context a real penalty.

An alternative approach, though unconventional, might be to base the design methodology on a pre-existing knowledge about the influence of parameters. From this knowledge, it would be a priori possible to guess the variation of the antenna characteristics for the various parameter changes. Unfortunately, in a general case the number of design parameters is enormous, so that a deterministic approach to the problem is a losing approach. In science, we have known for more than two centuries that phenomena that are difficult to predict from deterministic laws can be predicted, to a certain level of uncertainty, from the theory of probabilities. The statistical modeling of antennas is based on this very general recognition. Although it is very uncommon to use statistical and probabilistic methods in the world of antennas, there is no fundamental reason why it should be forbidden, or even uninteresting. This thesis is, besides, by no means a founding work, since the theory of probability has been used in the context of electromagnetism and antennas for several decades, as recalled in the state of the art below.

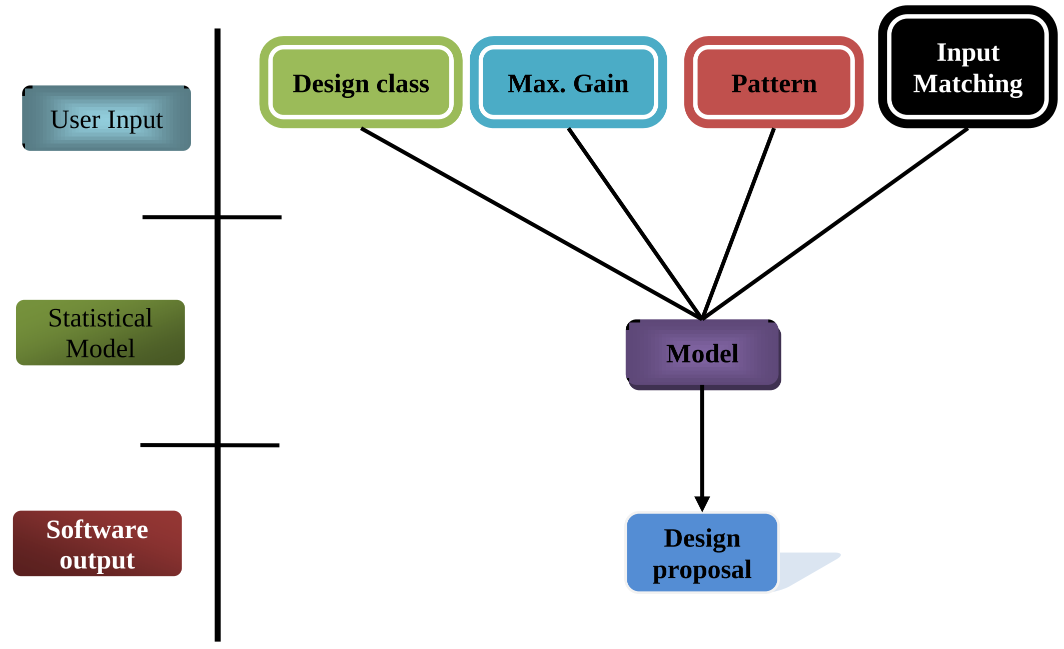

Fig. 1.7 A possible application example for statistical approach

Turning back to the goal of antenna design, we therefore have a new way to reach a design goal from the start, as shown in Fig. 1.6b. Here, starting from the given design requirements, the statistical model, which is supposed to have been developed previously, proposes the selection of certain design parameters such as the shape, the size or in some cases the operation principle. Based on its pre-existing statistical knowledge of the influent parameters, such a "statistical module" would be very helpful in computer aided design, by discouraging the designer to try this or that parameter variation. As a consequence, there would be more chance for the designer to approach the design goal quickly, after which a fast refinement with the

EM simulator would be sufficient to achieve the optimal design. This approach provides a clear advantage of time over the conventional approach by eliminating the steps shown inside the dotted red border (Fig. 1.6a).

This application concept is illustrated in Fig. 1.7. Here, the "design class" refers to e.g. monopole or dipole designs, or patch design, log-periodic design etc. Additional user inputs can also be imagined such as input feed technology (CPW, strip-line etc) and antenna subclasses such as disc monopole and triangular monopole.

Another application of such an approach is in the design process of UWB communication systems. When calculating the link budget of the overall communication link, designers usually assume a certain value for the gain of the antenna that will be incorporated in their system. However this target value is all but guaranteed without ensuring that the constraints allow it.

Appropriate Estimation of Effective
Gain vs avalaible Space

$$\frac{P_R}{P_T} = G_T G_R \left(\frac{\lambda}{4\pi R} \right)^2$$

Fig. 1.8 Friis transmission equation

By using previous statistical modeling, it would be easier to estimate the antenna gain with respect to available size in their system. In addition, and this is where UWB specificities take their full character, requirements on the level of distortion could also be considered. Since UWB antennas put an even stronger pressure on the antenna designer due to the necessity to take into account new − time domain − requirements, it is clear that the increasing complexity of the design problem further pleads for statistical methods. Finally the methodology could reduce the overall cost of the system, which is one of the objectives of UWB applications, expected to concentrate towards small, cheap and widely disseminated devices.

1.4. State of the Art

Though the history of statistical antenna modeling is several decades old, it has been mostly applied to the field of antenna manufacturing process. A number of papers have been published in this regard [23]–[34]. Most of them are mainly devoted to the study of the mean radiation pattern and the mean gain. The approach adopted in these papers is usually based on the statistical modeling of the tolerance that is permissible in manufacturing of the antenna elements.

Yakov Solmonovich SHIFRIN, in particular, has investigated many antenna field related problems and has established the formulation of general statistical antenna theory [35]. He developed his theory around "time statistics" i.e. statistics taken in time from an individual antenna rather than "ensemble statistics" which is the statistics taken over the ensemble or group of similar antennas. To some extent, the latter case is much closer to the work carried out within this thesis.

SHIFRIN has investigated the antenna statistics by dividing the antenna analysis problem into two partial problems: the internal and the external problem. The internal problem intends to find the statistics of the amplitude and the phase excitation of the antenna. The external problem deals with the statistics of the field, elaborating on the results given by the solution of internal problem. Shifrin focused on the statistics of the field and assumed that the statistics of the amplitude and phase of the excitation were given inputs.

With respect to the focus of this thesis, the first relevant paper in this domain can be found in [36], in which a preliminary approach towards the statistical modeling for small UWB antennas has been proposed. In this paper, the author argues about the characterization of an average behavioral model of the antenna radiated field, through a reduced number of parameters. He showed that a reduction in the number of parameters expressing the antenna behavior could be achieved using spherical mode expansion method (SMEM). A 90% reduced parametric model has also been shown.

In the same paper he investigates the two types of problem sets; firstly an antenna statistical description with its near application dependent environment, secondly, the definition of entire classes of antennas and the extraction of a statistical model called "generator" of this class.

Another paper in the same spirit has been published by the same author [37]. In this paper he presented the ultra-compression technique to reduce the required number of parameters for antenna characterization. He uses the Singularity Expansion Method (SEM) to synthesize the antenna response in poles and residues and subsequently applies the SMEM on the antenna residues. In this way, up to 98%

reduction in the number of parameters can be achieved without compromising the quality of the reconstructed antenna radiation.

1.5. Objectives

The subject of antenna modeling is very vast and in case of UWB antenna its complexity is further enhanced. For that reason, the thesis concentrates the investigation of statistical antenna modeling methods on UWB antennas. Given the large amount of published UWB antenna designs; it also mainly focuses on planar antennas, which are particularly interesting for their compactness and cost effectiveness, in-line with the major requirements imposed by commercial UWB systems.

- The first objective of the work is to propose an efficient way of designing UWB antennas. More precisely, the goal is to propose a generic design approach through which many designs, similar or different, can be generated.
- Since the most stringent requirement of UWB antennas i.e. compactness while respecting the conventional ceiling of -10 dB for the reflection coefficient in an input bandwidth of $[3.1-10.6]$ GHz, the second objective of the thesis is to achieve an optimal design from the proposed method.
- The effective statistical modeling requires an adequately large population of random samples and the final modeling capability is sensitive to the choice of the population. Thus, the third objective is to describe a procedure that is best suited for the generation of populations of UWB antennas. This brings up two more questions:
  - What type of statistical distributions can be found for the radio-electric parameters of such a population?
  - Is there any relation between or among the different global radio electric parameters that would help in the assessment of the statistical properties?

  Both are vast questions, which can only be tackled in the present work.
- Statistical antenna modeling implies the access to the antenna radio-electric behavior, in particular the far-field pattern. The statistical modeling of this important characteristic of the antenna constitutes the fourth objective of the thesis.

In addition to these objectives the general methodology adopted to answer the above mentioned questions, is a key issue, which will be addressed as such. This will imply, in particular, the development of specific software tools and algorithms.

1.6. Methodology

To cope with the various objectives of the thesis the adopted methodology also has many aspects. Starting with the first objective, the generic design (discussed in chapter 2) is based on a combination of trapezoidal patches that can be arranged in various shape or profiles. Let a generic antenna design, parameterized for minimum degree of freedom, then geometrical constraints are imposed on this generic design to have different profiles (such as triangular, disc, staircase etc). The parameterized design can be divided into independent and dependent parameters. The parameter space (or sample space) is defined for independent parameters which are uniformly distributed within the design specific ranges.

Searching an optimal design that respects the stringent requirements of UWB antenna is now relatively less complex due to the effective parameterization. Compactness and good input matching ($|S_{11}| \leq -10$ dB) are two main objectives at this step. Optimization can be performed manually by parametric study or through built-in optimizers such in CST MWS® EM software.

Once the optimal design is obtained, a new parameter space is defined around the optimal values. Various samples are then created through the Monte Carlo scheme – that is by creating a population from this design. Alternatively, the same initial parameter space for the optimization can be used. This is discussed in detail in chapter 4.

Each antenna sample (antenna realization) is simulated and eventually the population of antennas constituting a *subclass* is created. Statistical analyses with respect to certain criteria can be performed on the simulated results. The question of which antenna subclass is better according to any global radio electric parameter — Mean Matching Efficiency (MME), Mean Realized Gain (MRG) etc can be answered at this stage.

Modeling of these global radio-electric parameters is the next objective of the thesis and can be explored at this stage. Statistical models of the input matching and the MRG can be exploited for the population. This constitutes the third objective of the thesis.

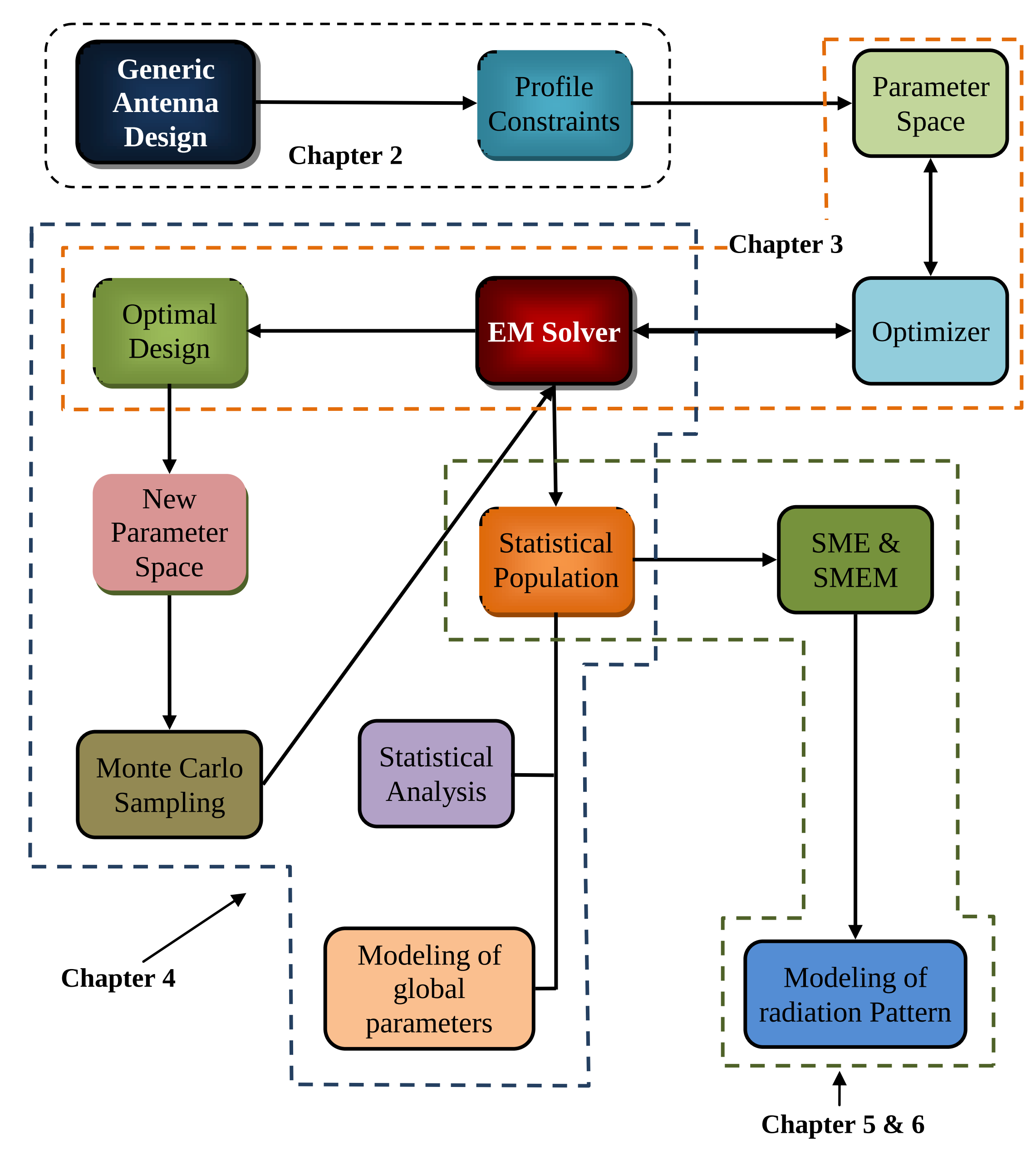

Fig. 1.9 Adopted methodology

The modeling of the far-field radiation of any antenna class or subclass is a very complex job, since the number of parameters required to define a typical full 3D UWB radiation pattern are in the order of 10^5. Hence it is impractical to model the behavior of each parameter for the whole population. The alternative approach is to reduce these pattern related complex parameters to a level where modeling is practically possible.

The singularity expansion method (SEM) and the Spherical mode expansion method (SMEM) are two antenna parametric modeling techniques which provide the required compression to pattern related complex parameters: compression rates to more than 99% are achievable. Modeling the output of these two techniques yields a model for the radiation patterns.

1.7. Organization of the thesis

The body of the manuscript is organized as follows: chapter 2 describes the generic design of planar UWB antennas. Various designs of monopoles antennas such as disc, triangular, crab-claw, etc, are variants of the generic design and have been described in this part. The generic design of the planar balance dipole has also been addressed, with two commonly known designs examples: triangular and disc balance dipoles. A multiband version of the generic design has also been investigated, as well as the 3D biconical design.

Optimization procedures for different designs, their parameter spaces and their goals have been discussed in chapter 3. The optimized designs of each of the antenna type (class or subclass) discussed in chapter 2, have been then described and analyzed. The Antenna transfer function and its specificities have also been discussed in this chapter.

Chapter 4 is devoted to the generation of a statistical population of UWB antennas, together with its statistical analysis. This concern the global radio-electric parameters, such as the (MME) and the maximum mean realized gain (MRG_{max}) for each population of the antenna subclass. Modeling of the global radio-electric parameters has also been studied in this chapter.

The technique used for the ultra-high compression of antenna characteristics data sets has been explained in chapter 5. The spherical mode expansion method (SMEM) and the singularity expansion method (SEM) have been presented with some examples. This chapter ended by explanation on the efficiency of compressed data modeling, based on the combination of the two above methods. The role of the antenna’s structural symmetry on the compression performance has also been discussed.

Finally, far-field radiation modeling of biconical antenna using the ultra-compression technique is summarized in chapter 6.

Chapter 2

Antenna Designs

2.1. Introduction

In the context of statistical modeling of UWB antennas, one of the fundamental problems is the creation of a sizeable and representative statistical population. The constitution of such an antenna database requires some appropriate strategy, to be efficient and relevant. A statistical model or even a statistical inference is sensitive to errors in sampling such as the selection bias and random sampling. In addition errors that are caused by other problems in data collection and processing can also lead to wrong conclusion.

Conventional antenna design requires an initial gross idea of the design and a parametric study in order to reach the suitable performance through an iterative process, complemented in general by a fabrication and test of the designed antenna. This process is a very time consuming exercise.

This well known difficulty led us to investigate a technique that is both flexible in terms of designing various antennas and simple to operate. It could be very helpful in studying the behavior of the antennas and possibly faster than conventional methods in producing specified antennas. In short, the method is based on a “generic” antenna design, and has been applied to planar UWB antennas in order to accommodate all the aforementioned characteristics.

In this chapter a generic geometry for planar antennas is first discussed and its versatility is illustrated by various examples such as triangular, disc and dual feed monopoles. The balanced version (dipole) of this generic design is explained on the basis of two examples: a triangular and a disc dipole. Finally 3D bi-conical design has been discussed at the end in the same spirit for generation of statistical population.

2.2. Generic Geometry

The main idea of a generic design [39] is to elaborate a variety of shapes as large as possible, involving a parameterization process as simple as possible. It is focused here on planar UWB antennas, although it could be applied to other categories of antennas. A possible solution to construct a generic design is to build it from elementary objects, which are both very simple and sufficiently flexible. Given these constraints, trapezoids have been selected to be such objects, as they offer a good compromise between versatility and simplicity. The antenna geometry is indeed simply the juxtaposition of trapezoids as shown in Fig. 2.1. The versatility is illustrated by the variability of antenna geometry, which can cover known designs as well as unknown ones.

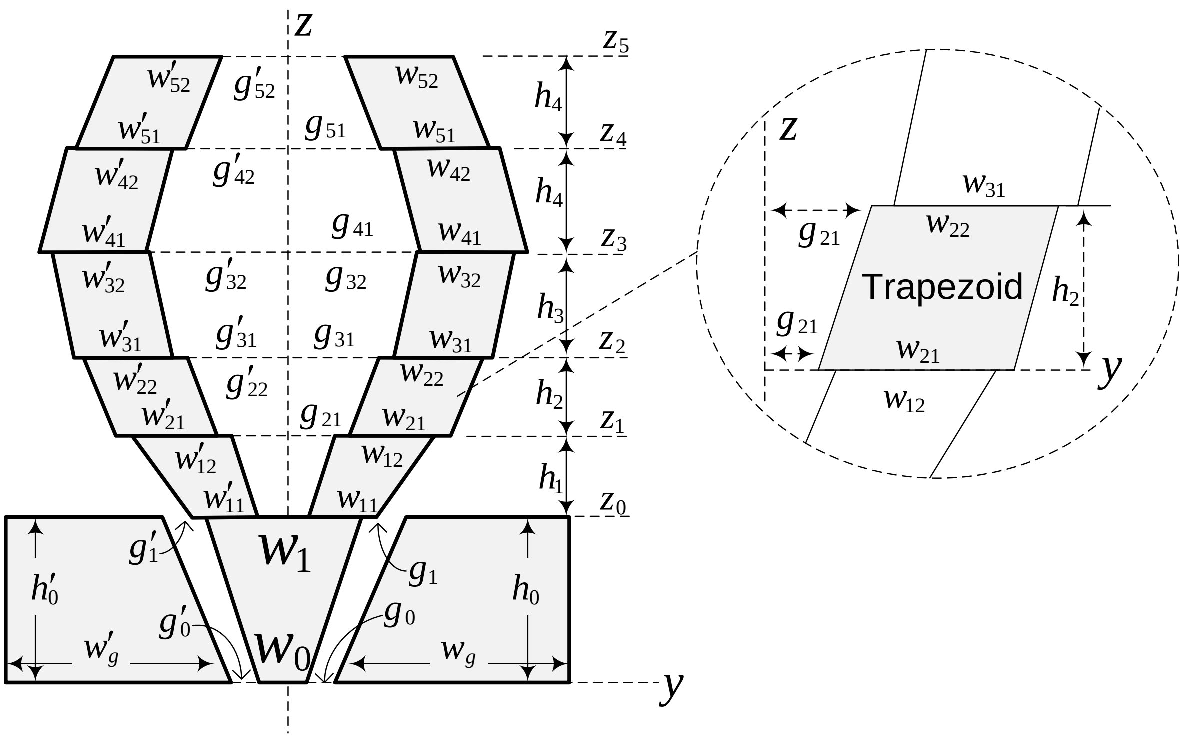

Fig. 2.1. Generic geometry for UWB planar antennas.

Each trapezoid of the k^{th} layer is defined by its height h_k, lower (w_{k1}) and upper (w_{k2}) widths, and lower (g_{k1}) and upper (g_{k2}) gaps, as shown in the inset of Fig. 2.1. In the following, for simplicity and practical reasons, the geometry is supposed symmetrical with respect to the xOz plane, although primed parameters are used on the left side to be able to address the more general non symmetrical case; one such design example is shown in Fig. 2.2.

A Coplanar Waveguide (CPW) technology has been chosen for the feeding part, as it is known to be less sensitive to the common mode than its microstrip counterpart, and, of course, since it is a single layer technology. The feed is a priori a non-uniform transmission line, only from the geometrical point of view (i.e. at constant aspect ratio $w/(w+2g)$ corresponding to constant characteristic impedance Z_C), but also if required non-uniform in the classical sense (variable Z_C). The CPW feeding is defined by the parameters w_0, g_0, h_0, w_1, g_1 and w_g.

Different designs can be conceived by varying the parameters $\{w_{k1}, w_{k2}, g_{k1}, g_{k2}, h_k\}$ of the trapezoid at each layer k. Fig. 2.4 shows some of the possible designs. For example, to form a “bow tie” or triangular shape (Fig. 2.4c), all gaps g_{k1} and g_{k2} are set to zero and the condition $w_{k2} > w_{k1}$ is imposed. Similarly, the staircase geometry (Fig. 2.4b) is obtained by setting g_{k1}, g_{k2} to zero and $w_{k2} = w_{k1}$. Any circular (or elliptic) disc monopole (Fig. 2.4e) can be formed by setting gaps to zero and conveniently performing the discretization of the circle (ellipse) with the trapezoid external vertices. The Dual Feed Monopole is known for its compactness [40]–[43]. It was originally designed in strip line (DFMS) [42] and microstrip (DFMM) [43] technologies. Here a CPW version of this antenna can be envisaged (Fig. 2.4d). Finally, a multiband behavior can be achieved with a double slot design (Fig. 2.4f). All these antenna designs are discussed in detail in the subsequent sections.

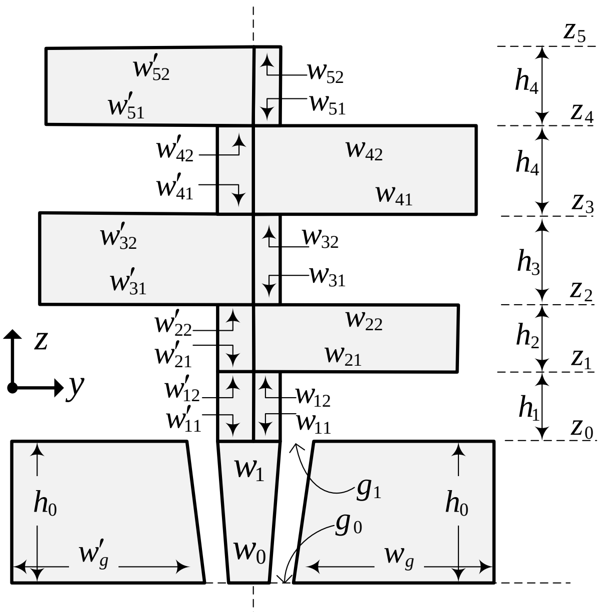

Fig. 2.2. A non-symmetrical design example

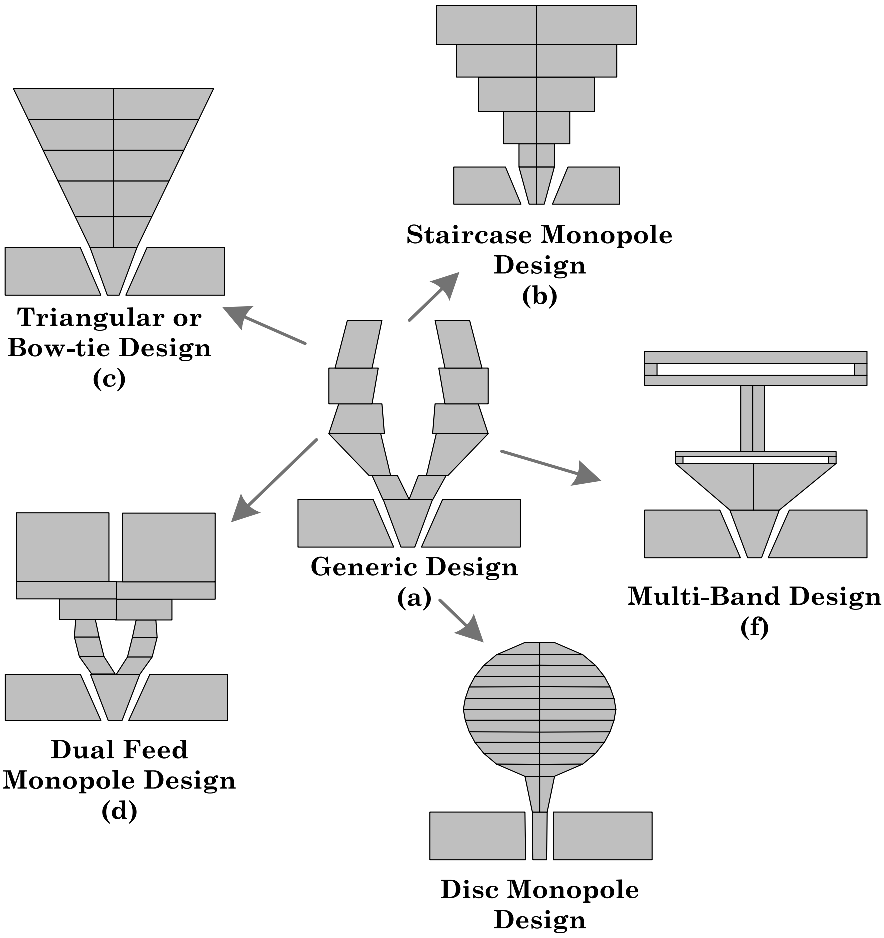

Fig. 2.4 various design derivatives of generic geometry

This concept of generic geometry can also be applied to balanced antennas such as dipoles; At least two alternative designs may be derived: first, the ground plane can be "shaped". Second, a purely balanced version can be designed thanks to a lateral feed, either preserving a single layer technology – a wideband CPW to Coplanar Strip (CPS) balun being required in this case –, or with a bi-layer technology and a microstrip to symmetrical strip (broadside) balun (Fig. 2.3).

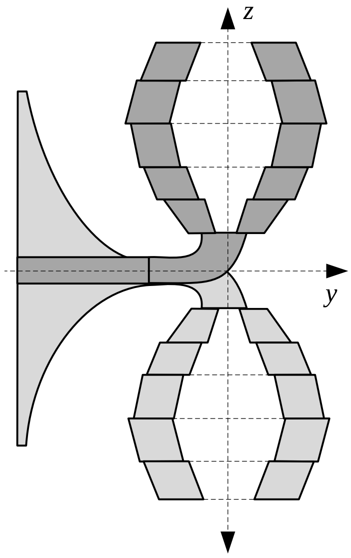

Fig. 2.3 Generic BALANCE dipole design

2.3. Parameterization

One of the most important free parameters is the radius R_{min} of the smallest circumscribing sphere[1], from which most of the design parameters depend directly or indirectly. It is indeed directly related to the lower corner frequency, hence to the frequency bandwidth.

The angles ψ and γ determine the upper $y_K = g_{K2} + w_{K2}$ and the lower ($y_{01} = \frac{1}{2}w_0 + g_0 + w_g$) widths respectively. In addition these angles control the total height H_{total}.

$$H_{Total} = d_1 + d_2 = R_{\min}\left[\cos\left(\frac{\psi}{2}\right) + \cos\left(\frac{\gamma}{2}\right)\right] \quad (2.1)$$

The top width y_K and bottom width y_{01} are defined as

$$y_{01} = R_{\min}\sin\left(\frac{\gamma}{2}\right) \quad (2.2)$$

$$y_K = R_{\min}\sin\left(\frac{\psi}{2}\right) \quad (2.3)$$

In practice, R_{min} is fixed at first, and ψ and γ are uniformly distributed random variables (rv) within the desired ranges. As can be seen, numerous geometries with different heights and widths can be addressed for a given circumscribing sphere

Let $\kappa = H/h_0$, the radiating part height (H) to the ground plane height (h_0), then by changing κ various samples of different ground plane heights can be generated.

$$H = \left(\frac{H_{Total}}{1+\kappa}\right)\kappa \quad (2.4)$$

$$h_0 = \left(\frac{H_{Total}}{1+\kappa}\right) \quad (2.5)$$

The CPW feed is defined by the independent parameters w_0, g_0, α, ζ (Fig. 2.5) and the dependent parameters w_1, g_0, w_g, calculated as:

[1] Actually, the minimal sphere may be larger than the sphere of radius R_{min} as defined in Fig. 2.5 (for its simplicity), since any inner layer k ($k < K$) may have an outside part for large values of $g_{kn} + w_{kn}$. But for most practical cases the criterion is verified (or "almost verified"). Alternatively, to strictly fulfill the criterion, the following conditions can be added:

$$\forall k < K,\ g_{k1} + w_{k1} \le \sqrt{R_{min}^2 - z_k^2} \text{ and } g_{k2} + w_{k2} \le \sqrt{R_{min}^2 - z_{k+1}^2}$$

$$w_1 = w_0 + 2\left[\frac{h_0}{\tan\alpha}\right], \quad \text{with} \quad \left(\frac{13\pi}{30}\right) \le \alpha \le \left(\frac{\pi}{2}\right) \tag{2.6}$$

$$g_1 = \left(1+\zeta\right) g_0 \tag{2.7}$$

$$w_g = y_{01} - g_0 - \frac{w_0}{2} \tag{2.8}$$

Thus, the angle α decides the width w_1 (Fig. 2.5), ζ is a random variable uniformly distributed in the range of [0—1]. All the parameters and their relations defined so far are common to the various geometries. Table 2.1 summarizes these parameters.

Different antenna profiles/designs can be conceived by varying the width $\{w_{k1}, w_{k2}\}$, heights h_k and gaps $\{g_{k1}, g_{k2}\}$ of the individual trapezoids.

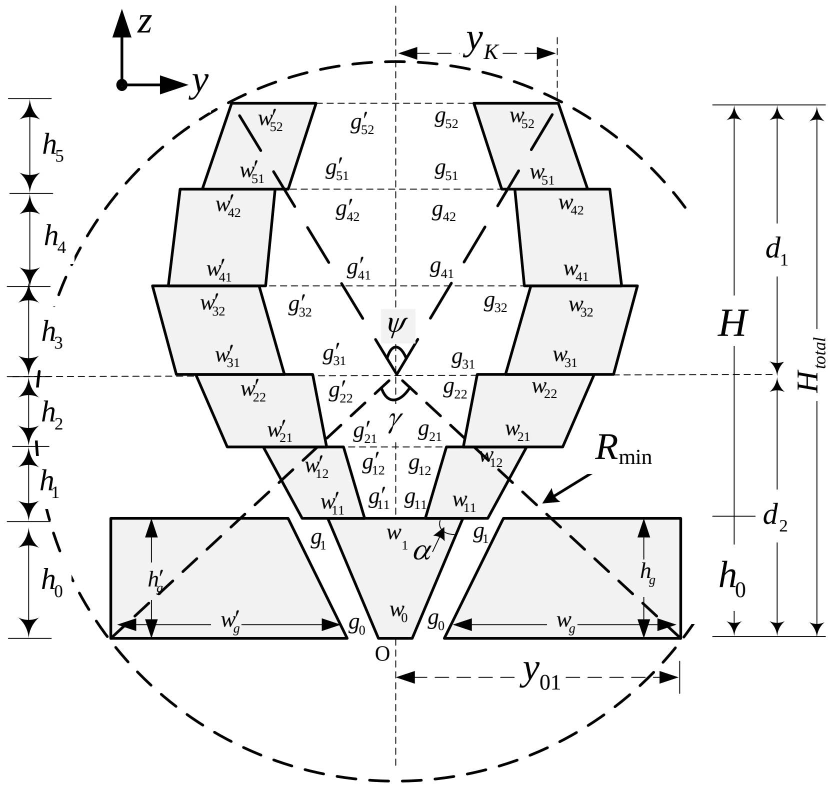

Fig. 2.5 Parameterization of generic geometry

2.4. Monopole Designs

The broadband planar monopole antennas have proved to be excellent radiators over very large BW. They commonly find their place in numerous applications. Some of their characteristics are mentioned below:

- Very large impedance bandwidth. For example, until now, the achieved impedance BW for VSWR = 2:1 have reached about 10:1 for an elliptical planar monopole and 80% for other planar monopoles [44]−[57].

Table 2.1 Summary of common parameters

Parameter	Description
R_{min}	Radius of the circumscribing sphere
ψ	Angle that decides the top edge width of the antenna
γ	Angle that decides the bottom edge width of the antenna
κ	Ratio of radiating part height to ground plane height
w_0	CPW beginning width
g_0	CPW beginning gap
α	Angle between h_0 and w_1; decides the value of w_1
ζ	Random number; decides the value of g_1 the end gap for CPW

- Maximum flexibility in reconfigurable radios [53].
- Stable radiation patterns with a reflection coefficient in excess of 10 dB over an extremely wide frequency range [56][57][61][62].
- Capability of multi band operations with Omni-directional radiation patterns in azimuth for all operation bands [57][60][63][64]—[68].
- Low fabrication cost and ease of manufacture.
- Compact size, linear phase response and acceptable radiation efficiency.
- Electrical heights less than λ/4 achieved.
- Interference immunity with existing wireless networking technologies by using band-notched planar monopole antenna[53] [56].

In the literature a number of monopole UWB design have been published, such as heart-shape, U-shape, circular-shape and elliptical-shape, etc. In the subsequent sections Triangular, Staircase, Crab-Claw, Circular or Disc and Dual feed monopole designs are discussed.

2.4.1. Triangular Monopole Design

A triangular or bow tie monopole design can be formed with only two layers (Fig. 2. 6a), k = {0, 1} thus the k = 0 layer for the CPW feed and k = 1 for radiating part. We set the following parameters as:

$$w_{11} = \frac{w_1}{2} \quad \text{--} \quad (2.9)$$

$$g_{11} = g_{12} = 0 \quad \text{--} \quad (2.10)$$

Relation (2.9) prevents the short circuit of radiating patch to ground plane. The flare angle β is controlled by angle ψ. The parameters necessary to control the geometry are the same as in Table 2.1. This is a simple possibility that has been shown whereas many other design schemes can be considered.

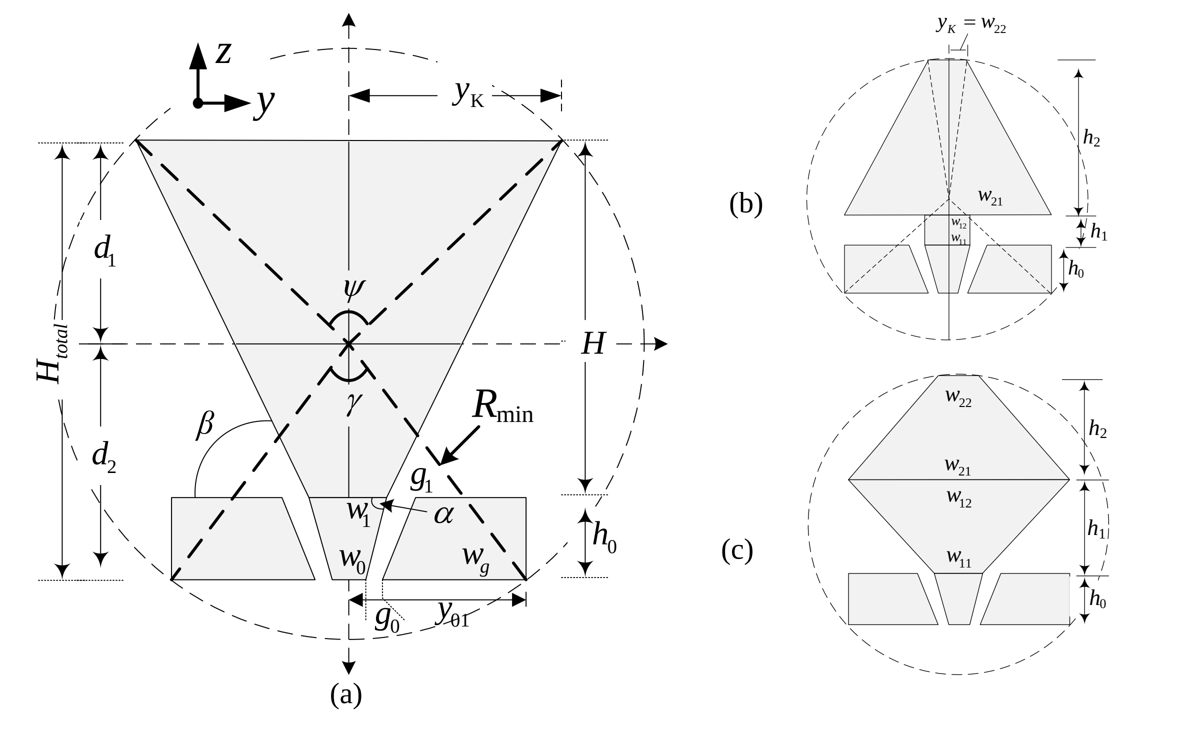

Fig. 2. 6 (a) Triangular monopole design, parameterized in circumscribed sphere (b) Reverse bow tie monopole (c) Diamond monopole

Reverse Bow-Tie monopole: a "reverse bow tie" design can be obtained by using three layers (K = 2), in addition to (2.9), we set $g_{kn}\big|_{k,n\in\{1,2\}} = 0$, $w_{12} = w_{11}$, $w_{21} > w_{12}$ and $w_{22} < w_{21}$, under the restriction given in note (1), or for simplicity, $w_{21} < y_0$. Eventually, h_1 is a rv and $h_2 = H - h_1$.

Diamond monopole: choosing w_{21} = w_{12} and the other previous parameters settings gives the diamond monopole.

2.4.2. Staircase Monopole Design

2.4.2.1. Evenly distributed steps

One way for the staircase or step monopole design (Fig. 2.7) is to distribute the step width and height evenly for such profile set $w_{11} = w_1/2$, $g_{k1} = g_{k2}$, $w_{k1} = w_{k2}$ and for the rest use:

$$w_{k+1,1} = w_{k1} + \frac{w_{K2} - w_{k1}}{K-1}, \quad \forall k = 1,\ldots, K-1 \text{ --(2.11)}$$

$$h_k = \frac{H}{K}, \quad \forall k = 1,\ldots, K \text{ ---(2.12)}$$

The relation (2.11) makes sure that $w_{k+1,1} > w_{k2}$. The number of layers (number of steps) are arbitrary, we have set k = [0—5] thus K = 5.

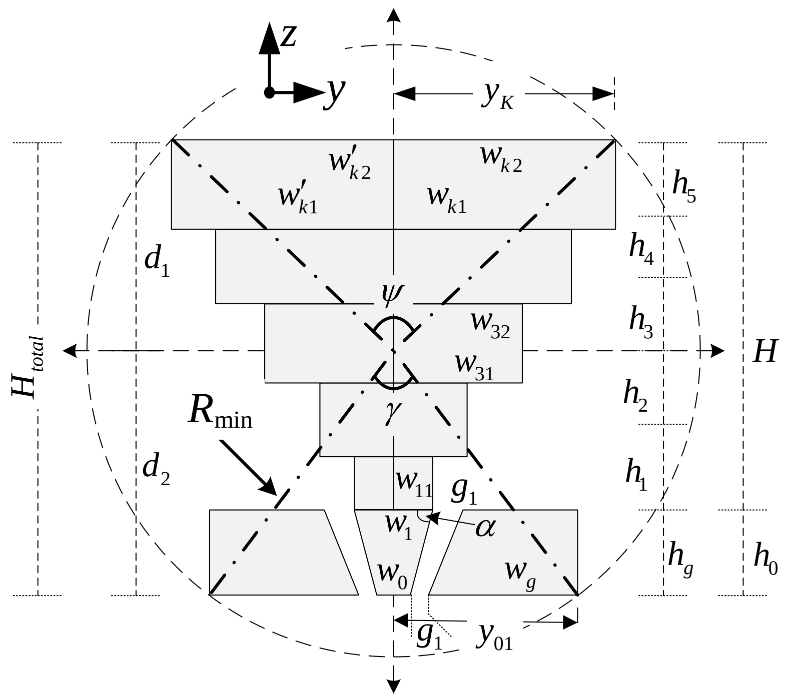

Fig. 2.7 Staircase monopole design, parameterized in circumscribed circle

2.4.2.2. Random Step Size:

Another possibility is to randomly vary each step height and width. This may excite multiple resonances. For this case instead of (2.11) and (2.12), we use (2.13) and (2.14) for variation in widths and heights respectively:

$$\begin{cases} w_{k+1,1} = w_{k1} + \left(w_{K2} - w_{k1}\right)\beta_k \\ \beta_k \in [0,1[\end{cases} \quad \forall k = 1,\ldots, K-1 \quad \text{-----(2.13)}$$

$$\begin{cases} h_k = \left(H_{total} - \sum_{n=0}^{k-1} h_n\right)\delta_k, \forall k = 1,\ldots, K-1 \\ \delta_k \in \left[0.1, 0.9\right], \forall k = 1,\ldots, K-1, \text{ and } \delta_K = 1 \end{cases} \quad \text{-----(2.14)}$$

where K = 5, β_k and δ_k are uniformly distributed rv. The range of δ_k avoids a layer with zero height.

In addition to the parameters listed in Table 2.1, 8 (β_k and δ_k) more parameters are required to control the geometry.

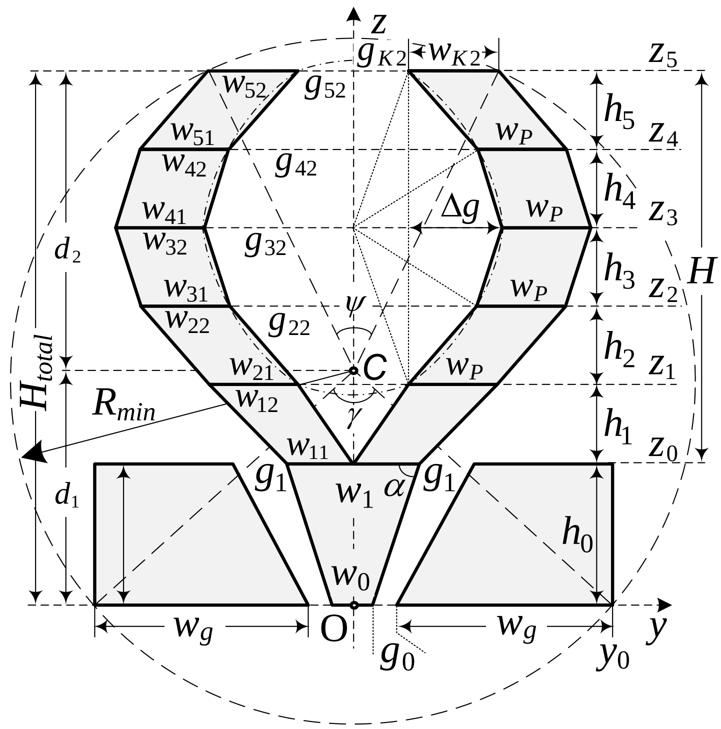

Fig. 2.8 Crab-claw monopole design, consist of K = 5 patch layers.

2.4.3. Crab-claw Monopole Design

The crab-claw monopole is another example, consisting of two "crab claws" (Fig. 2.8) with K = 5. For simplicity, apart for the first set $w_{11} = w_1/2$, the patches are restricted to parallelograms of constant widths w_P ($w_{k1} = w_{k2} = w_P$, $\forall$k = 2, …, K) and the heights are evenly distributed as in (2.12), where the vertices pairs belong to an ellipse arc. The patches width w_P is a uniformly distributed rv in the range {1, (w_{K2} - g_{K2})}. The gaps g_{kn}, are computed accordingly as follows (setting g_{11} = 0):

$$g_{k+1,1} = g_{k2} = \sqrt{g_M^2 - \tfrac{1}{4}\left(\tfrac{K+1}{2} - k\right)^2 \Delta g (g_{K2} + g_M)} \quad \text{----- (2.15)}$$

$g_M = g_{K2} + \Delta g$ being the largest gap value, (Fig. 2.8), with g_{K2} given by $g_{K2} = y_K - w_P$ and (2.3). Δg is uniformly distributed rv.

A further possible generalization is to apply an affinity of ratio b along $y'Oy$ on each layer but the last (K^{th}), under the size constraint of course (i.e. the antenna must belong to the minimal sphere).

In this design, we need w_p and Δg as additional parameters to control the geometry.

2.4.4. Disc Monopole

A disc monopole design requires more layers of trapezoids to make an acceptable circular curvature (Fig. 2.9). A 14 layers (K = 13) generic geometry is selected, with an even number of layers for the sake of ease in the parameterization.

To prevent the feed to be in short circuit with the ground, $w_{11} = w_1/2$, and for all gaps, $\{g_{k1}, g_{k2}\}$ are set to zero. In order to simplify the parameterization, the following rules are enforced.

$$\begin{cases} h_k = h_{K+2-k},\ \forall k = 2,\ldots,(K+1)/2 \\ w_{k2} = w_{\{K+1-k\},2},\ \forall k = 2,\ldots,(K+1)/2 \end{cases} \qquad \text{-----(2.16)}$$

Also,

$$w_{k2} = w_{(k+1),1},\ \forall k = 1,\ldots,K-1 \qquad \text{-----(2.17)}$$

This means that we only need to find the values for h_2 to h_7 and w_{22} to w_{72} to complete the vertices of the patches that define the disc profile. The width $w_{12} = w_{21}$ can have uniformly distributed random numbers between [$w_1/2$—w_1]. Let r_{zaxis} be the semi axis of ellipse along the z-axis and r_{yaxis} be the semi axis along y-axis (Fig. 2.9), verifying the following constraints:

$$\begin{cases} r_{zaxis} = (H - h_1)/2 \\ r_{yaxis} < \sqrt{R_{\min}^2 - r_{zaxis}^2} \end{cases} \qquad \text{-----(2.18)}$$

where, h_1 decides the gap between the disc and the feed. The applicable region of the condition for r_{yaxis} is above the disc center.

Then, with the parametric equations of the circle, the remainders of heights (h_k) are defined as:

$$\begin{cases} h_2 = r_{zaxis} - r_{zaxis}\cos\theta_2 \\ h_k = r_{zaxis} - r_{zaxis}\cos\theta_k - \sum_{n=2}^{k-1} h_n \quad \forall k = 3,\ldots,(K+1)/2 \end{cases} \qquad \text{-----(2.19)}$$

and widths (w_{k1}, w_{k2}) can be defined as:

$$w_{k2} = r_{yaxis} \sin\theta_k \qquad \forall k = 2,...,(K+1)/2 \text{ --(2.20)}$$

$$\begin{cases} \theta_k = \left[2\left(\dfrac{\pi/2 - \theta_M}{K-1} \right)(k-1) + \theta_M \right] & \forall k = 2,...,(K+1)/2 \\ \theta_M = \max\left(\theta_{m1}, \theta_{m2}\right) \end{cases} \text{ -------------------------(2.21)}$$

where, θ_k is the angle between the k^{th} layer and the disc center whereas, θ_{m1} and θ_{m2} (see inset of Fig. 2.9) are calculated as:

$$\begin{cases} \theta_{m1} = \tan^{-1}\left({w_{21}}/{r_{zaxis}} \right) \\ \theta_{m2} = \tan^{-1}\left({y_K}/{r_{zaxis}} \right) \end{cases} \text{ ---(2.22)}$$

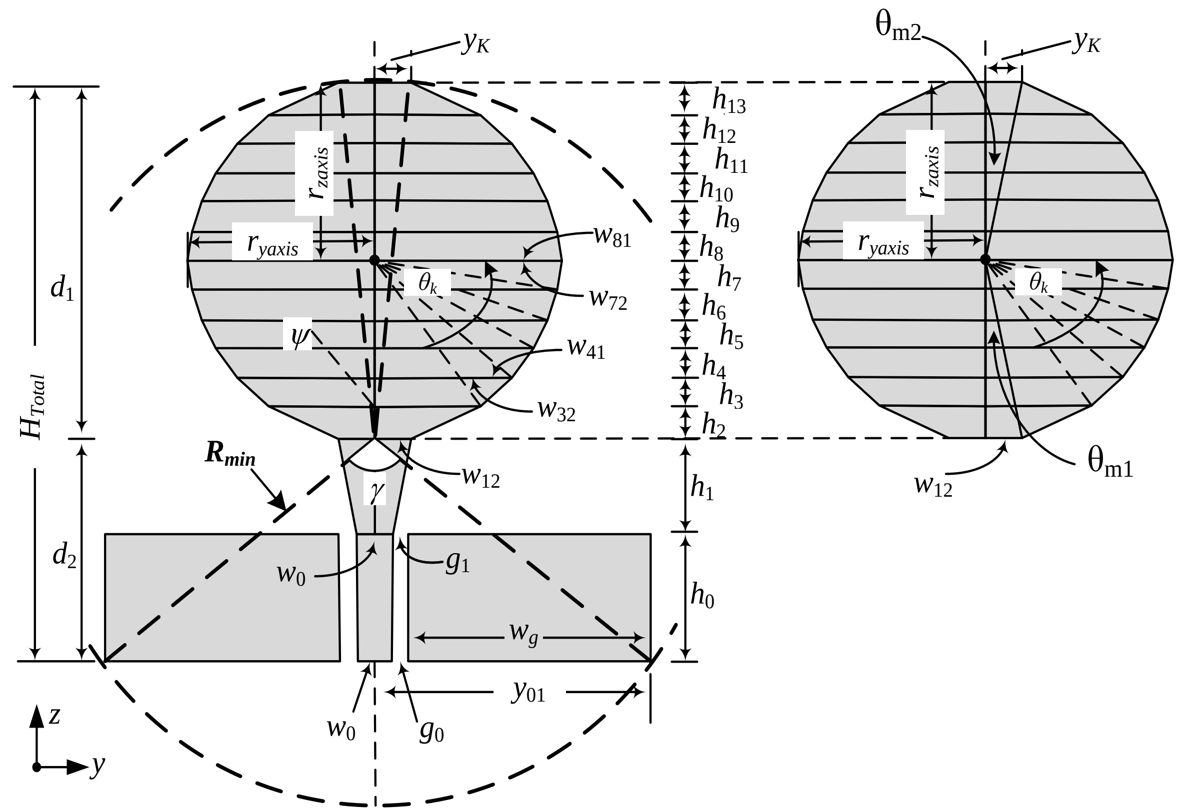

Fig. 2.9 Disc monopole design with 14 trapezoidal layer.

This constitutes a quarter of the disc, from which by making symmetry in *xy* plane (2.16) about the disc center, a half disc can be formed. Finally, since the geometry has symmetry in *x*O*z* plane, a complete disc is formed. Various disc shapes, either circular or elliptical, can be made by appropriate values of these semi axes.

In this case, in order to control the geometry the addition parameters are w_{12}, h_1 and r_{yaxis}.

2.4.5. Dual feed monopole

The design is inspired from its microstrip counterpart [40]–[43]. In this design seven layered geometry (K = 6) is used Fig. 2.10. The gaps are set as;

$$\left.\begin{aligned} g_{41} = g_{42} = 0 \\ g_{51} = g_{52} = 0 \end{aligned}\right\} \qquad (2.23)$$

$$g_{61} = g_{62} \qquad (2.24)$$

$$\left.\begin{aligned} g_{12} = g_{21} = (0.7)\, g_{32} \\ g_{22} = g_{31} = (0.8)\, g_{32} \end{aligned}\right\} \qquad (2.25)$$

The coefficients for g_{12} and g_{22} calculations are inspired by its microstrip counterpart. The gap between the two feed fingers is determined by g_{32}, distributed uniformly in the range of {1—($Ws/2-w_{32}$)} where Ws is the substrate width which is maximum of y_k and y_{01}. The slot width is controlled by g_{61} and is also distributed uniformly.

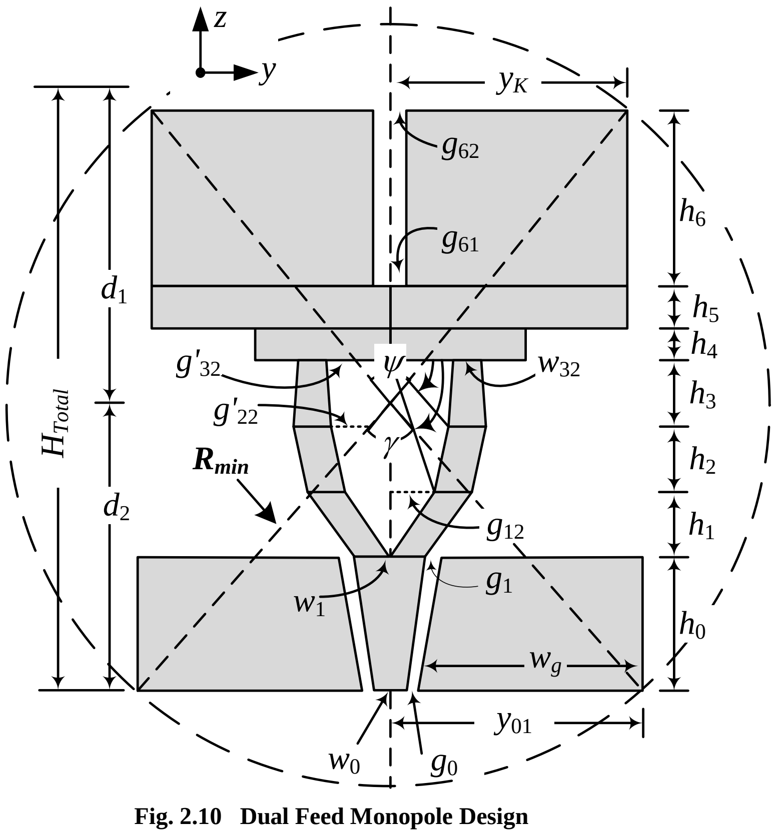

Fig. 2.10 Dual Feed Monopole Design

Widths of the individual trapezoid are defined as;

$$\begin{cases} w_{k1} = w_{k2} = \dfrac{w_1}{2} \quad \forall k = \{1,2\} \\ w_{31} = w_{22} \end{cases} \quad \text{------} \quad (2.26)$$

$$w_{51} = w_{52} = y_K \quad \text{------} \quad (2.27)$$

$$w_{61} = w_{62} = y_K - g_{62} \quad \text{------} \quad (2.28)$$

w_{41} and w_{42} are random values that can take uniform distribution in the range of $\{g_{32} + w_{32}, Ws/2\}$ whereas w_{32} is also a uniformly distributed random number in range of $[w_1/4—w_1/2]$. The heights h_k are defined as;

$$h_1 = h_2 = h_3 = \left[\frac{H}{6}\right] R_{h_{feed}} \quad \text{------} \quad (2.29)$$

$$h_4 = \left[\frac{H}{10}\right] R_{h_4} \quad \text{------} \quad (2.30)$$

$$h_5 = \frac{7}{2}[H] R_{h_5} \quad \text{------} \quad (2.31)$$

$$h_6 = H - h_1 - h_2 - h_3 - h_4 - h_5 \quad \text{------} \quad (2.32)$$

Where, $R_{h\text{feed}}$, R_{h4}, and R_{h5} are uniformly distributed random numbers in the range of [0.1–1], the lower range being intended to avoid zero height trapezoids. The weight ranges in (2.29), (2.30), (2.31) are mainly influenced by the microstrip counterpart.

2.5. Dipole Designs

Dipoles have advantages over monopoles, such as the radiation pattern stability in elevation and a more constant gain over frequencies. Differential antennas are often preferable over single-ended ones, since they can be easily integrated with modern low-cost RFICs, which inherently have a differential structure. In this case, the connection of the antenna to the RFIC is direct, and the undesired noise-figure degradation due to the balun, which is required in the case of a single-ended antenna, is avoided

When an unbalanced line, like a coaxial cable, is connected to a balanced antenna like a dipole, the discontinuity in the impedance line structure can lead to currents on the outer sheathing of the cable. These exterior currents can radiate or receive signals, causing degradation in the performance of the antenna. Among the various solutions to this problem, the use of a balun transformer is perhaps the cheapest. One particularly simple balun to implement is the tapered line transformer. This motivated us to investigate a planar balanced dipole antenna design.

2.5.1. The Generic Design for Planar Balanced Dipole Antennas

The generic design for balanced planar dipole antennas is shown in Fig. 2.11). Designing an UWB antenna with the desired impedance requires thinking the UWB antenna as an extension of a transmission line, where the impedance varies smoothly and continuously from the feed line through the feed region towards the radiating elements and free space.

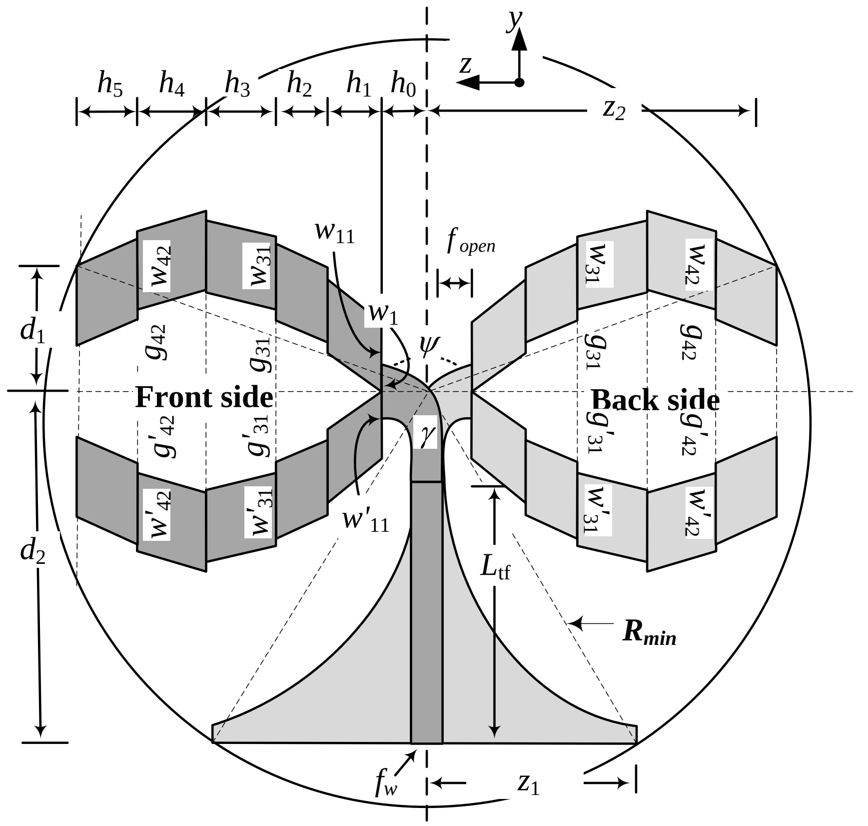

Fig. 2.11 Generic Design for Planar dipole antennas

The feed is a coplanar strip balun, which has four parameters: f_w (the feed line width), z_1 (the ground plane for the balun), L_{tf} length (of the tapered feed) and f_{open} (feed opening width) (Fig. 2.11), which adds the gap between the two radiating parts (Front and back). This has an effect of broad band input matching. The Feed line width can be same from one end to the other, by setting $f_w = w_1$, or it may be different as desired. The width of the ground plane is related to R_{min} as:

$$z_1 = R_{\min} \sin\left(\frac{\gamma}{2}\right) \text{ --(2.33)}$$

$$z_2 = R_{\min} \sin\left(\frac{\psi}{2}\right) = \sum h_k \text{ --(2.34)}$$

For the d_1 and d_2 ;

$$d_1 = R_{\min} \cos\left(\frac{\psi}{2}\right) \text{ --(2.35)}$$

$$d_2 = R_{\min} \cos\left(\frac{\gamma}{2}\right) \text{ --(2.36)}$$

The patch layers k = 0 constitute the feed layer, and in this case there are two parameters w_1 and h_0. h_0 is determined as follows:

$$h_0 = \frac{f_w}{2} + f_{open} \text{ ---(2.37)}$$

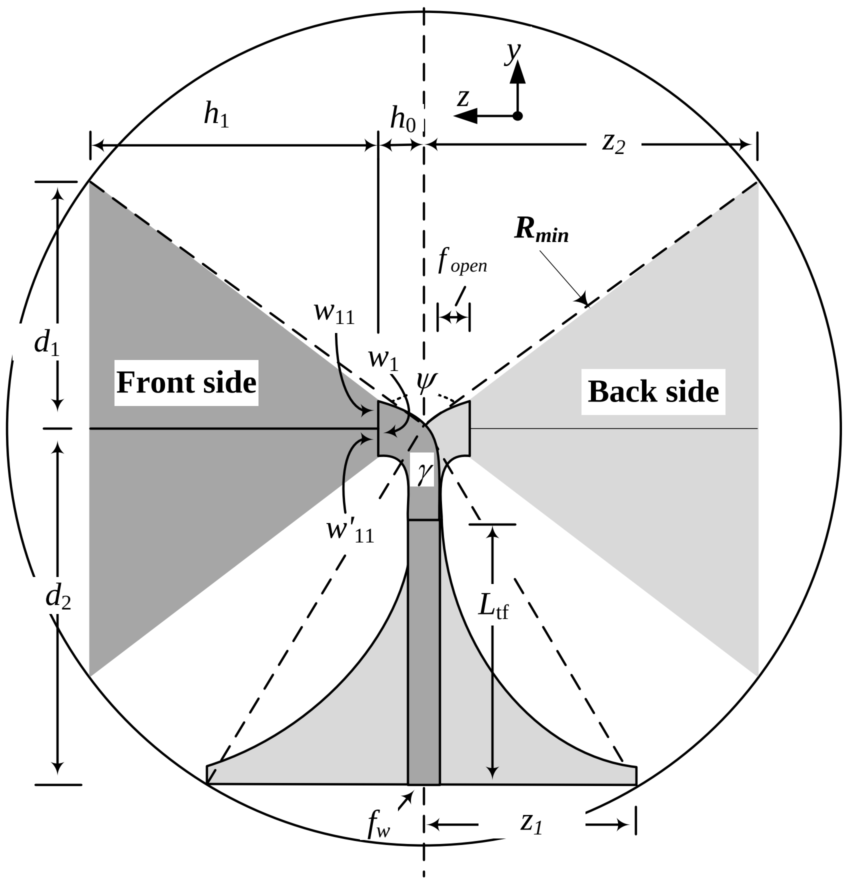

Fig. 2.12 Triangular or Bow tie balanced dipole antenna.

The radiating part is defined by the widths $\{w_{k1}, w_{k2}\}$, the heights h_k and the gaps $\{g_{k1}, g_{k2}\}$. The radiating part has the symmetry property with respect to xz plane, the prime notations w'_{k1}, w'_{k2}, and g'_{k1}, g'_{k2} are used to show this symmetry.

The second symmetry is with respect to xOy, and in this case patches on the front side and back side are the same — an antipodal symmetry. It is worth mentioning that these symmetries are applied to radiating part of the antenna.

2.5.2. Triangular Balanced Dipole Antenna

This antenna can be formed in a similar fashion as in its monopole version. Only one radiating patch layer is required as shown in (Fig. 2.12) Setting $w_{11}=w_1/2$, and $g_{k1} = g_{k2} = 0$, the ψ controls the angle between the two radiating anti-podal elements, whereas γ governs the ground plane width for the balun.

The independent parameters that control the geometry are R_{min}, ψ, γ, w_1, f_{open}, f_w and L_{tf}.

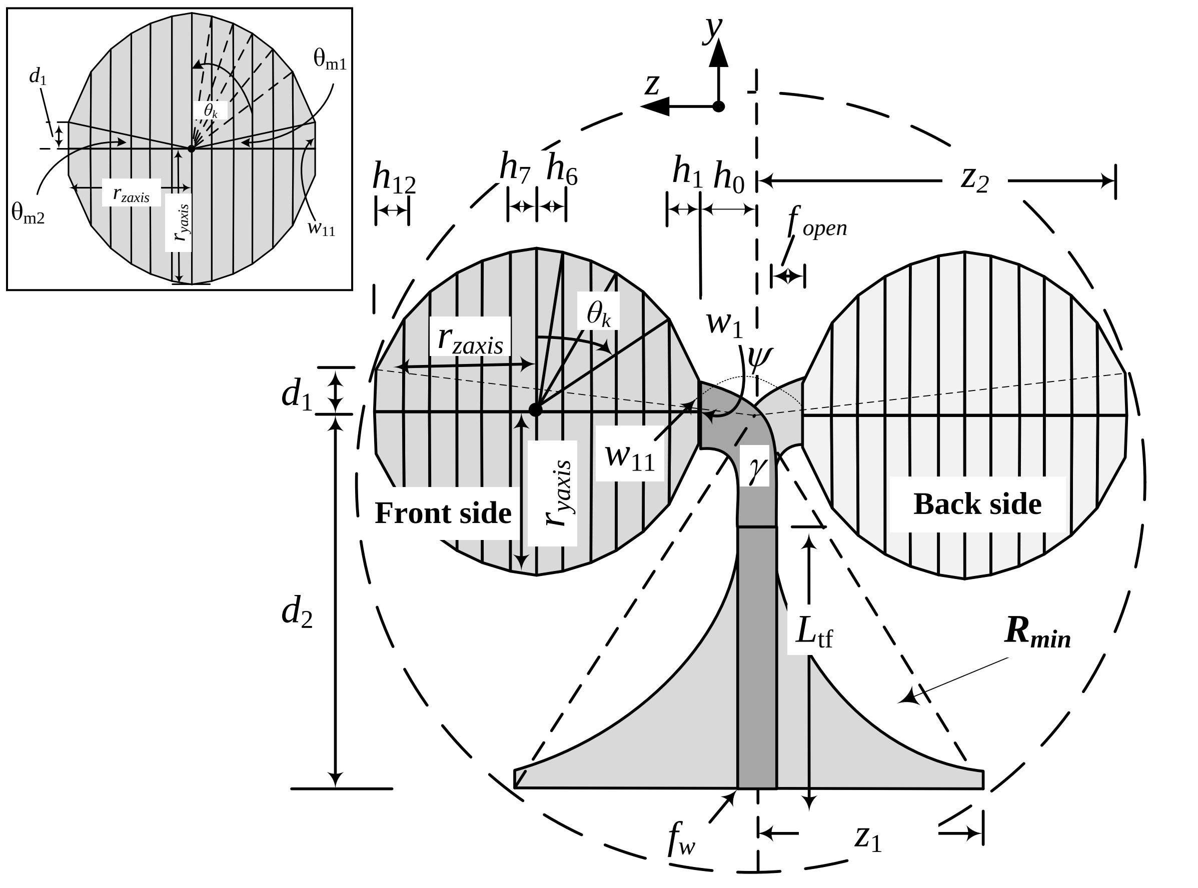

Fig. 2.13 Disc Planar Balanced dipole antenna

2.5.3. Disc Balanced Dipole Design

The disc balanced dipole (Fig. 2.13) can be designed with 13 layers of patch (K = 12). In this design, we set all gaps (g_{k1}, g_{k2}) to zero and $w_{K,2}$ = d_1 , which implies that the angle should have large values so that $w_{K,2}$ can be kept small for good circular curvature. Then w_{11} can be fixed as $w_{11} = w_1/2$.

In order to simplify the parameterization, the following rules are enforced.

$$\begin{cases} h_k = h_{K+1-k}, \ \forall k = 1,\dots, K/2 \\ w_{k2} = w_{\{K-k\},2}, \ \forall k = 1,\dots, K/2 \end{cases} \quad \text{--(2.38)}$$

Also,

$$w_{k2} = w_{(k+1),1}, \ \forall k = 1,\dots, K-1 \text{--(2.39)}$$

This means that we need to find the values for h_1 to h_6 and w_{12} to w_{62}, to complete the vertices of the patch that define the disc profile. Let r_{zaxis} be the semi axis of the ellipse along the z-axis and r_{yaxis} be the semi axis along y-axis (Fig. 2.13), with the following constraints:

$$\begin{cases} r_{zaxis} = (z_2 - h_0)/2 \\ r_{yaxis} < \sqrt{R_{\min}^2 - r_{zaxis}^2} \end{cases} \text{--(2.40)}$$

The applicable region of the condition for r_{yaxis} is beyond the disc center. Then with the parametric equations of circle, the remainder of heights (h_k) and widths (w_{k1}, w_{k2}) can be defined:

$$\begin{cases} h_1 = r_{zaxis} - r_{zaxis}\cos\theta_1 \\ h_k = r_{zaxis} - r_{zaxis}\cos\theta_k - \sum_{n=1}^{k-1} h_n \quad \forall k = 2,\dots, K/2 \end{cases} \quad \text{--------------------(2.41)}$$

$$w_{k2} = r_{yaxis}\sin\theta_k \qquad \forall k = 1,\dots, K/2 \quad \text{--- (2.42)}$$

where, θ_k is the angle between the k^{th} layer and the disc center and is defined as:

$$\theta_k = \left[2\left(\frac{\pi/2 - \theta_M}{K} \right)(k) + \theta_M \right] \qquad \forall k = 1,\dots, K/2 \quad \text{-------------------------------- (2.43)}$$

θ_M is the maximum of θ_{m1} and θ_{m2}, these angles are shown in the inset of Fig. 2.13 and are calculated as:

$$\begin{cases} \theta_{m1} = \tan^{-1}\left(w_{11}/r_{zaxis} \right) \\ \theta_{m2} = \tan^{-1}\left(d_1/r_{zaxis} \right) \end{cases} \quad \text{---(2.44)}$$

This constitutes a quarter of the disc. By creating symmetry in xy plane (2.38) about the disc center, a half disc can be formed. Finally, since the geometry has symmetry in xz plane, a complete disc is formed.

The parameters that control the geometry are R_{min}, ψ, γ, w_1, f_{open}, f_w L_{tf} and r_{yaxis}.

2.6. Multiband Design

In the previous section the monopole and dipole designs from the generic design were demonstrated in the context of UWB. In this section a design of multiband antenna is presented, illustrating another capability of this approach.

The goal here is to design a tri-band planar antenna, with reasonably small size and good in-band matching and out-of-band rejection. For this purpose the following WLAN bands are selected:

Although most of the work in multiband antennas has been done with PIFA like antennas, a significant literature on CPW fed multiband antennas is also available [63]—[68]. In particular, W.C. Liu [63] has optimized a CPW fed tri-band planar monopole antenna using a genetic algorithm. However, the achieved antenna is large (63.1 × 30 mm^2) and has poor stop-band characteristics ($|S_{11}|$ ~ – 6 dB).

Table 2.2 Selected WLAN bands and stop bands

IEEE 802.11	Freq. Band GHz	BW (MHz)	Remarks
b/g/n	2.4 – 2.5	100	Pass Band
---	2.75 – 3.4	650	Stop Band
Y	3.65 – 3.7	35	Pass Band
---	3.95 – 4.75	800	Stop Band
a/n	5 – 6	1000	Pass Band

Slot antennas have demonstrated advantages in many multiband designs, for instance in multiband PIFAs [67]. Using the approach for a slot based multiband antenna, a design with two slots A and B is here proposed (Fig. 2.14), such that the slot-A would resonate at 5 GHz (IEEE 802.11a band) and slot B would be responsible for 3.7 GHz operation (IEEE 802.11y band), while the lowest frequency band 2.4 GHz (IEEE 802.11b/g) would be the function of overall antenna height. To achieve this set of postulated geometrical constraints, an 8-layer generic design has been used. The parameterization of the generic design for a double slot antenna can be achieved by setting the following constraints on gaps and widths:

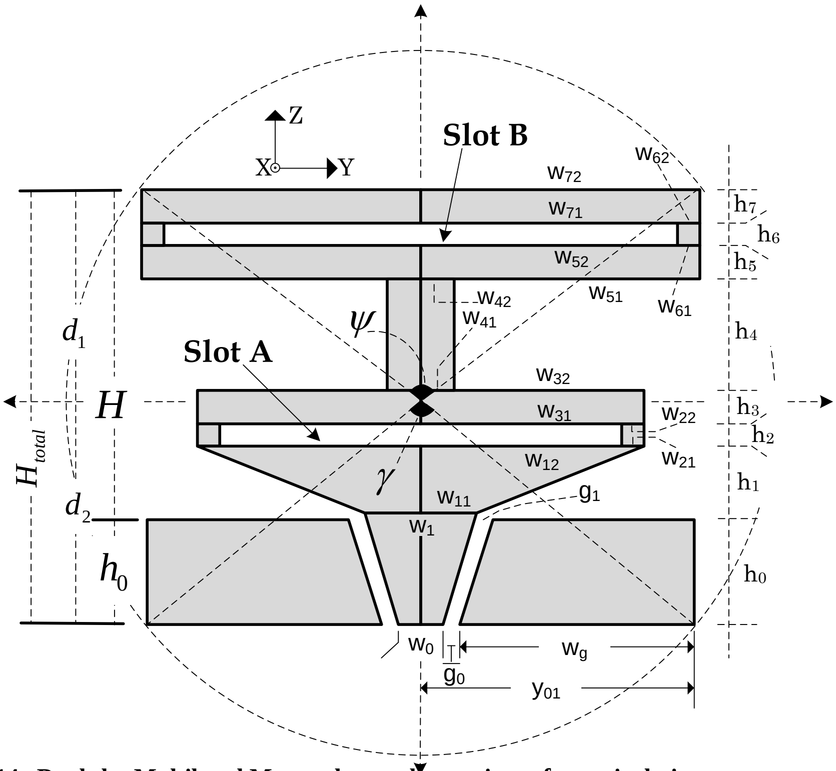

Fig. 2.14 Dual slot Multiband Monopole, another variant of generic design

$$\left.\begin{aligned} w_{11} &= \frac{w_1}{2} \\ w_{51} &= w_{52} \\ w_{21} &= w_{22} \\ w_{61} &= w_{62} \\ w_{31} &= w_{32} \\ w_{71} &= w_{72} \end{aligned}\right\} \quad \text{------------------------} \quad (2.45)$$

$$w_{12} = w_{31} = \left(sw_a/2\right) + w_{21} \quad \text{------------------------} \quad (2.46)$$

$$w_{51} = w_{71} = \left(sw_b/2\right) + w_{61} \quad \text{------------------------} (2.47)$$

Where, sw_a, sw_b are the slot widths of slot A and B respectively.

$$g_{21} = g_{22} = \frac{sw_a}{2} \quad \text{------------------------} \quad (2.48)$$

$$g_{21} = g_{22} = \frac{sw_b}{2} \quad \text{------------------------} (2.49)$$

$$g_{1x}, g_{3x}, g_{4x}, g_{5x}, g_{7x} = 0 \quad \text{------------------------} \quad (2.50)$$

Where, x={1, 2}. The heights h_k are constrained as;

$$h_4 = H_{Total} - (h_0 + h_1 + h_2 + h_3 + h_5 + h_6 + h_7) \quad \text{------------------------} \quad (2.51)$$

The ranges for each independent parameter along with their distributions will be discussed in chapter 3.

2.7. 3D Bicone design

The generic approach discussed in the previous sections offered a way to design various UWB monopoles and dipoles antennas lending themselves to the construction of a statistical population. In the same spirit, a bicone design is now studied for a class of volumic antennas.

The biconical antenna was invented by Lodge in the 1890s and extensively studied by Schelkunoff and others in the 1930s. It is made up of two opposing metal cones, the feed being located between the tips of the cones. Its use in UWB is based on the fact that it would theoretically be capable of providing frequency independent impedance if it was of infinite length, whose value is given by the following expression:

$$Z_{in} = Z_0 = \frac{Zs}{\pi}\ln\left[\cot\left(\frac{\theta_{hc}}{2}\right)\right] \quad \text{--} \quad (2.52)$$

Where Z_s = 120π is the free space impedance and θ_{hc} is the half angle of the bicone. This impedance is purely real because there are only travelling waves on the antenna. In practice, the size is truncated, which causes higher modes to induce a reactive component in the input impedance and increases the standing-wave ratio. In other words, the input reflection coefficient increases. This truncation also limits the operating bandwidth, since the lower frequency limit is governed by the overall height of the bicone. This truncation problem is solved by gradual truncation of the ends of bicone, proposed by Schelkunoff and Friis [70], Carl Baum also studied a similar configurations [71],[72].

Biconical antennas show a dipolar radiation pattern, omnidirectional in the plane perpendicular to the axis of the cone, and of linear polarization. At θ_{hc}=60° and one wavelength diameter, a bicone offers an excellent matching over a bandwidth of 6:1 [69].

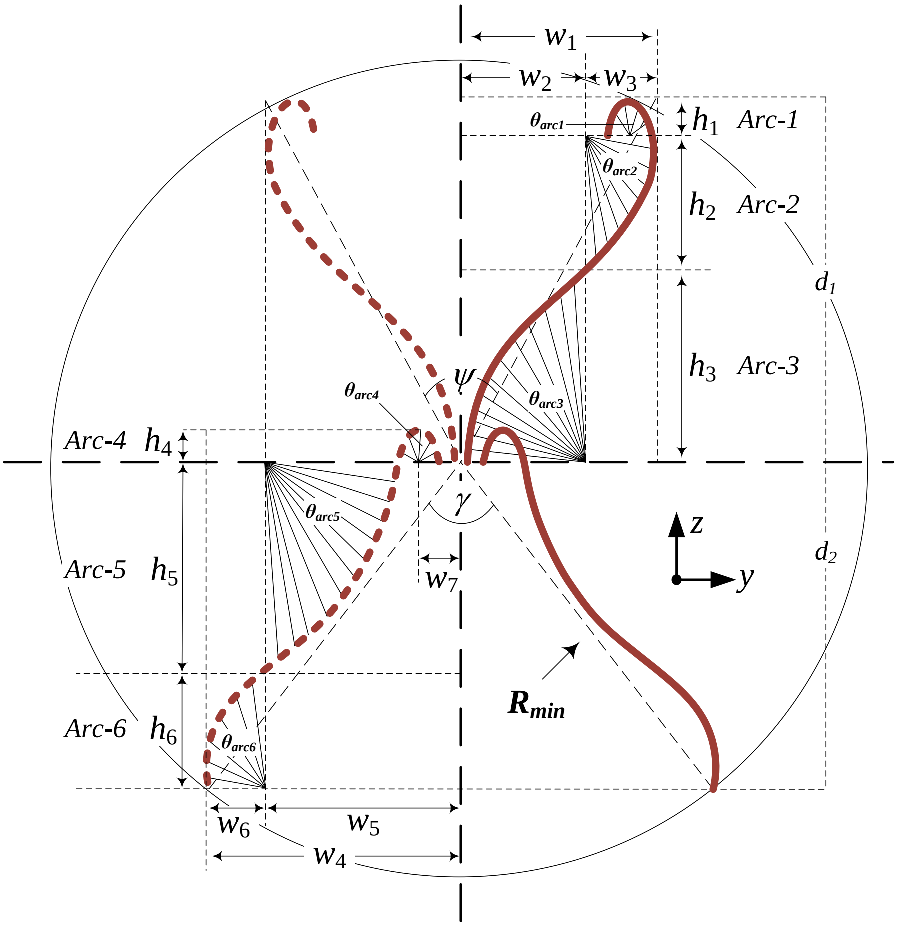

Fig. 2.15 Bicone profile parameterized in circumscribed circle, rotation of this profile generate volumic or 3D structure

2.7.1. Details on the Design

It is desired to have a bi-conical "generic" design that has gradual tapered ends and that can offer different flare angles for both cones. Fig. 2.15 shows the profile of such a bicone. 360° rotation of this profile curve generates a 3D or volumic biconical structure. The left side dotted curve is just for clarity and ease in annotation. Angles ψ and γ control the flare angle of upper and lower cones respectively. General parametric relations are chiefly common as in generic design for planar UWB antenna.

$$H_{Total} = d_1 + d_2 = R_{\min}\left[\cos\left(\frac{\psi}{2}\right) + \cos\left(\frac{\gamma}{2}\right)\right] \quad (2.53)$$

$$w_4 = R_{\min}\sin\left(\frac{\gamma}{2}\right) \quad (2.54)$$

$$w_1 = R_{\min}\sin\left(\frac{\psi}{2}\right) \quad (2.55)$$

The diameter for the upper cone is thus $2w_1$, whereas for lower cone it is $2w_4$. The parametric equations of each arc are given below, along with the necessary relations of heights and widths. In each of the following arc, z_{arc} denotes the z-axis coordinate whereas y_{arc} denotes the y-axis coordinate.

- **Arc 1**

$$z_{arc1} = (d_1 - h_1) + h_1 \sin(\theta_{arc1}) \quad \text{------} \quad (2.56)$$

$$y_{arc1} = \left(w_1 - \frac{w_3}{2} \right) + \frac{w_3}{2} \cos(\theta_{arc1}) \quad \text{------} \quad (2.57)$$

$$w_3 = \left[\frac{w_1}{3} \right] R_{w_3} \quad \text{------} \quad (2.58)$$

$$h_1 = \left[\frac{d_1}{10} \right] R_{h_1} \quad \text{------} \quad (2.59)$$

Where, R_{w3} and R_{h1} are uniformly distributed random numbers in the range of [0.1—1] whereas θ_{arc1} is in the range of [0 — π].

- **Arc 2**

$$z_{arc2} = (d_1 - h_1) - h_2 \sin(\theta_{arc2}) \quad \text{------} \quad (2.60)$$

$$y_{arc2} = w_2 + w_3 \cos(\theta_{arc3}) \quad \text{------} \quad (2.61)$$

$$w_2 = w_1 - w_3 \quad \text{------} \quad (2.62)$$

$$h_2 = \left[\frac{2}{5} d_1 \right] R_{h_2} \quad \text{------} \quad (2.63)$$

Where, R_{h2} is a uniformly distributed random number in the range of [0.5—1] and θ_{arc2} is in the range of [0 — π/2].

- **Arc 3**

$$z_{arc3} = h_3 \sin(\theta_{arc3}) \quad \text{------} \quad (2.64)$$

$$y_{arc3} = w_2 - w_2 \cos(\theta_{arc3}) \quad \text{------} \quad (2.65)$$

$$h_3 = d_1 - h_1 - h_2 \quad \text{------} \quad (2.66)$$

where, θ_{arc3} is in the range of [0 — π/2].

- **Arc 4**

$$z_{arc4} = h_4 \sin(\theta_{arc4}) \quad \text{------} \quad (2.67)$$

$$y_{arc4} = w_7 + \frac{w_7}{2} \cos(\theta_{arc4}) \quad \text{------} \quad (2.68)$$

$$w_7 = \left[\frac{w_4}{5}\right] R_{w_7} \quad \text{-----} \quad (2.69)$$

$$h_4 = \left[\frac{d_2}{10}\right] R_{h_4} \quad \text{-----} \quad (2.70)$$

Where, θ_{arc4} is in the range of [0 — π] whereas R_{w7} and R_{h4} are uniformly distributed random numbers in the range of [0.1–1].

- **Arc 5**

$$z_{arc5} = -h_5 \sin(\theta_{arc5}) \quad \text{-----} \quad (2.71)$$

$$y_{arc5} = w_5 - \left(w_5 - \frac{3}{2} w_7\right)\cos(\theta_{arc5}) \quad \text{-----} \quad (2.72)$$

$$w_5 = w_4 - w_6 \quad \text{-----} \quad (2.73)$$

$$h_5 = d_2 - h_6 \quad \text{-----} \quad (2.74)$$

where, θ_{arc5} is in the range of [0 — π/2]

- **Arc 6**

$$z_{arc6} = -d_2 + h_6 \sin(\theta_{arc6}) \quad \text{-----} \quad (2.75)$$

$$y_{arc6} = w_5 + w_6 \cos(\theta_{arc6}) \quad \text{-----} \quad (2.76)$$

$$h_6 = \left[\frac{2}{5} d_2\right] R_{h_6} \quad \text{-----} \quad (2.77)$$

$$w_6 = \left[\frac{w_4}{3}\right] R_{w_6} \quad \text{-----} \quad (2.78)$$

where, θ_{arc4} is in the range of [0 — π/2] whereas, R_{w6} and R_{h6} are uniformly distributed random numbers in the range of [0.1—1]. The lower range of all these random numbers is set to avoid null values.

The number of arc coordinates $\{z_{arc}, y_{arc}\}$ can be different for each arc depending on the required level of smoothness, for example the arcs at the feed region can have more number of coordinates than others since this region is more sensitive. Once the numbers of graduations; for each arc, are fixed they are kept the same for all the antenna samples.

The independent parameters are, R_{min}, ψ, γ, R_{w3}, R_{h1}, R_{h2}, R_{w4}, R_{h4}, R_{w6} and R_{h6}.

2.8. Conclusion

In this chapter, the approach of a Generic design for planar antennas has been proposed. The generic geometry helps in easy and flexible arrangement of patches to form different antenna profiles. The main purpose of a generic geometry is to build a tool for generating many antenna samples, of either of the same or different profiles, which conform to the minimal sphere around the antenna, and are required for eventual subsequent statistical analysis and modeling. Secondly, it turns out that UWB antenna designs are in some cases very complex. Owing to generic design, this complexity can be reduced to a certain acceptable level. In addition, since UWB antennas impose additional requirements to those commonly met in narrow band antennas, it is less cumbersome to use optimizing techniques with a generic design approach, owing to the fewer parameters controlling the geometry.

In this chapter, five monopoles (Triangular, staircase, Crab-claw, disc, Dual feed) and two balanced dipole profiles have been discussed as variants of the generic design geometry. Moreover, the versatility of the design has been demonstrated by proposing a multiband antenna for three WiFi bands. We have also described a generic design for bicone antennas.

From these results, it clearly appears that it is feasible to generate populations of antennas with varying characteristics, which will be of interest towards the statistical analysis and modeling of antenna properties.

Chapter 3

Optimization

3.1. Introduction

In the previous chapter various antenna designs obtained from the generic design were discussed from the geometrical point of view. The main purpose was to propose an antenna design that is flexible enough to allow easy variations in the value of its parameters, within the design constraints and parameter space. This permits to address many design samples, variants of a particular antenna class intended to be subsequently tested in an EM solver. In addition, by selecting a suitable sampling scheme, a population of antenna samples can in this way be created for eventual statistical modeling.

In communication systems, once the system and/or technological constraints are defined, the antennas are usually designed independently from the other elements of the communication chain (RF front-end, propagation channel, physical layer). This is can be considered valid in the case of narrow and moderate band communications, since the interaction with the other elements of the chain is determined by simple quantities such as the impedance matching efficiency, the gain, etc. In UWB systems, this is more complicated since it is hard to uncouple the interactions, especially in impulse radio. The temporal behavior of the antenna is more difficult to understand, to characterize and eventually to model and it critically impacts the overall performance.

The design of UWB antennas is subject to ordinary constraints like cost, size, integration, efficiency but also to more specific constraints, such as the matching bandwidth, the control over the dispersion and more generally waveform distortion, etc. The antenna transfer function (ATF) is a suitable concept to express the antenna characteristic and thus to qualify its radiation performance.

In this chapter the ATF is first presented and highlighted, from which we define several synthetic indicators that are appropriate to qualify the antenna performance. Since the goal of this chapter is to address antenna optimization, the procedure making use of these indicators is discussed, after which the optimal designs for each sub-class (triangular, staircase, disc etc) are presented, along with their key performance characteristics both in the frequency and in the time domains.

Two particular cases of a multiband patch antenna and a bi-conic volumic antenna are also discussed. Finally, the chapter ends by the comparison of key characteristics of each optimized design.

3.2. Antenna Transfer Function (ATF)

The radiated far field of the antenna can be written:

$$\mathbf{E}^{\infty}\left(f,\mathbf{r}\right)=\frac{e^{-jkr}}{r}\sqrt{\frac{\eta_0}{4\pi}}\mathcal{A}\left(f,\hat{\mathbf{r}}\right) \quad \text{---(3.1)}$$

where k is the wave number $k = 2\pi/\lambda = \omega/c$, $\eta_0 = 120\pi\ \Omega$ is the free space impedance, $\hat{\mathbf{r}}=\mathbf{r}/r$ is the unit radius vector [read $\hat{\mathbf{r}}=(\theta,\varphi)$] and $\mathcal{A}(f,\hat{\mathbf{r}})$ is the vector amplitude of the field. All the relevant information of the far-field radiations is in this vector amplitude of the field and depends linearly on the wave complex amplitude a_1 of the incident signal. The antenna vector transfer function in the transmitting mode can thus be described as follows [73]:

$$\mathcal{H}^{T}\left(f,\hat{\mathbf{r}}\right)=\frac{\mathcal{A}\left(\hat{\mathbf{r}},f\right)}{a_1\left(f\right)}=\sqrt{\frac{4\pi}{\eta_0}}\cdot\frac{re^{jkr}\mathbf{E}^{\infty}\left(f,\mathbf{r}\right)}{a_1\left(f\right)} \quad \text{---(3.2)}$$

From the system point of view, the source signal is the incident partial wave a_1, measured at the selected reference plane, which is usually the antenna connector.

The antenna impulse response (AIR) is simply the inverse Fourier transform of the ATF:

$$\mathcal{h}\left(t,\hat{\mathbf{r}}\right)=\mathcal{F}^{-1}\left\{\mathcal{H}\left(f,\hat{\mathbf{r}}\right)\right\}\left(t\right) \text{---(3.3)}$$

At the receiver level, the antenna is illuminated by a plane wave (Fig. 3.1). The input signal is a vector quantity proportional to the incident electric field that generates a proportional partial wave b_2 as output signal. It is proved for example in [74] that in reception, the ATF is given by:

$$\mathcal{H}^{R}\left(f,\hat{\mathbf{r}}\right)=-j\frac{\lambda}{4\pi}\mathcal{H}^{T}\left(f,\hat{\mathbf{r}}\right) \quad (3.4)$$

And the corresponding AIR in reception is

$$\hbar^{R}\left(t,\hat{\mathbf{r}}\right)=\mathcal{F}^{-1}\left\{\mathcal{H}^{R}\left(f,\hat{\mathbf{r}}\right)\right\}(t) \quad (3.5)$$

For the rest of the chapter, and for simplicity, the ATF $\mathcal{H}^{\mathrm{T}}$ and the AIR $\hbar^{\mathrm{T}}$ will be denoted $\mathcal{H}$ and $\hbar$, respectively.

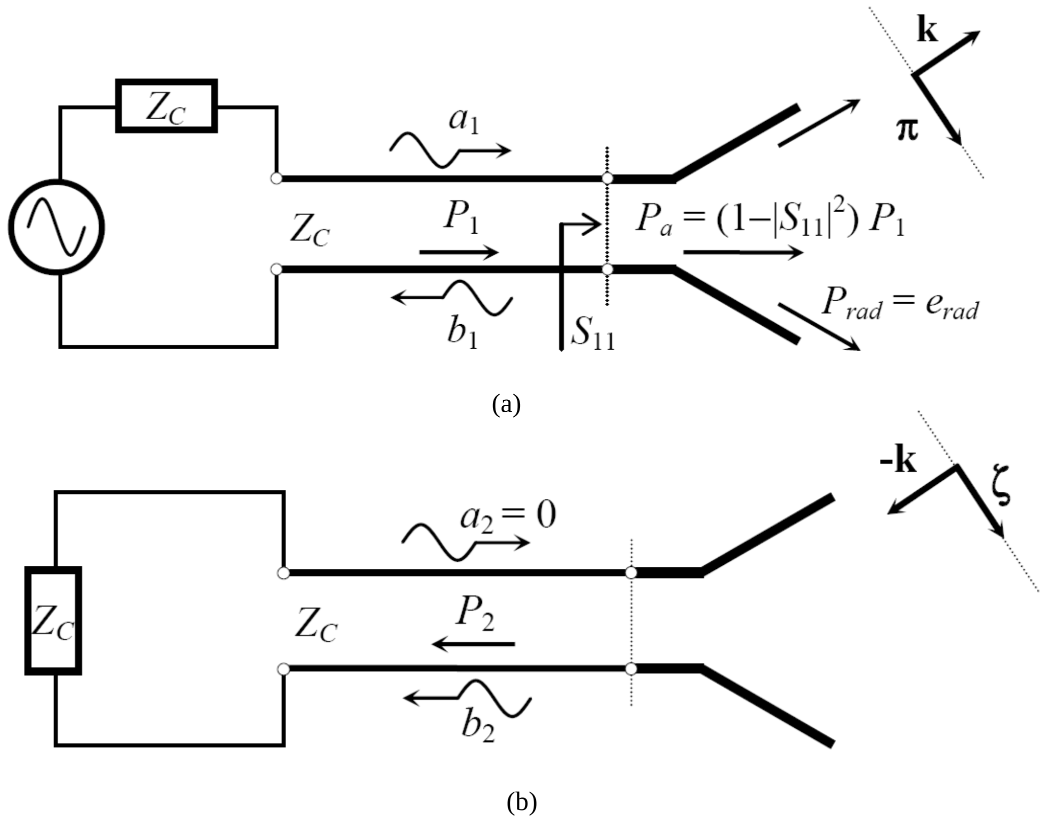

Fig. 3.1 Schematic of the antenna system (a) in transmission source model including a transmission line of characteristics impedance Z_c. The input signal of the system is the incident partial wave a_1. The output signal $\mathcal{A}$ is proportional to the far field E (k,π) in the state (k,π); (b) in reception, the input signal is proportional to electric field of the incident plane wave in the state (−k, ζ), of the identical polarization if ζ = π*.[73]

3.3. Synthetic performance indicators

The ATF and the AIR are fundamental quantities describing the UWB antenna behavior regarding the radiation properties of the antenna in the far field, as complemented by impedance matching information (e.g. $S_{11}(f)$).

3.3.1. Mean realized gain (MRG)

The mean realized gain is the mean of the realized gain G_r, also expressed as an effective gain over the input bandwidth BW_i,

$$MRG(\hat{\mathbf{r}}) = \frac{1}{BW_i}\int_{f_1}^{f_2} G_r(\hat{\mathbf{r}}, f)\,df \text{ --(3.6)}$$

where G_r is shown to be related to the ATF by:

$$G_r(f,\hat{\mathbf{r}}) = \left\|\mathcal{H}(f,\hat{\mathbf{r}})\right\|^2 = \mathcal{H}(f,\hat{\mathbf{r}})\cdot\mathcal{H}^*(f,\hat{\mathbf{r}}) \text{ --(3.7)}$$

The MRG is useful in the sense that it expresses the overall energy transfer from the source towards free space. In addition, the average direction of the main lobe (Θ_M, Φ_M) and the beam width of the radiated field, which are important quantities, can be determined from the MRG.

3.3.2. Group delay (τ_g)

One of the important indicators of the distortion in the radiated pulse is the group delay τ_g. An ideal UWB antenna has a constant group delay for the signals propagating from the input port to free space through the antenna at any frequency. In practice, this indicator will be computed over the band of interest. In real antennas, it is commonplace to observe a variation in group delay at differing look angles, which can be called “phase distortion” and is the cause of varying distortion over the radiation pattern.

The group delay is the rate of change of the ATF phase with respect to the angular frequency.

$$\tau_g(f) = -\frac{\partial\phi}{\partial\omega}(f) = -\frac{1}{2\pi}\frac{\partial\phi}{\partial f}(f) \text{ ---(3.8)}$$

The ATF is a complex vector field thus it is appropriate to consider the group delay per polarization state (***k***,***π***):

$$\tau_g^{\pi}(f,\hat{\mathbf{r}}) = -\frac{1}{2\pi}\frac{\partial\phi_\pi}{\partial f}(f,\hat{\mathbf{r}}) \text{ ---(3.9)}$$

with $\mathcal{H}_\pi(f,\hat{\mathbf{r}}) = \left|\mathcal{H}_\pi(f,\hat{\mathbf{r}})\right| e^{j\phi_\pi(f,\hat{\mathbf{r}})}$. For simplicity, unless necessary, the notation of polarization will not be explicitly shown in the following.

3.3.3. Differential group delay ($\Delta\tau_g$)

The differential group delay is more suitable for characterization of highly dispersive antennas, where the difference between the minimum and maximum group delay is more important. It can be written as follows:

$$\Delta\tau_g(\hat{\mathbf{r}}) = \max_{f \in BW_i} \tau_g(f,\hat{\mathbf{r}}) - \min_{f \in BW_i} \tau_g(f,\hat{\mathbf{r}}) \text{ --(3.10)}$$

3.3.4. Standard deviation of group delay (σ_{τ_g})

The standard deviation of group delay gives the indication of group delay variations with respect to the average group delay ($\overline{\tau}_g(\hat{\mathbf{r}})$):

$$\sigma_{\tau_g}(\hat{\mathbf{r}}) = \sqrt{\frac{1}{BW_i}\int_{f_1}^{f_2}\left[\tau_g(f,\hat{\mathbf{r}}) - \overline{\tau}_g(\hat{\mathbf{r}})\right]^2 df} \text{ ---(3.11)}$$

where the average group delay is given by:

$$\overline{\tau}_g(\hat{\mathbf{r}}) = \frac{1}{BW_i}\int_{f_1}^{f_2}\tau_g(f,\hat{\mathbf{r}})\,df \text{ --(3.12)}$$

The standard deviation of group delay is suitable for slightly dispersive antennas or those that have low fluctuation in their group delays in the band of interest.

3.3.5. Antenna Delay Spread (τ_{ds})

The delay spread rather takes into account all the sources of distortion. It expresses the dispersion of the group delay and can be defined as the second order moment of the delay of the AIR, weighted by the instantaneous power:

$$\tau_{ds}(\hat{\mathbf{r}}) = \sqrt{\frac{\int_0^\infty (\tau-\overline{\tau})^2\, p(\tau,\hat{\mathbf{r}})\,d\tau}{\int_0^\infty p(\tau,\hat{\mathbf{r}})\,d\tau}} \text{ --(3.13)}$$

where $p(\tau,\hat{\mathbf{r}})$ is the instantaneous power defined as:

$$p(\tau,\hat{r}) = h^2(\tau,\hat{r}) \text{ ---(3.14)}$$

and $\overline{\tau}$ is the mean excess delay and is written as:

$$\overline{\tau}(\hat{\mathbf{r}}) = \frac{\int_0^\infty \tau\, p(\tau,\hat{\mathbf{r}})\,d\tau}{\int_0^\infty p(\tau,\hat{\mathbf{r}})\,d\tau} \text{ ---(3.15)}$$

3.4. Optimization

The optimization procedure investigated in this work is illustrated in Fig. 3.2. Starting from a generic design, the shape constraints are then imposed such that, while changing the parameter values, the general shape (triangular, disc and dual feed monopole etc) of the design — i.e. the antenna class — should not change, as explained in chapter 2.

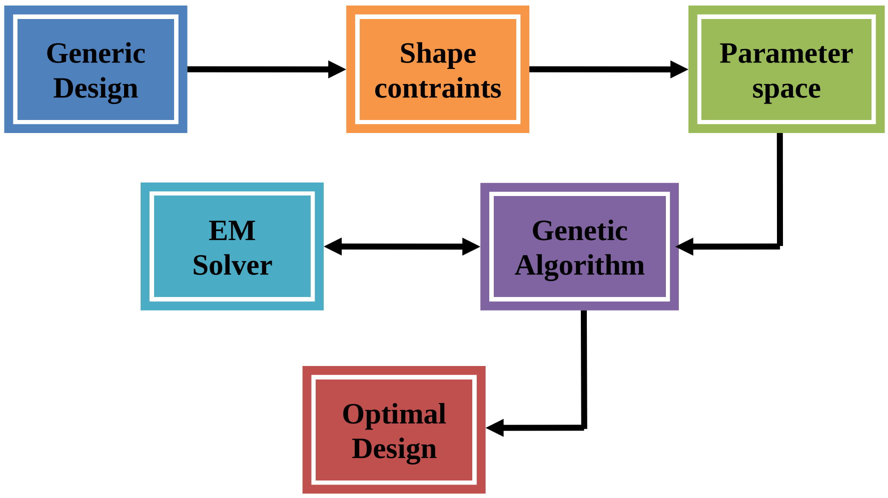

Fig. 3.2 Procedure for Antenna Optimization

The parameter space is particular for each shape; it mainly depends upon the complexity of the shape, upon an a priori knowledge about the design and upon the technological limitation in the practical fabrication of the antenna.

The CST-MWS solver is used throughout this thesis but any other solver can, in principle, be used. In the following section, a short introduction to genetic algorithm is provided.

3.4.1. Genetic Algorithm

Genetic algorithm (GA) optimization has become increasingly popular for antenna design problems where a clear approach to a solution does not exist [75]. For example, GA has been used to generate non conventional wire-based and patch-based antenna designs that demonstrated improved impedance matching bandwidth, when compared with designs generated using traditional techniques. The benefits of applying GA in this case are twofold: improved designs can be developed, and an analysis of the solutions generated by the GA results in a better understanding of the operating principle of these antennas.

GA differs from the conventional optimization techniques, for three reasons: first it operates on a group (or population) of trial solutions in parallel; secondly, it normally operates on a coding of the parameters (chromosomes) rather than on the parameters themselves; finally, it uses stochastic operators (selection, crossover, and mutation) to explore the solution domain in searching an optimal solution.

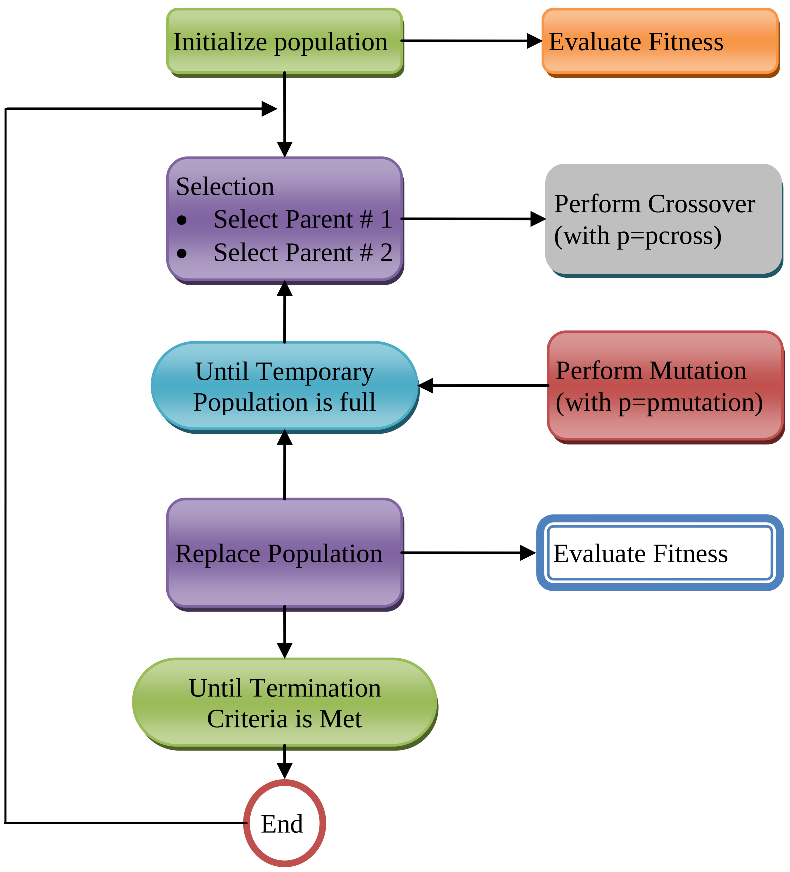

Fig. 3.3 Block diagram of simple Genetic algorithm Optimizer [75]

In a simple GA optimizer (Fig. 3.3), a set of trial solutions is caused to evolve toward an optimal solution under the selective pressure of the fitness function. The trial solutions are represented by a string of parameters, generally encoded in binary numbers. The operators of selection, crossover and mutation act on the population of trial solutions to produce a new generation from the current generation. The optimization objectives are used to influence the constitution of the new generation, through the evaluation of the fitness function, which assigns a numerical value to each individual.

3.4.2. Cost function (or Goal /fitness function)

The cost function is a particular type of objective function that summarizes the antenna response in a single figure-of-merit that explains how close the design is from the set goals/aims.

In GA, the cost function is the only connection between the physical problem being optimized and the algorithm. Each time when the GA finds a solution to EM problem the cost function then assigns a value to the solution. This assigned value (Cost) is then compared to the predefined targets or goals. Based on this compared value GA makes the decision for the next generation in sequence.

The CST MWS software offers various cost functions for different types of EM problems, the one which is most commonly used in antenna field is the reflection coefficient $|S_{11}|$ at the antenna input. One difficulty with this cost function is its method for calculating the cost. For instance, if an antenna input matching is to be optimized for a reflection coefficient less than −10 dB over a bandwidth of [3—11] GHz with CST built-in $|S_{11}(f)|$ cost function using GA, it will calculate its cost by taking the average of $|S_{11}(f)|$ over the desired frequency band and then subsequently compare this cost to the target (−10 dB). In this case, if the $|S_{11}(f)|$ response has deep resonances (−20 dB to −30 dB) at some frequency groups in the band and rest of the band is near to the targeted value, the cost of this response will still be good according to CST MWS built-in cost function and will be ranked higher for the next generation. This goes on, and the GA keeps trying to optimize with this cost and eventually converges to a design that is not desired.

The alternative is to enforce a threshold such that whenever the point in the response has lower value than the target, this point is replaced by the target value. In other words, performing a clipping action, we can write;

$$\text{cost} = [m_1]\frac{1}{\Delta f}\int_{f_1}^{f_2} g\left(\left|S_{11}(f)\right|\right)df + [m_2]V \quad \text{--(3.16)}$$

where, $g(|S_{11}(f)|)$ is a clipping function, as defined in (3.17). V is the volume of the substrate and m_1, m_2 are respective normalizing weights. The target for input matching bandwidth is –10 dB (0.3126) whereas for volume (V) is ~290 mm^3 (for monopoles), this corresponds to lowest radius of circumscribing sphere around the antenna (R_{min}) and widest angles $\{\psi, \gamma\}$. This cost function drives the GA to converge to a small overall design size, while keeping $|S_{11}(f)| < -10$ dB.

$$g\left(\left|S_{11}(f)\right|\right)=\begin{cases}0.3126 & , \quad \left|S_{11}(f)\right|\le 0.3126\\ \left|S_{11}(f)\right| & , \quad \left|S_{11}(f)\right|>0.3126\end{cases} \text{--(3.17)}$$

The clipping function restrains the GA not to focus on deep resonances in the band of interest.

3.5. The optimal designs

The aim of searching an optimal design is to find a "best available" extremum of the cost function in the given parameter space. Each planar antenna design that has been discussed in chapter 2 is now examined here in this perspective.

In the following, frequency and time domain key characteristics have been described to demonstrate the performance of the optimal designs. The frequency domain characteristics have been demonstrated for, the reflection coefficient response, for the realized gain vs frequency response in few radiation directions and for the total MRG response computer over [3—11] GHz band. In addition MRG meridian cuts at $\varphi = 0°$ and $\varphi = 90°$ and equatorial cut at $\theta = 90°$ have been considered.

The time domain characteristics have been presented through the impulse response after preprocessing with Blackman windowing and zero-padding. They have been analyzed through group delay (τ_{g}) response in a few directions, the responses of differential group delay ($\Delta\tau_g$) and standard deviations ($\sigma\tau_g$) of the group delay and lastly by presenting the delay spreads results (τ_{ds}) to show the overall distortion of the antenna.

The dielectric material for all the antenna is FR4 ($\varepsilon = 4.9$) with the thickness of 1.524 mm.

3.5.1. Triangular monopole

The parameter space for the triangular monopole design is listed in Table 3.1, along with the best found parameter values at the end of optimization cycle. The parameters in Table 3.1 are the same as given in Table 2.1 (chapter 2), R_{cond} is the radius of the central conductor of SMA connector and d_{coax} is the outer diameter of this connector. The optimized design is shown in Fig. 3.4. The total height is less than the quarter of the lowest wavelength of the band.

In the reflection coefficient response (Fig. 3.5a) at 3 GHz and 5 GHz, the $|S_{11}|$ value is −8.5 dB and at 10.6 GHz it is −9 dB which are acceptable values. The realized gain (Fig. 3.5b) in the direction (θ,φ) = (90°,0°) presents less variations than at the maximum realized gain direction (θ,φ) = (65°,180°). The MRG of the antenna (computed over [3 – 11] GHz) is plotted in Fig. 3.5c.

Table 3.1 Parameter Space for Triangular Monopole with Optimal values

	Parameter	Interval		Best
		Lower	Upper	
1	R_{min}	12	25	13.55
2	w_0	$2R_{cond}$	$d_{coax} - 2g_0$	1.169
3	g_0	0.15	1	0.624
4	γ	45°	120°	70.97
5	ψ	45°	170°	71.59
6	κ	1	5	2.891
7	α	78	90	82.770
8	ζ	0	1	0.6421

The MRG appears quasi omnidirectional when looking at the 3D pattern of Fig. 3.5c. This can be clearly noticed in Fig. 3.5d from the azimuth plane cut at θ = 90°. There is a little gain advantage that can be noticed at φ = 180° (towards the substrate direction). The elevation cuts at φ = 0° (Fig. 3.5e) and at φ = 90° (Fig. 3.5f) of the MRG shows a dipole like pattern. This phenomenon perhaps can be explained by Fig. 3.4 where it can be seen the directions of the current density vector at the connector output and over the outer sheath of the connector. They are similar to a dipole like radiator.

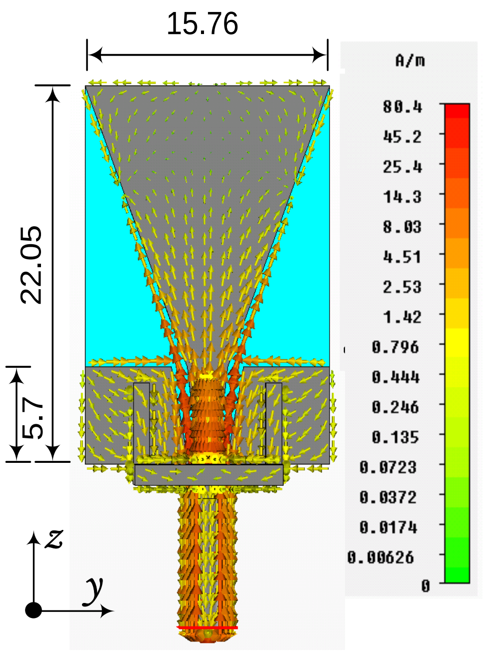

Fig. 3.4 Optimal design with Peak surface current distribution at 3.4 GHz.

The time domain performances are shown in Fig. 3.6. The impulse responses in different directions (Fig. 3.6a), show that the maximum pulse duration is 0.7 ns in the main beam direction. Group delay responses (Fig. 3.6b) at (θ,φ) = {(90°,180°), (90°, 0°)} directions show a relatively constant group delay. The differential group delay ($\Delta\tau_g$) (Fig. 3.6c) and the standard deviation ($\sigma_{\tau g}$) (Fig. 3.6d) of the group delay show that for θ = [30°—120°] and for all values of φ , the fluctuation in the group delay is less ($\sigma_{\tau g}$ ~0.2 ns).

This angular variation in delay is clearer with delay spreads results (Fig. 3.6f). The minimum distortion occurs when θ = [70°—95°] for φ = [140°—225°] and φ = [0°—45°]. This is also shown in meridian cut at φ = 0° (Fig. 3.6e) where a time spreading of less than 100 ps is noted.

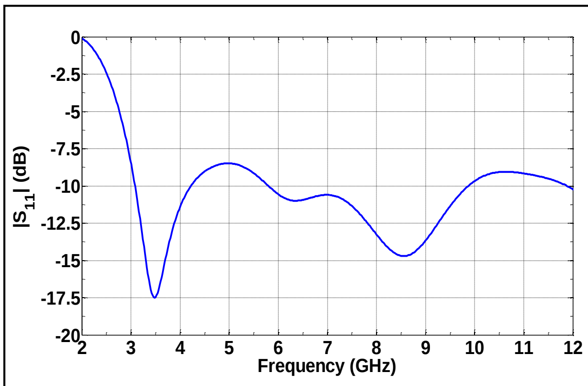

(a) $|S_{11}|$ response

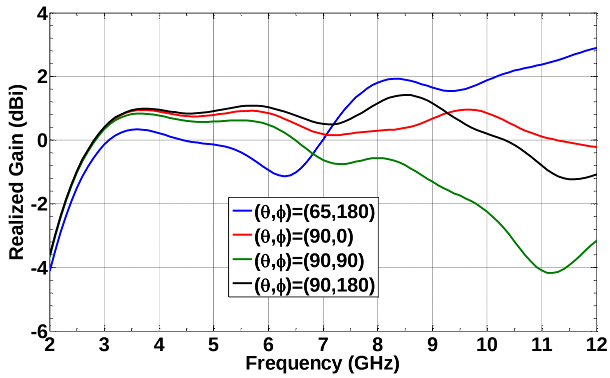

(b) Realized Gain on different look angles

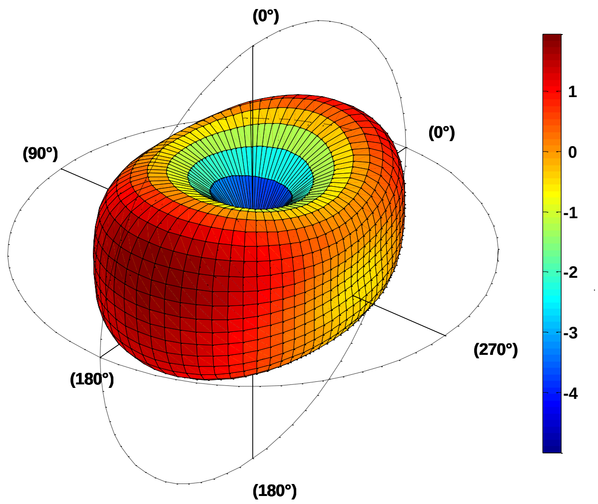

(c) MRG_{max} = 1.96 dBi, {(θ,φ) = (60°,180°)}

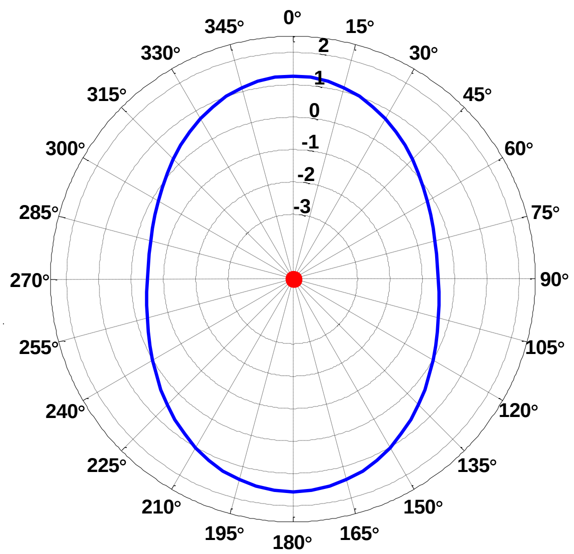

(d) co-polar (blue), cross polar (Red)

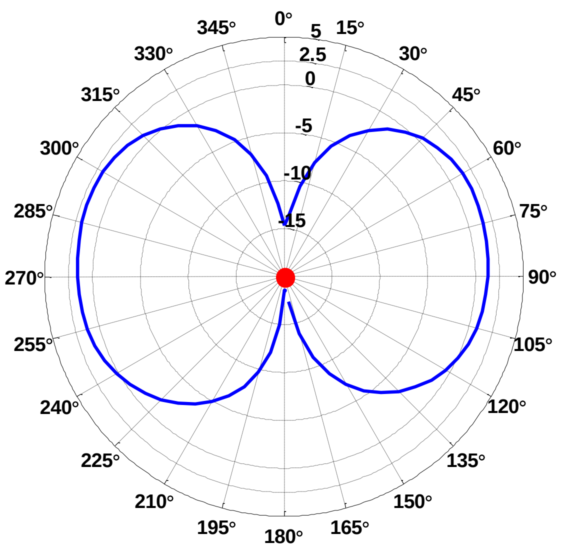

(e) co-polar (blue), cross polar (Red)

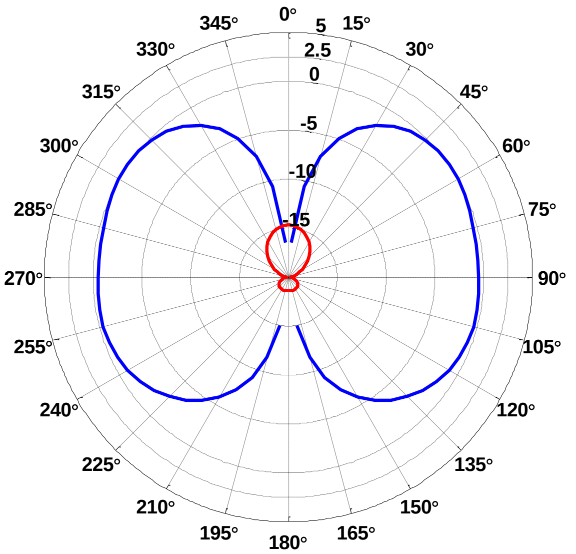

(f) co-polar (blue), cross polar (Red)

Fig. 3.5 Optimal Triangular Monopole Antenna's frequency domain performance characteristics, (a) Reflection coefficient, (b) Realized gain vs. frequency in different directions, (c) Total MRG 3D representation, (d) MRG, Azimuth cut θ = 90°, (e) MRG, Elevation cut at ϕ = 0°, (f) MRG, Elevation cut at ϕ=90°

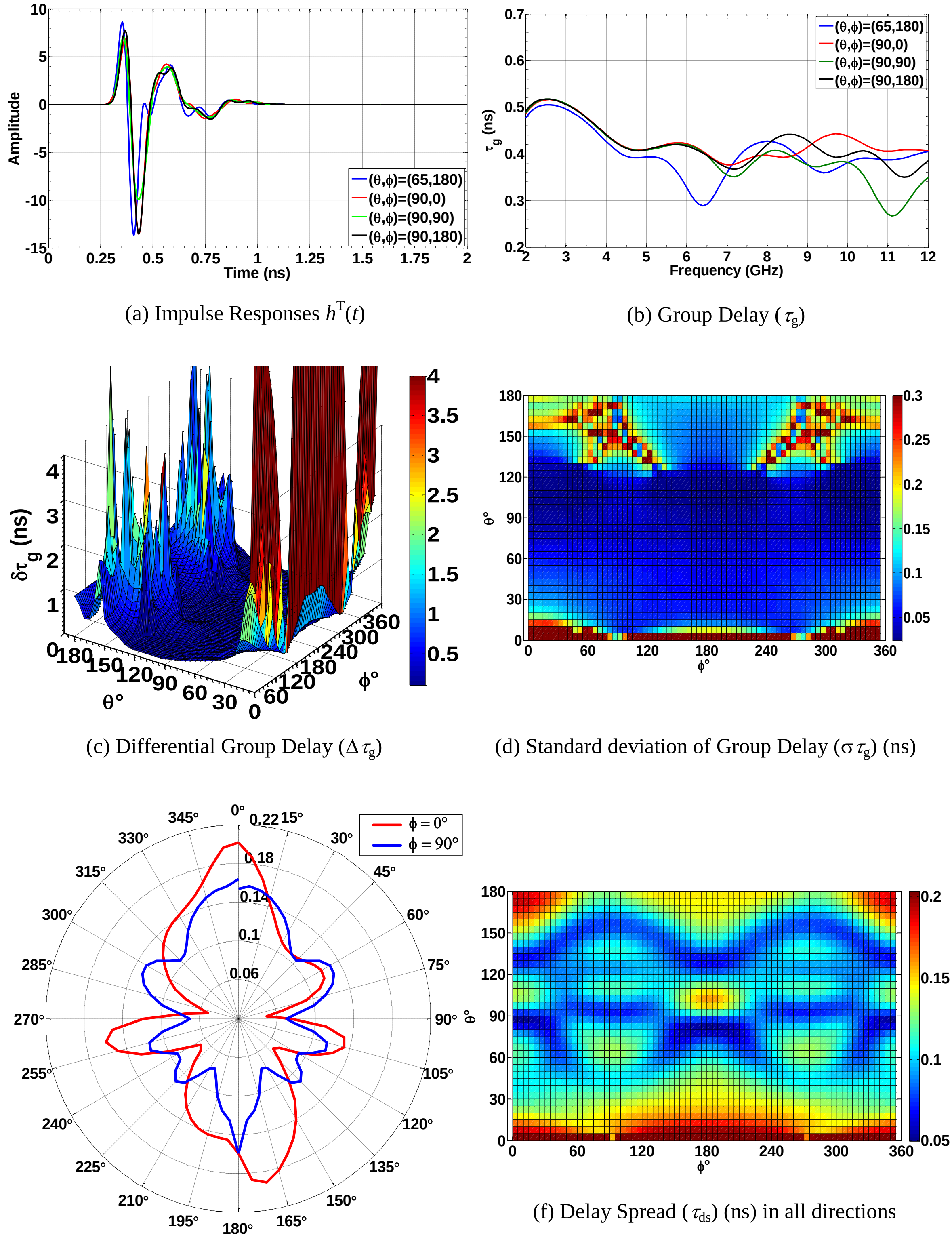

(a) Impulse Responses $h^T(t)$

(b) Group Delay (τ_g)

(c) Differential Group Delay ($\Delta\tau_g$)

(d) Standard deviation of Group Delay ($\sigma\tau_g$) (ns)

(f) Delay Spread (τ_{ds}) (ns) in all directions

(e) Delay Spread (ns) elevation cuts

Fig. 3.6 Time domain performance characteristics of Optimal Triangular Monopole Antenna, (a) Impulse response $h^T(t)$ (b) Group delay (τ_g) at different directions (c) Differential Group delay ($\Delta\tau_g$) (d) Standard deviation of group delay ($\sigma\tau_g$) (e) Delay spread elevation cuts at $\varphi = 0°$ and $\varphi = 90°$ (f) Delay spread in all directions

3.5.2. Staircase Monopole

The parameter space is presented in Table 3.2 with the optimal values achieved at the end of optimization cycle. It is worth mentioning that this is the random step size version (chapter 2, section 2.4.2.2) of a staircase monopole.

Table 3.2 Parameter Space for Staircase Monopole with Optimal values

Parameter		Interval		Best
		Lower	Upper	
1	R_{min}	12	25	13.80
2	w_0	$2R_{cond}$	$d_{coax} - 2g_0$	1.6431
3	g_0	0.15	1	0.71
4	γ	45°	120°	63.5
5	ψ	45°	170°	64.4
6	κ	1	5	1.98
7	α	78	90	84.3
8	ζ	0	1	0.531
	δ_k	0.1	0.9	--
	β_k	0	1	--

The optimal values for uniformly distributed random variables δ_k and β_k for each step height and width respectively are not of interest. Instead the actual optimal values of height and width of each step are shown in Fig. 3.7. R_{min} is 13.8 mm and the total height is less than the quarter wavelength at 3 GHz. The reflection coefficient response (Fig. 3.8a) presents -10 dB input matching bandwidth of [3-12] GHz. The realized gain (Fig. 3.8b) in the direction (θ,φ) = (90°,0°) has less variations than at the maximum realized gain direction (θ,φ) = (65°,180°). The total MRG of the

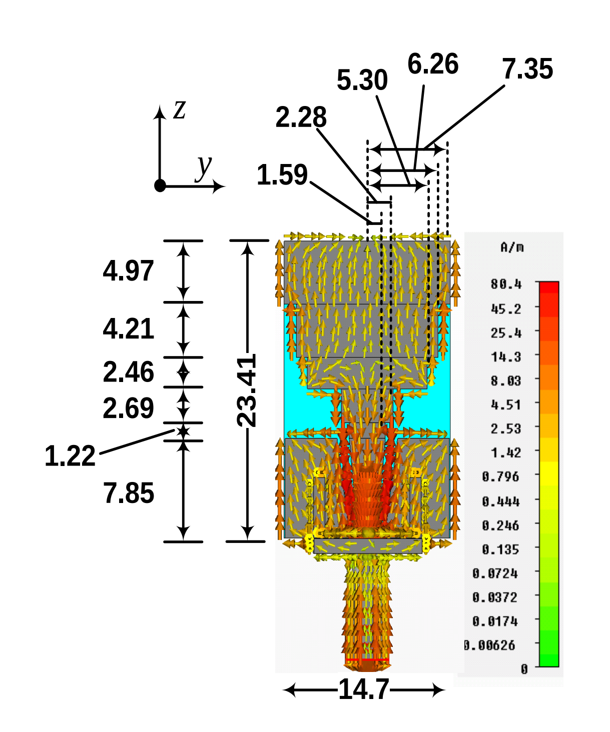

Fig. 3.7 Optimal design with Peak surface current distribution at 3.4 GHz. (The values are in *mm*.)

antenna (computed over [3-11] GHz) is plotted in Fig. 3.8c. The MRG appears quasi omnidirectional when looking at the 3D pattern of Fig. 3.8c. This can be clearly noticed in Fig. 3.8d from the azimuth plane cut at θ = 90°. A clear gain advantage due to the dielectric substrate is observed at φ = 180°. The direction of maximum gain can be noticed in elevation cut at φ = 0° (Fig. 3.8e) and the small depression in the total MRG (Fig. 3.8c) is clear in elevation cut in φ = 90° (Fig. 3.5f).

The time domain performances are shown in Fig. 3.9. The impulse responses in different directions (Fig. 3.9a), show that the maximum pulse duration is around 0.75 ns in the main beam direction. Group delay responses (Fig. 3.9b) at (θ,φ) = {(90°,180°), (90°, 0°)} directions have relatively less variations in group delay when compared to main beam direction where a group of frequencies from 5 to 7 GHz takes small group delay. The differential group delay ($\Delta\tau_g$) (Fig. 3.9d) and the standard deviation ($\sigma_{\tau g}$) (Fig. 3.9c) of the group delay show that for θ = [60°—120°] and for all values of φ, the fluctuation in the group delay is less than 1 ns.

This angular variation in delay is clearer with delay spreads results (Fig. 3.9f). The minimum distortion occurs when θ = [60°—120°] for φ = [140°—225°] and φ = [−35°—35°]. This is also shown in meridian cut at φ = 0° (Fig. 3.9e) where a time spreading of less than 400 ps.

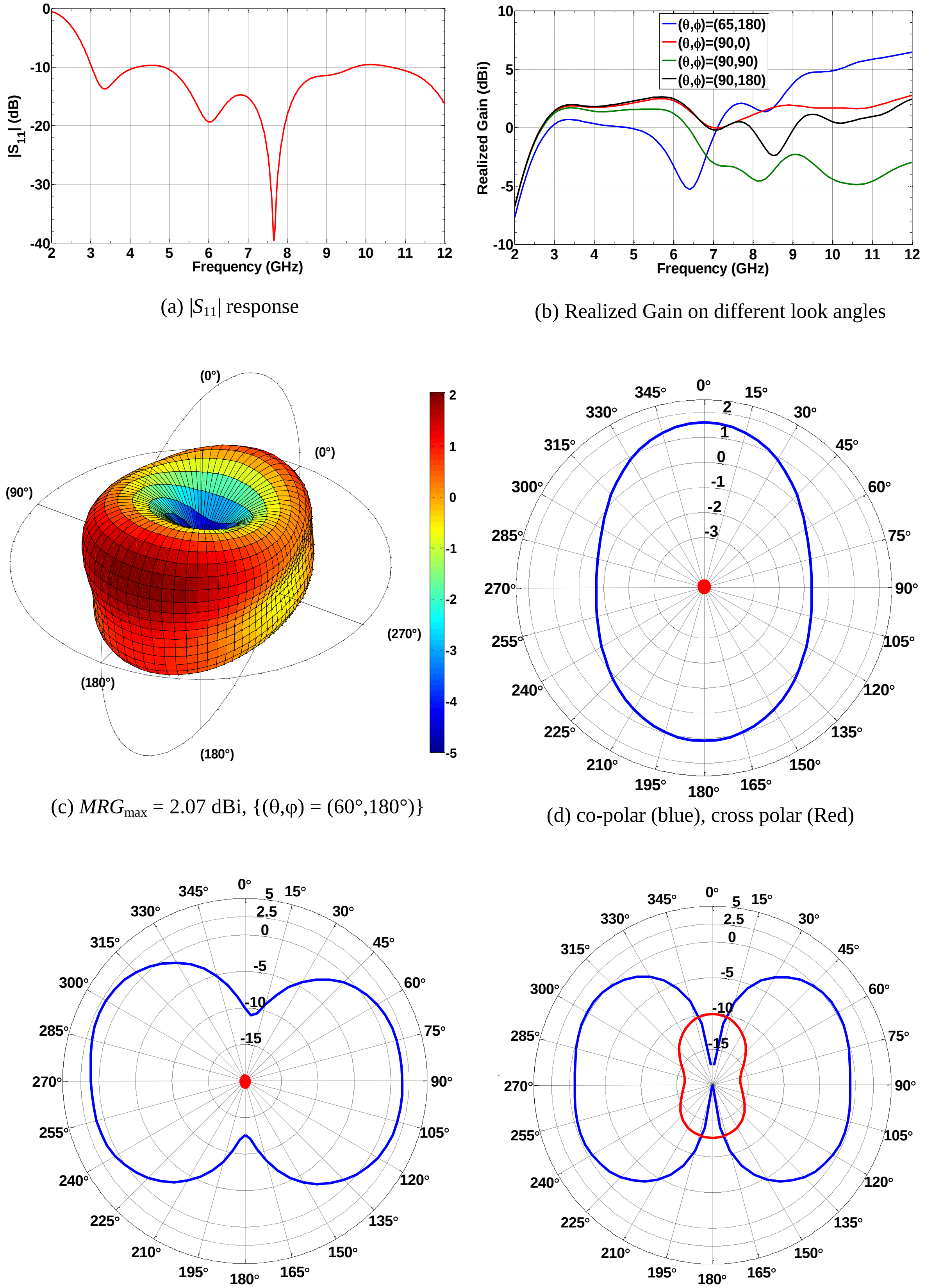

(a) $|S_{11}|$ response

(b) Realized Gain on different look angles

(c) $MRG_{\max}$ = 2.07 dBi, {(θ,φ) = (60°,180°)}

(d) co-polar (blue), cross polar (Red)

(e) co-polar (blue), cross polar (Red)

(f) co-polar (blue), cross polar (Red)

Fig. 3.8 Frequency domain performance characteristics of optimal Staircase Monopole Antenna, (a) Reflection coefficient, (b) Realized gain vs. frequency in different directions, (c) Total MRG 3D representation, (d) MRG, Azimuth cut θ = 90°, (e) MRG, Elevation cut at ϕ = 0°, (f) MRG, Elevation cut at ϕ=90°

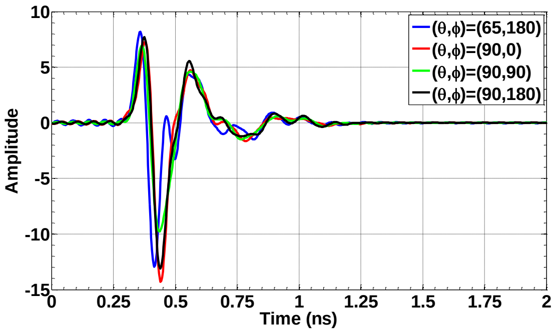

(a) Impulse Responses $h^{T}(t)$

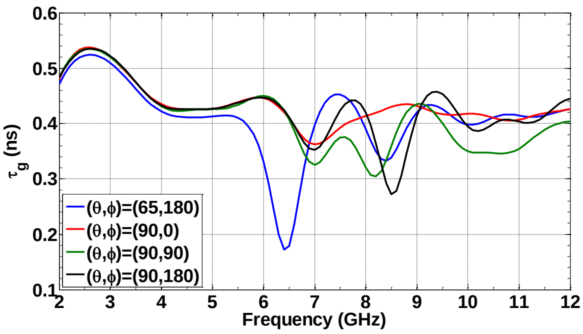

(b) Group Delay (τ_g)

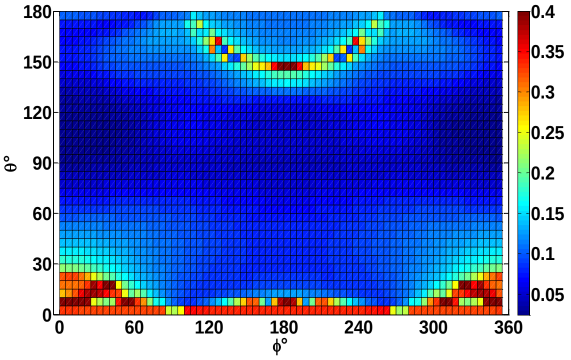

(c) Standard deviation of Group Delay ($\sigma\tau_g$) (ns)

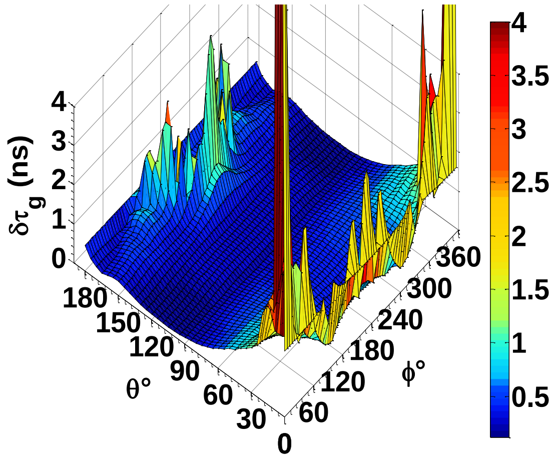

(d) Differential Group Delay ($\Delta\tau_g$) (ns)

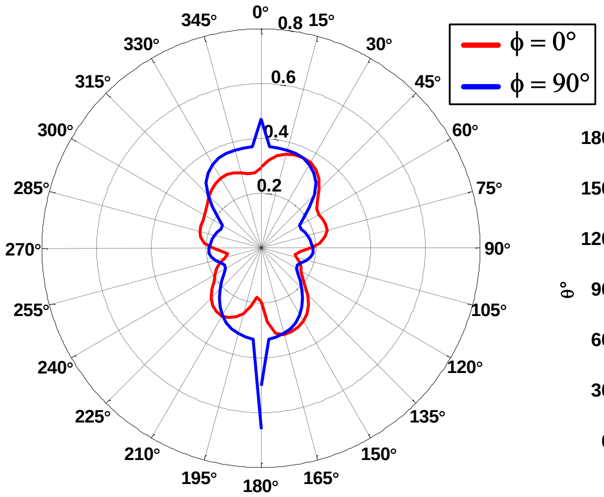

(e) Delay Spread (ns) elevation cuts

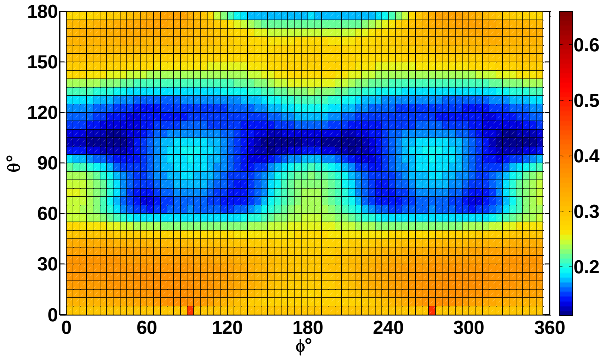

(f) Delay Spread (τ_{ds}) (ns) in all directions

Fig. 3.9 Time domain performance characteristics of the Optimal Staircase Monopole Antenna, (a) Impulse response $h^{T}(t)$ (b) Group delay (τ_g) at different directions (c) Standard deviation of group delay ($\sigma\tau_g$), (d) Differential Group delay ($\Delta\tau_g$) (e) Delay spread elevation cuts at $\varphi = 0°$ and $\varphi = 90°$ (f) Delay spread in all directions

3.5.3. Crab-claw Monopole

The parameter space is shown in Table 3.3 with the achieved optimal values. R_{min} is 15.1 mm and the total height and width are shown in the Fig. 3.10. The design has 6 layers (K = 5) of patches, the gaps $\{g_{k2} = g_{k+1,1}\}$ are {3.049, 3.59, 3.68, 3.59} and θ_k = {30°, 60°, 90°, 60°} for k = [1-4] (chapter 2, section 2.4.3).

Table 3.3 Parameter Space for Crab-claw Monopole with Optimal values

	Parameter	Interval		Best
		Lower	Upper	
1	R_{min}	12	25	15.1
2	w_0	$2R_{\mathrm{cond}}$	$d_{\mathrm{coax}} - 2g_0$	2.02
3	g_0	0.15	1	0.613
4	γ	45°	100°	52.77
5	ψ	30°	120°	33.95
6	κ	1	5	4.6
7	α	78	90	82.9
8	ζ	0	1	0.58
9	Δg	1	$Ws/2 - w_{\mathrm{p}}$	1.99
10	w_p	1	y_{K2}	2.713

The substrate width (Ws) is due to the maximum of the angles γ and ψ. The opening between the upper tips of two crab tentacles is g_{K2} = 1.69.

The reflection coefficient response (Fig. 3.11a) shows that a number of frequencies in [4.5-9.6] GHz have above -10 dB response; the maximum is −8.2 dB, which is still acceptable value. The realized gain (Fig. 3.11b) in the direction (θ,φ) = (65°,180°) (MRG_{max} direction) has relatively low variations. The total MRG of the antenna (computed over [3-11] GHz) is plotted in Fig. 3.11c. The MRG presents noticeable reductions again in the dielectric direction i.e. φ = 180°. This can be clearly noticed in Fig. 3.11d in the azimuth plane cut at θ = 90°. The direction of maximum gain can be observed in elevation cut at φ = 0° (Fig. 3.11e) and the attenuation in the total MRG (Fig. 3.11c) in the lateral directions is clear in elevation cut in φ = 90° (Fig. 3.11f).

The time domain performances are shown in Fig. 3.12. The impulse responses in different directions (Fig. 3.12a), show the ringing effect which is relatively less in (θ,φ) = (90°, 180°) direction. The maximum pulse duration is around 1.2 ns in the main beam direction. Group delay responses (Fig. 3.12b) at (θ,φ) = (90°,0°) direction demonstrate a positive phase slop for this band [7.2-7.5] GHz, this effect should be seen in conjunction to the realized gain response (Fig. 3.11b). The differential group delay ($\Delta\tau_g$) (Fig. 3.12d) and the standard deviation ($\sigma_{\tau g}$) (Fig. 3.12c) of the group delay show that for θ = [55°—80°] and for all values of φ, the fluctuation in the group delay is less than 0.5 ns.

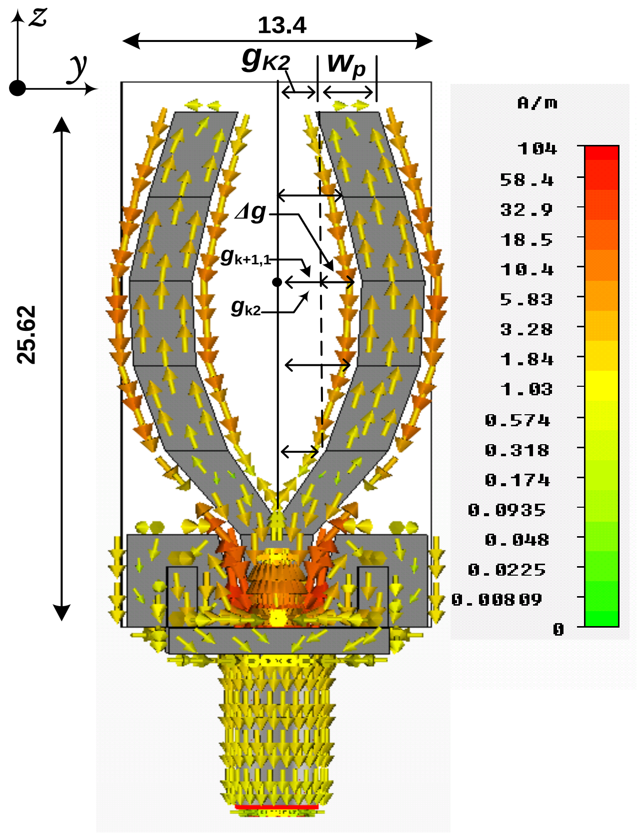

Fig. 3.10 Crab-claw optimal design with Peak surface current distribution at 3.5 GHz.

This angular variation in delay is clearer with delay spreads results (Fig. 3.12f). The minimum distortion occurs when θ = [35°—65°] for all values of φ, and also for θ = [85°—105°], φ = [110°-250°]. This has also been presented in meridian cut at φ = 0° (Fig. 3.6e) where a time spreading of less than 175 ps can be observed.

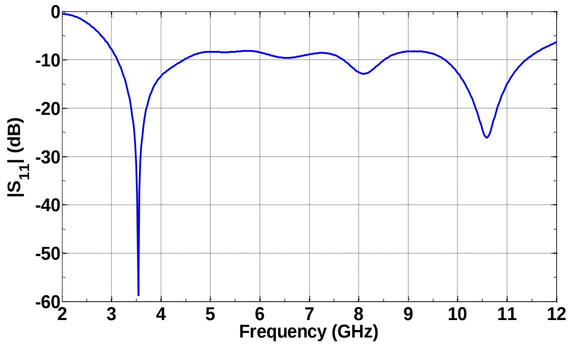

(a) $|S_{11}|$ response

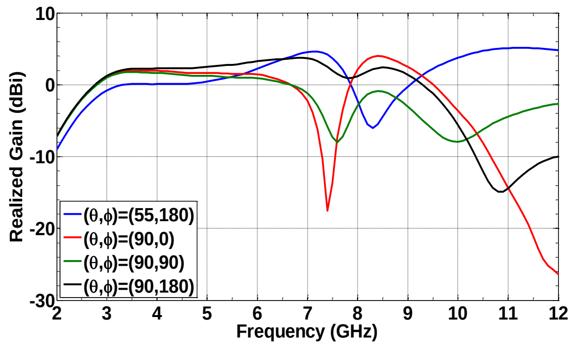

(b) Realized Gain on different look angles

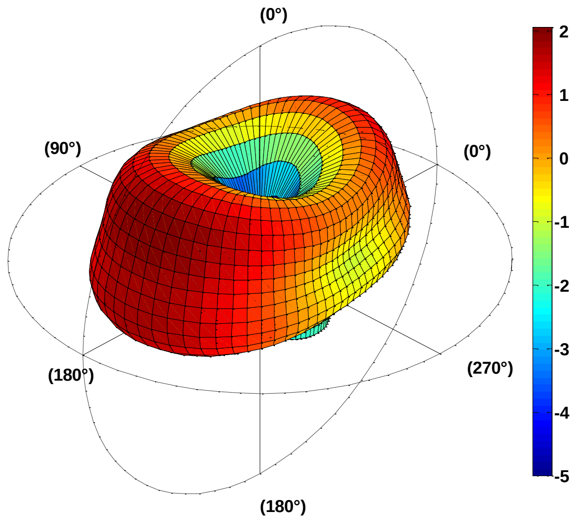

(c) $MRG_{\max}$ = 2.129 dBi, {(θ,φ) = (55°,180°)}

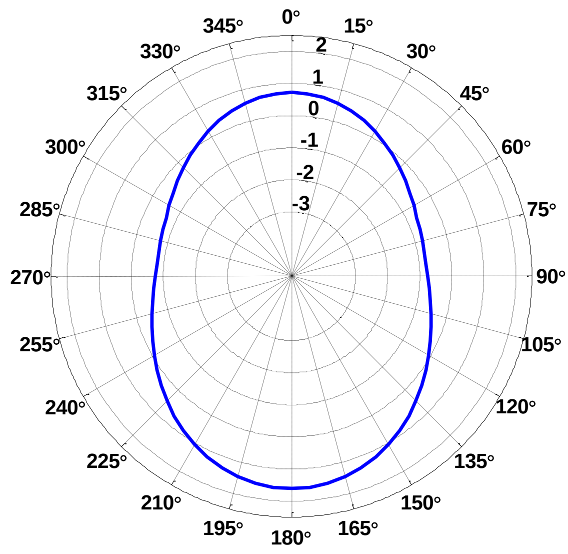

(d) co-polar (blue), cross polar (Red)

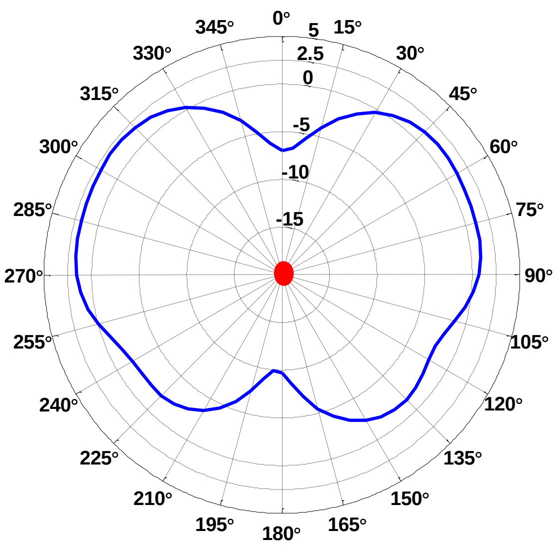

(e) co-polar (blue), cross polar (Red)

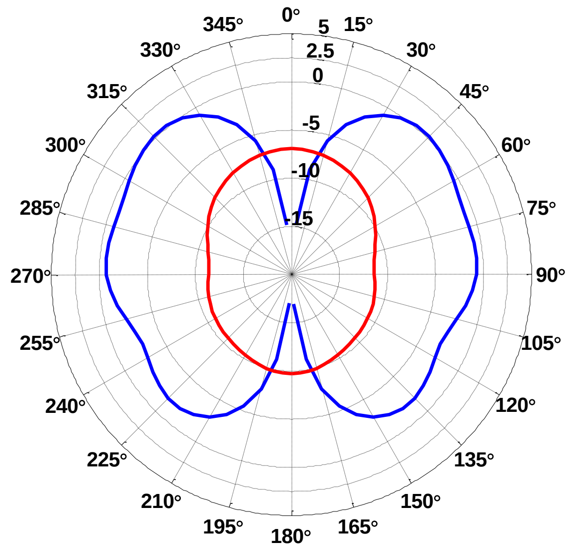

(f) co-polar (blue), cross polar (Red)

Fig. 3.11 Frequency domain performance characteristics of optimal Crab-claw Monopole Antenna, (a) Reflection coefficient, (b) Realized gain vs. frequency in different directions, (c) Total MRG 3D representation, (d) MRG, Azimuth cut θ=90°, (e) MRG, Elevation cut at ϕ = 0°, (f) MRG, Elevation cut at ϕ=90°

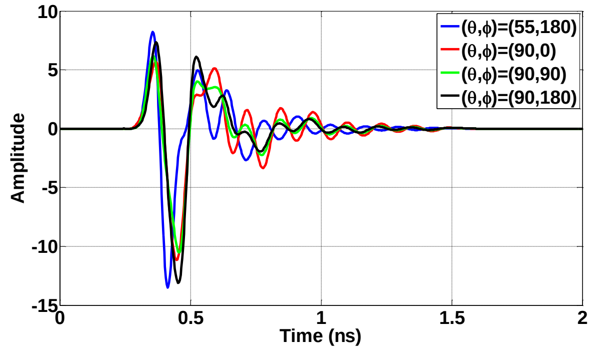

(a) Impulse Responses $h^{T}(t)$

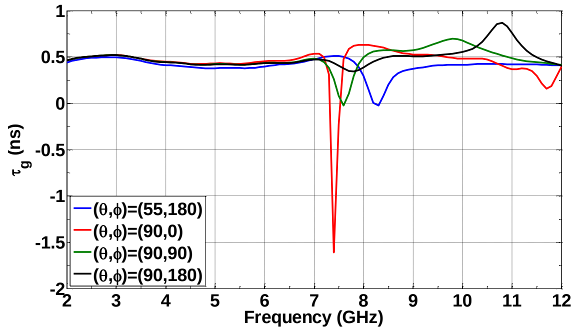

(b) Group Delay (τ_g)

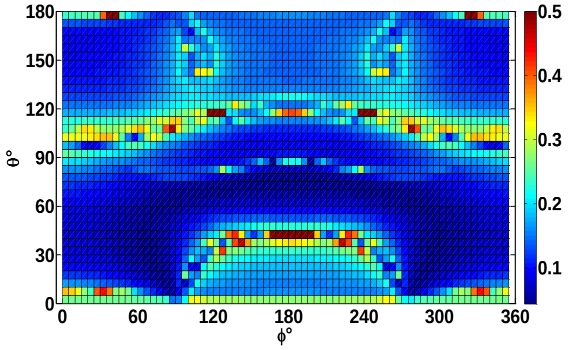

(c) Standard deviation of Group Delay ($\sigma\tau_g$) (ns)

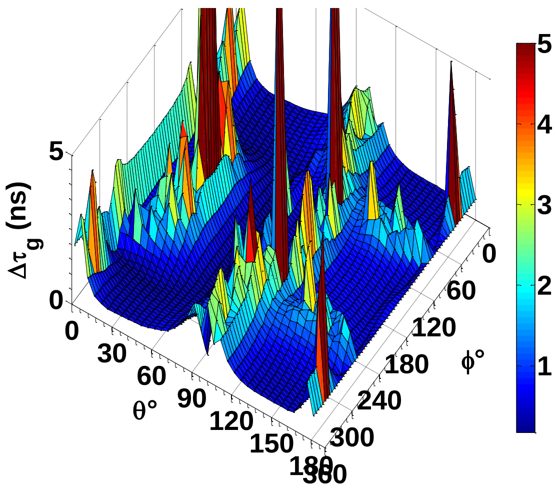

(d) Differential Group Delay ($\Delta\tau_g$)

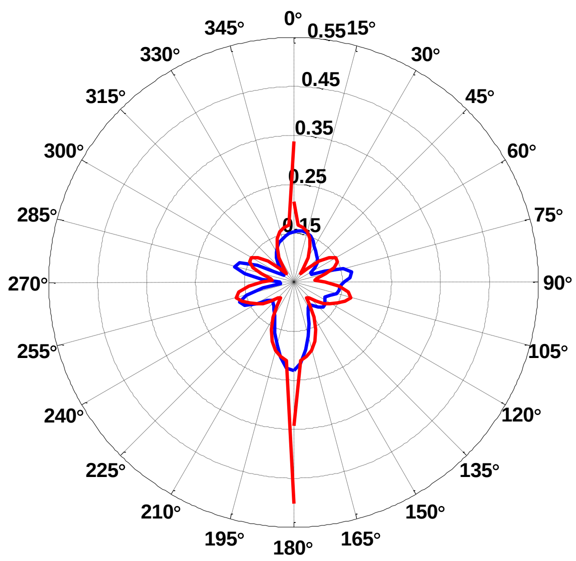

(e) Delay Spread (ns) elevation cuts

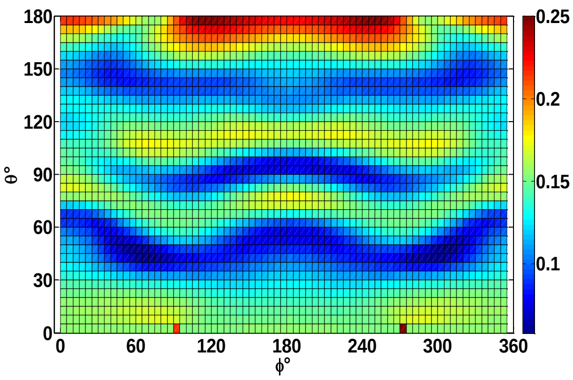

(f) Delay Spread (τ_{ds}) (ns) in all directions

Fig. 3.12 Time domain performance characteristics of Optimal Crab-claw Monopole Antenna, (a) Impulse response $h^{T}(t)$ (b) Group delay (τ_g) at different directions (c) Standard deviation of group delay ($\sigma\tau_g$), (d) Differential Group delay ($\Delta\tau_g$) (e) Delay spread elevation cuts at $\varphi = 0°$ and $\varphi = 90°$ (f) Delay spread in all directions

3.5.4. Dual Feed Monopole

The design is explained in chapter 2 (section 2.4.5), optimization is performed using 16 independent parameters (Table 3.4). R_{min} is 14 mm and the antenna overall size is 16.6 × 12.9 mm^2 (Fig. 3.13). The range of the random variable ζ is increased to [0-3], which in turns increase the range of values of g_1 since it was experienced during the optimization that the values of ζ reached the upper boundary of the parameter space for the acceptable designs. The substrate width (Ws) is decided by maximum of the angles γ and ψ.

Table 3.4 Parameter Space for Dual Feed Monopole with Optimal values

	Parameters	Interval		Best
		Min.	Max.	
1	R_{min}	12	22	14
2	γ	50	90	72.928
3	ψ	50	90	66.45
4	w_0	$2R_{cond}$	$d_{coax} - 2g_0$	2.3
5	α	78°	90°	89.11°
6	g_0	0.3	1	0.414
7	ζ	0	3	0.58
8	κ	1	5	3.22
9	w_{32}	$w_1/4$	$w_1/2$	0.7655
10	$w_{41} = w_{42}$	$g_{32} + w_{32}$	$Ws/2$	3.15
11	g_{61}	0.3	1	0.3715
12	g_{32}	1	$Ws/2 - w_{32}$	3.152
13	R_{h0}	0.1	1	0.2365
14	R_{hfeed}	0.1	1	0.26
15	R_{h4}	0.1	1	0.144
16	R_{h5}	0.1	1	0.136

The peak current distribution at 3.4 GHz is shown in Fig. 3.13, the feed fingers have greater influence over the radiation than other parts of the antenna. The reflection coefficient response (Fig. 3.14a) shows that a number of frequencies in the [4-5.3] GHz range have above -10 dB response the maximum being −8.8 dB which is acceptable. The realized gain (Fig. 3.14b) in the direction (θ,φ) = {(90°, 0°), (90°, 180°)} has stable gains for over [3-9.5] GHz. The total MRG of the antenna (computed over [3-11] GHz) is plotted in Fig. 3.14c. The gain in the antenna plane and also the attenuation (w.r.t. MRG_{max}) in lateral directions can be observed. This can be clearly seen in Fig. 3.14d for the azimuth plane cut at θ = 90°. The direction of maximum gain can be noticed in the elevation cut at φ = 0° (Fig. 3.14e) and the attenuation in the total MRG (Fig. 3.14c) in the lateral directions is evident in the elevation cut in at φ = 90°.

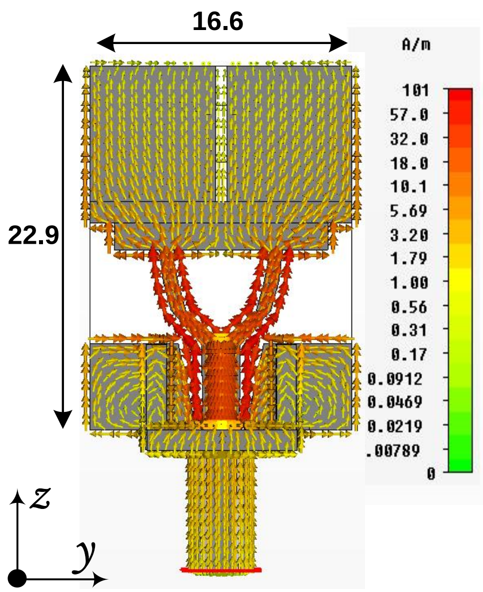

Fig. 3.13 Dual Feed Monopole: optimal design with Peak surface current distribution at 3.4 GHz.

The time domain performances are shown in Fig. 3.15. The Impulse responses in different directions (Fig. 3.15a), show that the maximum pulse duration is around 0.75 ns in the main beam direction. Group delay responses (Fig. 3.15b) in the directions (θ,φ) = {(90°,0°), (90°,180°)} have a relatively stable group delay, as compared to the main beam direction. The differential group delay ($\Delta\tau_g$) (Fig. 3.15d) and the standard deviation ($\sigma_{\tau g}$) (Fig. 3.15c) of the group delay show that for θ = [75°—125°] and for all values of φ, the fluctuation in the group delay is less than 0.15 ns.

This angular variation in delay is clearer on the delay spreads results (Fig. 3.15f). A distortion lower than 80 ps occurs when θ = [40°—110°] for all values of φ,. This can be seen in the blue color (Fig. 3.15f). This has also been presented in the meridian cut at φ = 0° (Fig. 3.15e) where a time spreading of less than 80 ps has been measured in θ = [65°—110°] and [255°-320°].

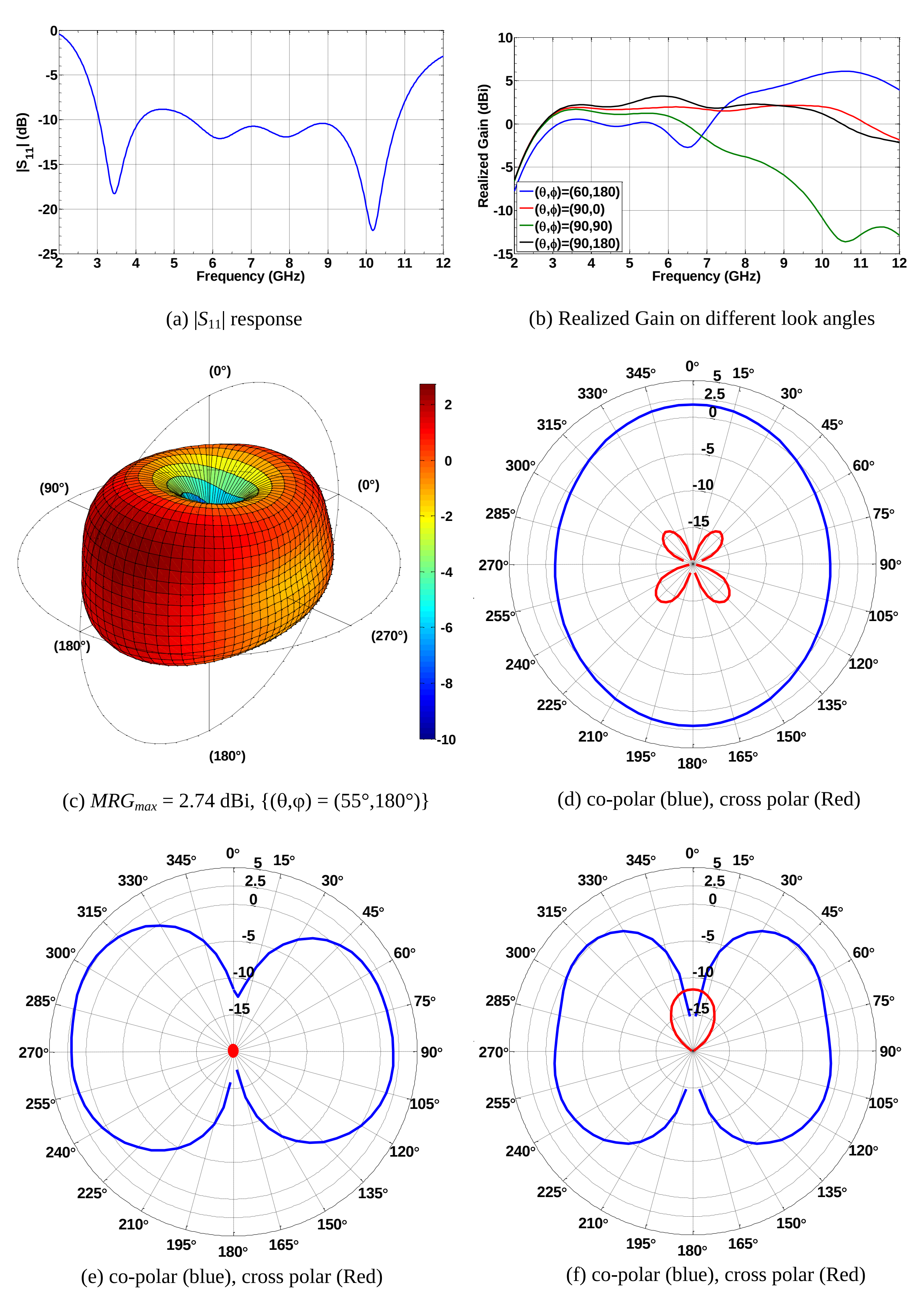

(a) $|S_{11}|$ response

(b) Realized Gain on different look angles

(c) MRG_{max} = 2.74 dBi, {(θ,φ) = (55°,180°)}

(d) co-polar (blue), cross polar (Red)

(e) co-polar (blue), cross polar (Red)

(f) co-polar (blue), cross polar (Red)

Fig. 3.14 Frequency domain performance characteristics of optimal Dual feed Monopole Antenna, (a) Reflection coefficient, (b) Realized gain vs. frequency in different directions, (c) Total MRG 3D representation, (d) MRG, Azimuth cut θ=90°, (e) MRG, Elevation cut at ϕ = 0°, (f) MRG, Elevation cut at ϕ=90°

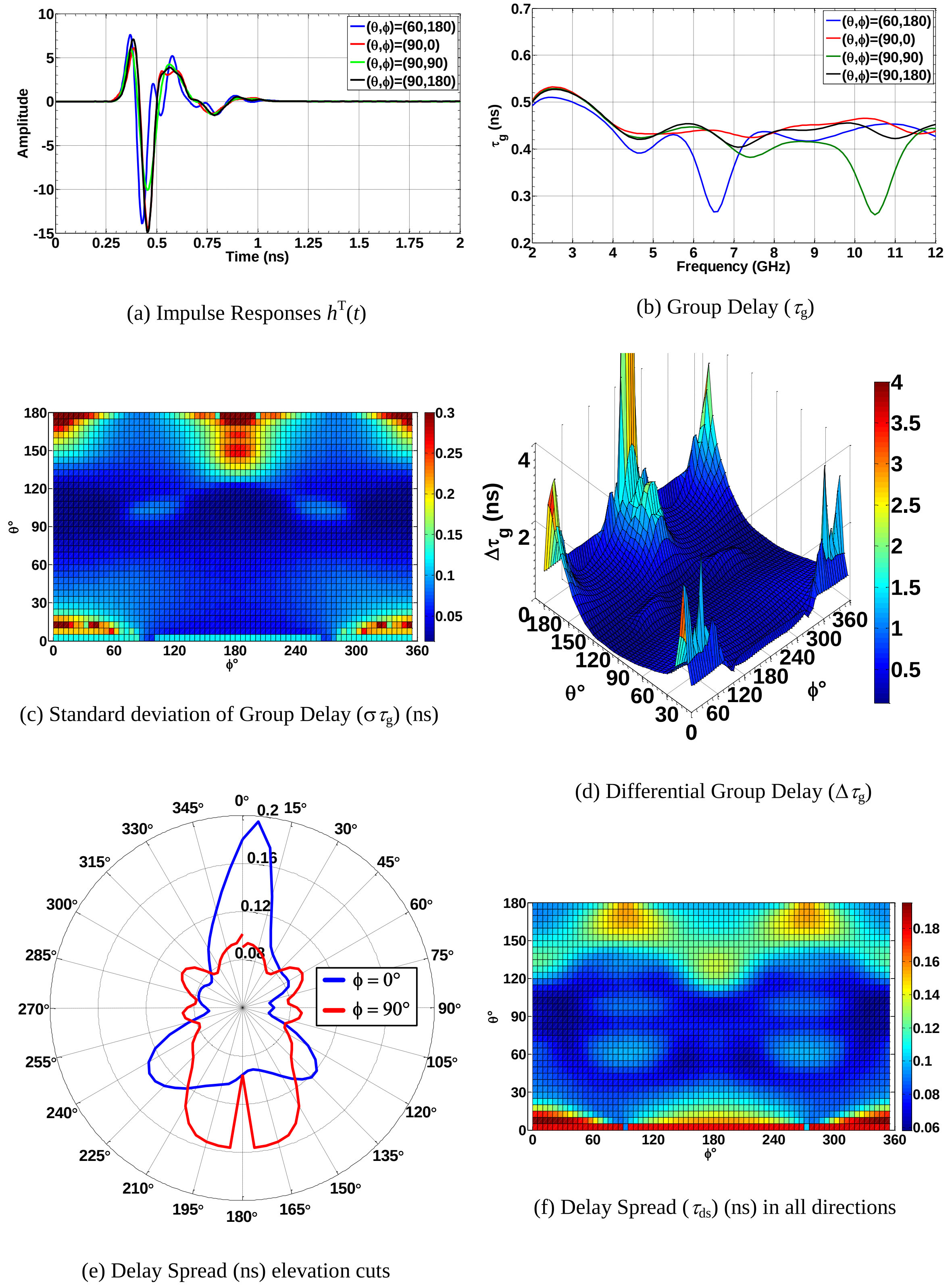

(a) Impulse Responses $h^T(t)$

(b) Group Delay (τ_g)

(c) Standard deviation of Group Delay ($\sigma\tau_g$) (ns)

(d) Differential Group Delay ($\Delta\tau_g$)

(e) Delay Spread (ns) elevation cuts

(f) Delay Spread (τ_{ds}) (ns) in all directions

Fig. 3.15 Time domain performance characteristics of Optimal Dual feed Monopole Antenna, (a) Impulse response $h^T(t)$ (b) Group delay (τ_g) at different directions (c) Standard deviation of group delay ($\sigma\tau_g$), (d) Differential Group delay ($\Delta\tau_g$) (e) Delay spread elevation cuts at $\varphi = 0°$ and $\varphi = 90°$ (f) Delay spread in all directions

3.5.5. Disc monopole

The optimization of this design is performed using 11 independent parameters (Table 3.5). Three additional independent parameters have been added, in addition to the common ones (chapter 2, section 2.4.4), R_{min} is 12.6 mm and the antenna overall size is 22.3 × 17.02 mm^2 (Fig. 3.16). The range of angle ψ has been set to a small range [2°-10°] since this angle defines the top edges of the disc and hence is deemed necessary to be small. The optimal design is shown in Fig. 3.16 together with the surface current distribution. Strong currents can be seen at the bottom perimeter of the disc.

Table 3.5 Parameter Space for Disc Monopole with Optimal values

	Parameters	Interval		Best
		Min.	Max.	
1	R_{min}	12	20	12.6
2	γ	50	90	77.8°
3	ψ	2°	10°	6.44°
4	w_0	$2R_{cond}$	$d_{coax} - 2g_0$	1.81
5	α	78°	90°	89.8°
6	g_0	0.3	1	0.414
7	ζ	0	1.5	1.0048
8	κ	1	5	2.5
9	r_{yaxis}	$R_{min}/4$	$R_{min}/2$	5.421
10	$w_{12} = w_{21}$	$w_1/2$	w_1	2
11	h_1	$H_{total}/10$	$H_{total}/5$	3.686

The reflection coefficient response (Fig. 3.17a) at 3 GHz has a reflection coefficient $|S_{11}| = -7.5$ dB while the rest of the frequency band is below -10 dB. The realized gain (Fig. 3.17b) in the direction (θ,φ) = {(90°, 0°), (90°, 180°)} has gain above 0 dBi for [3-9.5] GHz. The total MRG of the antenna (computed over [3-11] GHz) is plotted in Fig. 3.17c. The gain along dielectric plane can be seen and the attenuation (w.r.t. MRG_{max}) in lateral directions can also be noticed. This has also been observed in Fig. 3.14d over the azimuth plane cut at θ = 90°. The direction of maximum gain can be noticed in elevation cut at φ = 0° (Fig. 3.17e) and the attenuation in the total MRG (Fig. 3.17c) in the lateral directions is clear in the elevation cut in $\varphi = 90°$.

The time domain performances are shown in Fig. 3.18. Low amplitude ringing effects can be seen in the impulse responses (Fig. 3.18a), at different directions. The maximum pulse duration is around 0.75 ns neglecting small energy in the ripples. Group delay responses (Fig. 3.18b) in the directions (θ,φ) = {(90°,0°), (90°,180°)} have relatively stable group delay as compared to the direction of MRG_{max}.. The differential group delay ($\Delta\tau_g$) (Fig. 3.18d) and the standard deviation ($\sigma_{\tau g}$) (Fig. 3.18c) of the group delay show that for θ = [70°—95°] and for all values of φ , the fluctuation in the group delay is less than 0.1 ns, this is also true for θ = [45°—135°] and φ = [−55° —55°].

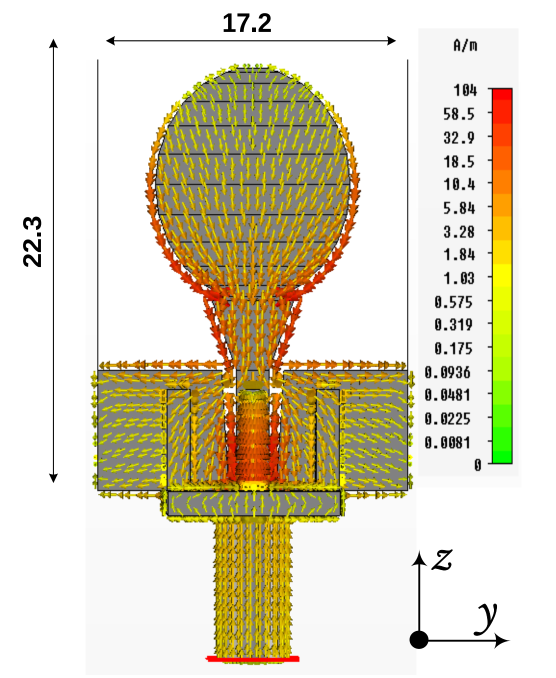

Fig. 3.16 Disc Monopole: Optimal design with Peak surface current distribution at 8.2 GHz.

These delay spreads results (Fig. 3.18f) show the distortion to be less than 150 ps (dark blue area) in the direction θ = [30°—135°] for all values of φ = [−30° —40°]. The distortion in the lateral directions φ = [40°—145°] and φ = [215°—325°] is around 270 ps (Fig. 3.18f). The meridian cuts at φ = 0° and φ = 90° (Fig. 3.18e) of the delay spread present less than 150 ps spreading in θ = [30°—135°].

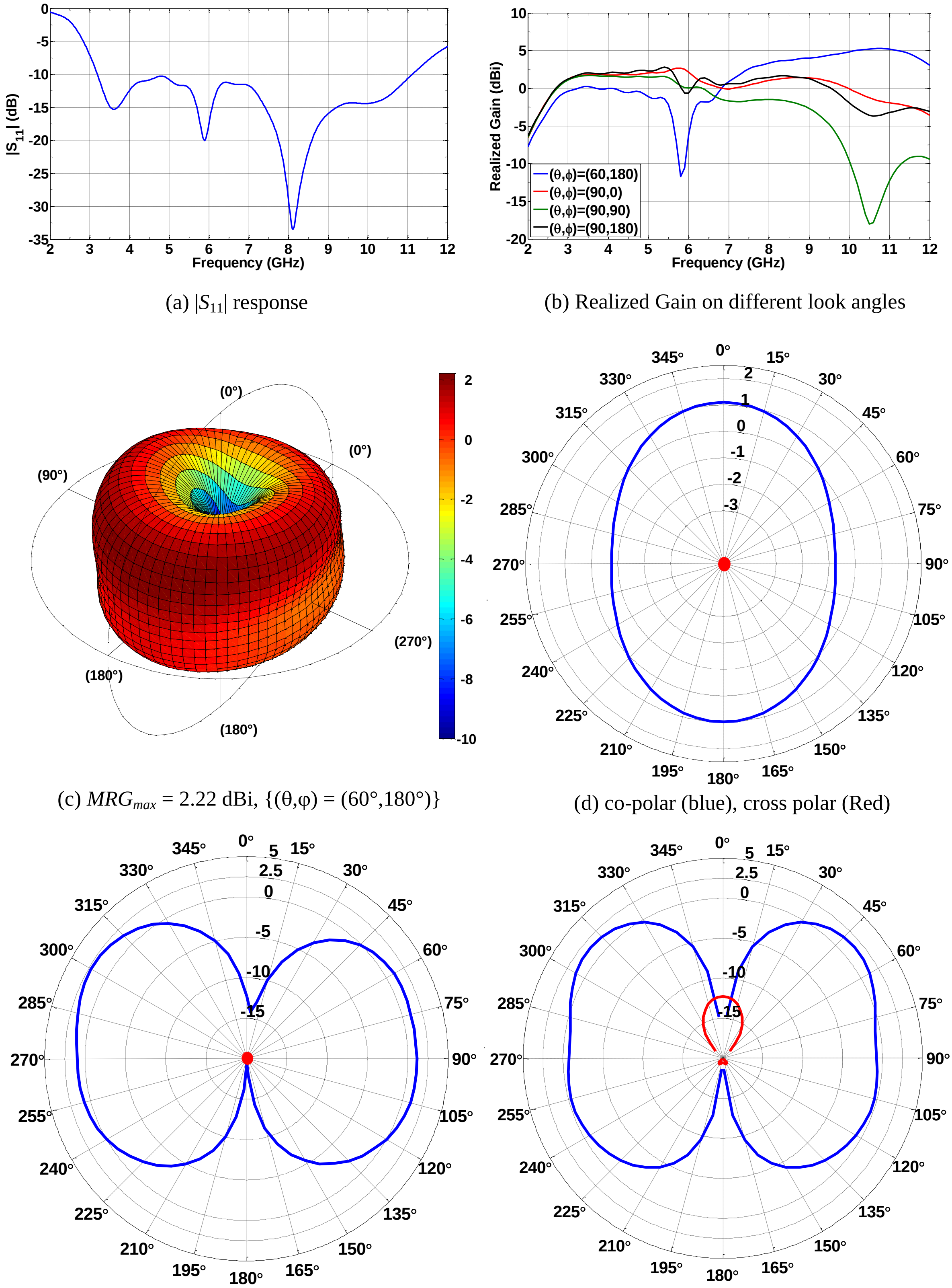

(a) $|S_{11}|$ response

(b) Realized Gain on different look angles

(c) MRG_{max} = 2.22 dBi, {(θ,φ) = (60°,180°)}

(d) co-polar (blue), cross polar (Red)

(e) co-polar (blue), cross polar (Red)

(f) co-polar (blue), cross polar (Red)

Fig. 3.17 Frequency domain performance characteristics of optimal Disc Monopole Antenna, (a) Reflection coefficient, (b) Realized gain vs. frequency in different directions, (c) Total MRG 3D representation, (d) MRG, Azimuth cut θ=90°, (e) MRG, Elevation cut at ϕ = 0°, (f) MRG, Elevation cut at ϕ=90°

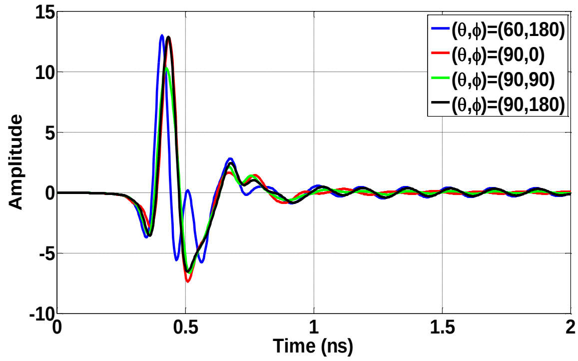

(a) Impulse Responses $h^{T}(t)$

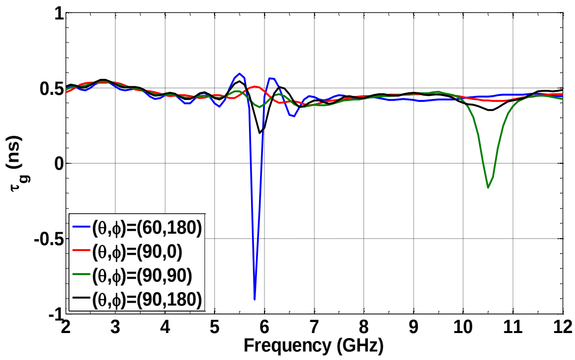

(b) Group Delay (τ_g)

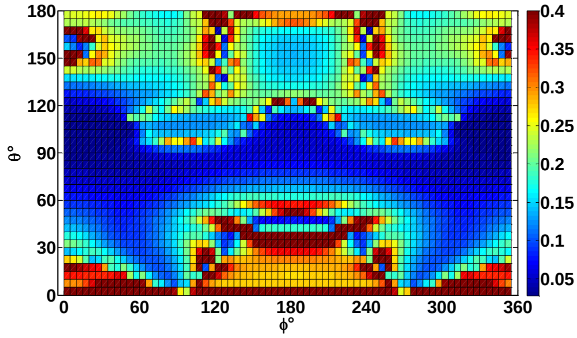

(c) Standard deviation of Group Delay ($\sigma \tau_g$) (ns)

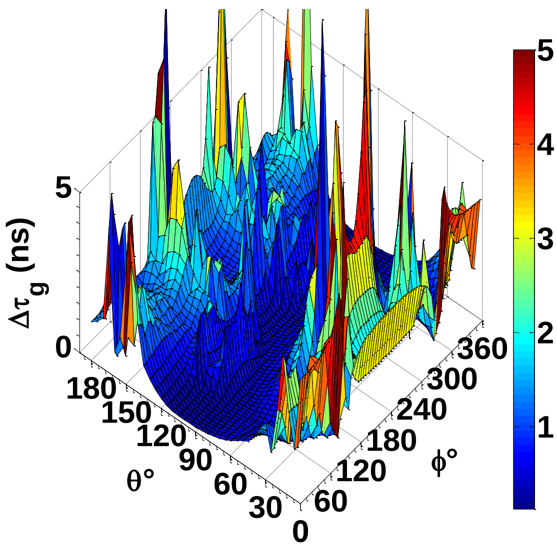

(d) Differential Group Delay ($\Delta \tau_g$)

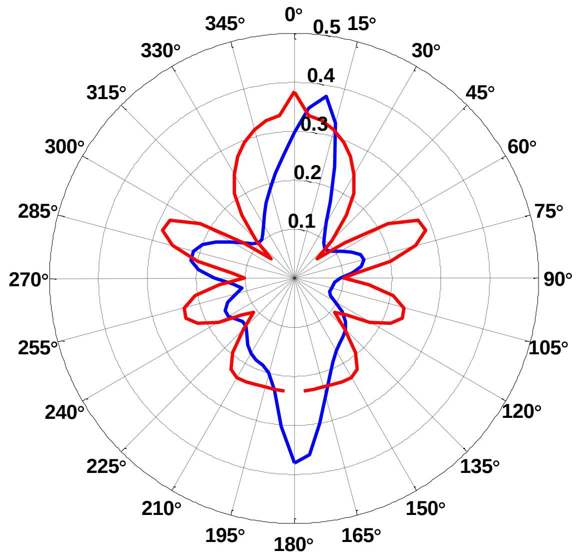

(e) Delay Spread (ns) elevation cuts

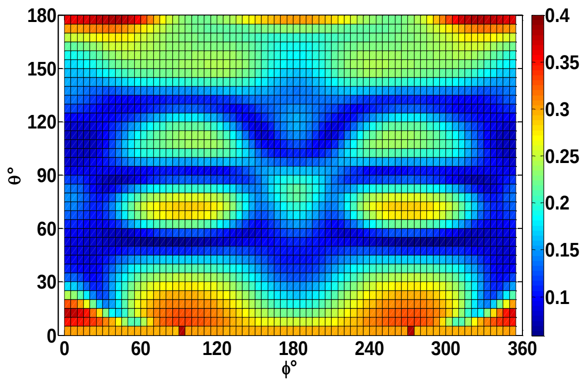

(f) Delay Spread (τ_{ds}) (ns) in all directions

Fig. 3.18 Time domain performance characteristics of Optimal Disc Monopole Antenna, (a) Impulse response $h^{T}(t)$ (b) Group delay (τ_g) at different directions (c) Standard deviation of group delay ($\sigma\tau_g$), (d) Differential Group delay ($\Delta\tau_g$) (e) Delay spread elevation cuts at $\varphi = 0°$ and $\varphi = 90°$ (f) Delay spread in all directions

3.5.6. Triangular Planar Balance Dipole (PBD)

The details of the geometry have been presented in chapter 2 (section 2.5.2). The design has been optimized with 7 independent parameters (Table 3.6). As was the case with the triangular monopole design, this design also requires a minimal number of parameters to control its different parts. The triangle flare angle is controlled by the angle ψ whereas input to the triangular part (the radiating part) is controlled by the parameter w_1. In the optimization, the volume goal was set to 1500 mm^3 which is at the lowest values of γ, ψ and R_{min}. The lower bound of R_{min} correspond to λ/2 of the lowest operating frequency (over [3 11] GHz). The best found value of R_{min} is 27 mm, resulting in antenna overall size of 40.62 × 38.9 mm^2 (Fig. 3.19). Strong currents can be seen at the feed line and at the edge of the triangular patch (Fig. 3.19) at 7.2 GHz.

Table 3.6 Parameter Space for Triangular PBD with Optimal values

	Parameters	Interval		Best
		Min.	Max.	
1	R_{min}	25	35	27
2	γ	50	100	84.775°
3	ψ	50°	170°	80°
4	w_1	1	$4f_w$	3.5
5	f_{open}	0	$2f_w$	1.1
6	L_{tf}	6	$d_2 - 2$	9.34
7	f_w	1	3	1.676

The reflection coefficient response (Fig. 3.20a) at 8.6 GHz has $|S_{11}|$ = −8.6 dB and the remainder of the frequency band ([3 11] GHz) is below -10 dB. The direction of MRG_{max} is (θ,φ) = (90°, 90°). The total realized gain (considering both polarizations) (Fig. 3.20b) in the direction of MRG_{max} (θ,φ) = (90°, 90°) has a minimum of −2 dBi gain below 0 dBi for [5—5.6] GHz and for the rest of the band it is adequate well above 0 dBi with a maximum of 7.3 dBi. The total MRG of the antenna (computed over [3-11] GHz) is plotted in Fig. 3.20c. The direction of MRG_{max} and can be clearly seen in Fig. 3.20d — the azimuth plane cut at θ = 90°. This has also been presented in elevation cut at φ = 90° (Fig. 3.20f), the MRG of less than −3 dBi can be seen in the plane θ = [180°—360°] at φ = 90°. The low

MRG values are also can be seen in the elevation cut at φ = 0° (Fig. 3.20e). It is therefore, evident that this antenna is efficiently directing the energy towards (θ,φ) = (90°, 90°).

The time domain performances are shown in Fig. 3.21. The impulse responses have been produced after pre-processing with Blackman windowing (Fig. 3.21a). In the main beam impulse response the maximum pulse time is around 2 ns. Group delay response (Fig. 3.21b) in the main beam direction (θ,φ) = (90°, 90°), has a relatively stable group delay and a variation of 0.3 ns can be seen. These variations in the time delay are visible in the differential group delay ($\Delta\tau_g$) (Fig. 3.21d) and the standard deviation ($\sigma_{\tau g}$) (Fig. 3.21c) of the group delay for all the directions. As can be seen that for θ = [70°—100°] and φ = [25°—165°], the fluctuation in the group delay is less than 0.5 ns. This is shown with dark blue color.

The delay spreads results (Fig. 3.21f) show the distortion to be less than 200 ps (dark blue area) in the direction mentioned above. This distortion level (< 200 ps) is also true for θ = [140°—165°] and φ = [240°—325°] but since the gain in these directions is low, this characteristic is not of interest. The distortion around θ = 90° in both meridian cuts at φ = 0° and φ = 90° (Fig. 3.21e) is less than 250 ps.

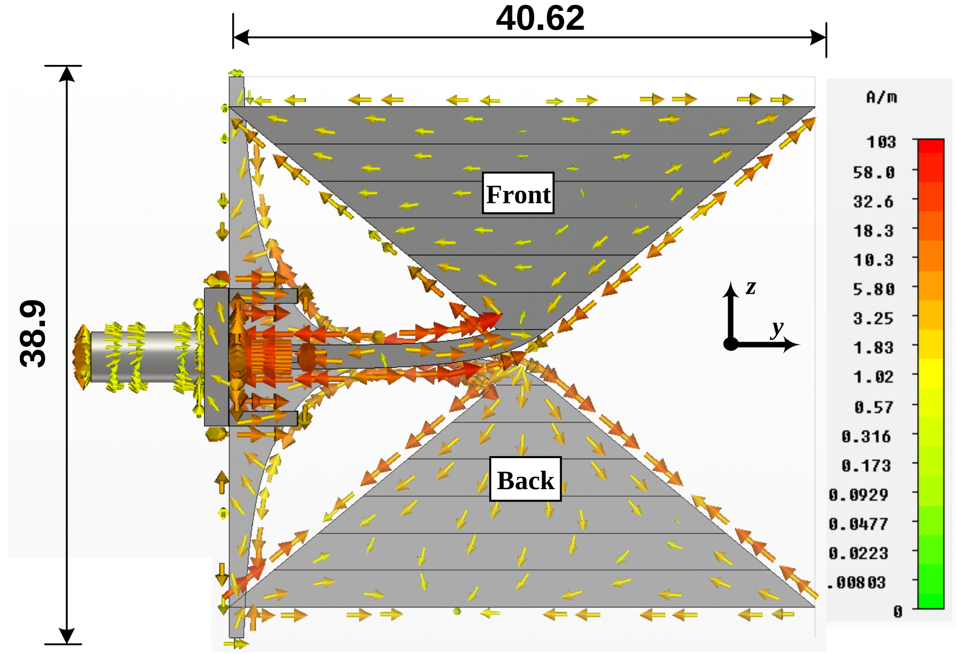

Fig. 3.19 Triangular PBD: Optimal design with Peak surface current distribution at 7.2 GHz

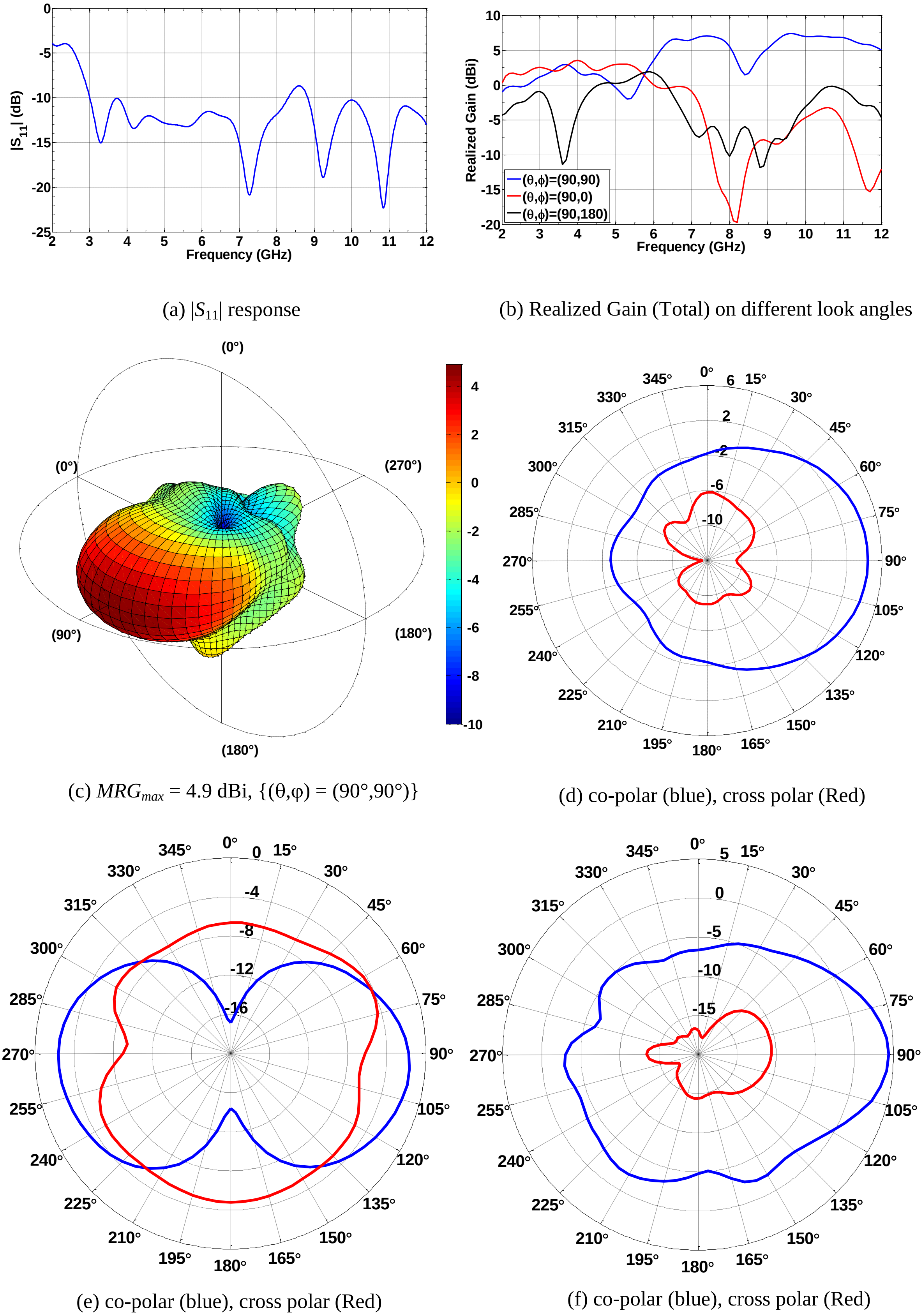

(a) $|S_{11}|$ response

(b) Realized Gain (Total) on different look angles

(c) MRG_{max} = 4.9 dBi, {(θ,φ) = (90°,90°)}

(d) co-polar (blue), cross polar (Red)

(e) co-polar (blue), cross polar (Red)

(f) co-polar (blue), cross polar (Red)

Fig. 3.20 Frequency domain performance characteristics of optimal Triangular Balanced Dipole Antenna, (a) Reflection coefficient, (b) Realized gain vs. frequency in different directions, (c) Total MRG 3D representation, (d) MRG, Azimuth cut θ=90°, (e) MRG, Elevation cut at ϕ = 0°, (f) MRG, Elevation cut at ϕ=90°

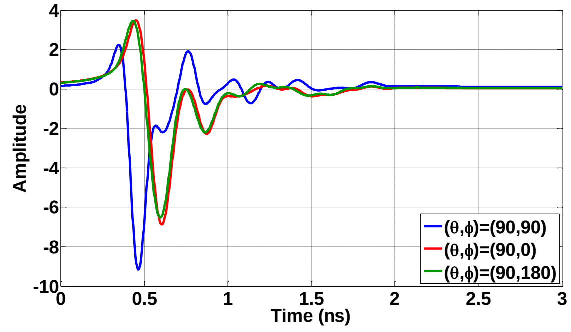

(a) Impulse Responses $h^{T}(t)$

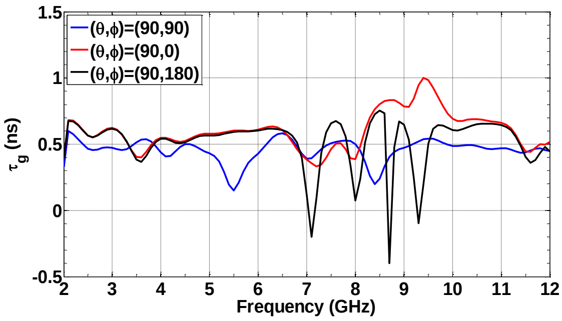

(b) Group Delay (τ_g)

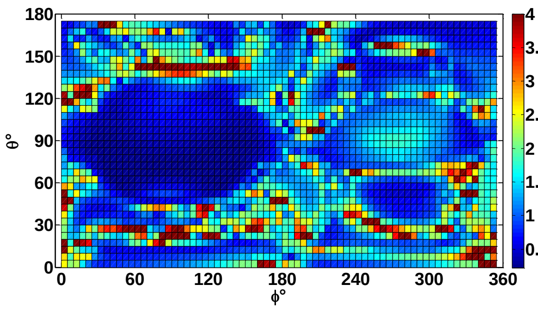

(c) Standard deviation of Group Delay ($\sigma\tau_g$) (ns)

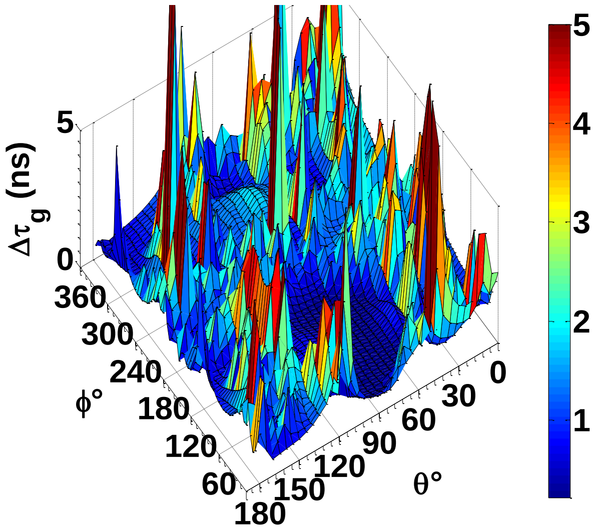

(d) Differential Group Delay ($\Delta\tau_g$)

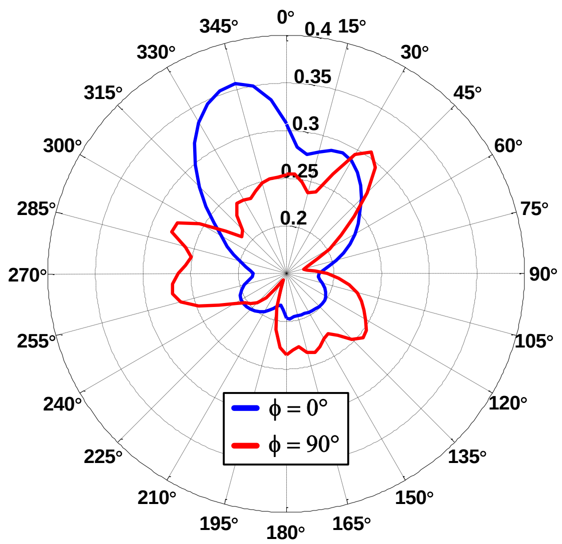

(e) Delay Spread (ns) elevation cuts

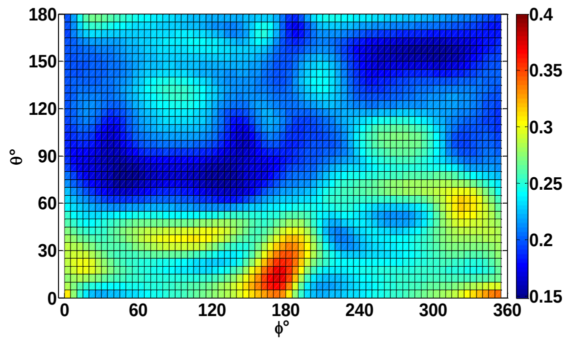

(f) Delay Spread (τ_{ds}) (ns) in all directions

Fig. 3.21 Time domain performance characteristics of Optimal triangular Balanced dipole antenna, (a) Impulse response $h^{T}(t)$ (b) Group delay (τ_g) at different directions (c) Standard deviation of group delay ($\sigma\tau_g$), (d) Differential Group delay ($\Delta\tau_g$) (e) Delay spread elevation cuts at $\varphi = 0°$ and $\varphi = 90°$ (f) Delay spread in all directions

3.5.7. Disc Planar Balanced Dipole (PBD)

The details of the geometry can be seen in chapter 2 (section 2.5.3). The design has been optimized with 8 independent parameters (Table 3.7). The parameters r_{yaxis} and γ control the disc profile. In the optimization, the volume goal was set to 1500 mm^3, which is at lowest values of γ, ψ and R_{min}. The best found value of R_{min} is 27 mm and the antenna overall size is 40.62 × 38.9 mm^2 (Fig. 3.22). Strong surface current distribution can be seen at the feed line and around the balun ground which explains the good matching at 3.2 GHz.

Table 3.7 Parameter Space for Disc PBD with Optimal values

	Parameters	Interval		Best
		Min.	Max.	
1	R_{min}	25	35	27.02
2	γ	50	100	87.83°
3	ψ	158°	176°	172.7°
4	w_1	1	$4f_w$	4.5
5	f_{open}	0	$2f_w$	0.25
6	L_{tf}	6	$(H_{\mathrm{total}}/2) - 2$	8.04
7	f_w	1	3	2.9
8	r_{yaxis}	$R_{min}/4$	$R_{min}/2$	13.2

The reflection coefficient response (Fig. 3.23a) shows that the matching in [3-11] GHz band contains multiple resonances and is less than −10 dB, even above 11 GHz. The direction of MRG_{max} is (θ,φ) = (70°, 85°). The total realized gain (considering both polarizations) (Fig. 3.23b) in the direction of MRG_{max} has minimum of −0.5 dBi gain below 0 dBi for [7.6-8] GHz. In the direction (θ,φ) = (90°, 90°), a minimum of −1.7 dBi in the band [6.7-7.9] GHz is observed.

The total MRG of the antenna (computed over [3-11] GHz) is plotted in Fig. 3.23c. The direction of MRG_{max} can be clearly observed in Fig. 3.23d — the conical cut at θ = 70°. In addition, the elevation cut at φ = 90° (Fig. 3.23f), the MRG of less than 0 dBi is observed in the plane θ = [180°—360°]. The low MRG values (< 0 dBi) is observed in elevation cut at φ = 0° (Fig. 3.23e). It is therefore, evident that the antenna is adequately radiating the energy into the direction (θ,φ) = (70°, 85°).

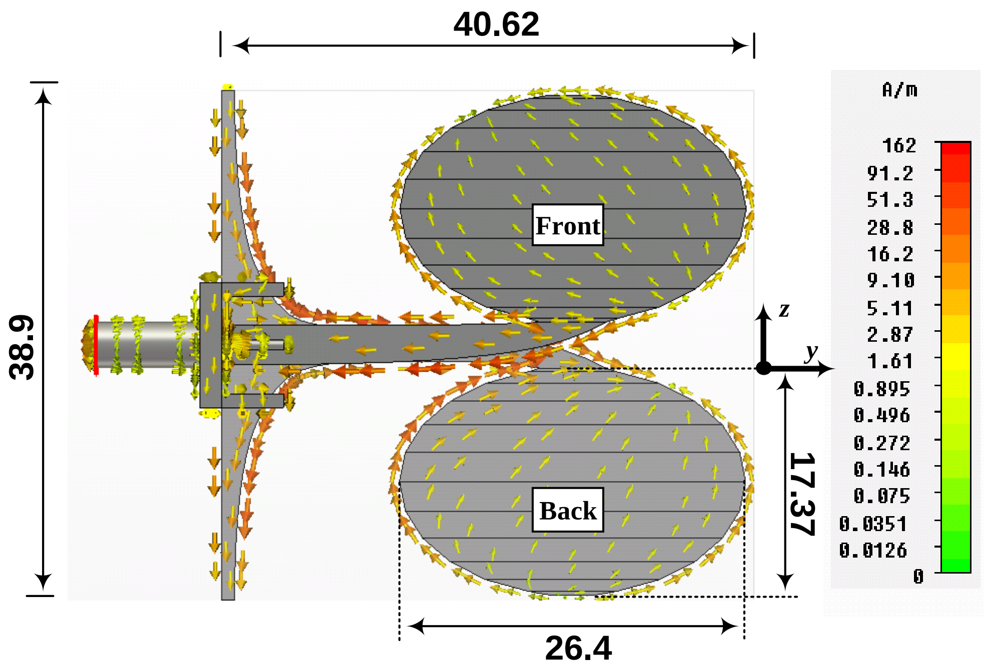

Fig. 3.22 Disc PBD: Optimal design with Peak surface current distribution at 3.2 GHz

The time domain performances are shown in Fig. 3.24. The impulse responses have been produced after pre-processing with Blackman windowing (Fig. 3.24a). In the main beam impulse response the maximum pulse duration is around 2 ns. The group delay response (Fig. 3.24b) in the main beam direction (θ,φ) = (70°, 85°), show relatively large delay at low frequencies due to the longer propagation paths when compared to higher frequencies. The group delay is more stable in the range [4—12] GHz and a variation of 0.25 ns has been monitored. These variations in the time delay are more evident in the differential group delay ($\Delta\tau_g$) (Fig. 3.24d) and in the standard deviation ($\sigma_{\tau g}$) (Fig. 3.24c) of the group delay for all the directions. As can be observed for θ = [40°—100°] and φ = [45°—140°], the fluctuation in the group delay is less than 0.25 ns. This is shown in dark blue color.

The delay spreads results (Fig. 3.24f) show the distortion is to be less than 200 ps (the dark blue area) in the direction mentioned above. This distortion level (< 200 ps) is also true for some other directions where the gain is low, thus they are not really valuable. A more precise representation is presented in (Fig. 3.24e) and it has been observed that the distortion for θ = [35°—75°] in meridian cuts at φ = 90° (Fig. 3.24e) is less than 200 ps.

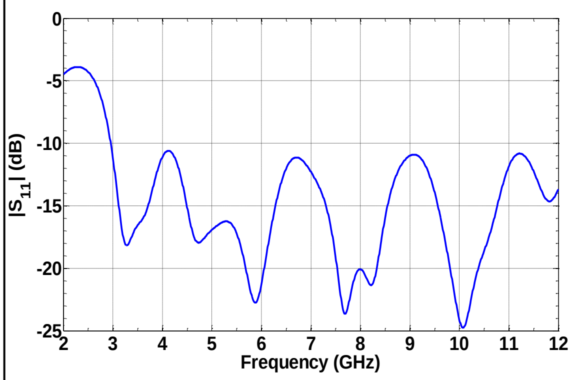

(a) $|S_{11}|$ response

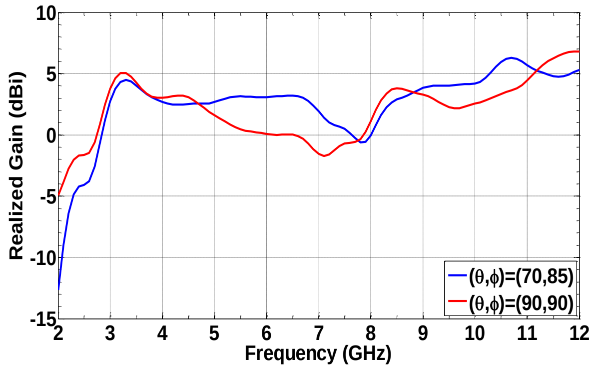

(b) Realized Gain on different look angles

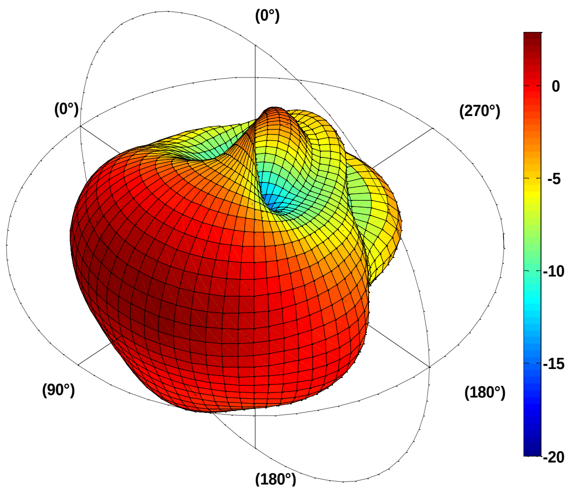

(c) MRG_{max} = 3.49 dBi, {(θ,φ) = (75°,85°)}

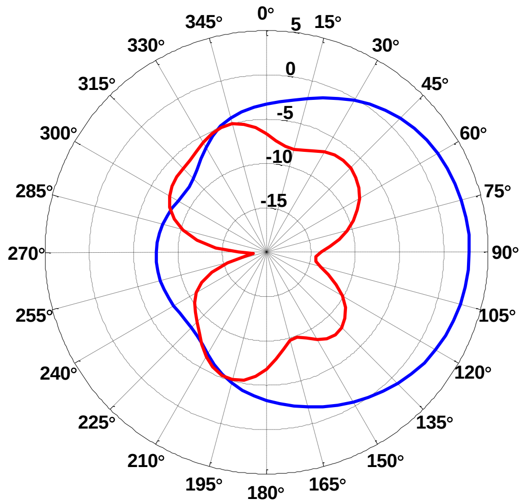

(d) co-polar (blue), cross polar (Red)

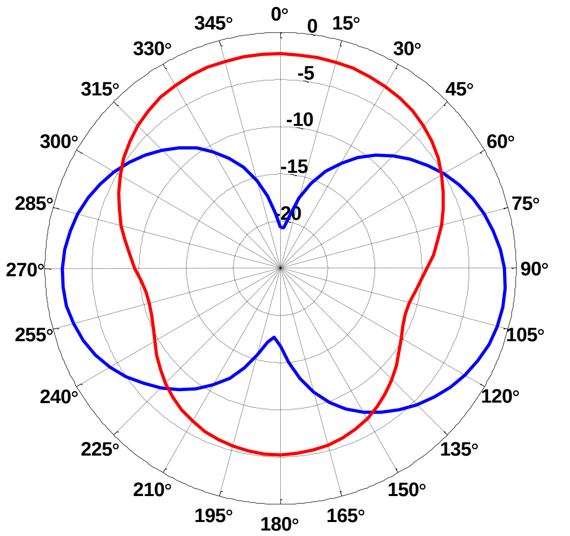

(e) co-polar (blue), cross polar (Red)

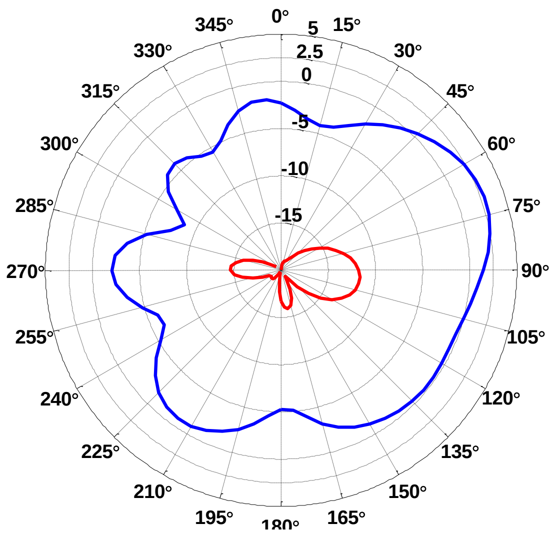

(f) co-polar (blue), cross polar (Red)

Fig. 3.23 Frequency domain performance characteristics of optimal Disc Balanced Dipole Antenna, (a) Reflection coefficient, (b) Total Realized gain vs. frequency in different directions, (c) Total MRG 3D representation, (d) MRG, Azimuth cut θ=70°, (e) MRG, Elevation cut at ϕ = 0°, (f) MRG, Elevation cut at ϕ=90°

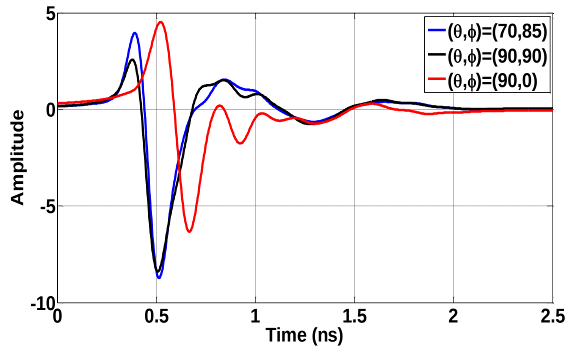

(a) Impulse Responses $h^{T}(t)$

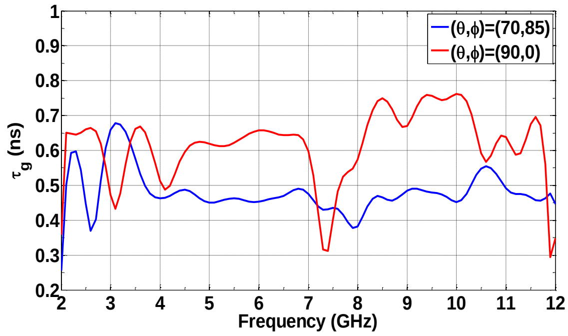

(b) Group Delay (τ_g)

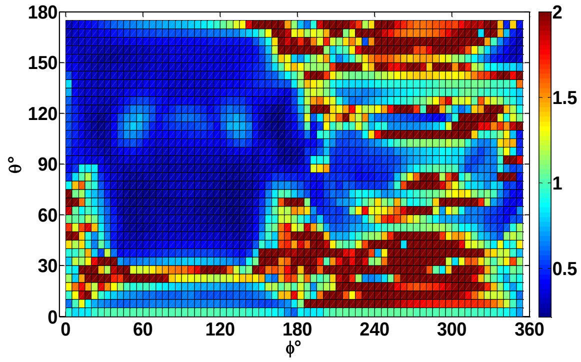

(c) Standard deviation of Group Delay ($\sigma\tau_g$) (ns)

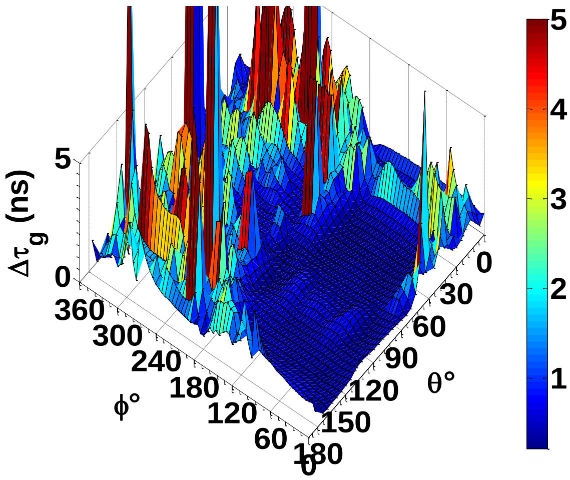

(d) Differential Group Delay ($\Delta\tau_g$)

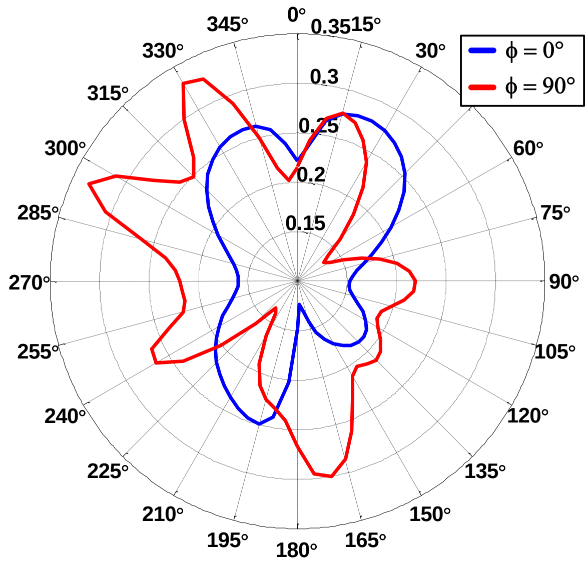

(e) Delay Spread (ns) elevation cuts

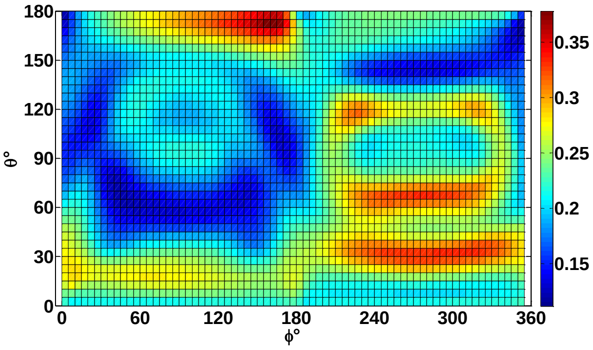

(f) Delay Spread (τ_{ds}) (ns) in all directions

Fig. 3.24 Time domain performance characteristics of Optimal Disc Balanced dipole antenna, (a) Impulse response $h^{T}(t)$ (b) Group delay (τ_g) at different directions (c) Standard deviation of group delay ($\sigma\tau_g$), (d) Differential Group delay ($\Delta\tau_g$) (e) Delay spread elevation cuts at $\varphi = 0°$ (blue) and $\varphi = 90°$ (red) (f) Delay spread in all directions

3.6. Biconical Design

The details of the geometry can be seen in chapter 2 (section 2.7). The design has been optimized with 8 independent parameters (Table 3.8). In the optimization cost function, the targeted volume of the sphere has been set to 7238 mm^3 at the lowest R_{min} value. The diameters of the upper and lower cones are different and controlled by parameters ψ and γ respectively. The best found value of R_{min} is 15.48 mm and the antenna height being 26.3 mm whereas the upper cone diameter is 15.6 mm and the lower cone has the diameter of 18 mm (Fig. 3.25).

Table 3.8 Parameter Space for Bicone Design with Optimal values

	Parameters	Interval		Best
		Min.	Max.	
1	R_{min}	12	25	15.48
2	γ	45°	150	60.56°
3	ψ	45°	150°	66.6°
4	R_{w3}	0.1	1	0.3
5	R_{w7}	0.1	1	0.76
6	R_{w6}	0.1	1	0.45
7	R_{h1}	0.1	1	0.6
8	R_{h2}	0.1	1	0.71
9	R_{h4}	0.1	1	0.36
10	R_{h6}	0.1	1	0.89

The reflection coefficient response (Fig. 3.26a) shows a good matching in the complete [3-11] GHz band. At 6.4 GHz a sudden change can be observed. This is perhaps due to the noticeable transition at the upper-cone. The distance from this transition to the input port is λ/2 at this frequency and this feature may have caused the phase change and hence the response.

The direction of MRG_{max} is (θ,φ) = (100°, 45°), and the effect of the transition explained above can be observed in the realized gain values (Fig. 3.26b) that are below 0 dBi at these group of frequencies. However, since it is a small group of frequencies, the effect on the energy of the complete band can be disregarded.

The total MRG of the antenna (computed over [3-11] GHz) is plotted in Fig. 3.26c. The design is a good example of pure vertical polarization thus cross polar components are almost zero. In addition, due to the structural symmetry in azimuth, all the elevation cuts are similar. Two such cuts are shown in Fig. 3.26d for demonstration purpose. The azimuth cut at θ = 0° can be compared with the conical cut at θ = 100° to demonstrate the difference in levels between them Fig. 3.26d.

The impulse response in the direction of MRG_{max} and towards (θ,φ) = (90°, 0°).are compared in (Fig. 3.27a), but no significant difference can be observed. The maximum pulse duration of 0.5 ns can be observed. The group delay responses (Fig. 3.27b) also show the effect of the transition mentioned above.

The differential group delay ($\Delta\tau_g$) (Fig. 3.27d) and the standard deviation ($\sigma_{\tau g}$) (Fig. 3.27c) of the group delay for all the directions show no significant variations when compared to other antennas. The fluctuation is least at θ = [70°—115°] for all φ values. This is shown in dark blue color (Fig. 3.27c).

The delay spreads results are shown in Fig. 3.27f in azimuth. As expected, the delay is constant due to structural symmetry. For the elevation cut at φ = 0°, variations in delay spread can be observed and the minimum spread occurs at θ = 90° about 100 ps.

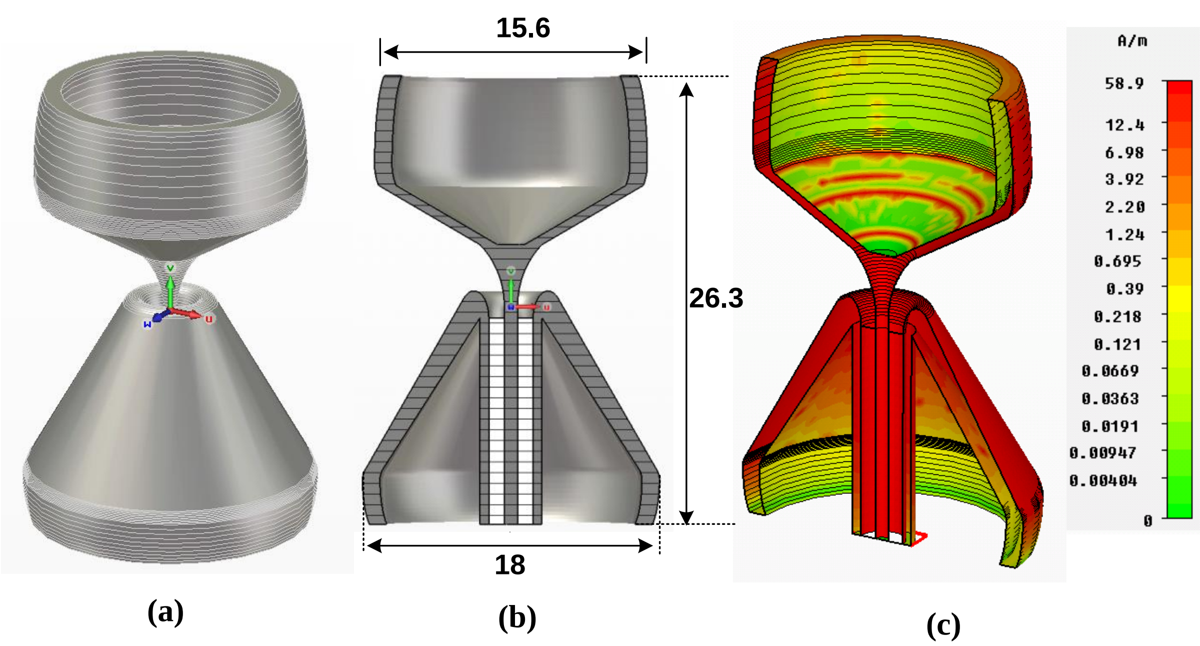

Fig. 3.25 Optimal Bicone Antenna, (a) perspective view, (b) cross-sectional front view (c) Surface current distribution at 6.4 GHz.

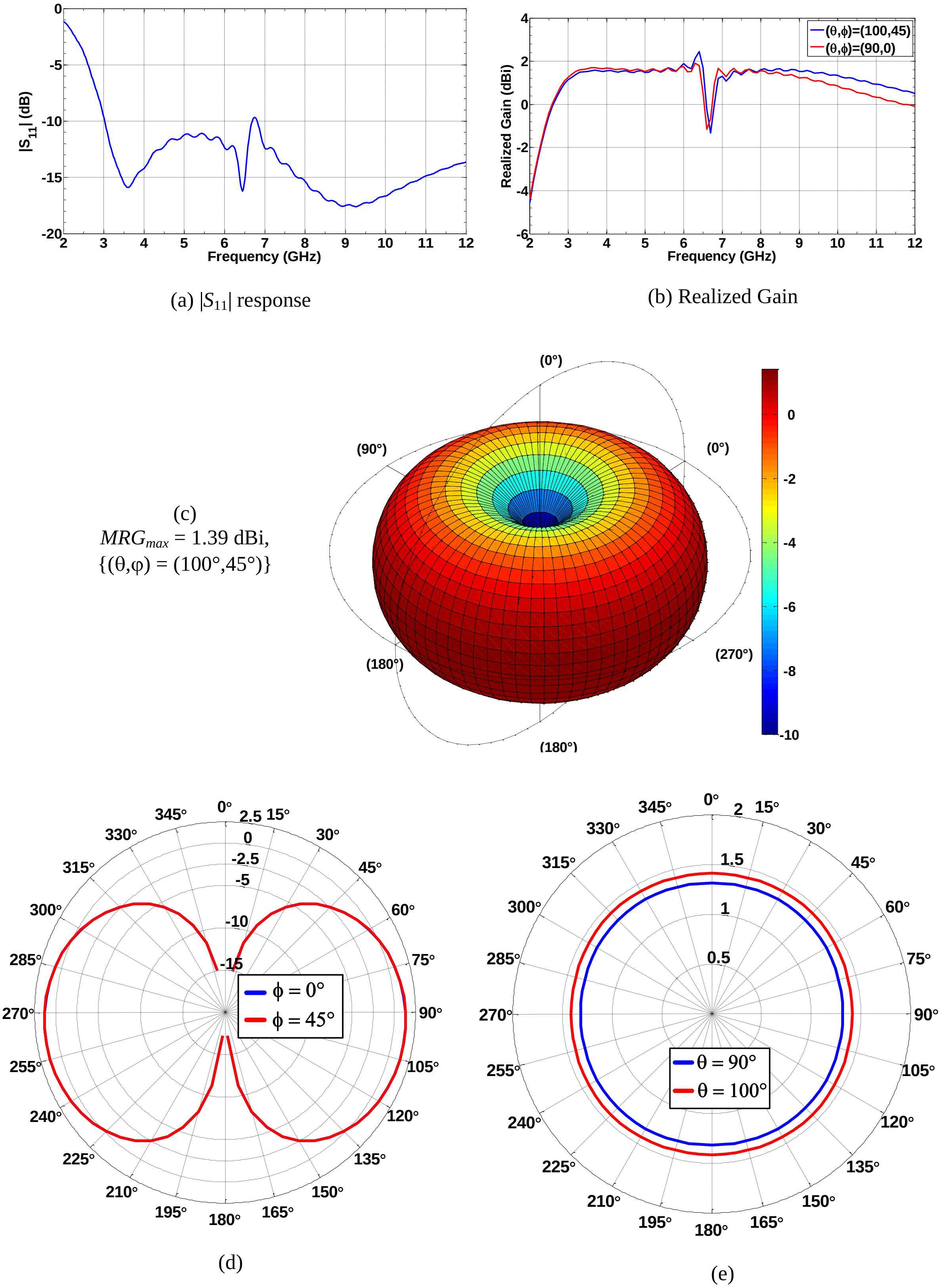

(a) $|S_{11}|$ response

(b) Realized Gain

(c)
MRG_{max} = 1.39 dBi,
{(θ,φ) = (100°,45°)}

(d)

(e)

Fig. 3.26 Frequency domain performance characteristics of optimal Biconical antenna, (a) Reflection coefficient, (b) Realized gain vs. frequency in different directions, (c) Total MRG 3D representation, (d) MRG, Elevation cuts, cuts, (e) MRG, Azimuth cuts

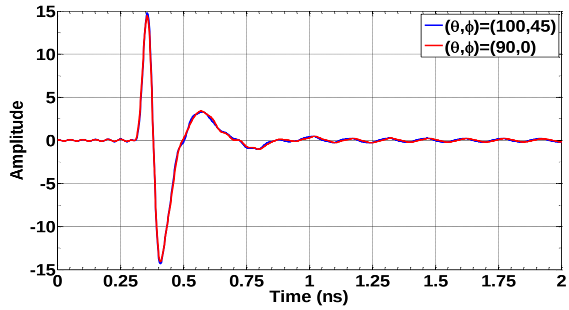

(a) Impulse Responses $h^T(t)$

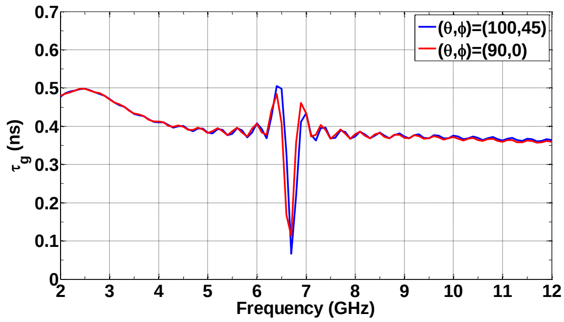

(b) Group Delay (τ_g)

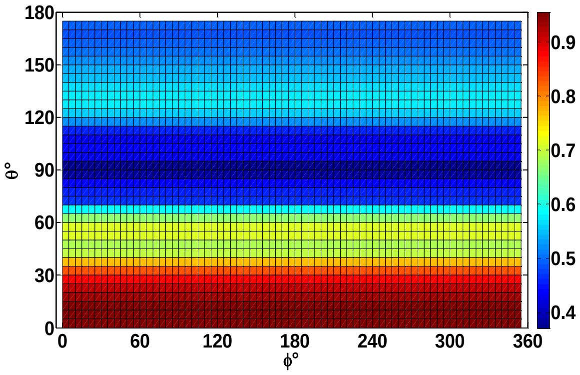

(c) Standard deviation of Group Delay ($\sigma\tau_g$) (ns)

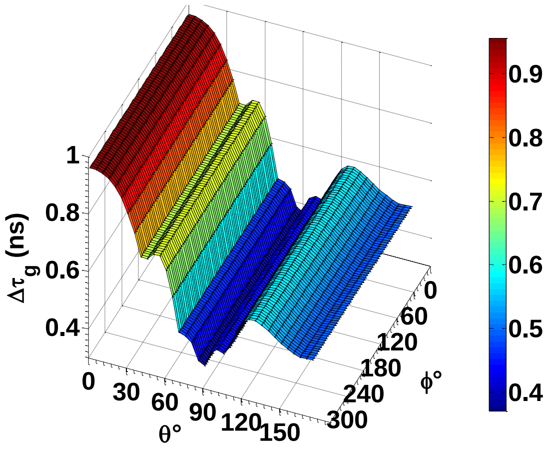

(d) Differential Group Delay ($\Delta\tau_g$)

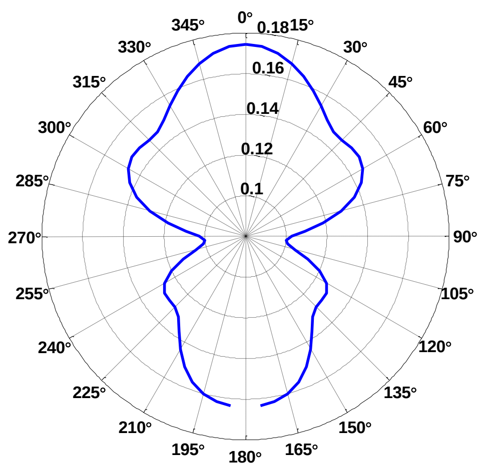

(e) Delay Spread (ns) elevation cut

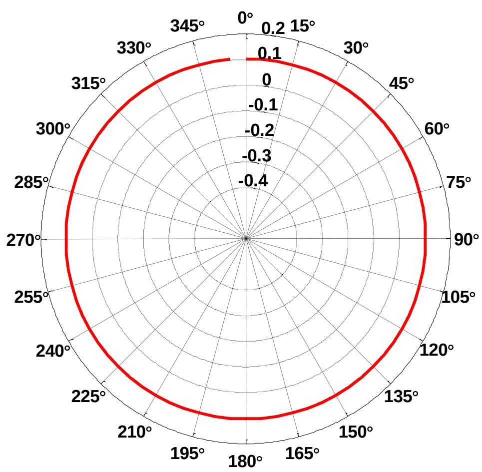

(f) Delay Spread (ns) azimuth cut

Fig. 3.27 Time domain performance characteristics of Optimal Biconical antenna, (a) Impulse response $h^T(t)$ (b) Group delay (τ_g) at different directions (c) Standard deviation of group delay ($\sigma\tau_g$), (d) Differential Group delay ($\Delta\tau_g$) (e) Delay spread elevation cut at $\varphi = 0°$ (f) Delay spread azimuth cut at $\theta = 90°$

3.7. Multiband Design

Details of the design have been explained in chapter 2 (section 2.6) The objective is to show the versatility of the "generic design" and the aim/goal is to search an antenna for three WiFi band (Table 3.9) which has good in-band matching and out-of-band rejection.

Table 3.9 Selected WLAN bands and stop bands

IEEE 802.11	Freq. Band (GHz)	BW (MHz)	Remarks
b/g/n	**2.4 – 2.5**	100	Pass Band
---	**2.75 – 3.4**	650	Stop Band
Y	**3.65 – 3.7**	35	Pass Band
---	**3.95 – 4.75**	800	Stop Band
a/n	**5 – 6**	1000	Pass Band

3.7.1. Methodology & Design

The procedure is the same as for all previously discussed antenna designs. Here a quick review is presented. Starting from a generic design with a CPW feed (Fig. 3.28a), suitable geometrical constraints are imposed so as to restrain the design to various particular shapes (bowtie, staircase, etc.), including appropriate bounds. The corresponding parameter space is explored with an evolutionary algorithm in order to search for an optimal design.

Slot antennas have proved their relevance in many multiband designs, for instance, in multiband PIFAs [82]. Using the approach for slot multiband antenna, a dual slot design is proposed as shown in Fig. 3.28b. A priori it is thought that slot-A would resonate at 5 GHz (IEEE 802.11a) band and slot B would be responsible for 3.7 GHz (IEEE 802.11y) band, while the lowest frequency band 2.4 GHz (IEEE 802.11b/g) would be related to the overall antenna height.

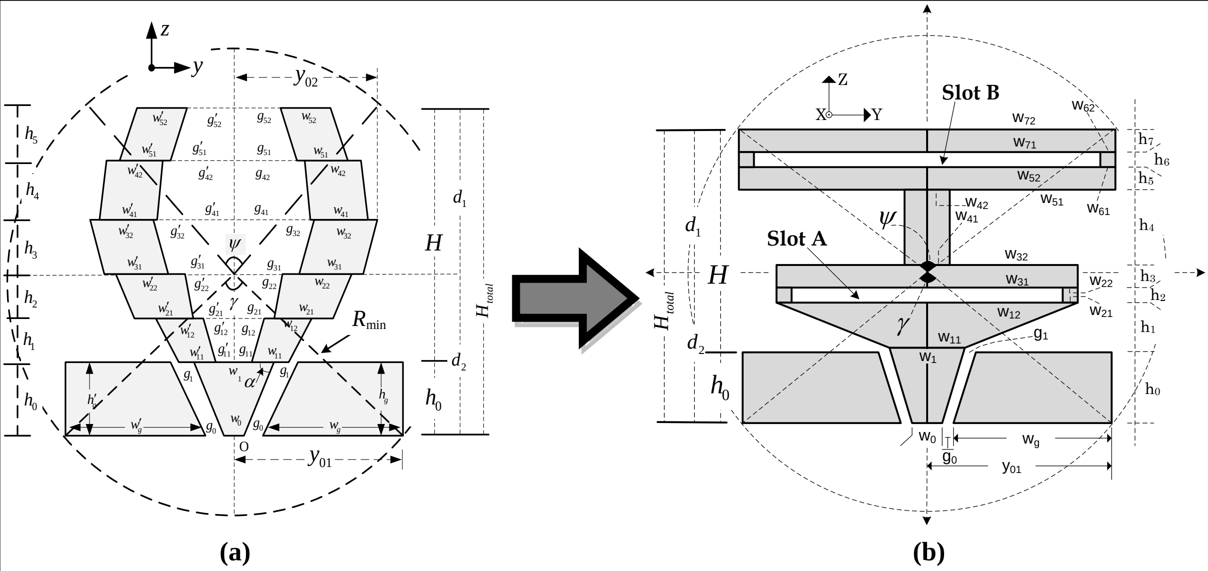

Fig. 3.28 Generic to Multiband design, (a) The generic design, (b) Dual slot Multiband design

To achieve the above postulated geometrical constraints, an 8-layer generic design (Fig. 3.28a) is used. The parameterization of this generic design according to a double slot antenna (Fig. 3.28b) can be achieved by setting constraints on gaps and widths. These constraints and parametric relations have been discussed in chapter 2.

3.7.2. Cost function

The optimization is performed on the antenna input matching $|S_{11}|$ by monitoring the response on three pass-bands and two stop-bands. The optimization algorithms are very sensitive to the cost-function (fitness function), as discussed earlier and this impacts the algorithm convergence. Therefore, the cost function is here defined in four steps:

1/ First, the clipping is applied on each $|S_{11}(f)|$ response with respect to a threshold in pass bands and stop bands.

$$g_p\left(|S_{11}(f)|\right)=\begin{cases}0.3126 & , \ |S_{11}(f)|\le 0.3126 \\ |S_{11}(f)| & , \ |S_{11}(f)|>0.3126\end{cases} \quad \text{-------------------------------------}(3.18)$$

$$g_s\left(|S_{11}(f)|\right)=\begin{cases}1 & , \ |S_{11}(f)|\ge 0.8912 \\ |S_{11}(f)| & , \ |S_{11}(f)|<0.8912\end{cases} \quad \text{-------------------------------------}$$

(3.19)

where g_p and g_s are the clipping functions for pass-band and stop-band respectively. The threshold for the pass-band is set to 0.3126 (−10 dB) whereas, for stop-band it is set to 0.8912 (−1 dB). These clipping functions avoid the genetic algorithm to focus on deep in-band resonances and good out-of-band mismatches.

2/ In a second step, the mean of these clipping functions is calculated, using the following relations:

$$cp_n = \frac{1}{\Delta f}\int_{f_{pl_n}}^{f_{pu_n}} g_p\left(\left|S_{11}(f)\right|\right)df \quad \text{--(3.20)}$$

$$cs_n = \frac{1}{\Delta f}\int_{f_{sl_n}}^{f_{su_n}} g_s\left(\left|S_{11}(f)\right|\right)df \quad \text{---(3.21)}$$

Where, cp_n and cs_n denote the cost of pass-band and stop-band respectively, whereas, n is the frequency band index. The upper frequency corner for pass-band is denoted by f_{pu_n} whereas for the lower one, f_{pl_n} is used. Similarly, f_{su_n} and f_{sl_n} are used for the upper and lower frequency corners of stop-bands respectively.

3/ In the third step, we denote μ_{cp} as the mean value of the cost of all three pass-bands and σ_{cp} as the standard deviation of these pass-band costs. Similarly, we denote μ_{cs} as the mean value of costs of two stop-bands and σ_{cs} as the standard deviation of these stop band's costs. Finally, the overall cost function is defined as:

$$Cost = \left(\mu_{cp} + \sigma_{cp}\right) + \left|1 - \left|\mu_{cs} - \sigma_{cs}\right|\right| \quad \text{---(3.22)}$$

This cost should be minimized to the target value of 0.3126 (–10 dB). The insertion of the standard deviations in (3.22) imposes equalization or balancing effect on the respective bands.

3.7.3. Parameter Space

The parameter space is listed in Table 3.10. Both slot A (sw_a) and B (sw_b) width ranges are to be about λ/4 of the corresponding frequency band. Slots are also thought to need a thin profile, thus the values of the widths w_{2x}, w_{6x} and heights h_3, h_5, h_7 are kept small, where x = {1, 2} denotes the upper and lower sides of the patches. The resonance or the frequency band of interest at slot B is narrow band (35 MHz); therefore, the values of height h_6 (sh_b) are in a small range. On the other hand a large band is required at slot A, thus the range of values of height h_2 (sh_a) are comparatively larger.

The minimal circumscribing sphere radius $R_{\min}$ is fixed to 19 mm, since reducing this value would make it difficult to accommodate the length of slot B while keeping the proper required height for the lowest required frequency (2.4 GHz). The Input feeding characteristic impedance is set to 50 Ω with parameters w_0, g_0 and ε_r.

R_{min} and the lower values of angles ψ and γ decide the shortest width and upper limit decide the maximum width of the antenna

Table 3.10 Parameter Space for multiband Antenna design

Parameter	Value (mm)		Parameter	Value (mm)	
	Lower	Upper		Lower	Upper
ψ	60°	120°	h_0	4	7
γ	60°	120°	h_2	1	4
w_1	w_0	3.5	h_3, h_5, h_7	0.5	1.5
ζ	0	1	$sh_a = h_2$	0.1	3
sw_a	10	y_{01}	$sh_b = h_6$	0.1	1.5
sw_b	13	w_{K2}	w_{4x}	1	4
w_{2x}	0.5	2	w_{6x}	0.5	2

3.7.4. Optimization and Results

Optimization is performed through a “steady state” genetic algorithm optimization technique, using an “Initial population” size of 32 samples, a “normal population” of 16 samples and a maximum of 30 generations. This makes a total of 496 EM solver iterations.

At the end of the optimization cycle, the best found $|S_{11}|$ response is shown in Fig. 3.29 and the corresponding best found parameter values are listed in Table 3.11. The overall size of the antenna is 30 × 22.5 mm².

A very good input matching is achieved in the 1st (2.4 GHz) and 2nd (3.7 GHz) bands. The large bandwidth of the 3rd band (5 − 6 GHz) is achieved thanks to two close resonances, at 5.4 GHz and 5.9 GHz (Fig. 3.29). The obtained –10 dB impedance bandwidth is 200 MHz (2.36–2.56 GHz), 130 MHz (3.6–3.73 GHz) and 850 MHz (5.28–6.13 GHz) for the 1st, the 2nd and the 3rd band respectively.

For the sake of performance evaluation of the design, the fractional bandwidth ($bw = BW/f_0$) is calculated for each band, where f_0 is the arithmetic mean of lower and upper corner frequencies of the respective band. Table 3.12 summarizes this evaluation.

Table 3.11 Parameter values of the best found Design

Parameter	Value (mm)	Parameter	Value (mm)
ψ	107.4°	h_0	6
γ	107.4°	h_1	3
w_1	5.667	h_3, h_5, h_7	1
ζ	0.4	$sh_a = h_2$	2.5
sw_a	18	$sh_b = h_6$	0.5
sw_b	24.5	h_4	7.5
w_{2x}	2	w_{4x}	3.5
w_{6x}	1.25		

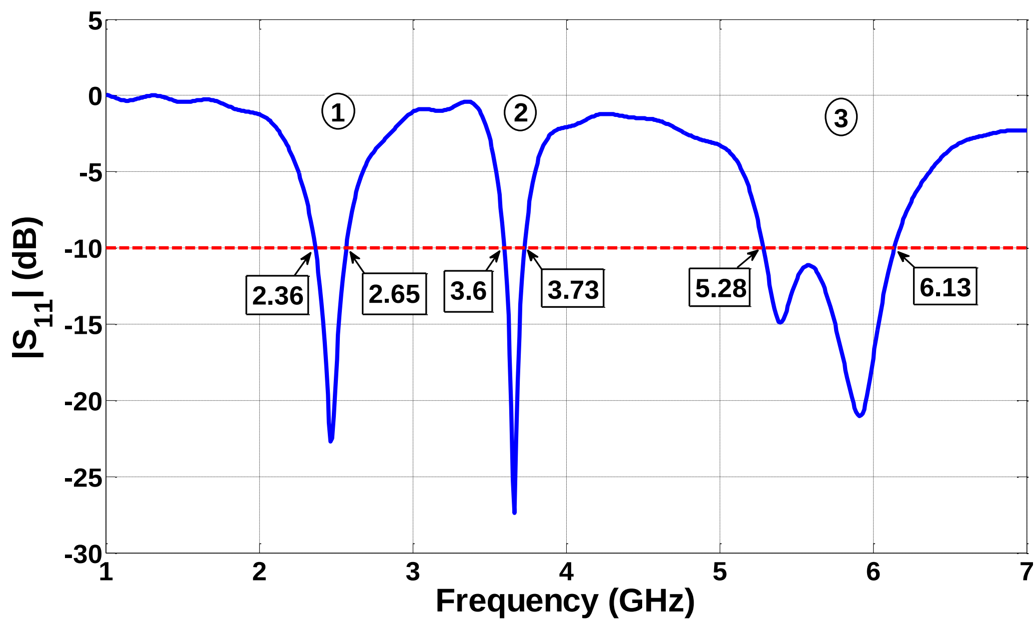

Fig. 3.29 Best found $|S_{11}|$ response for dual slot multiband antenna

Fig. 3.30 shows the realized gain in each corresponding WLAN band. This realized gain is calculated for the direction corresponding to the maximum realized gain of the resonant frequency in the respective band. It shows good pass-band gains (reference to 0 dB), when compared to stop-bands. Maximum realized gains of 1.66 dBi in the 1st band, –0.82 dBi in the 2nd band and 2.62 dBi in the 3rd band are achieved.

Table 3.12 Bandwidth per sub bands

	IEEE 802.11	Input Band (GHz)	f_0 (GHz)	BW (MHz)	bw (%)
1	b/g	2.36–2.56	2.46	200	8.13
2	y	3.6–3.73	3.66	130	3.54
3	a	5.28–6.13	5.70	850	14.89

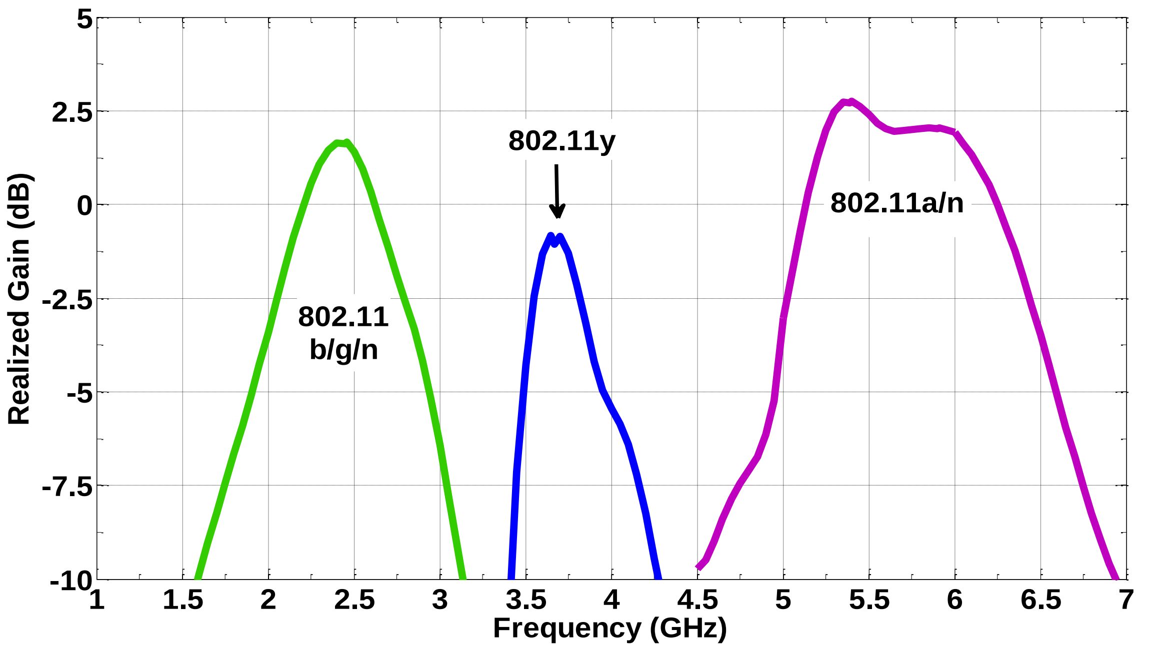

Fig. 3.30 Multiband Antenna — Realized gain in each WLAN band

3.7.5. Analysis

3.7.5.1. 1st band (resonant Frequency of 2.48 GHz)

Fig. 3.31 shows the results at 2.48 GHz. The realized gain pattern (Fig. 3.31c) is quasi omni-directional (Fig. 3.31d) and resembles the behaviour of a dipole antenna, as can be seen in Fig. 3.31e and Fig. 3.31f.

This dipole like behaviour is due to the currents along the height of the antenna as can be seen on the surface current distribution (Fig. 3.31a, b) below and above the slot A.

3.7.5.2. 2nd band: (Resonant Frequency of 3.67 GHz)

Strong and opposed currents can be seen at slot B (Fig. 3.32a, b). The radiation is not due to slot B, instead the upward currents along height are responsible for the radiation (Fig. 3.32a). Of course, this is also a dipole like behaviour which explains the elevation cuts in Fig. 3.32e and Fig. 3.32f. In addition, relatively low gain can also be explained by the low intensity of these upward currents (Fig. 3.32a).

3.7.5.3. 3rd band (Resonant Frequency of 5.39 GHz)

Slot A resonate at 5.3 GHz (Fig. 3.34a). The radiation is predominantly in the *yOz* plane (Fig. 3.34c). This may be due to the strong currents at the edges of the ground plane, which push the radiation upwards.

3.7.5.4. 3rd band (Resonant Frequency of 5.91 GHz)

This resonance is also due to slot A (Fig. 3.33a). The dielectric substrate may have an effect on the radiation; see Fig. 3.33d and Fig. 3.33e. At slot A, the horizontal dipole currents can be seen, whereas upward currents at edges of ground plane and at the edges of slot A can form vertical currents (Fig. 3.33a). This may also explain the moderate cross-polar component (Fig. 3.33d).

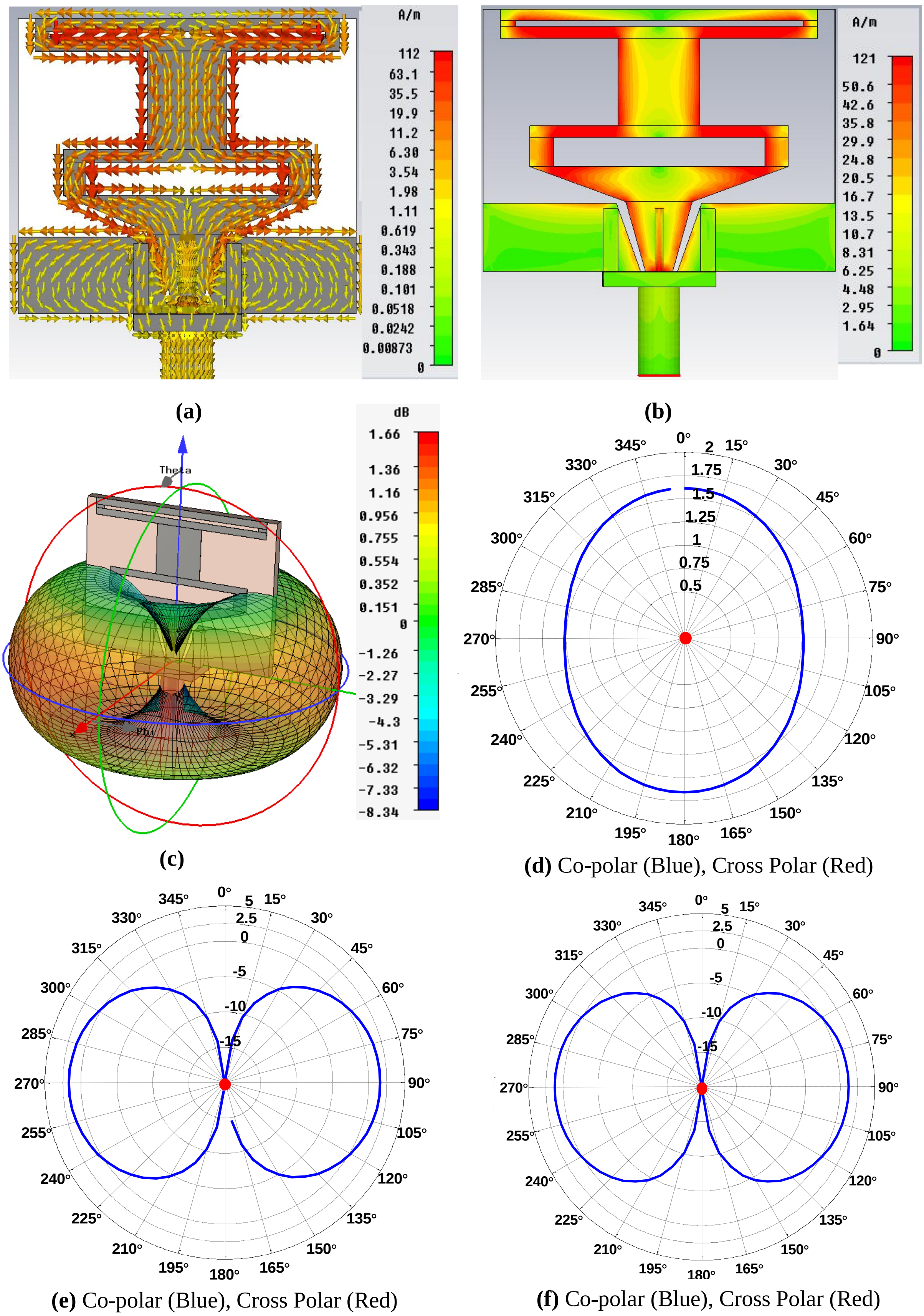

Fig. 3.31 Multiband Antenna Results at 2.46 GHz, (a) Peak Surface current direction, (b) Surface current distribution, (c) Total Realized Gain in 3D (d) Realized gain azimuth cut (e) Realized gain elevation cut (φ = 0°), (f) Realized gain elevation cut (φ=90°)

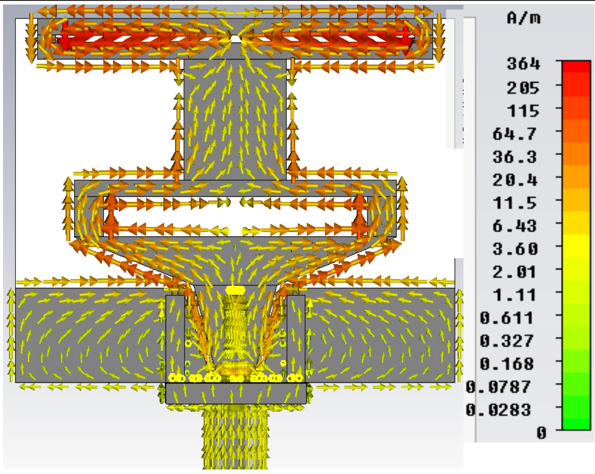

(a)

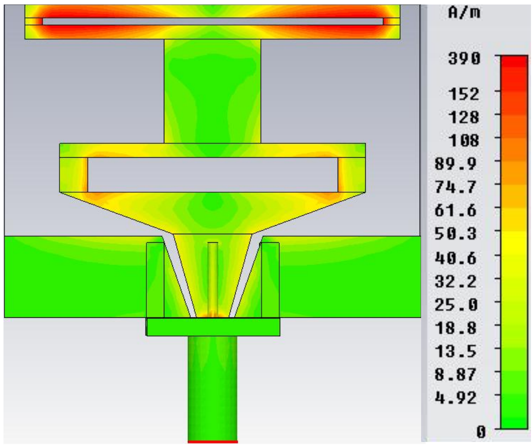

(b)

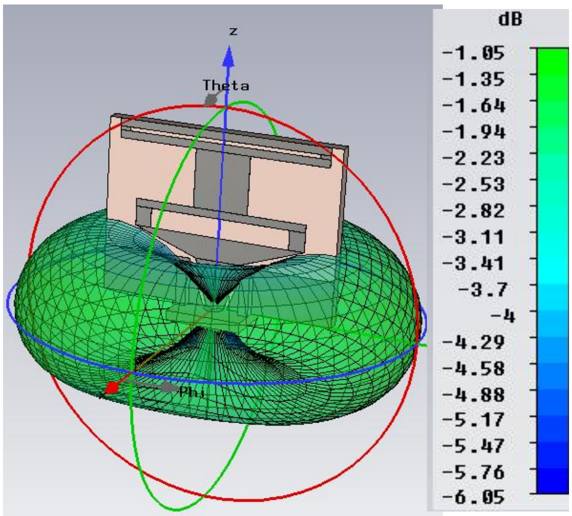

(c)

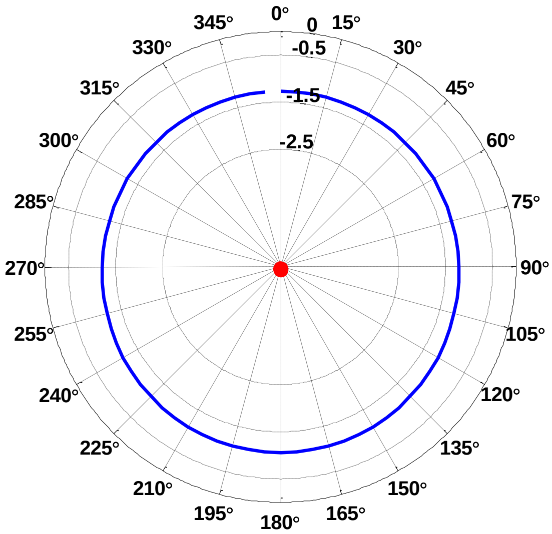

(d) Co-polar (Blue), Cross Polar (Red)

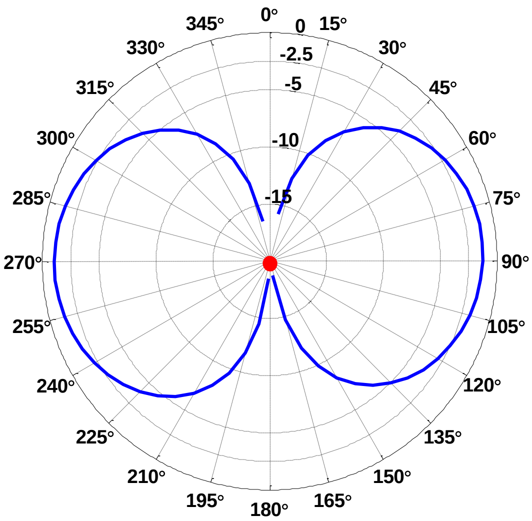

(e) Co-polar (Blue), Cross Polar (Red)

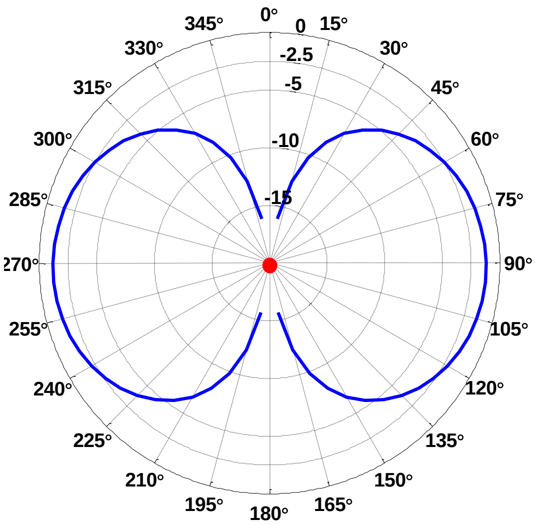

(f) Co-polar (Blue), Cross Polar (Red)

Fig. 3.32 Multiband Antenna Results at 3.67 GHz, (a) Peak Surface current direction, (b) Surface current distribution, (c) Total Realized Gain in 3D (d) Realized gain azimuth cut (e) Realized gain elevation cut (φ = 0°), (f) Realized gain elevation cut (φ=90°)

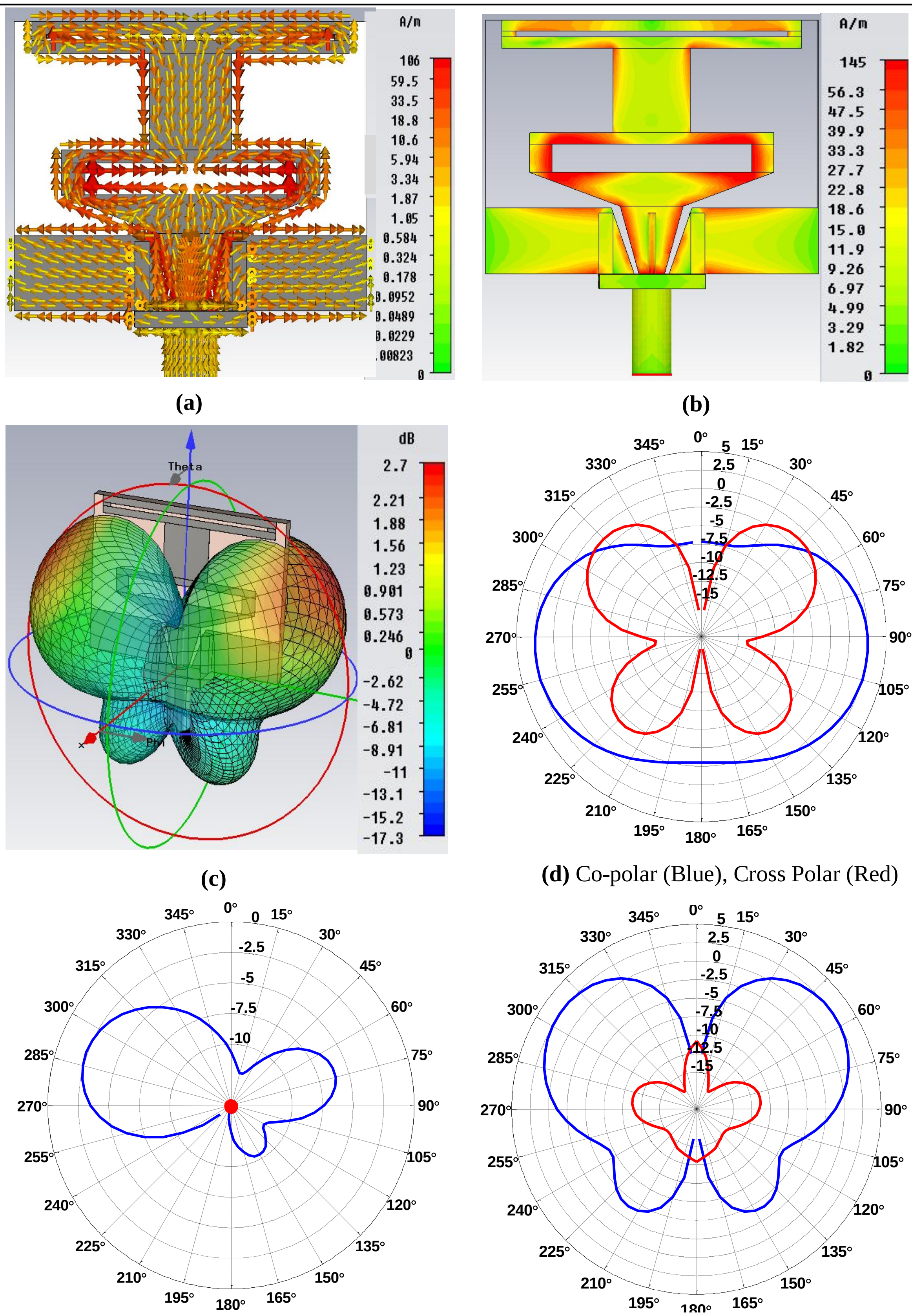

(a) (b)

(c)

(d) Co-polar (Blue), Cross Polar (Red)

(e) Co-polar (Blue), Cross Polar (Red)

(f) Co-polar (Blue), Cross Polar (Red)

Fig. 3.33 Multiband Antenna Results at 5.39 GHz, (a) Peak Surface current direction, (b) Surface current distribution, (c) Total Realized Gain in 3D (d) Realized gain conical cut (θ = 55°) (e) Realized gain elevation cut (φ = 0°), (f) Realized gain elevation cut (φ=90°)

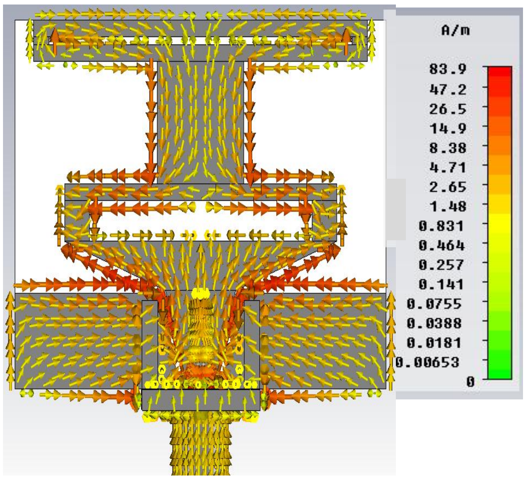

(a)

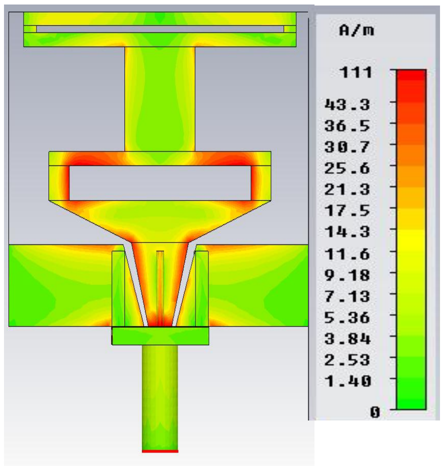

(b)

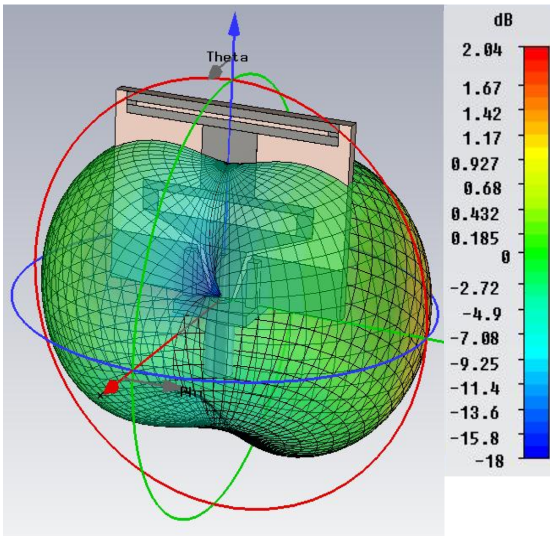

(c)

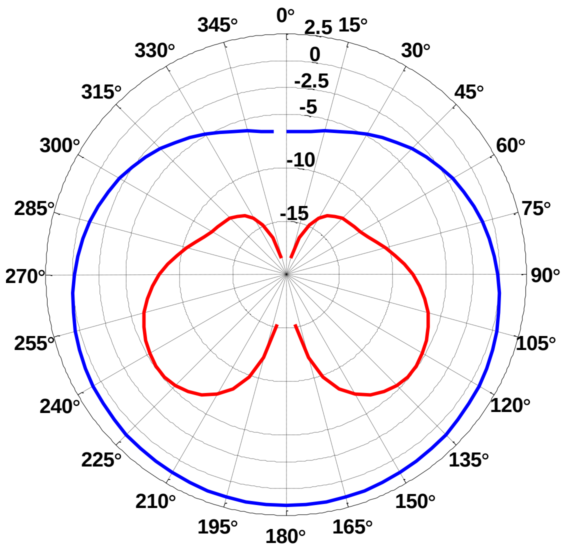

(d) Co-polar (Blue), Cross Polar (Red)

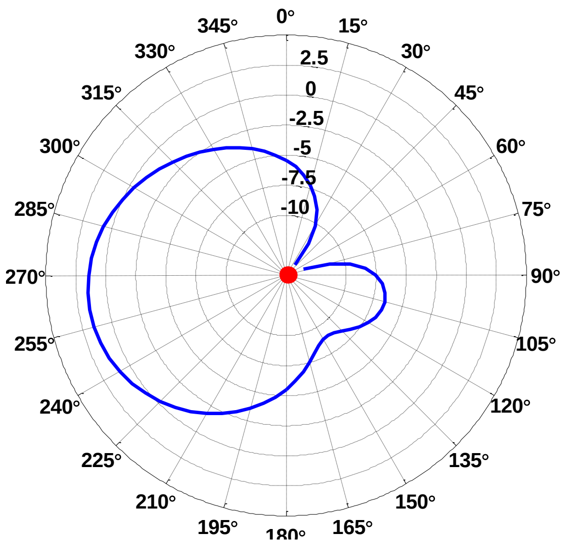

(e) Co-polar (Blue), Cross Polar (Red)

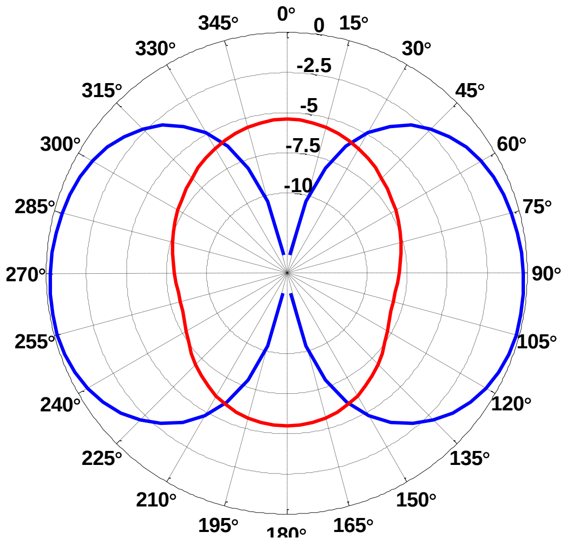

(f) Co-polar (Blue), Cross Polar (Red)

Fig. 3.34 Multiband Antenna Results at 5.91 GHz, (a) Peak Surface current direction, (b) Surface current distribution, (c) Total Realized Gain in 3D (d) Realized gain azimuth conical cut (θ = 100°), (e) Realized gain elevation cut (φ = 0°), (f) Realized gain elevation cut (φ=90°)

3.8. Conclusion

In this chapter we have validated the generic design approach by optimizing each design discussed in chapter 2. The chapter begins by explaining the procedure for optimization using genetic algorithm. Then some key specification indicators have been explained for frequency and time domains. In the second part of the chapter all key features of the optimized designs have been presented.

In the following, the summary of the key features of these antennas in time domain (Table 3.13) and in frequency domain (Table 3.14) are given.

Table 3.13 Time Domain key features of the optimized antennas

Antenna	Pulse duration in main beam (ns)	$\overline{\tau}_{ds}\big\vert_{-3\mathrm{dB}}$ (ps)	$\sigma_{\tau_{ds}}\big\vert_{-3\mathrm{dB}}$ (ps)
Triangular monopole	0.7	100	19.3
Staircase monopole	0.75	202	62.8
Crab-claw monopole	1.2	124	29.2
Dual feed monopole	0.75	81.3	12.6
Disc monopole	0.75	148	54.4
Triangular PBD	2.1	185	24.7
Disc PBD	2	170	28
Bicone	0.5	126	14.6

It can be seen that the smallest pulse duration is offered by the bicone antenna. In monopoles, the crab-claw offers longer pulse duration and ringing in its response has been observed. In the context of delay spread (τ_{ds}) in −3dB beam width, dual feed monopole offers the least distortion and standard deviation of the delay spread. Triangular and disc planar balanced dipoles (PBD) have comparable features in this regard.

As regards the frequency domain characteristics (Table 3.14), the MRG_{max} of Disc and Dual feed monopoles offers higher gains than other monopole designs. The monopoles have their main beam towards the dielectric substrate (i.e. φ = 180°). The direction of MRG_{max} for Bicone antenna may be due to a slightly larger lower bicone, nevertheless; the difference of gains between the main beam direction and at (θ, φ) = (90°, 0°) is marginal.

The overall sizes of each antenna are also given in (Table 3.14). The heights of monopoles are less than the quarter wavelength, as measured at the lowest frequency of the operating band [3—11] GHz. The same is found for dipole designs. In this case the heights are less than half wavelength.

Table 3.14 Frequency domain Key features of Optimized designs

Antennas	R_{min}	Size (HxW) (mm)	MRG_{max} (dBi)	Main beam	-6 dB beamwidth
Triangular monopole	13.55	22.05 x 15.76	2.21	[65 ° , 180°]	[130 ° , 360°]
Staircase monopole	13.80	23.4 x 14.7	2.06	[65 ° , 180°]	[105 ° , 360°]
Crab-claw monopole	15.1	25.62 x 13.4	2.12	[55 ° , 180°]	[145 ° , 360°]
Dual feed monopole	14	22.9 x 16.6	2.74	[60 ° , 180°]	[130 ° , 360°]
Disc monopole	12.6	22.4 x 17.2	2.51	[60 ° , 180°]	[130 ° , 360°]
Triangular PBD	27	40.62 x 38.9	4.9	[90 ° , 90°]	[85 ° , 170°]
Disc PBD	27.02	40.62 x 38.9	3.49	[70 ° , 85°]	[145 ° , 180°]
Bicone	15.48	26.3 x 18	1.43	[100 ° , 45°]	[130 ° , 360°]

In view of the above it is concluded that antennas presented in this chapter are well suited for UWB short range communications.

Chapter 4

Statistical Analysis

4.1. Introduction

In the previous chapter the optimal designs of several antenna subclasses have been presented, together with their performance results. The present chapter deals with two related topics: the first is the way to generate populations for antennas in general; the second is the statistical analysis and the statistical modeling of the antenna properties. With respect to the latter, we will focus on two important radio-electric parameters, which are the mean matching efficiency (*MME*) and the maximum mean realized gain (MRG_{max}).

The purpose here is to obtain quantitative statistical estimates about the performance indicators (*MME*, MRG_{max}) of a given antenna population. In addition to the complexity of an antenna statistical design, the comparison of the performance indicators can be used to select a population prior to performing the far-field radiation modeling. One immediate advantage of this study is the selection of the antenna design class or subclass, for a particular application.

The antenna classes here considered are the planar monopoles, the balanced dipoles and the conical design, whereas the subclasses can be differentiated with respect to their shapes or profiles, as shown in Fig. 4.1.

4.2. Procedure

The general procedure for generating an antenna population is depicted in Fig. 4.2. Starting from a generic design, the profile constraints are imposed to restrains the design to a certain shape (triangular, disc etc). A parameter space for the independent parameters is then defined — we call this parameter space as initial parameter space. At this stage, there can be two possible methods to generate the antenna's statistical population (Fig. 4.2). One can carry out a Monte Carlo like method and generate the required number of samples of independent parameters and then simulate the design with each combination of independent parameters; this path is shown in red line (Fig. 4.2).

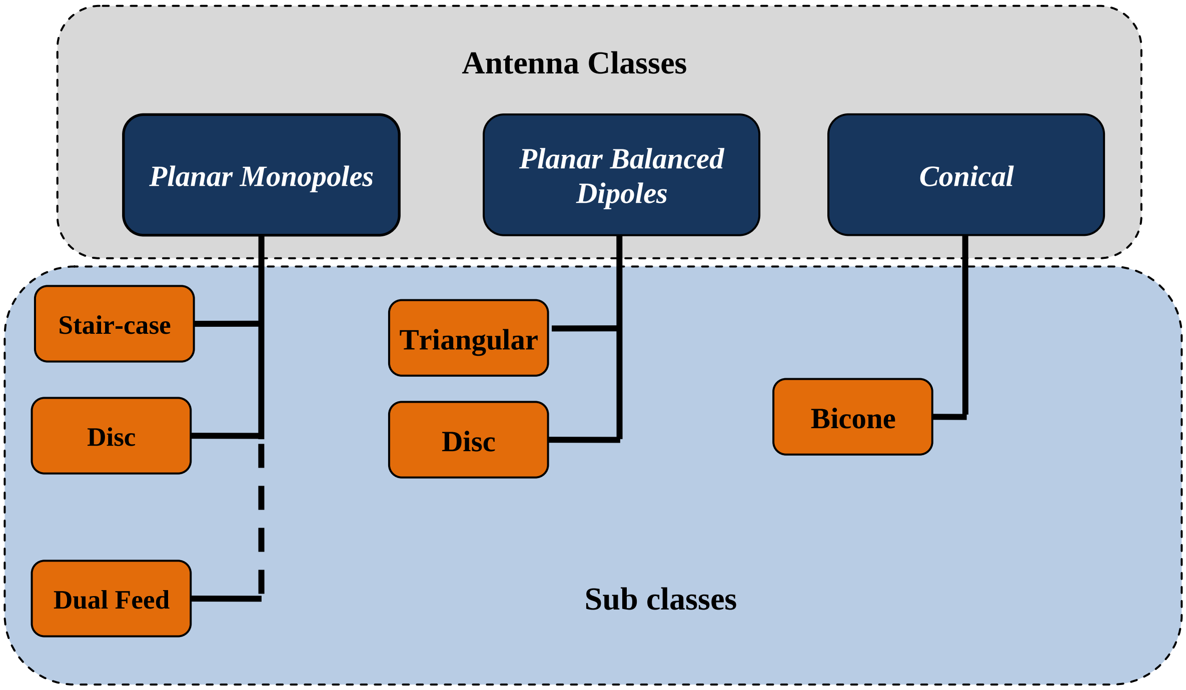

Fig. 4.1 Antenna design Classes and subclasses.

The second method comprises two steps, first an optimal design is searched within the initial parameter space using an evolutionary algorithm such as genetic algorithm (as has been demonstrated in chapter 3). In the second step, the optimal design values are used to create a new parameter space in such a way that the ranges of the independent parameters are centered around the optimal values, wherever possible. Then through Monte Carlo sampling within the parameter space, many samples are generated for the population. This is shown in green line (Fig. 4.2). The optimal design in this case is known as *generator* as it is used to create the antenna population. This method has the potential of generating more good samples that could pass the UWB criterion to some extent — of course it is conditioned by the design complexity.

In the field of statistics, the "design of experiment" methodology aims at sparing costly experiments by cleverly selecting the set of parameters of each experiment. This would certainly be a way to be more economical in the generation of the statistical populations for GA based optimization simulations (as populations are actually generated with these techniques, and their results memorized). However, this option has been left for further development.

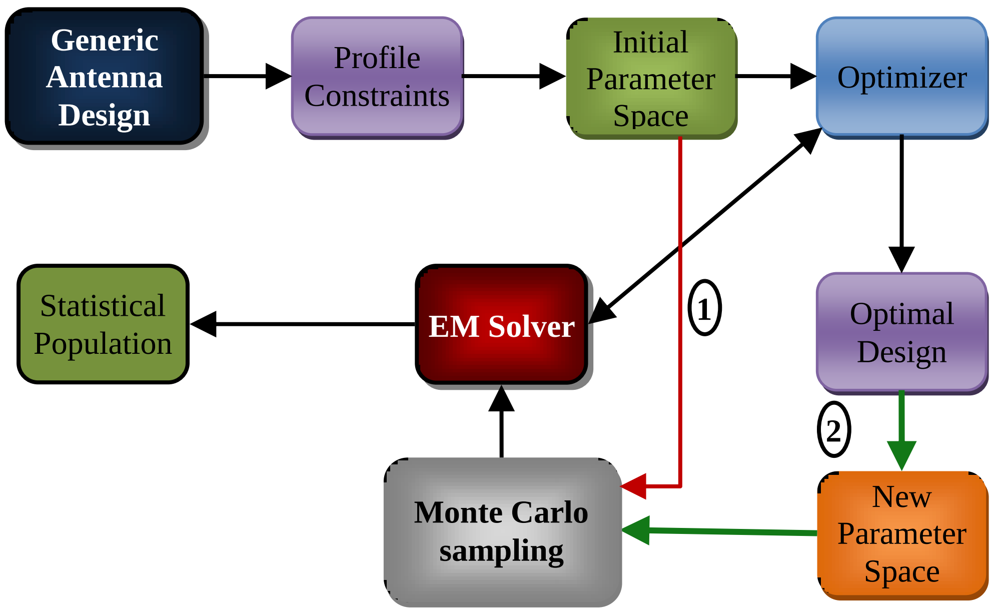

Fig. 4.2 Procedure for generating an antenna population. Method 1 (Red) uses the same parameter space as for optimization process. Method 2 (Green), creates a new parameter space around the optimal values.

In the first method, the optimal design can be found at the later stages, using the same initial parameter space. The initial parameter space may or may not be centered on the optimal parameter set, giving more or less chances of finding designs which approximately satisfy the requirements. But, as a matter of fact, this is not really the purpose at this stage: only (at least) satisfactory designs —i.e. satisfying relaxed constraints— are searched for. A simple illustration of that, in the case of a three parameters space, is shown in Fig. 4.3: the optimal design may exist at the top right corner of the cube (Fig. 4.3a) in the case of method 1, but for the second case (Fig. 4.3b) it is always at the center since the parameter space is created around the optimal values.

The populations of monopole subclasses triangular, staircase, crab-claw and of the bicone, are generated with the first method. All the independent parameters are uniformly distributed within the parameter space, irrespective of the method.

4.3. Population Statistics

For each sub-class, a population of 351 samples (i.e. antenna realizations), including the optimal design, have been generated. These populations are categorized according to the two radio-electric parameters of Mean Matching Efficiency (*MME*) and maximum *MRGmax* of the Mean Realized Gain (MRG), defined below:

$$MME = \frac{1}{\Delta f}\int_{f_1}^{f_2}\left(1-\left|S_{11}(f)\right|^2\right)df \quad \text{--------(4.1)}$$

$$MRG(\theta,\varphi) = \frac{1}{\Delta f}\int_{f_1}^{f_2}\left(1-\left|S_{11}(f)\right|^2\right)G(f,\theta,\varphi)\,df \quad \text{--------(4.2)}$$

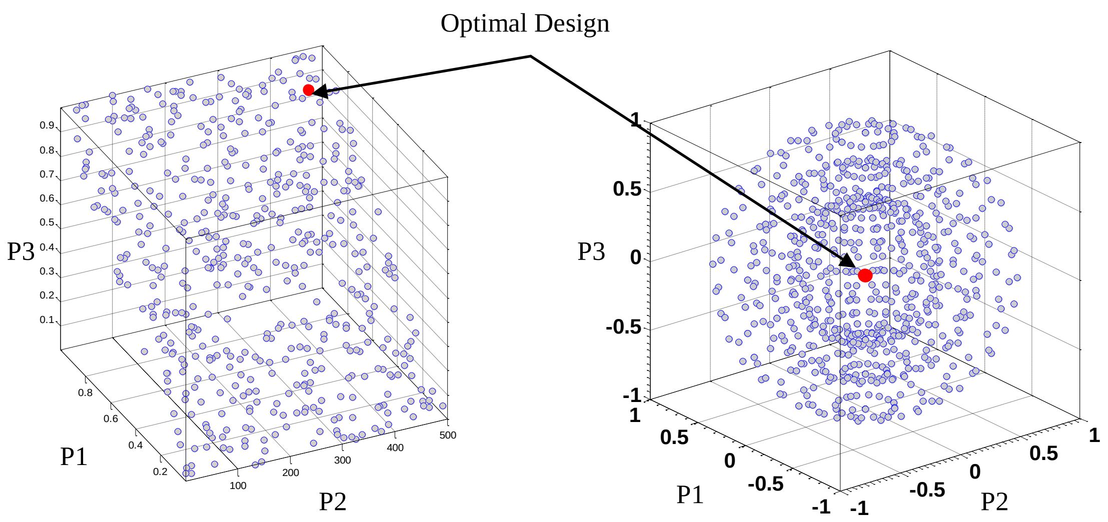

(a) Method 1 (b) Method 2

Fig. 4.3 Difference in two methods. In method 2 the parameter space is around the optimal values.

Both of these quantities are important performance indicators for UWB antennas. The *MME* represents the average of the proportion of the power accepted by the antenna in the given bandwidth, whereas the MRG represents the energy radiated into free space, also in the considered bandwidth. In (4.2) the total gain —including both polarization components— is used. Unless specified, the total MRG will be used as well throughout this chapter, and the maximal MRG will be denoted MRG_{max}.

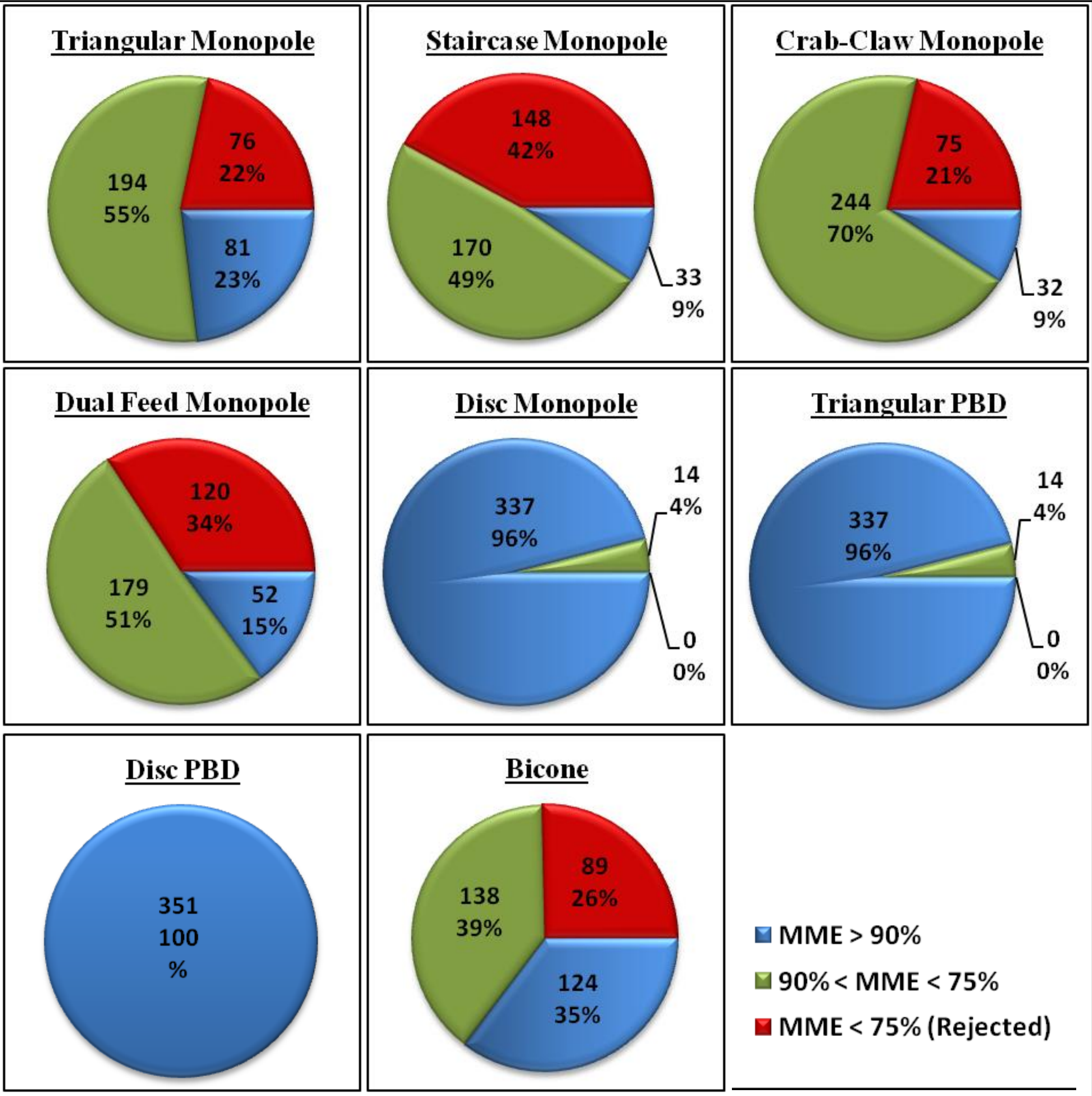

Fig. 4.4 Categorization according to *MME*.

Each population of an antenna subclass is categorized according to the "*MME*" (Fig. 4.4) and "MRG_{max}" (Fig. 4.5) criteria. Three categories are defined according to their *MME* values: above 90 %, between 75 % and 90 % and lower than 75 %; the last is considered as a rejection criterion. The disc monopole population outperforms all the other monopole populations, with 337 (96 %) successful realizations passing the 90 % threshold. For the planar balanced dipole (PBD) class, the Disc PBD population is the best subclass, with all the antenna realizations verifying the 90 % criterion. Note that the triangular PBD performs well also.

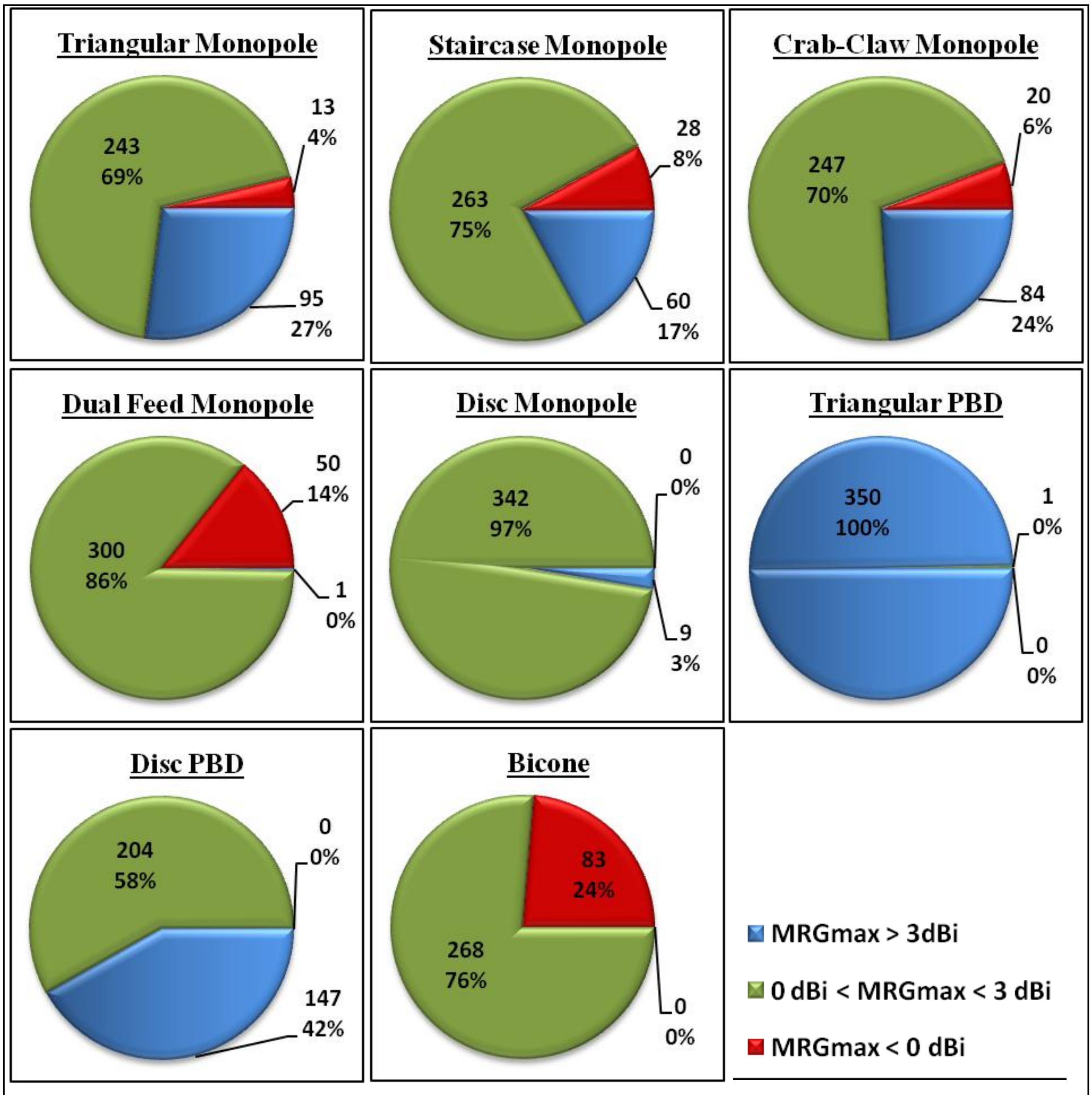

Fig. 4.5 Categorization according to MRG_{max}.

Three subsamples are also discriminated by the MRG_{max} criterion (Fig. 4.5): greater than 3 dBi, between 0 and 3 dBi, and lower than 0 dBi, the last one being a rejection criterion. Among the monopole populations the triangular monopole is the best with 95 realizations (27 %) above 3 dBi, closely followed by the crab-claw subclass with 84 realizations. In the planar balanced dipole class, the triangular PBD population outperforms the other with 350 successful realizations.

4.4. Modeling of radio EM parameters – Results

The *MME* and MRG_{max} empirical distributions for each population are examined, as well as possible theoretical distribution fits. Since the statistical modeling is impacted by the selection of samples on a quality basis, the rejected samples – discussed in the previous section – will not be considered in the distributions. Therefore, only antenna realizations which have an *MME* ≥ 75 % have been selected for computing the *MME* distributions, whereas for the MRG_{max} distribution this criterion is $MRG_{max} \geq 0$ dBi.

Two statistical hypotheses tests —Kolmogov-Smirnov (K-S) and Anderson-Darling (A-D)— have been used to check the goodness of fit (GoF) and the ranking, based on their respective test statistics. The chi-square (χ^2) GoF has been tried and found not suitable for the purpose of comparing data with theoretical distributions, however it was more suitable in comparing the distribution of two populations. On the other hand, K-S and A-D tests examined the vertical distances between the data and the best fit distribution, and hence it was found more suitable for our case. K-S and A-D tests are similar in nature but A-D put more weights on the tails of the distribution fit. These tests, however, sometimes lead to wrong conclusion, which is why we have selected both of them.

In addition, when there was a tie between the two good fit distributions, a measure of the relative GoF of considered models has been performed using the Akaike information criterion (AIC). This well known criterion allows the comparison of different distributions, according to their maximum log likelihood (MLE) and to the number of parameters used in the model. In particular, it introduces a penalty for the distributions using more parameters. The details of these tests are given in appendix 'A'.

In all these GoF tests, the null hypothesis (H_0) is the assumption that the empirical distribution belongs to the theoretical distribution within 95 % confidence bounds.

The modeling results have been organized according to the antenna subclasses in the subsequent sections. First, the *MME* cumulative distribution along with the three best found theoretical distributions (based on MLE and visually) are presented in a figure. The parameters of each fitted distribution (mean, standard deviation and sample size i.e. the number of realizations) of the *MME* data are also presented in the same figure. The three GoF tests results for *MME* data are summarized in a table. The AIC results are also incorporated in the same table. The corresponding GoF test critical values are also shown, for a quick comparison. It is recalled that if the test statistics value (the output of the test) value is less than the critical value, then the null hypothesis (H_0) is accepted and the distribution is said to be passed. Ranking by the GoF test to any number of given fits is based on the respective test statistics.

The normal distribution —as the most common and practical one — is included in the GoF tests for comparison purpose, whenever it has MLE values close to good fits and it visually appears suitable. This comparison is not equal to a test-of-normality but it gives a good oversight of the data distribution.

The MRG_{max} modeling results are then presented in the same manner. Lastly, a scatter plot of MME vs MRG_{max} is given, in order to show the trend of the population. The Pareto Front is also drawn in the same figure.

4.4.1. Triangular Monopole

The parameter space for the triangular monopole is given in Table 4.1. This is the same parameter space as that used for the optimization. This means that the "method 1" (see Ch. 3) has been used for the population generation.

Table 4.1 Parameter Space for triangular monopole population generation

Parameter		Interval	
		Lower	Upper
1	R_{min}	12	25
2	w_0	$2R_{cond}$	$d_{coax} - 2g_0$
3	g_0	0.15	1
4	γ	45°	100°
5	ψ	45°	170°
6	R_{Height}	1	5
7	α	78	90
8	ζ	0	1

275 realizations turned out to have an MME greater than 75 %. The statistical mean is $<MME>$ = 86 % and the standard deviation is about 5 %, as can be seen in Fig. 4.6. Based on visual estimation and MLE, good fits are found for the Weibull,

the beta and the generalized extreme value (GEV) distributions, which have subsequently been tested for GoF. The GEV fit passed the K-S test while the Weibull and the Beta distributions passed both the K-S and A-D tests. The ranking of these distributions based on the statistics (or test value), as shown in Table 4.2. On the other hand, the normal distribution did not pass any of the considered hypothesis tests and it was ranked 4th according to the Akaike criterion (Table 4.2).

Comparing the Beta and GEV distributions for the triangular monopole *MME* data, although the former passed all tests, the latter is ranked first by the AIC and passes the K-S test with first rank. Consequently, the GEV has been adopted.

For the MRG_{max} distribution (Fig. 4.7), the mean of the population was found to be 2.36 dBi and the standard deviation 0.872 dBi. The three distributions, Normal, Weibull and GEV have been observed as good fits. Except for Weibull, the other two distributions passed the GoF tests, as can be seen in Table 4.3 since the test statistics are lower than the test critical values. It is therefore concluded that the MRG_{max} distribution can be satisfactorily described by a GEV distribution, since it passed all the GoF tests and was ranked first according to AIC.

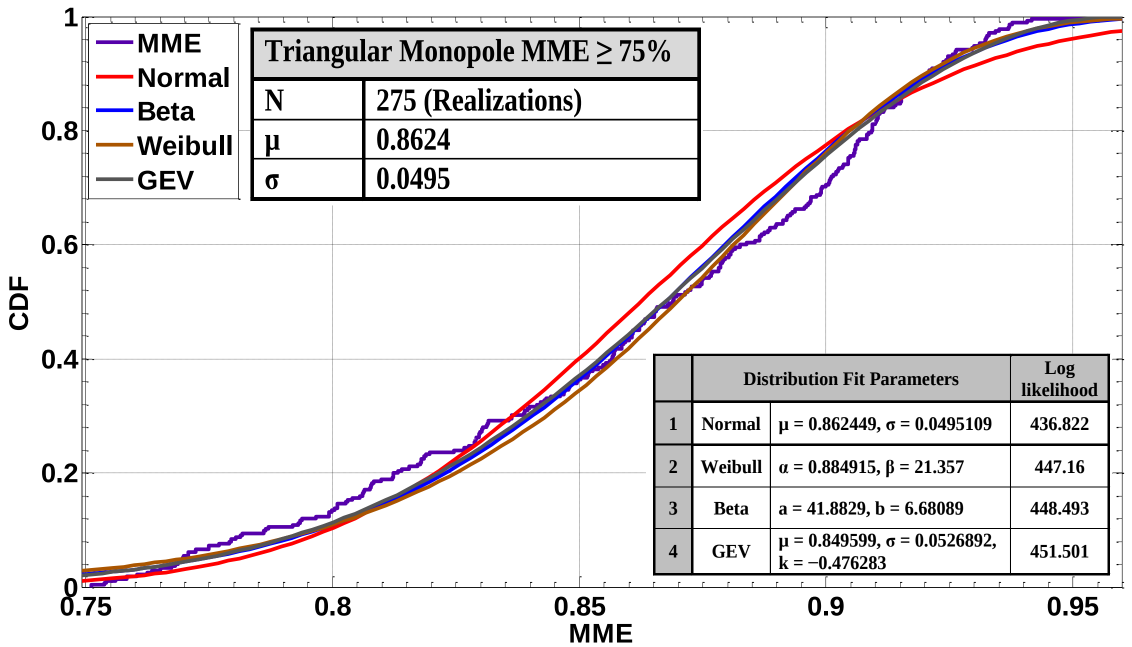

Fig. 4.6 ***MME*** **Cumulative distribution with possible fit for Triangular Monopole Population**

The scatter plot of MRG_{max} vs *MME* shows the trend of the population (Fig. 4.8). It is noted that the population is mainly concentrated within the MRG_{max} range of 1.5—3.5 dBi. The red line joining the realizations at the extreme bottom left of the figure depict the Pareto front. The good antenna designs lie on this line, some designs performing particularly well in MRG_{max}, owing to their larger size.

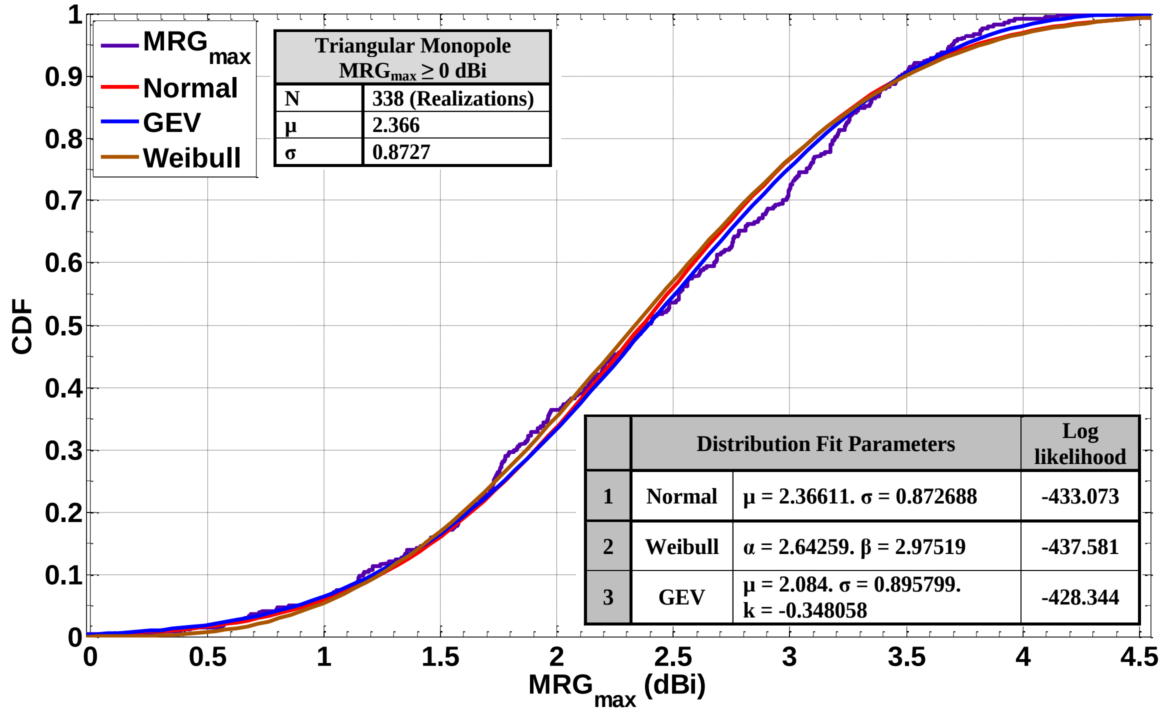

Fig. 4.7 ***MRG_{max}*** **Cumulative distribution with possible fit of Triangular Monopole Population**

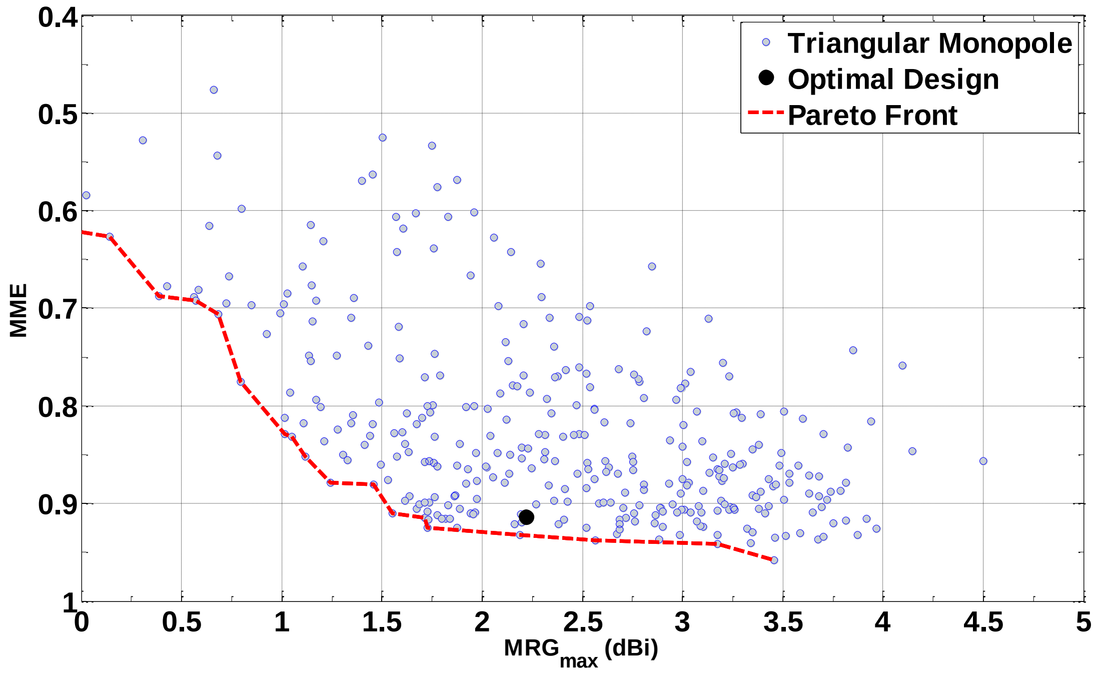

Fig. 4.8 ***MME*** **vs** ***MRG_{max}*****, Triangular Monopole Population.**

Table 4.2 Ranking of fitted distribution on Triangular *MME* data according to GOF tests and AIC

	Distribution	K-S (0.08189)		A-D (2.5018)		**AICc**	
		Stat	Rank	Stat	Rank	Stat	Rank
1	Normal	0.08695	4	3.5553	3	−869.6	4
2	Weibull	0.06939	3	1.704	2	−890.28	3
3	Beta	0.06204	2	1.5531	1	−892.94	2
4	GEV	0.05072	1	4.9243	4	−896.91	1

Table 4.3 Ranking of fitted distribution on Triangular Monopole MRG_{max} data according to GOF tests and AIC

	Distribution	K-S (0.07387)		A-D (2.5018)		**AICc**	
		Stat	Rank	Stat	Rank	Stat	Rank
1	Normal	0.06056	2	1.2303	2	870.18	2
2	Weibull	0.09639	3	5.6205	3	879.2	3
3	GEV	0.04286	1	0.58546	1	862.76	1

4.4.2. Staircase Monopole

The staircase population has been generated with method 1, the parameter space being listed in Table 4.4. The *MME* distribution has a statistical mean of about 84 % and a standard deviation of 5 %. (Fig. 4 9).

For the *MME* statistics, four distributions, Lognormal, Beta, Normal and GEV, offer visually good fits. All these four fits passed the two GoF tests at 95 % confidence bounds. The test statistics values are given in Table 4.5. The visual inspection suggests that Lognormal, Normal and GEV are nearly similarly performing, but test values show that the normal distribution is at a certain distance from the other three. Though the GoF tests ranked Beta as the second best distribution, AIC ranked it 4^{th} due to its lower MLE. Hence, we consider the *MME* data can be well represented by the GEV distribution, since it is ranked first in Table 4.5 for all the tests.

Table 4.4 Parameter Space for Staircase Monopole Population Generation

	Parameter	Interval	
		Lower	Upper
1	R_{min}	12	25
2	w_0	$2R_{cond}$	$d_{coax} - 2g_0$
3	g_0	0.15	1
4	γ	45°	100°
5	ψ	45°	170°
6	R_{Height}	1	5
7	α	78	90
8	ζ	0	1
9	β_k	0	1
10	δ_k	0.1	1

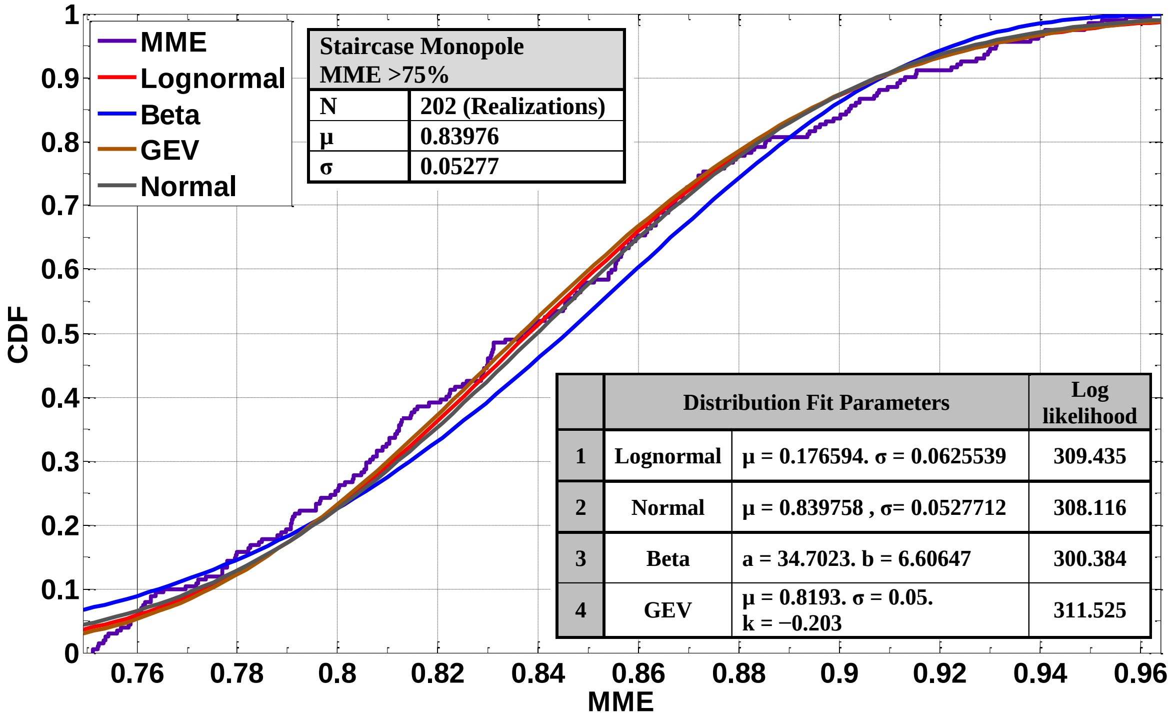

Fig. 4 9 ***MME*** **Cumulative distribution with possible fit for Staircase Monopole Population.**

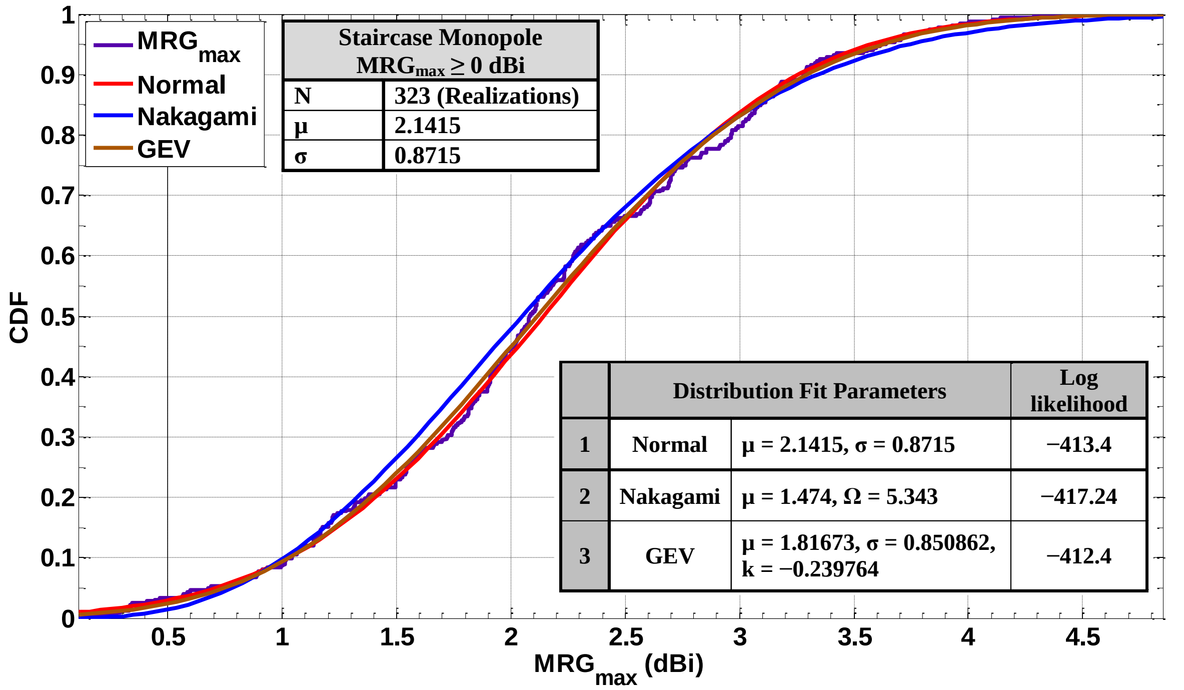

Fig. 4.10 MRG_{max} Cumulative distribution with possible fit of Staircase Monopole Population.

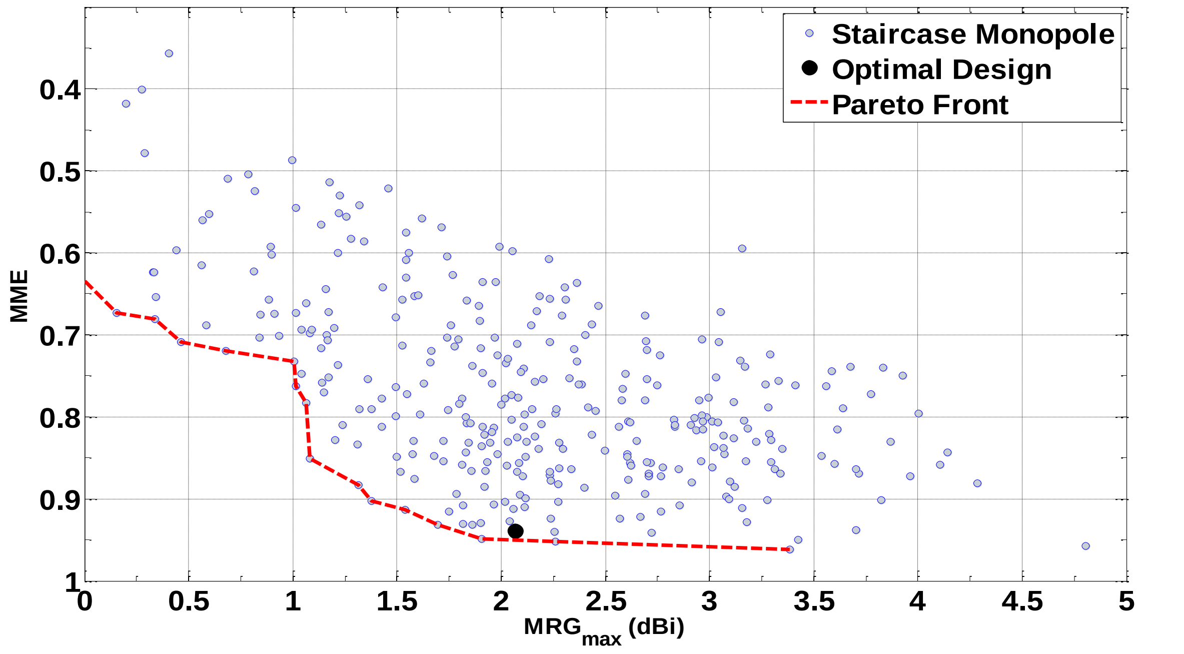

Fig. 4.11 *MME* vs MRG_{max} , Staircase Monopole population

For the MRG_{max} statistics (Fig. 4.10), the Normal, Nakagami and GEV distributions were found to be good candidates and passed all the three GoF tests at 95 % confidence bounds. The GoF test statistics rank the GEV first, but it is ranked second by the AIC due to its higher number of parameters (Table 4.6). Since the Normal fit is ranked first according to AIC, and the difference between the results of the hypothesis tests of the GEV and Normal fits are low, the latter should be chosen for obvious reasons.

The *MME* vs MRG_{max} scatter plot shows a concentration of antenna realizations with *MME* above 80 % and MRG_{max} within the range 1.5—2 dBi

Table 4.5 Ranking of fitted distribution on Staircase *MME* data according to GOF tests and AIC

	Distribut-ion	K-S (0.09555)		A-D (2.5018)		**AICc**	
		Stat	Rank	Stat	Rank	Stat	Rank
1	Normal	0.06123	4	1.0044	4	−614.83	2
2	lognormal	0.05445	3	0.8519	3	−612.19	3
3	Beta	0.04853	2	0.62665	2	−596.72	4
4	GEV	0.04086	1	0.55692	1	−616.96	1

Table 4.6 Ranking of fitted distribution on Staircase MRG_{max} data according to GOF tests and AIC

	Distribution	K-S (0.07556)		A-D (2.5018)		**AICc**	
		Stat	Rank	Stat	Rank	Stat	Rank
1	Normal	0.044	2	0.51043	2	830.84	1
2	Nakagami	0.04724	3	1.8898	3	838.52	3
3	GEV	0.03758	1	0.4081	1	830.88	2

4.4.3. Crab-claw Monopole

Again method 1 has been used for generating the population, within the parameter space shown in Table 4.7. The population statistical mean has been found to reach 84 % with a standard deviation of about 4.4 %. The perceptibly good fit distributions for the *MME* data are the Normal, Nakagami, Gamma and GEV distributions (Fig. 4. 12).

At 95 % confidence bounds, all the aforementioned distributions have passed the two K-S and the A-D tests. The Normal distribution has been ranked first by K-S test while GEV has been ranked first by A-D test. This discrepancy has been solved by the AIC test, which ranked 1st the GEV distribution (Table 4.8). The difference among the AIC test values is not significant, thus any of the distribution can be used. The GEV distribution has been preferred, owing to its efficient modeling features.

Table 4.7 Parameter Space for Crab-Claw Monopole Population Generation

	Parameter	Interval	
		Lower	**Upper**
1	R_{min}	12	20
2	w_0	$2R_{cond}$	$d_{coax} - 2g_0$
3	g_0	0.15	1
4	γ	45°	100°
5	ψ	45°	120°
6	κ	1	5
7	α	78	90
8	ζ	0	1
9	Δg	1	$Ws/2 - w_p$
10	w_p	1	y_{K2}

The MRG_{max} distribution turned out to have a statistical mean of 2.3 dBi and a standard deviation of 1 dBi. The data was compared with the Log-logistic, Gamma and GEV distributions (Fig. 4.13). All the fitted distributions did pass the two GoF tests at 95 % confidence bounds. The normal distribution has also been tested for GoF for comparison. Test statistics have revealed that it was far from the MRG_{max} distribution (Table 4.9). The GEV distribution has been ranked 1st by all the tests including the AIC (Table 4.9). The crab-claw population appears to be concentrated in the region above 80% for the *MME* and between 1.3 to 2.3 dBi for the MRG_{max} horizontal axis (Fig. 4.14).

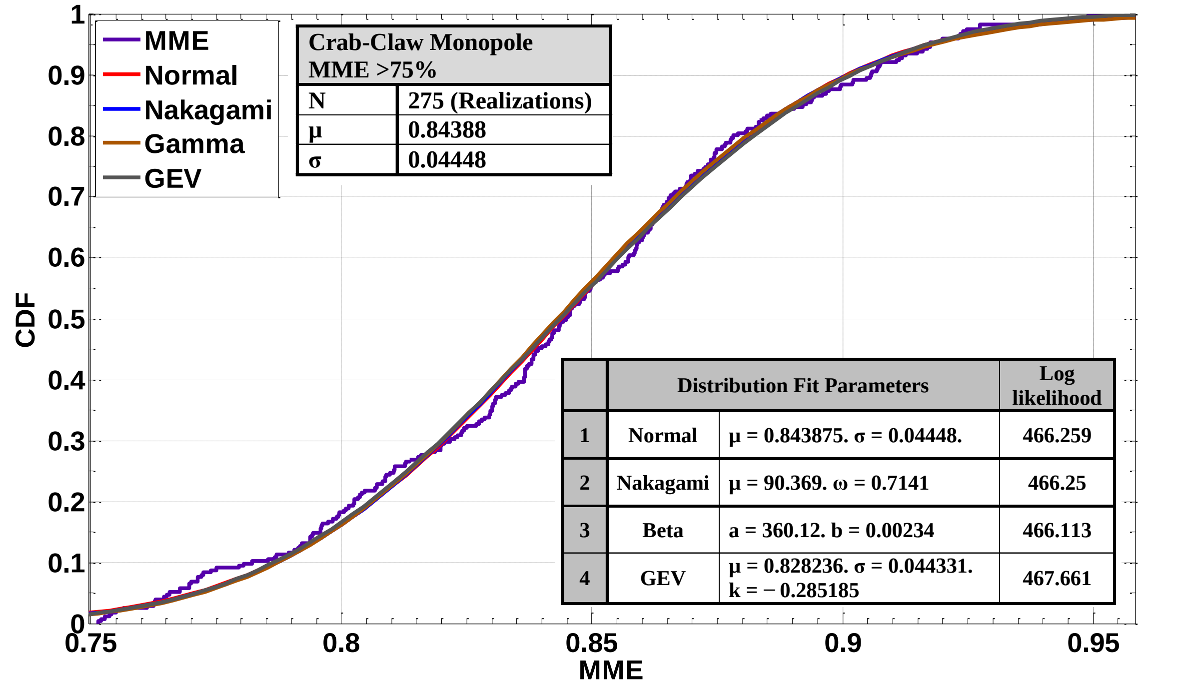

Fig. 4. 12 ***MME* Cumulative distribution with possible fit for Crab-claw Monopole Population**

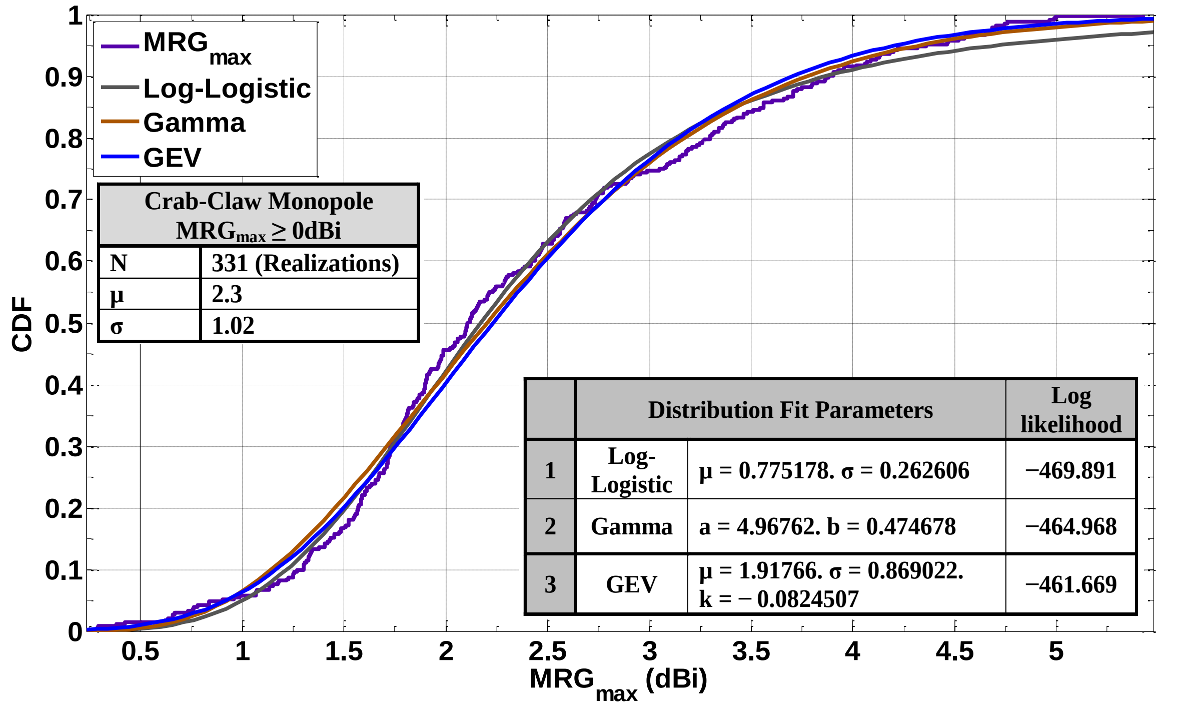

Fig. 4.13 ***MRG_{max}* Cumulative distribution with possible fit for Crab-claw Monopole Population**

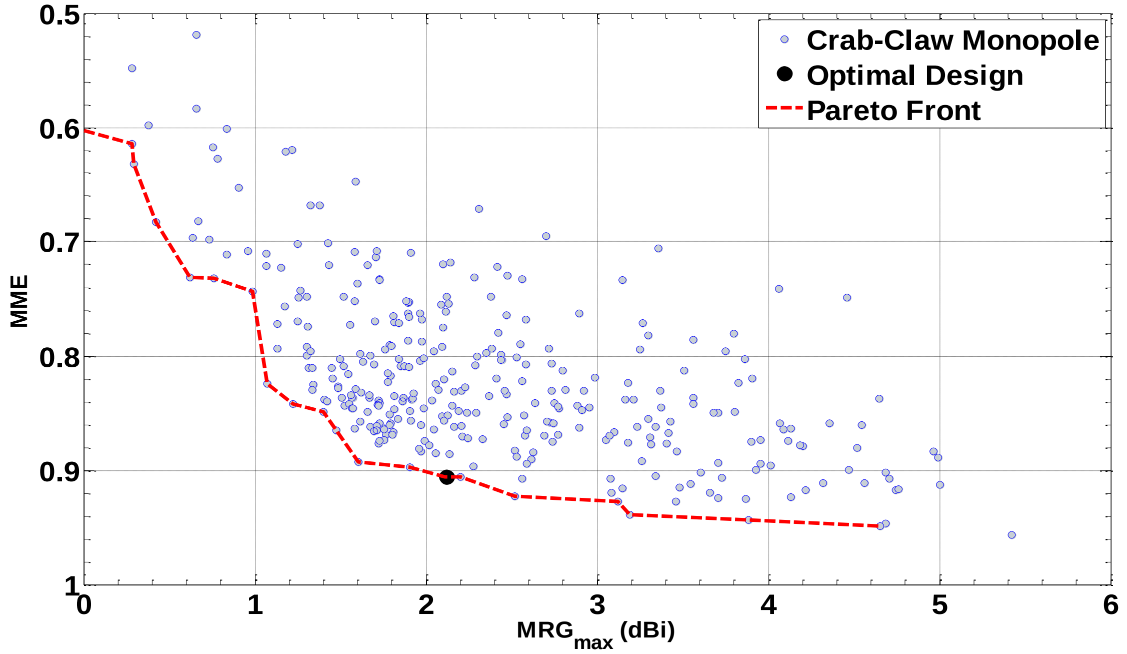

Fig. 4.14 *MME* vs *MRG*$_{max}$, Crab-claw Monopole population

Table 4.8 Crab-claw monopole, Ranking of fitted distribution on *MME* data according to GOF tests and AIC

	Distribution	K-S (0.08189)		A-D (2.5018)		AICc	
		Stat	Rank	Stat	Rank	Stat	Rank
1	Normal	0.03679	1	0.48788	2	−928.47	2
2	Nakagami	0.0401	3	0.53489	3	−928.46	3
3	Gamma	0.04352	4	0.59093	4	−928.18	4
4	GEV	0.03921	2	0.4562	1	−929.23	1

Table 4.9 Crab-claw monopole, Ranking of fitted distribution on *MRG*$_{max}$ data according to GOF tests and AIC

	Distribution	K-S (0.07464)		A-D (2.5018)		AICc	
		Stat	Rank	Stat	Rank	Stat	Rank
1	Normal	0.10911	4	5.1425	4	957.11	4
2	Log-Logistic	0.06473	3	2.0122	3	943.82	3
3	Gamma	0.05338	2	1.5275	2	933.97	2
4	GEV	0.04939	1	1.2987	4	929.41	1

Table 4.10 Parameter Space for Dual Feed Monopole Population Generation

	Parameters	Interval	
		Min.	Max.
1	R_{min}	13	20
2	γ	65	80.3
3	ψ	60	73
4	w_0	$2R_{cond}$	$d_{coax} - 2g_0$
5	α	85°	90°
6	g_0	0.3	1
7	ζ	0	3
8	κ	2	4
9	g_{61}	0.3	1
10	w_{32}	$w_1/4$	$w_1/2$
11	R_{h0}	0.1	1
12	R_{hfeed}	0.1	1
13	R_{h4}	0.1	1
14	R_{h5}	0.1	1
15	w_{32}	$w_1/4$	$w_1/2$
16	$w_{41} = w_{42}$	$g_{32} + w_{32}$	$Ws/2$

4.4.4. Dual feed Monopole

Method 2 has been used for the generation of the population of dual feed monopoles, the parameter space (Table 4.10) being uniformly distributed around the optimal values.

The *MME* data has been found to have a statistical mean of 80 % and a standard deviation of about 5.6 %. The distribution has been tested for many theoretical fits, but none of them were observed to be visually appropriate. An inspection of the probability density function (PDF) suggests that the data is uniformly distributed, as also confirmed by the CDF plot (Fig. 4.15). In the GoF test, the normal distribution has also been added for comparison (Table 4.11). It can be seen that the uniform distribution passed the two tests comfortably well. No AIC test was required in this case and it is therefore omitted from the table (Fig. 4.15).

For the MRG_{max} empirical data, the statistical mean was determined to be 2.33 dBi, together with a standard deviation of 0.31 dBi. Visually good fits have been observed for the normal, Weibull and GEV distributions. These distributions passed the two GoF tests at 95 % confidence bounds. The AIC ranked the GEV first but since the differences in the test statistics were low, any of the distribution fit can be used to model the data. The GEV has been here preferred, on the basis of its simpler modeling.

The scatter plot shown in Fig. 4.17 validates the results of *MME* distribution, as the design realizations are dispersed almost uniformly in the *MME* scale (vertical)). MRG_{max} values are distributed within 2 to 2.7 dBi.

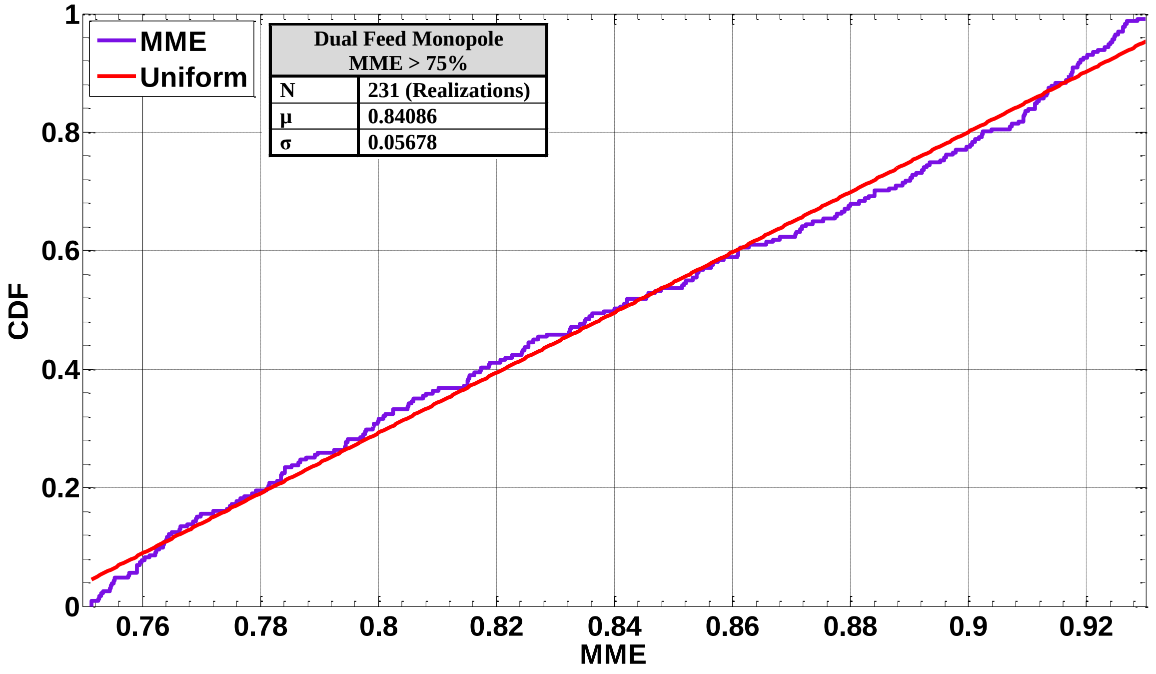

Fig. 4.15 *MME* Cumulative distribution with possible fit for Dual Feed Monopole Population

Table 4.11 Dual Feed Monopole, Ranking of fitted distribution on *MME* data according to GOF tests

	Distribution	K-S (0.08935)		A-D (2.5018)	
		Stat	Rank	Stat	Rank
1	Normal	0.09074	2	4.6978	2
2	Uniform	0.04967	1	1.1771	1

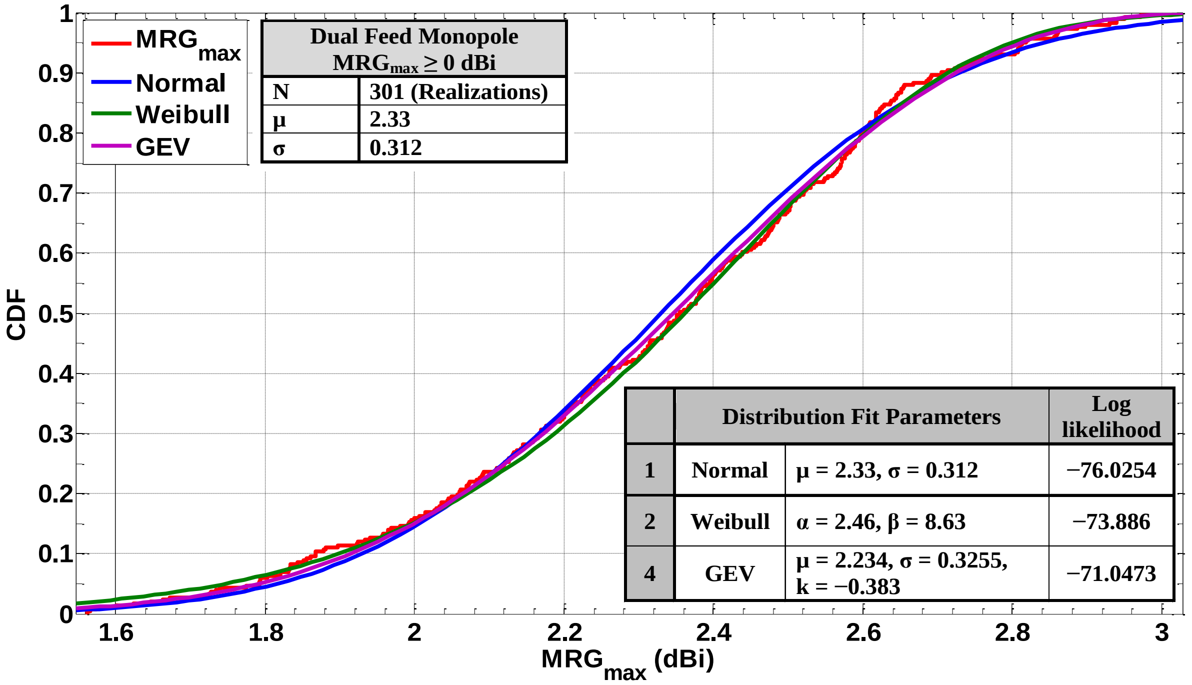

Fig. 4. 16 ***MRG_{max}* Cumulative distribution with possible fit for Dual Feed Monopole Population**

Table 4. 12 Dual Feed monopole, Ranking of fitted distribution on *MRG_{max}* data according to GOF tests and AIC

	Distribut-ion	K-S (0,07827)		A-D (2.5018)		**AICc**	
		Stat	Rank	Stat	Rank	Stat	Rank
1	Normal	0.05113	3	0.98868	3	156.1	3
2	Weibull	0.03623	1	0.63822	2	151.81	2
3	GEV	0.03817	2	0.31003	1	148.18	1

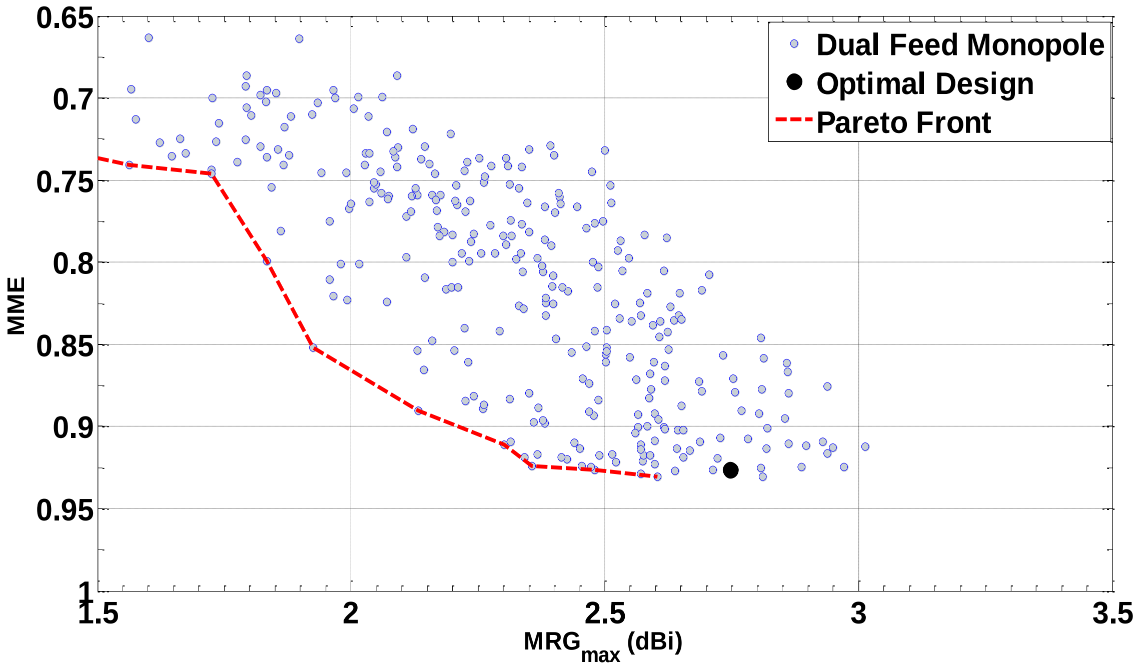

Fig. 4.17 ***MME*** **vs** ***MRG***$_{max}$ **, Dual Feed Monopole population**

4.4.5. Disc Monopole

The disc monopole population has also been generated around the optimal design values (method 2). See the parameter space in Table 4.13

All antenna realizations have an *MME* greater than 75 % and the statistical mean has been found to reach 93 %. The considered models were the Weibull, Beta and GEV distributions (Fig. 4.18). Except for the GEV, which passed the K-S GoF test only, the other two passed both the GoF tests at 95 % confidence bounds. The normal distribution did not pass any of them. The Weibull distribution was ranked first by K-S test and this was confirmed by the AIC (Table 4.14). The A-D test results could be misleading here since the normal distribution is more distant from the data, especially at the tails, when compared to the GEV but was ranked above the GEV. The difference between the GEV and Weibull distributions as regards the AIC results was not found to be appreciable, thus the GEV can be selected for modeling the *MME* data.

The MRG_{max} empirical data presented a statistical mean of 2.4 dBi and a standard deviation of 0.34 dBi (Fig. 4.19). The perceptibly good fits are the Normal, Nakagami and GEV distributions. The K-S and A-D tests passed all of them at 95 %

confidence bounds. The GEV distribution was ranked first in all tests, which was also validated by AIC (Table 4.15).

The scatter plot (Fig. 4.20) shows that the population presents a concentration above 92 % *MME* and a MRG_{max} in the range 1.5 to 2.8 dBi.

Table 4.13 Parameter Space for Disc Monopole Population Generation

	Parameters	Interval	
		Min.	Max.
1	R_{min}	12	20
2	γ	65	85
3	ψ	2°	7°
4	w_0	$2R_{cond}$	$d_{coax} - 2g_0$
5	α	85°	90°
6	g_0	0.3	1
7	ζ	0.5	1.5
8	κ	1	3.5
9	r_{yaxis}	$R_{min}/4$	$R_{min}/2$
	$w_{12} = w_{21}$	$w_1/2$	w_1
	h_1	$H_{total}/10$	$H_{total}/5$

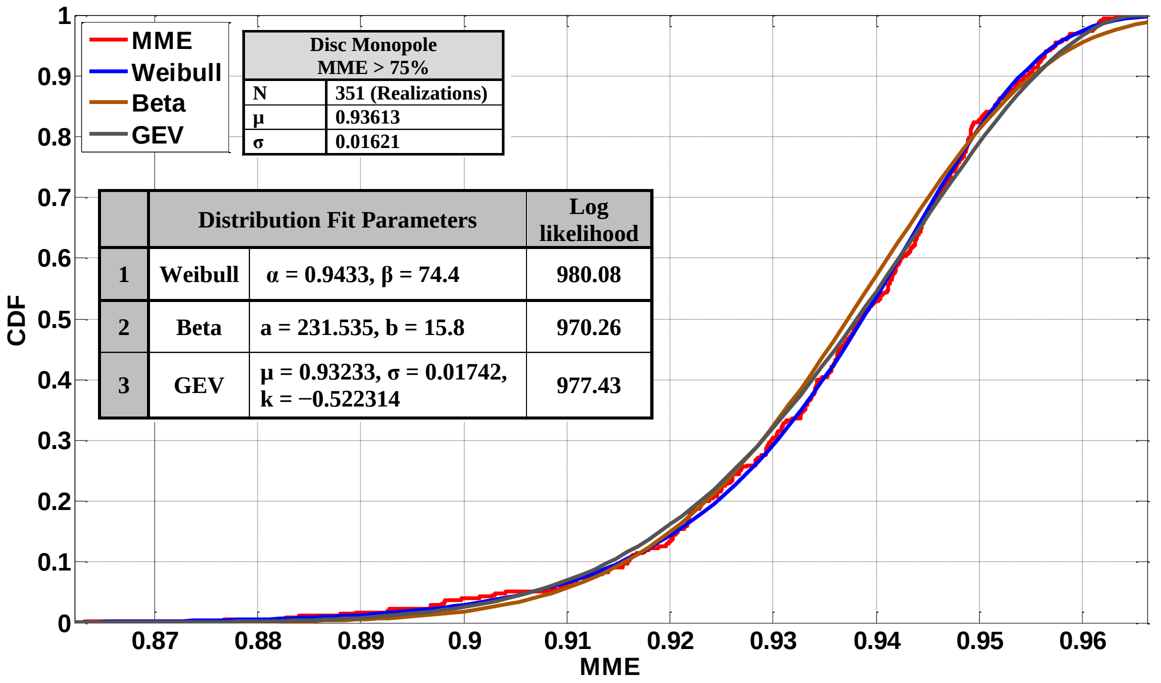

Fig. 4.18 ***MME* Cumulative distribution with possible fit for Disc Monopole Population**

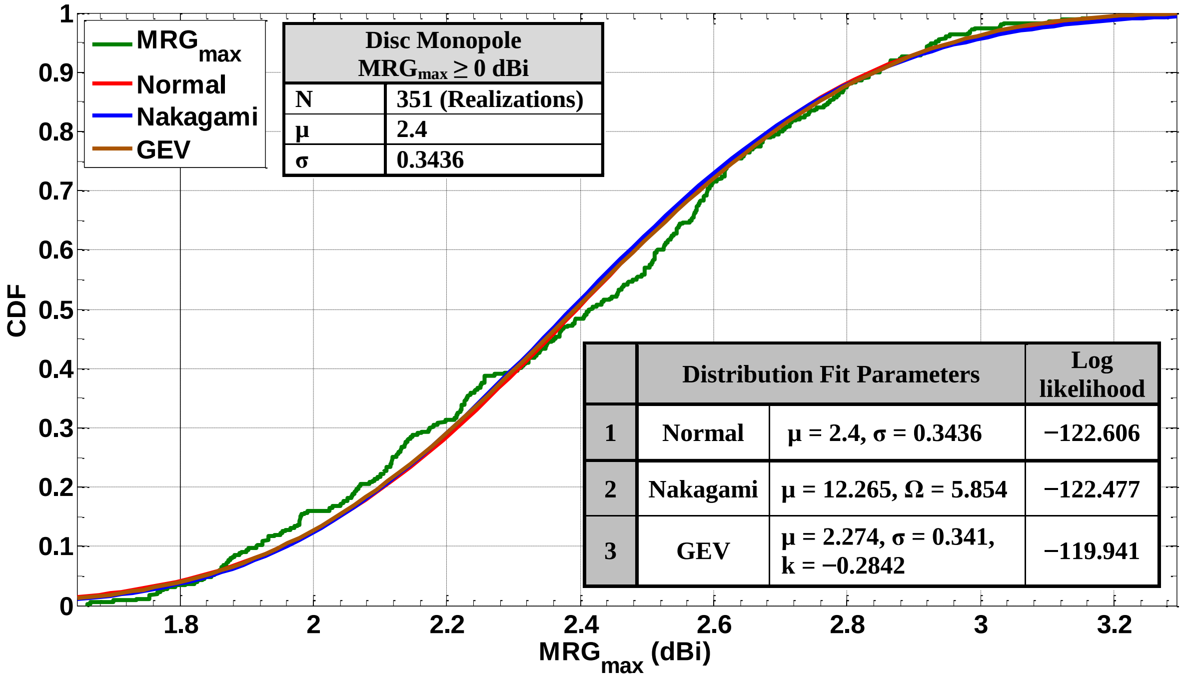

Fig. 4.19 *MRG_{max}* **Cumulative distribution with possible fit for Disc Monopole Population**

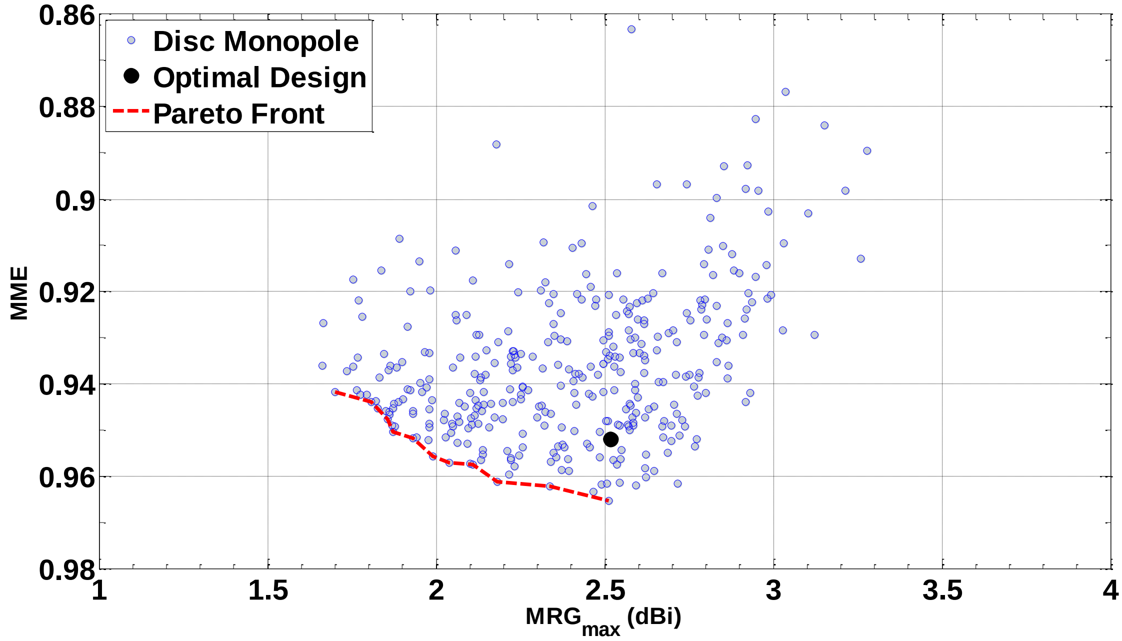

Fig. 4.20 *MME* **vs** *MRG_{max}***, Disc Monopole population**

Table 4.14 Disc monopole, Ranking of fitted distribution on *MME* data according to GOF tests and AIC

	Distribut-ion	Kolmogorov Smirnov		Anderson Darling		**AICc**	
		Stat	Rank	Stat	Rank	Stat	Rank
1	Normal	0.07896	4	4.2103	3	−1894.6	4
2	Weibull	0.02769	1	0.21652	2	−1956.1	1
3	Beta	0.03383	2	0.206	1	−1936.5	3
4	GEV	0.04391	3	16.551	4	−1948.8	2

Table 4.15 Disc Monopole, Ranking of fitted distribution on MRG_{max} data according to GOF tests and AIC

	Distribut-ion	Kolmogorov Smirnov		Anderson Darling		**AICc**	
		Stat	Rank	Stat	Rank	Stat	Rank
1	Normal	0.05813	2	1.3734	2	249.2	3
2	Nakagami	0.06682	3	1.7146	3	249	2
3	GEV	0.05018	1	0.91668	1	246	1

4.4.6. Triangular Planar Balanced Dipole (PBD)

The parameter space was created around the optimal design values, as shown in Table 4. 16. The *MME* empirical data was seen to be confined within a small range [0.89─0.955] (Fig. 4.21), but it presents a behavior which could require a mixture based model; this makes the *MME* data difficult to fit with single distributions. Anyway, the Beta, Weibull and GEV distributions have been selected to fit the data, merely because their log likelihood was better than the other tested distributions. The GEV distribution passed the K-S test at 95 % confidence bounds, but the other distributions were rejected by all three tests. The GEV model is thus considered of interest, at least provisionally.

The investigation of a bimodal distribution has also been performed (Fig. 4.22). As can be seen in the Fig. 4.22, a mixture of two normal distributions having statistical means μ_1 = 0.938 and μ_2 = 0.908 and standard deviations σ_1 = 0.00646 and σ_2 = 0.0072 have been found in agreement with the data, except for a small difference. The difference between the means of the two distributions of the mixture turned out to be more than two standard deviations, therefore it was concluded that the *MME* data exhibited two normal distributions.

Table 4. 16 Parameter Space for Triangular PBD Population Generation

	Parameters	Interval	
		Min.	Max.
1	R_{min}	27	35
2	γ	70	90
3	ψ	72	90
4	w_1	3	4
5	f_{open}	0.9	1.2
6	f_w	1.5	2
7	L_{tf}	8	10

The MRG_{max} distribution has been determined to have a statistical mean of 4.7 dBi. Also, all the 351 antenna realizations verify MRG_{max} > 0 dBi. The visually good models in this case were observed to be the Normal, Gamma and GEV distributions (Fig. 4.23). All of them passed the three GoF tests at 95 % confidence bounds. The ranking, as usual, was based on their test statistics: the GEV distribution has been ranked first, which is reflected by the AIC as well (Table 4.18). However, all these models are very close to each other, so that any of three can be used.

The population scatter plot shows clear evidence of the bimodality in the population (Fig. 4.24), since two separated groups of antenna realizations can be seen (circled in dotted green lines). Overall, the population has an MRG_{max} concentration in the range of 4.4 to 5.1 dBi for *MME* values greater than 93 % (Fig. 4.24).

Table 4.17 Triangular PBD, Ranking of fitted distribution on *MME* data according to GOF tests and AIC

	Distribution	K-S (0.07248)		A-D (2.5018)		**AICc**	
		Stat	Rank	Stat	Rank	Stat	Rank
1	Normal	0.16451	4	14.7	3	−1940.3	4
2	Weibull	0.1015	3	6.335	2	−2018.5	2
3	Beta	0.08131	2	4.3653	1	−1976.5	3
4	GEV	0.07043	1	14.978	4	−2032.7	1

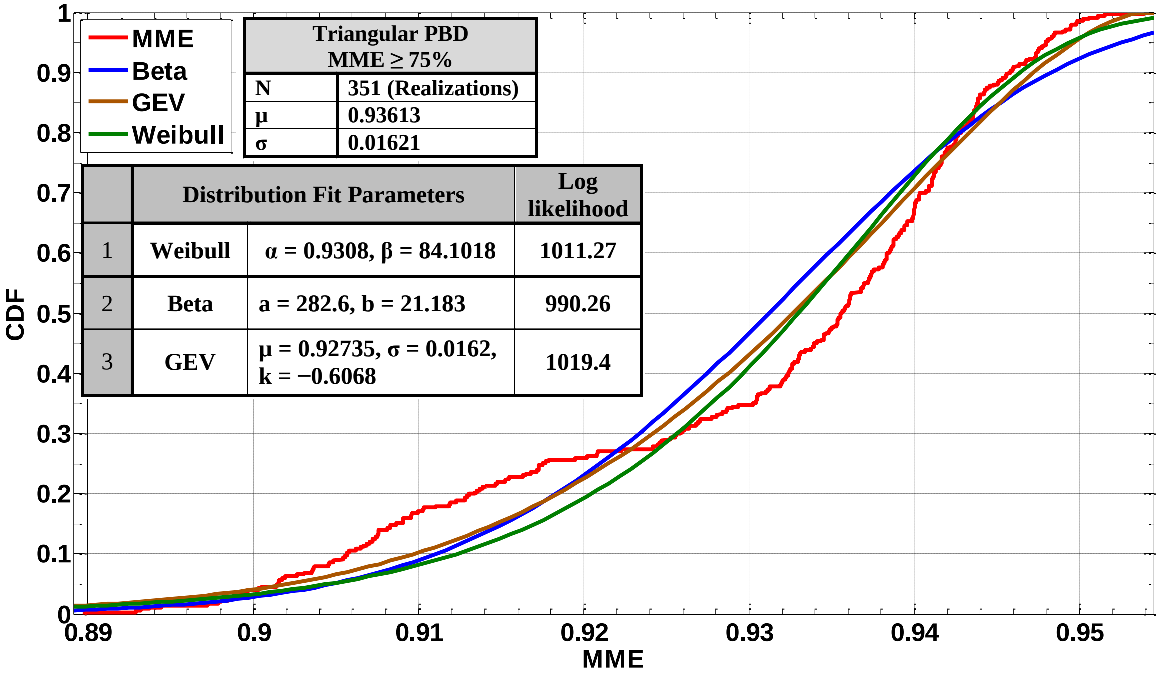

Fig. 4.21 ***MME*** **Cumulative distribution with possible fit for triangular PBD Population**

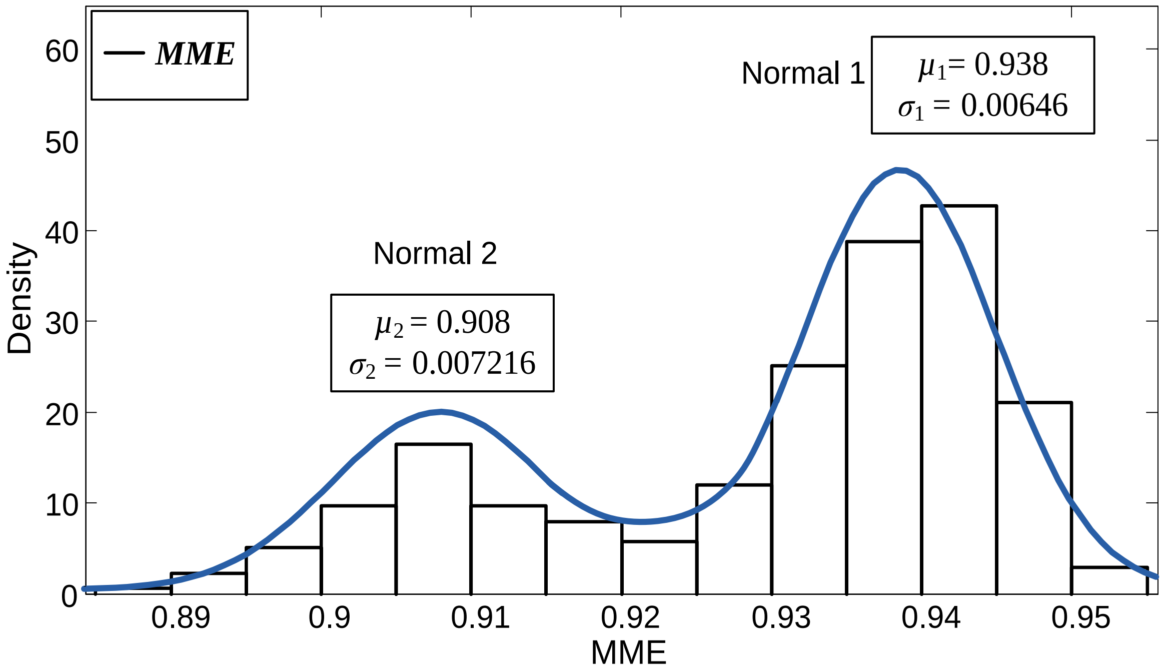

Fig. 4.22 Triangular PBD ***MME*****, Bimodal distribution investigation shows two normal distributions exist.**

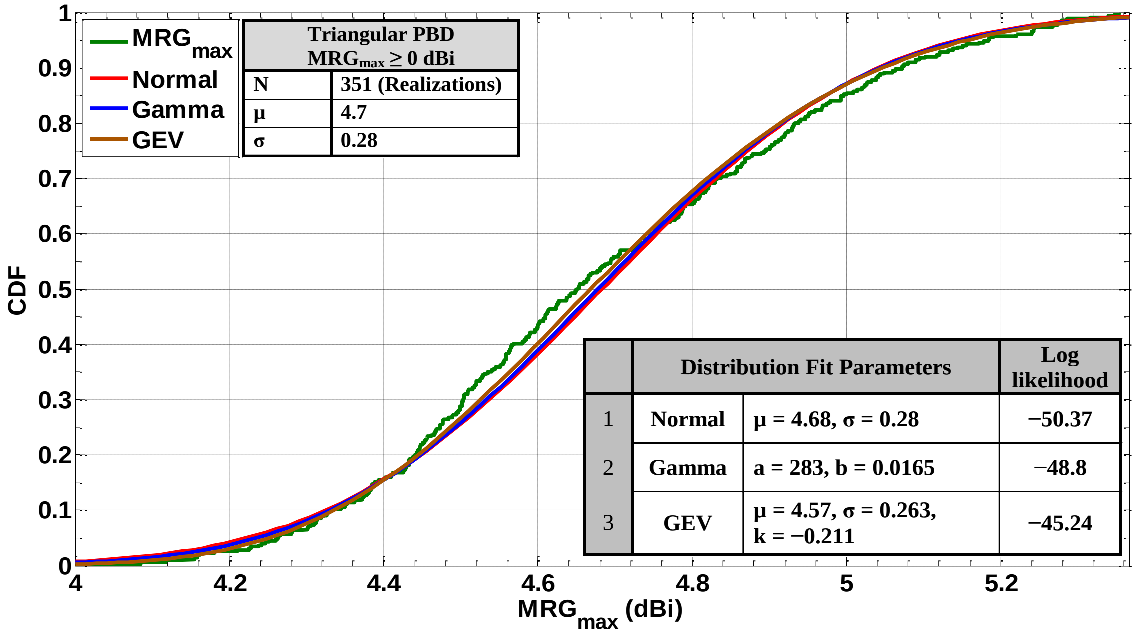

Fig. 4.23 *MRG_{max}* **Cumulative distribution with possible fit for Triangular PBD Population**

Table 4.18 Triangular PBD, Ranking of fitted distribution on *MRG_{max}* data according to GOF tests and AIC

	Distribution	K-S (0.07248)		A-D (2.5018)		**AICc**	
		Stat	Rank	Stat	Rank	Stat	Rank
1	Normal	0.06157	3	1.5758	3	104.77	3
2	Gamma	0.0547	2	1.2301	2	101.63	2
3	GEV	0.0356	1	0.57458	1	96.55	1

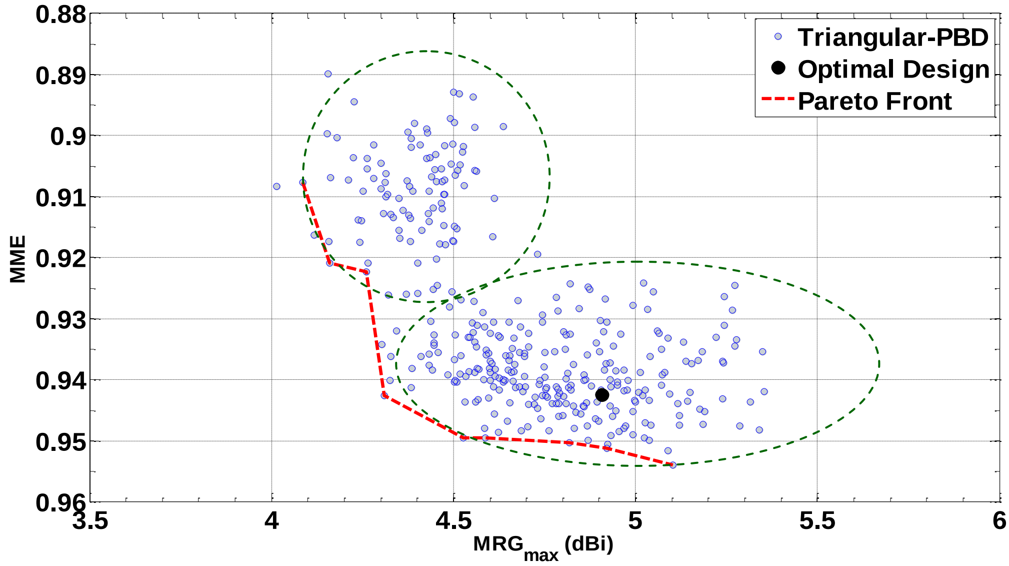

Fig. 4.24 *MME* **vs** *MRG_{max}***, Triangular PBD population**

4.4.7. Disc Planar balanced dipole

The parameter space for population generation has been created around the optimal values, as shown in (Table 4.19). The *MME* empirical distribution turned out to have a mean of 95 % , while all the antenna realizations had more than 90% *MME*.

Table 4.19 Parameter Space for Disc PBD Population Generation

	Parameters	Interval	
		Min.	Max.
1	R_{min}	27	35
2	γ	70	90
3	ψ	170°	176°
4	w_1	4	6
5	f_{open}	0.2	0.3
6	L_{tf}	8	11
7	f_w	3	4
8	r_{yaxis}	$R_{min}/4$	$R_{min}/2$

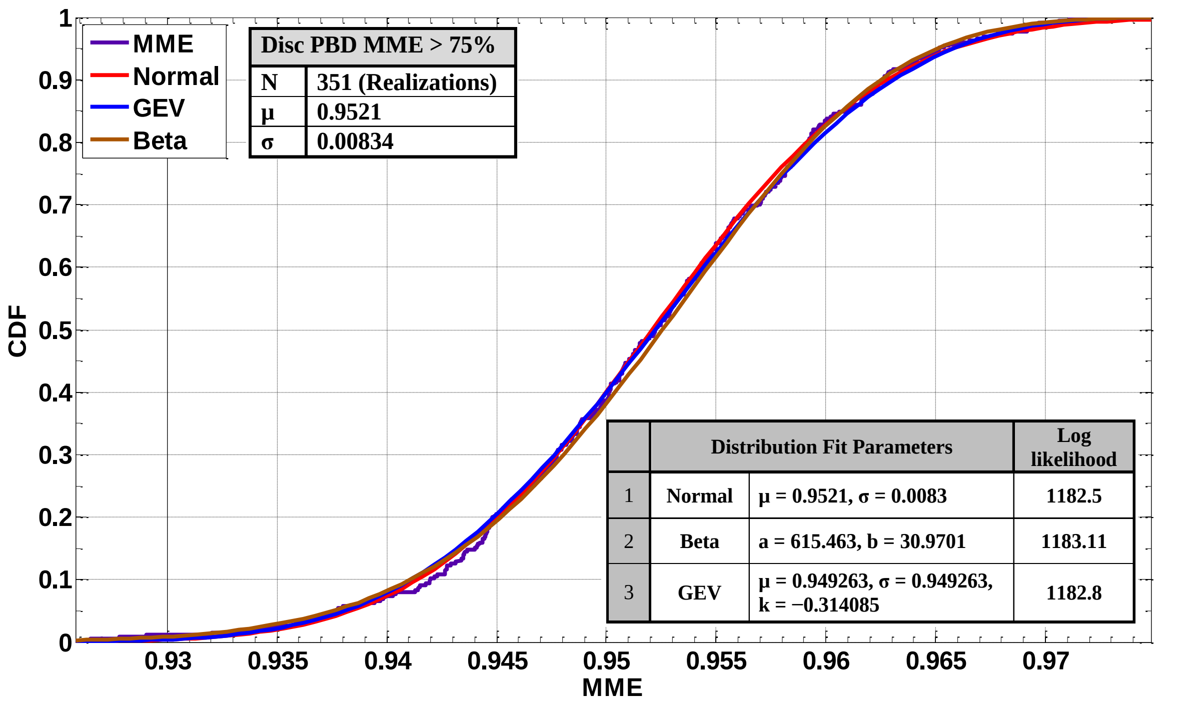

Fig. 4.25 ***MME*** **Cumulative distribution with possible fit for Disc PBD Population**

Table 4.20 Disc PBD, Ranking of fitted distribution on *MME* data according to GOF tests and AIC

	Distribution	K-S (0.07248)		A-D (2.5018)		**AICc**	
		Stat	Rank	Stat	Rank	Stat	Rank
1	Normal	0.02095	1	0.21625	2	−2361	2
2	Beta	0.02221	2	0.18861	1	−2362	1
4	GEV	0.02444	3	0.2396	3	−2359	3

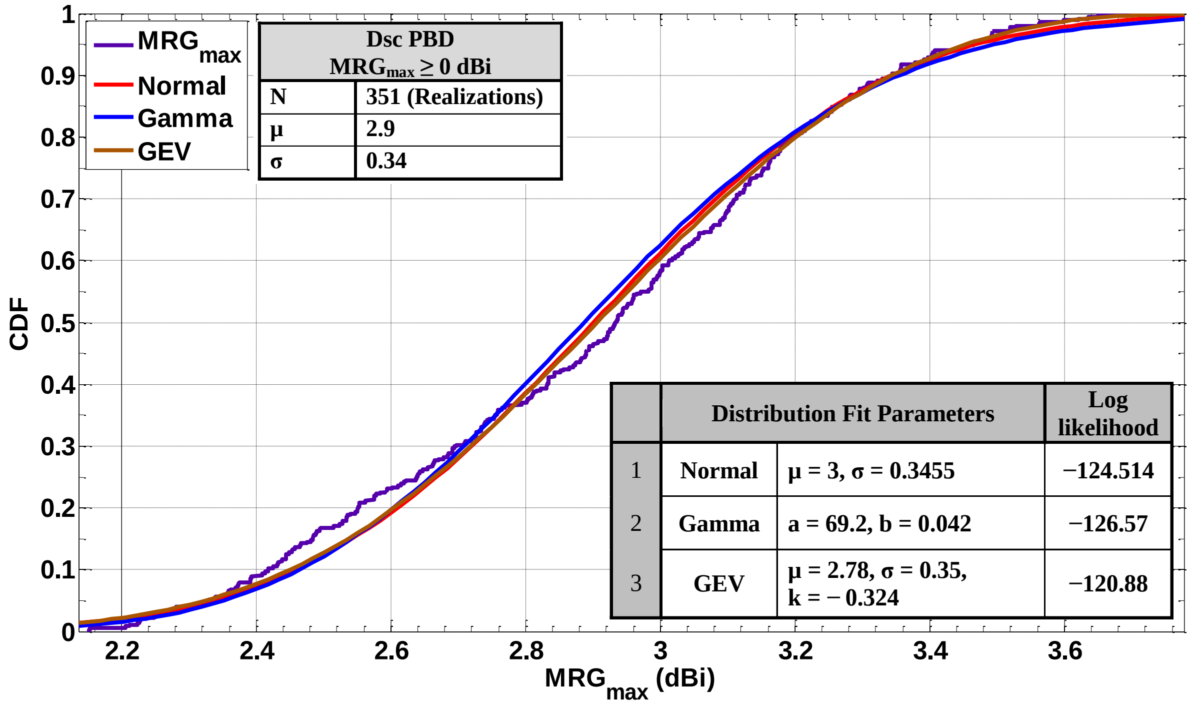

Fig. 4.26 ***MRG_{max}*** **Cumulative distribution with possible fit for Disc PBD Population**

The three distributions, Normal, Beta and GEV distributions have been found to be visually good fits for the *MME* data (Fig. 4.25). All distributions passed the GoF tests at 95% confidence bounds. Ranking of these distributions was not really important, since the test statistics results appear not to be far from each other (Table 4.21). This applies also to the AIC test, from which we conclude that any of the distribution can be used to model the *MME* data.

In the case of MRG_{max}, the population mean is 4.7 dBi and all the antenna realizations provide gains above 2 dBi. Normal, Gamma and GEV distributions have been found to be perceptibly good fits (Fig. 4.26). The two GoF tests passed all these distributions at 95 % confidence bounds. The GEV distribution was ranked first by the three GoF tests and also by the AIC test.

The scatter plot (Fig. 4.26) shows an almost uniform distribution of MRG_{max} data between 2.3 dBi to 3.4 dBi above 94 % *MME*.

Table 4.21 Disc PBD, Ranking of fitted distribution on MRG_{max} data according to GOF tests and AIC

	Distribution	K-S (0.07248)		A-D (2.5018)		**AICc**	
		Stat	Rank	Stat	Rank	Stat	Rank
1	Normal	0.06157	3	1.5758	3	253.06	2
2	Gamma	0.0547	2	1.2301	2	257.17	3
3	GEV	0.0356	1	0.57458	1	247.83	1

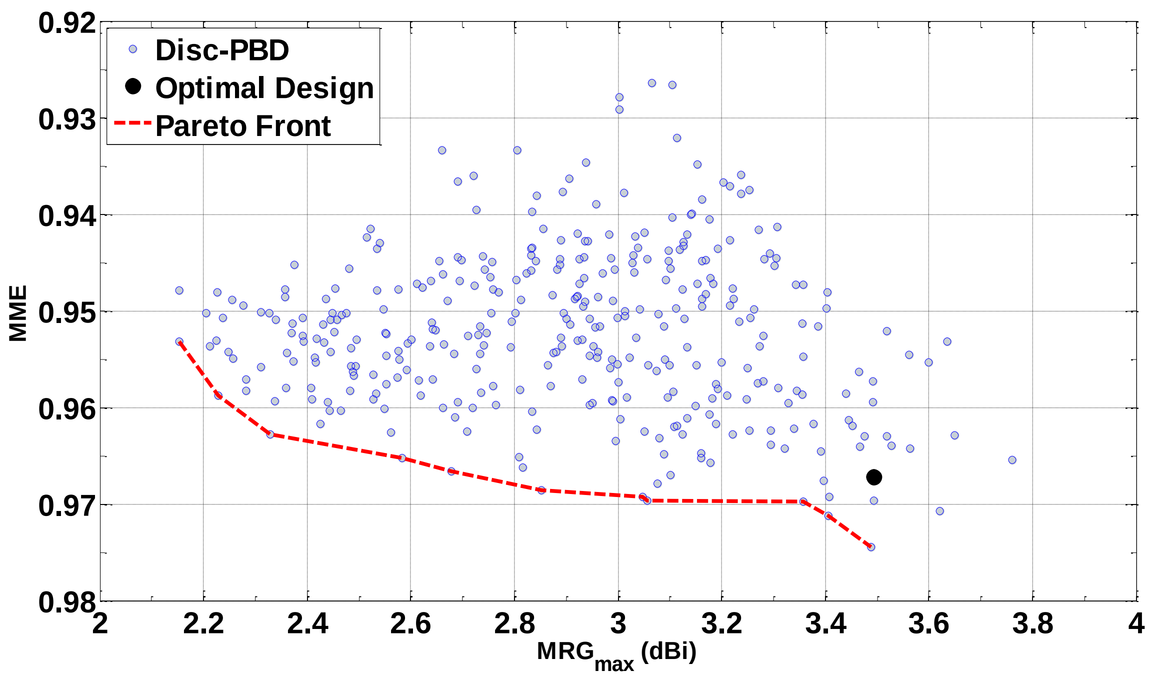

Fig. 4.27 *MME* vs *MRG*$_{max}$, Disc PBD population

4.4.8. Bicone Population

The bicone population has been generated with method 1, i.e. the same parameter space has used as that of optimization process. The parameter space is shown in Table 4.22.

The *MME* empirical distribution has been found to have a statistical mean of 88 %. 262 antenna realizations have above 75% *MME*. Weibull, Beta and GEV distributions have been found to be perceptibly good fits for *MME* (Fig. 4.28). All these distributions passed the two GoF tests at 95 % confidence bounds. The normal distribution has also been added in the test and. As can be seen, the test statistics were see to be close to the critical values of the two GoF tests (Table 4.23). The GEV distribution has been ranked 1st in all tests, including AIC. Therefore, we deduce that the *MME* data can be suitable modeled with the GEV distribution.

Table 4.22 Parameter Space Bicone Population Generation

	Parameters	Interval	
		Min.	Max.
1	R_{min}	12	25
2	γ	45°	150
3	ψ	45°	150°
4	R_{w3}	0.1	1
5	R_{w7}	0.1	1
6	R_{w6}	0.1	1
7	R_{h1}	0.1	1
8	R_{h2}	0.1	1
9	R_{h4}	0.1	1
10	R_{h6}	0.1	1

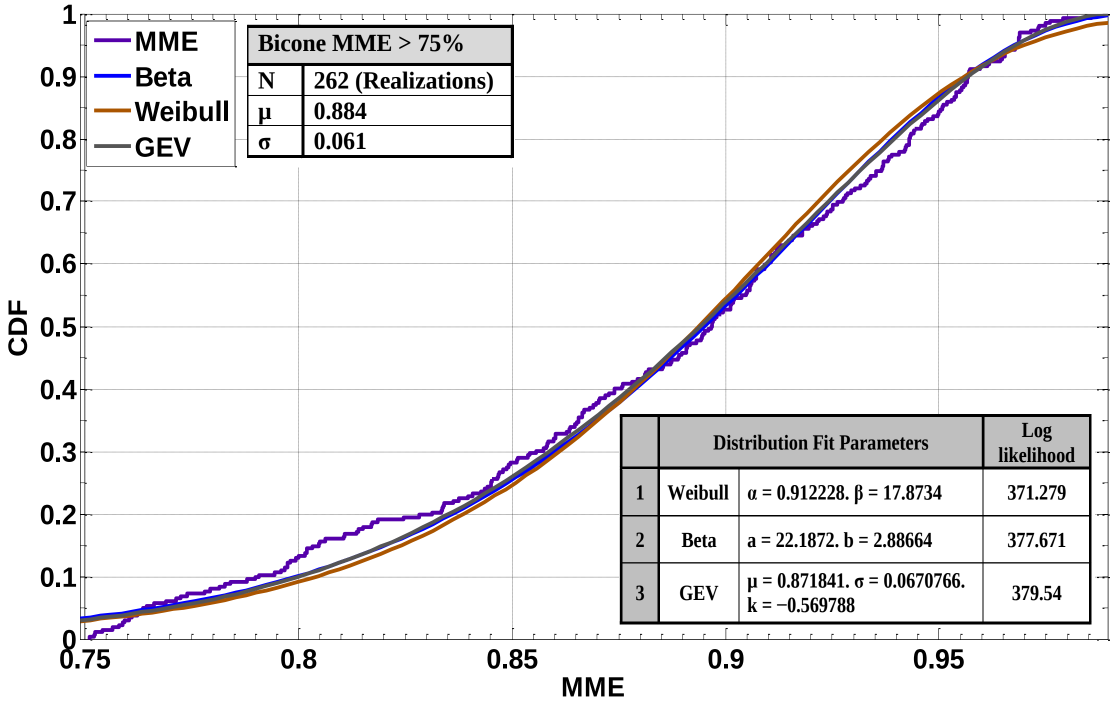

Fig. 4.28 ***MME*** **Cumulative distribution with possible fit for Biconical Antenna Population**

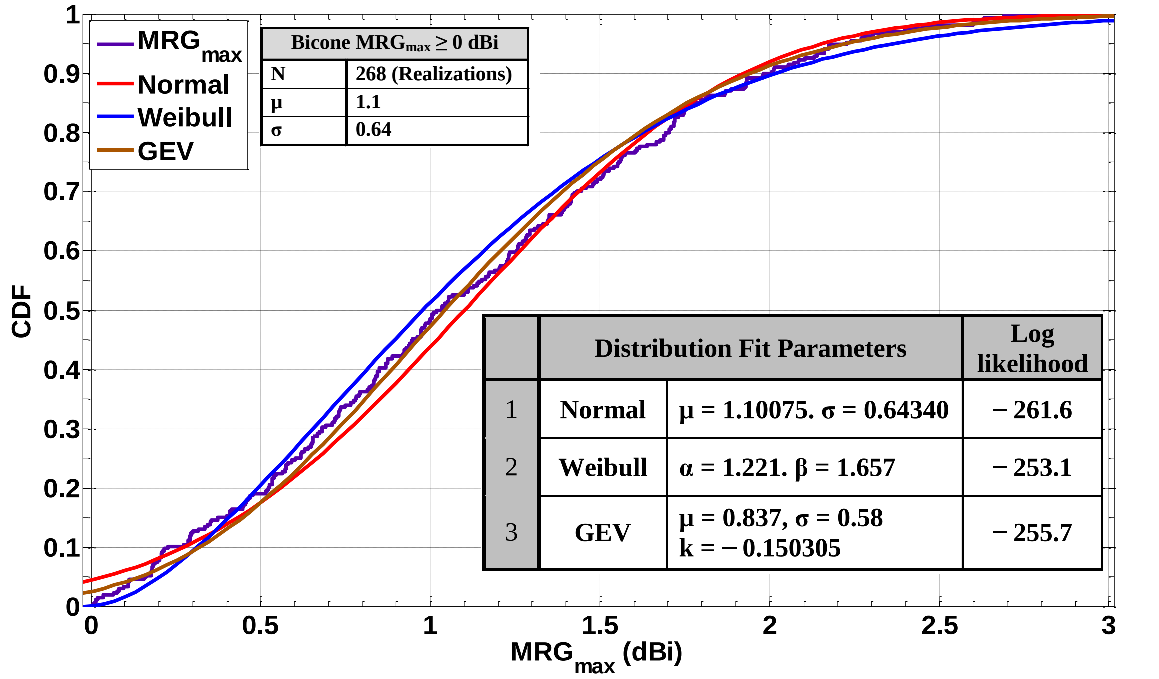

Fig. 4.29 *MRG_{max}* **Cumulative distribution with possible fit for Biconical antenna Population**

Table 4.23 Bicone Antenna, Ranking of fitted distribution on *MME* data according to GOF tests and AIC

	Distribution	K-S (0.0839)		A-D (2,5018)		AICc	
		Stat	Rank	Stat	Rank	Stat	Rank
1	Normal	0.08484	4	3.5873	4	−714.8	4
2	Weibull	0.04876	2	1.3291	2	−738.5	3
3	Beta	0.0628	3	1.4811	3	−751.3	2
4	GEV	0.04381	1	0.79103	1	−753	1

Table 4.24 Bicone Antenna, Ranking of fitted distribution on *MRG_{max}* data according to GOF tests and AIC

	Distribution	K-S (0.08295)		A-D (2.5018)		AICc	
		Stat	Rank	Stat	Rank	Stat	Rank
1	Normal	0,05503	3	1,2874	2	527.25	2
2	Weibull	0,0824	1	3,899	1	510.25	1
3	GEV	0,03078	2	0,56504	3	517.49	3

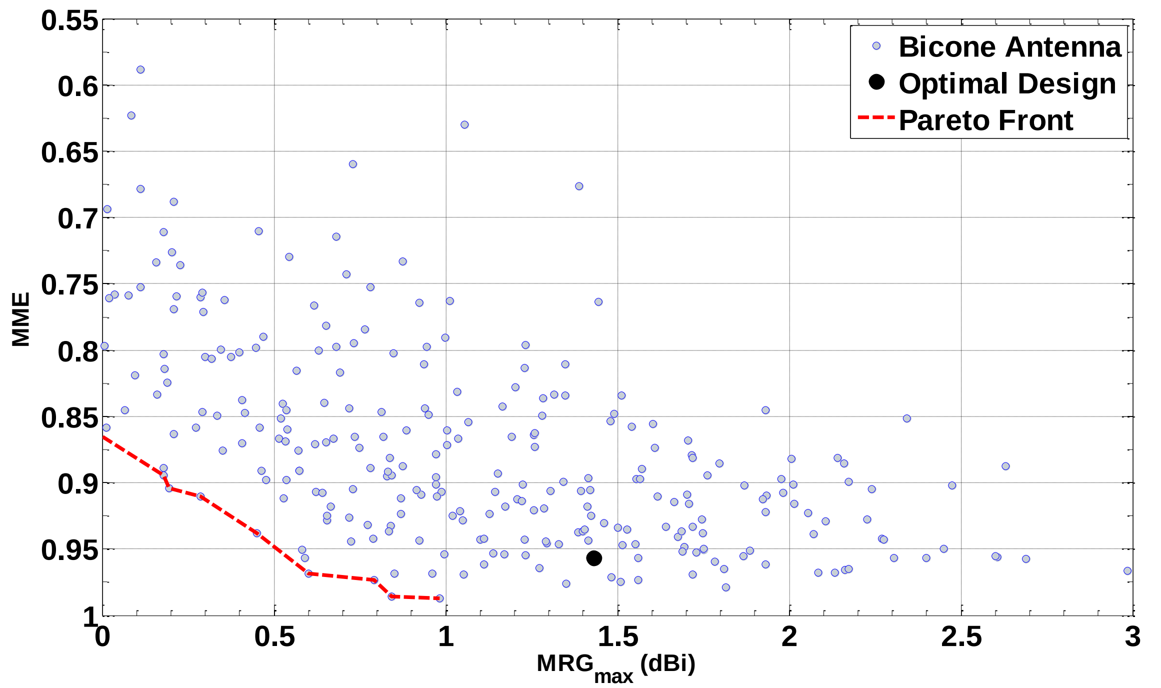

Fig. 4.30 ***MME*** **vs** ***MRG***$_{\mathbf{max}}$ **, Biconical Antenna population**

The MRG_{max} empirical distribution had a population mean of 1.1 dBi and a standard deviation of about 0.64 dBi. The normal, Weibull and GEV distributions are visually good fit in Fig. 4.29. The K-S test has been passed by all three distributions, but the A-D test rejected the null hypothesis for Weibull at 95% confidence bounds. AIC results have ranked Weibull above GEV, owing to the penalty on the number of parameters (Table 4.24). However the difference has not been evaluated to be significant, thus the GEV can be considered useable in order to model MRG_{max} data.

The scatter plot shows little concentration of the design samples towards the Pareto front (Fig. 4.30), In general, the population is dispersed and it is difficult to notice any sample concentration.

4.5. Statistics of Addition Key Performance Parameters

It could be interesting to model some key performance parameters such as presented in chapter 3 (i.e. group delay, delay spread and main beam direction) for an antenna subclass and compared with the initial design i.e. optimal or the *generator*.

In this respect, we have selected the Disc PBD population as its design offers some interesting features such as main beam direction. In the following we present the distributions of key performance parameters of Disc PBD population. In addition, we compare the population mean and standard deviation of the key performance parameters with the initial design. This comparison is extended to two more antenna populations namely Bicone and Dual feed monopole subclasses. The parameters distributions are demonstrated only for Disc PBD subclass.

The distributions of the mean group delay ($\overline{\tau_g}$) — mean over frequency bandwidth of [3—11] GHz — in the direction of MRG_{max} has been shown in Fig. 4.31a. This parameter can be adequately modeled with Normal and GEV distributions, the estimated parameters have also been shown in Fig. 4.31a. The distribution of standard deviation of mean group delay ($\sigma_{\overline{\tau_g}}$) has been shown Fig. 4.31b with GEV and Lognormal fits. Similarly, the mean delay spread ($\overline{\tau_{ds}}\big|_{-3\mathrm{dB}}$) and standard deviation of mean delay spread ($\sigma_{\overline{\tau_{ds}}}\big|_{-3\mathrm{dB}}$) in −3dB beam width have been shown in Fig. 4.31c and Fig. 4.31d respectively, along with possible distribution fits. It is noted that GEV distribution can satisfactorily model all the four above mentioned parameters.

Moreover, we have analyzed the distributions of the main beam direction and widths. The distributions of angle θ_{max} (elevation angle) and angle φ_{max} (azimuth angle) in the direction of MRG_{max}, have been shown in Fig. 4.32a and Fig. 4.32b respectively. The θ_{max} distribution can be adequately modeled with GEV distribution. A significant contribution of θ_{max} = 80° can be noticed (Fig. 4.32a). The φ_{max} has 80% density in φ_{max} = 90° thus it is clear that population has maximum direction of $(\theta,\varphi) = \{80°, 90°\}$.

The variations in −3dB main beam width have been shown with the distribution of $\theta|_{-3\mathrm{dB}}$ and $\varphi|_{-3\mathrm{dB}}$ Fig. 4.32c and Fig. 4.32d respectively. In the case of

$\theta|_{-3dB}$, a bimodal normal distribution has been noticed with means around 75° and 110° whereas, $\varphi|_{-3dB}$ data can be satisfactorily modeled with GEV fit.

The parameters presented in Fig. 4.31 and Fig. 4.32 have been compared with optimal design and summarized in Table 4.25 along with few additional parameters for Disc PBD population. It is noted that population means in each parameter are not significantly different when compared with the optimal design values, except for $\theta|_{-3dB}$ variations where a ~30° difference is noted.

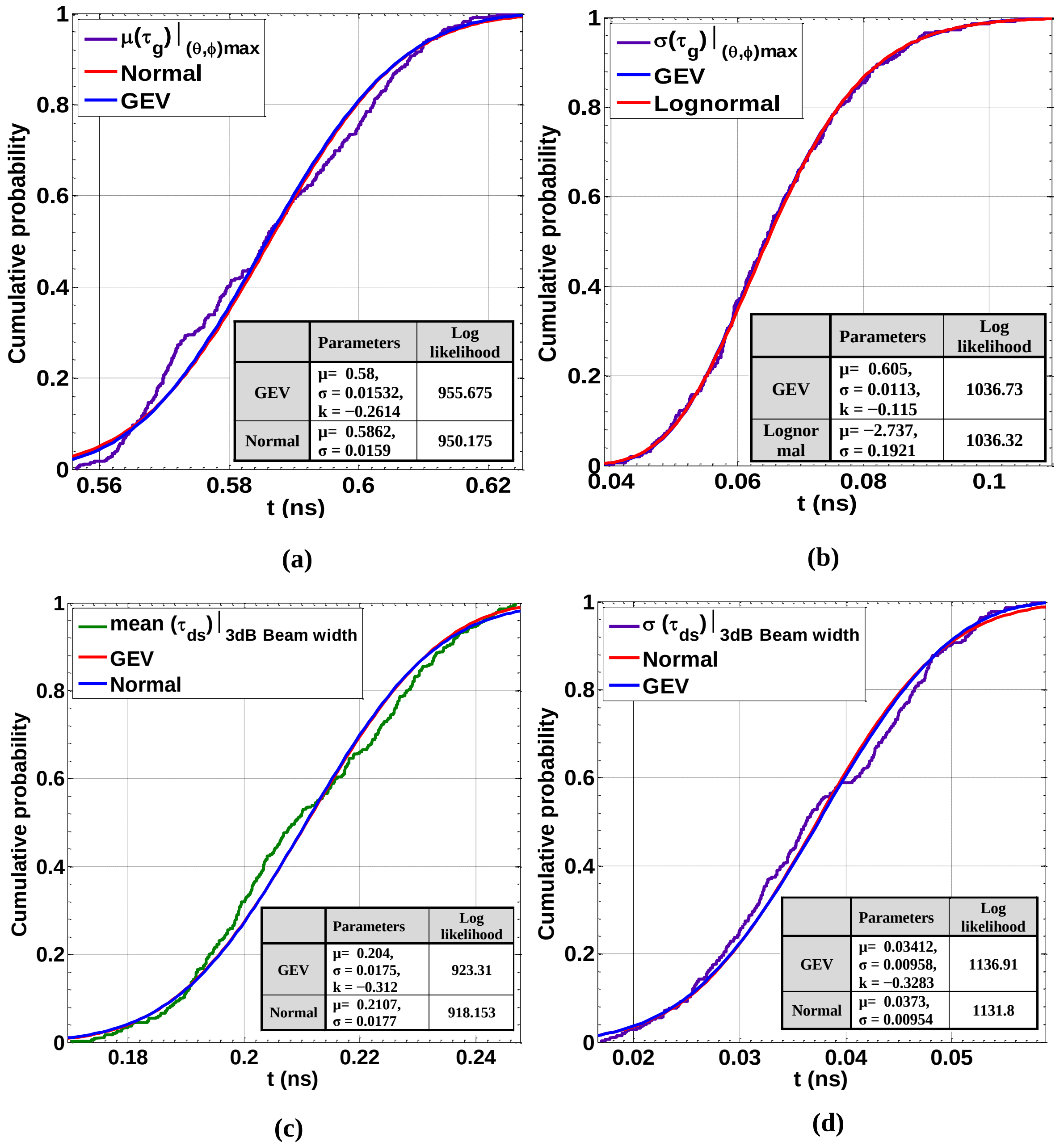

Fig. 4.31 Key performance statistics of the Disc PBD antenna subclass, (a) Mean Group delay in *MRG* direction (b) Standard deviation of Mean Group delay (c) Mean delay spread in −3dB beam width (d) Standard deviation of Mean delay spread in −3dB beam width

The Dual feed monopole population is compared with its optimal design in Table 4.26. Here, as well, the difference is not significant and of particular interest is the parameter, $\varphi|_{-3\text{dB}}$, in this case the difference is significant and it suggests that population has more samples with ~290° −3dB beam width in azimuth.

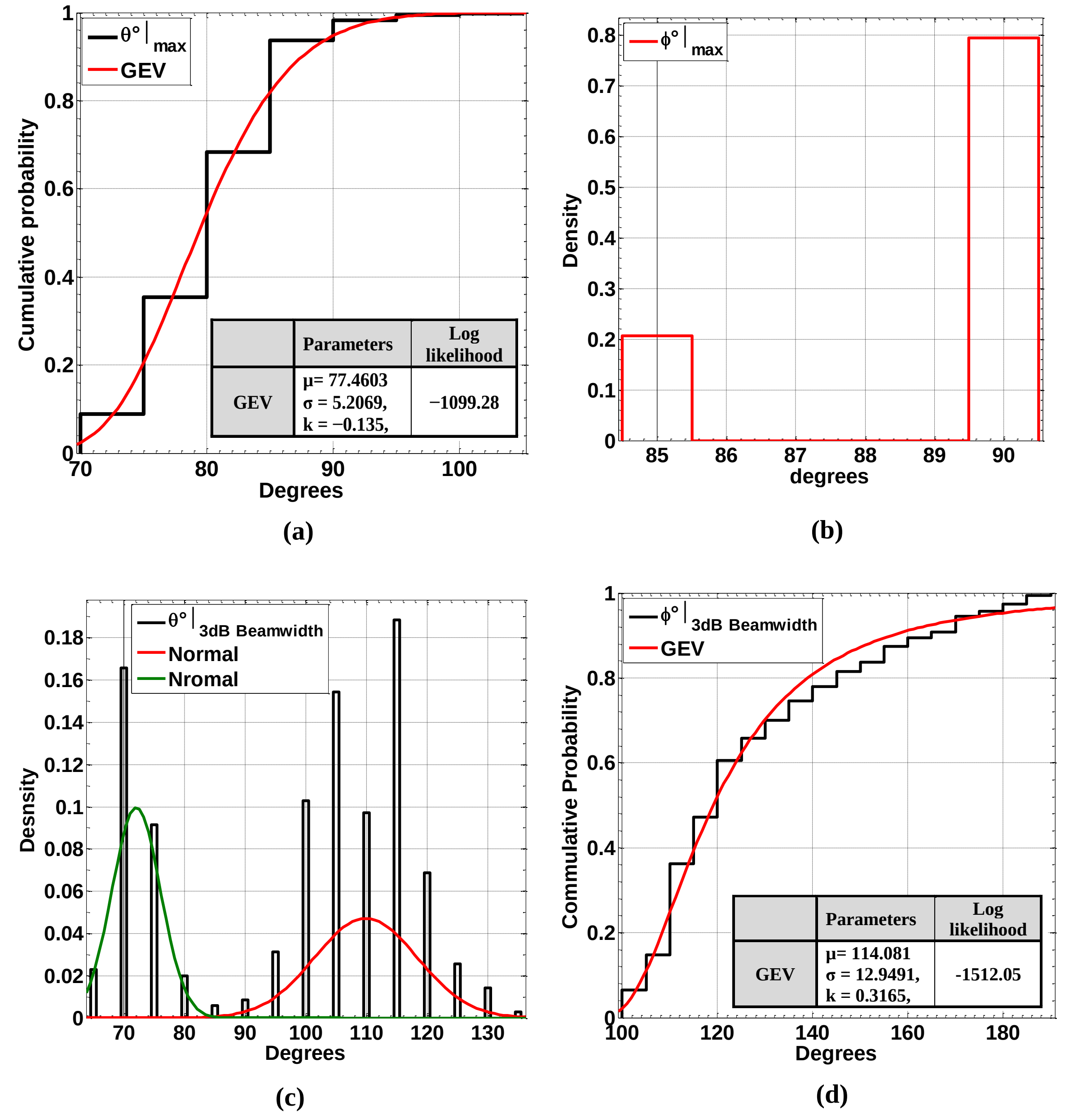

Fig. 4.32 Key performance parameter statistics of Disc PBD population. (a) Distribution of angle θ in direction of MRG_{max}. (b) Distribution of angle φ in direction of MRG_{max}. (c) Distribution of angle θ in −3dB beam width. (d) Distribution of angle φ in −3dB beam width

The Bicone population is compared in Table 4. 27. No significant difference has been noticed in mean group delay, delay spreads and $MRG_{\max}$ direction. In the cases of $\theta|_{-3\text{dB}}$ and $\theta|_{-6\text{dB}}$ the population has relatively large beam width.

Table 4.25 Comparison of Disc PBD population with Optimal Design

		Parameters	Optimal Design	Population μ	Population σ
1	Group delay (ns)	$\bar{\tau}_g$	0.4812	0.5847	0.0338
2		$\sigma_{\bar{\tau}_g}$	0.0567	0.0658	0.0132
3	Delay spread (ns)	$\bar{\tau}_{ds}\big\|_{-3dB}$	0.1703	0.2109	0.0176
4		$\sigma_{\tau_{ds}}\big\|_{-3dB}$	0.0280	0.0373	0.0095
5		$\bar{\tau}_{ds}\big\|_{-6dB}$	0.1955	0.2383	0.0106
6		$\sigma_{\tau_{ds}}\big\|_{-6dB}$	0.0441	0.0540	0.0099
7	MRG_{max} Direction (Degrees)	θ_{max}	70	80	6
8		φ_{max}	85	89	2
9	Main Beam (Degrees)	$\theta\big\|_{-3dB}$	70	98	19
10		$\varphi\big\|_{-3dB}$	120	126	23
11		$\theta\big\|_{-6dB}$	145	154	7
12		$\varphi\big\|_{-6dB}$	180	195	9

Table 4.26 Comparison of Dual Feed monopole population with Optimal Design

		Parameters	Optimal Design	Population μ	Population σ
1	Group delay (ns)	$\bar{\tau}_g$	0.4193	0.4447	0.0222
2		$\sigma_{\bar{\tau}_g}$	0.0608	0.1193	0.0652
3	Delay spread (ns)	$\bar{\tau}_{ds}\big\|_{-3dB}$	0.0813	0.1217	0.0337
4		$\sigma_{\tau_{ds}}\big\|_{-3dB}$	0.0126	0.0229	0.0108
5		$\bar{\tau}_{ds}\big\|_{-6dB}$	0.0865	0.1267	0.0346
6		$\sigma_{\tau_{ds}}\big\|_{-6dB}$	0.0166	0.0278	0.0115
7	MRG_{max} Direction (Degrees)	θ_{max}	60	59	4
8		φ_{max}	180	180	5
9	Main Beam (Degrees)	$\theta\big\|_{-3dB}$	105	95	10
10		$\varphi\big\|_{-3dB}$	360	289	87
11		$\theta\big\|_{-6dB}$	130	124	7
12		$\varphi\big\|_{-6dB}$	360	360	0

Table 4. 27 Comparison of Bicone population with Optimal Design

		Parameters	Optimal Design	Population μ	Population σ
1	Group delay (ns)	$\bar{\tau}_g$	0.4081	0.3994	0.0262
2		$\sigma_{\bar{\tau}_g}$	0.0613	0.0484	0.0246
3	Delay spread (ns)	$\bar{\tau}_{ds}\big\|_{-3dB}$	0.1273	0.1132	0.0238
4		$\sigma_{\tau_{ds}}\big\|_{-3dB}$	0.0148	0.0193	0.0101
5		$\bar{\tau}_{ds}\big\|_{-6dB}$	0.1326	0.1187	0.0280
6		$\sigma_{\tau_{ds}}\big\|_{-6dB}$	0.0164	0.0244	0.0135
7	MRG_{max} Direction (Degrees)	$\theta_{\max}$	100	93	37
8		$\varphi_{\max}$	45	52	35
9	Main Beam (Degrees)	$\theta\big\|_{-3dB}$	100	114	25
10		$\varphi\big\|_{-3dB}$	355	355	0
11		$\theta\big\|_{-6dB}$	130	146	13
12		$\varphi\big\|_{-6dB}$	355	355	0

4.6. Multi-objectivity

In this chapter *MME* and MRG_{max} Pareto fronts have been presented for all the antenna subclasses. It was noticed that the optimal designs were not always at the extreme right of the curve (c.f. Pareto fronts in scatter plots). The reason as mentioned earlier, is the size of the antenna, i.e. related to $R_{min.}$. In the following, we will demonstrate that the optimal design presented in this thesis have achieved the required multi-objective criterion.

Here, we will demonstrate a case of biconical antenna. It is recalled here the multi-objective cost function (c.f. chapter 3 *section 3.4.2*) that incorporate the R_{min} and $\left|\overline{S_{11}}\right|$ average over a bandwidth [3-11] GHz. We have plotted a scatter plot of these two objectives in Fig. 4.33 for all the designs in the population. It can be seen that the optimal design (in red) is at the top left corner of the plot achieving the optimal values of the two objectives.

In case of *MME* data, we need to look at the optimal design with respect to these two objectives as has been demonstrated in Fig. 4.34. It is noted that there are some samples that have the same or better *MME* than the optimal design (in red) (see also Fig. 4.30) but when comparing with respect to two aforementioned objectives the optimal design is ahead of all. This can be observed at the bottom left corner of the cube where R_{min} values are decreasing.

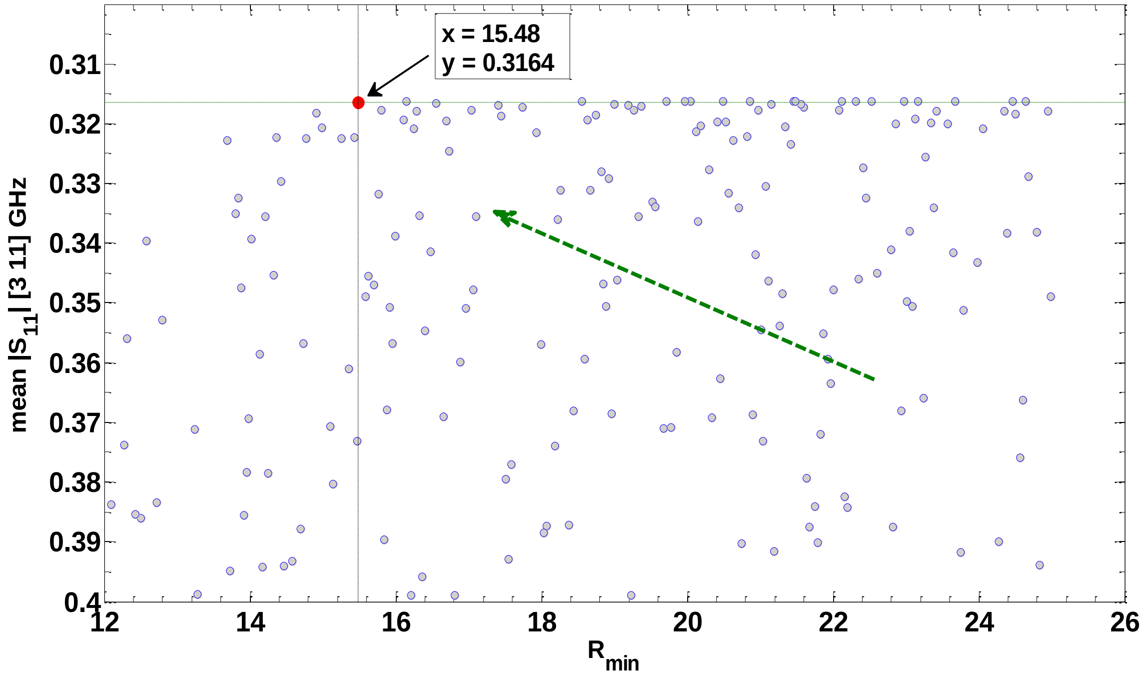

Fig. 4.33 Multi-objectivity of Optimal Bicone Design, the Optimal design is shown in red while green arrow shows the trend towards the optimality.

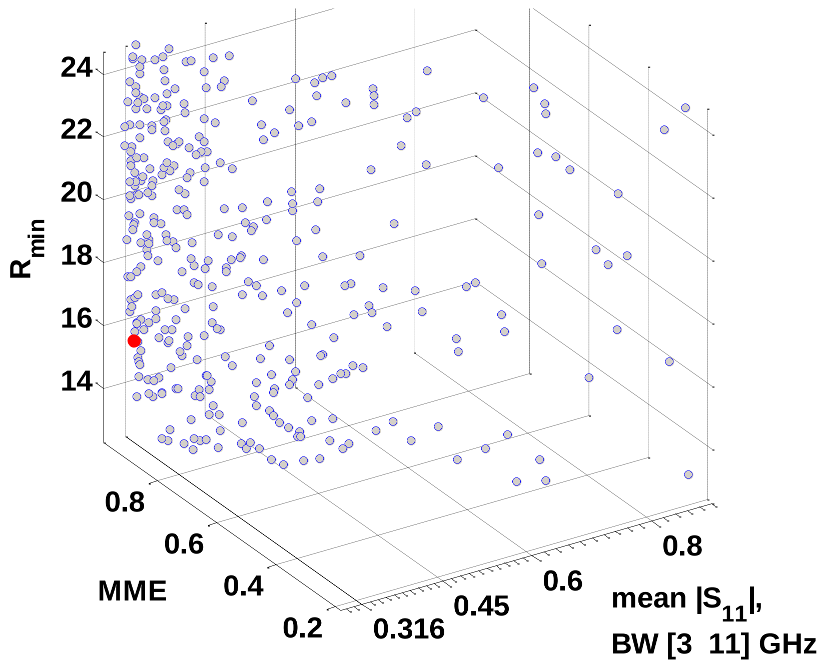

Fig. 4.34 *MME* and Optimal design in the bicone population, the optimal design is shown in red.

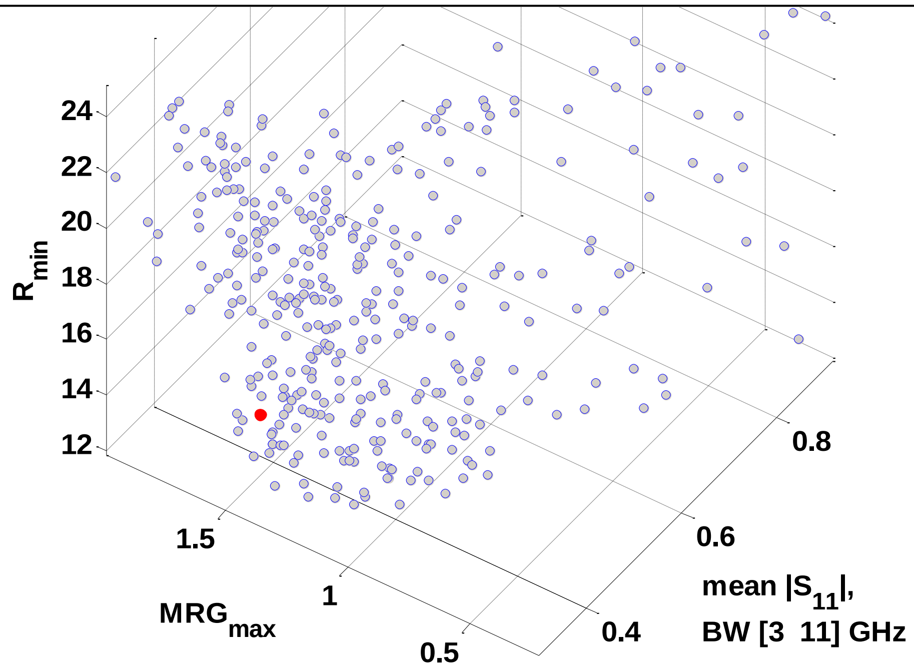

Fig. 4.35 ***MRG_{max}*** **and optimal design in bicone population. The optimal design is shown in red**

In the same way, the optimal design can be shown with MRG_{max} data (Fig. 4.35). Though it is not very evident in the figure but recalling the scatted plot (Fig. 4.33) between R_{min} and $\overline{|S_{11}|}$, we can confidently say that optimal design has lower gain than some of the antenna but the having smallest R_{min} while achieving the $\overline{|S_{11}|}$ goal ($\overline{|S_{11}|} \leq \sim -10$ dB).

In the light of the above discussion, it is clear that the optimal designs presented in the scatter plots in this chapter are the true solution of multi-objective optimization process.

4.7. Conclusion

In this chapter two procedures have been explained for generating statistical antenna populations. In the first method, the parameter space for independent variables did not depend on the optimal design, whereas in the second it was generated with the optimal parameters values found in the optimization process. In each antenna population, the Mean Matching Efficiency (*MME*) and the maximum Mean Realized Gain (MRG_{max}) parameters have observed and each population has been categorized with respect to them.

Two cases are particularly interesting to mention. First, the *MME* distribution of Dual Feed Monopole has been found to be uniformly distributed. A Beta distribution with four parameters has also been tested and found to provide a good fit, but this idea was dropped due to the large number of modeling parameters. Secondly, in the case of the *MME* distribution of Triangular PBD, a mixture of normal distributions has been proposed and it provides a good fit to the obviously bimodal character of the data.

Table 4.28 Summary of fit distribution of *MME* and MRG_{max} Data

Antenna Design	*MME*			MRG_{max}		
	μ	σ	Best fit	μ	σ	Best fit
Triangular Monopole	0.86245	0.05	GEV	2.36	0.87	GEV
Staircase Monopole	0.83976	0.05277	GEV	2.14	0.87	GEV
Crab-claw Monopole	0.8438	0.0444	GEV	2.36	1.02	GEV
Disc Monopole	0.936	0.016	GEV Weibull	2.4	0.343	GEV
Dual Feed Monopole	0.841	0.05678	Uniform	2.3	0.31	GEV
Triangular PBD	0.93	0.015	GEV	4.68	0.28	GEV
Disc PBD	0.952	0.008	GEV	2.9	0.34	GEV
Bicone	0.884	0.0615	Beta, GEV	1.1	1.3	GEV

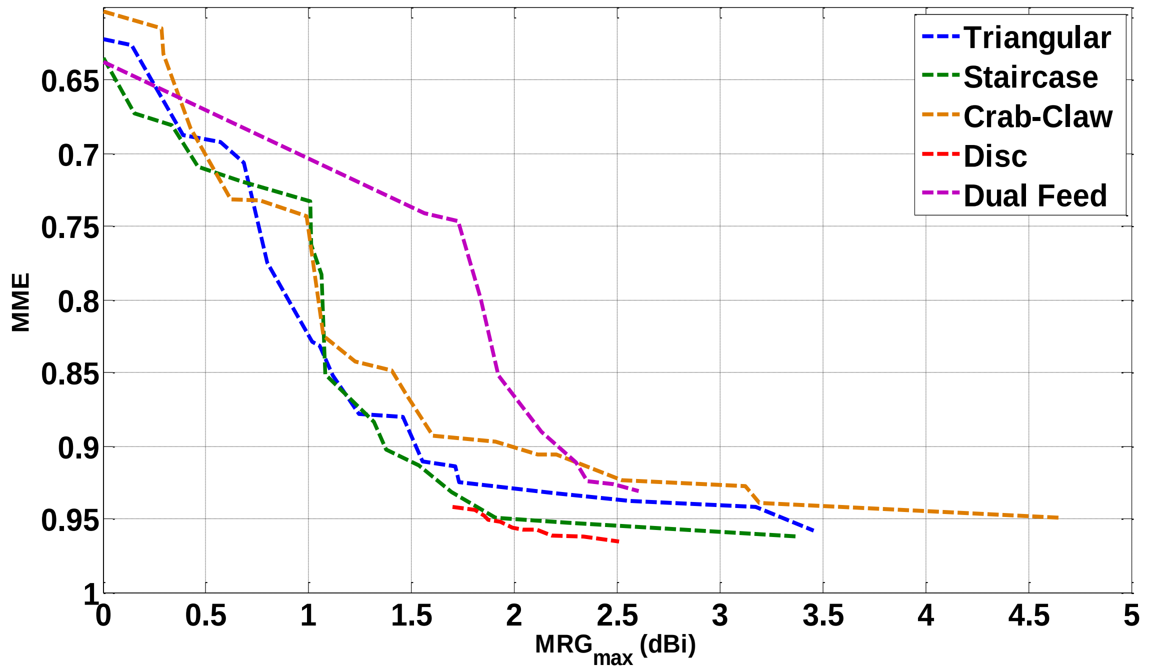

Fig. 4.36 Pareto Front of all the Monopole Antenna

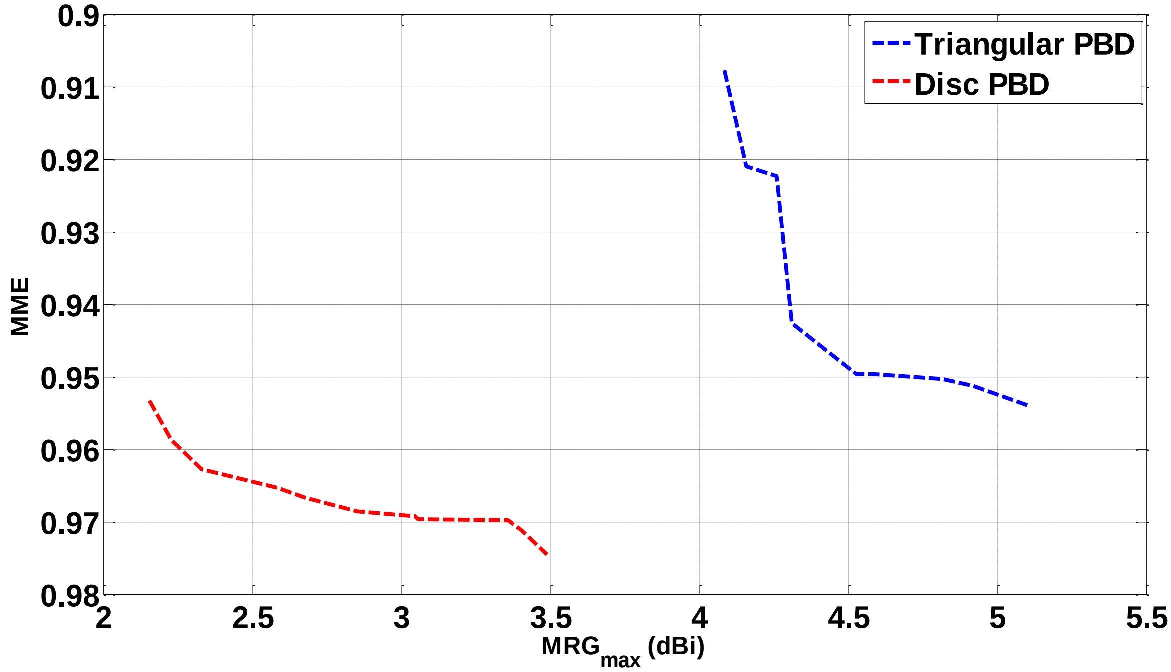

Fig. 4. 37 Pareto fronts of Planar Balanced Dipoles

The scatter plots of *MME* vs MRG_{max} have also been presented for each antenna subclass, in order to analyze the trend of the population. In those plots, the Pareto fronts have been shown, in order to highlight the best possible designs in the population with respect to *MME* and MRG_{max}. Fig. 4.36 shows the comparison of these Pareto fronts of all five monopoles. It can be seen that these crab-claw monopole design provides a wide range of MRG_{max}. The disc monopole design has the tendency of a good matching efficiency, while the dual feed monopole design provides gains above 1.7 dBi in general.

In the case of the planar balance dipole class the difference is very evident that triangular PBDs do not necessarily provide excellent matching, but surely produce high gains.

Chapter 5

Parametric Modeling

5.1. Introduction

The modeling issue can be simplified if the outcomes (system responses) are parameterized with a small number of parameters. As an example, let us consider the modeling of an antenna — i.e. a linear time invariant system (LTI) — whose response (the EM radiation) is a convolution of the Antenna Impulse Response (AIR) and any input pulse (or the excitation pulse). A typical radiation pattern may be sufficiently described by a certain finite number ($N_f \times N_\theta \times N\varphi$) of complex parameters, which depends on the angular variations of the radiated field and may be very large. This number increases even more with the bandwidth, in the case of UWB antennas. As an example, for a typical UWB antenna measurement or simulation, a sampling of 37 elevation and 72 azimuth angles and 100 frequencies, corresponds to a dataset of a total number of parameters $N_f \times N_\theta \times N_\varphi = 266\,400$. This makes the modeling problem on all these data values very complex, if not impossible.

Logically, a promising way to simplify the problem is to reduce the number of parameters. One possible solution is to use antenna parametric modeling, such as the singularity expansion method (SEM) or the spherical mode expansion method (SMEM). Both methods may offer a large reduction in the number of parameters (model orders), at the price of modeling errors.

The objective here is to extract models able to suitably render the main radiation characteristics – i.e. not necessarily perfectly accurate over the whole band – but with extremely high “compression rates”, i.e. very strongly reduced model orders.

Further reduction in model order can be achieved by using the advantage of symmetries or pseudo-symmetries of the object under study, which in practice are often present. These structural symmetries induce symmetries or anti-symmetries in the radiated field, which reduces the number of parameters required for the representation. Eventually, the statistical approach is expected to bring the “ultimate” order reduction for an entire subclass.

Based on these considerations, this chapter aims at explaining the procedure of modeling antenna radiation patterns exploiting the technique called "ultra compressed parametric modeling". As a preliminary to the explanation of this procedure, the SEM and SMEM techniques are first briefly described. Then the principle of ultra data compression, which is the combination of the aforementioned techniques, is explained.

5.2. The Procedure:

The procedure is as follows:

- The antenna transfer function (ATF)[2] $\mathcal{H}(f,\hat{\mathbf{r}})$ is computed in the Frequency Domain (FD), either from measurements or from EM simulations.
- The Antenna Impulse Response (AIR)[3] $\mathcal{h}(t,\hat{\mathbf{r}})$ is computed from the ATF by inverse Fourier Transform (IFFT) with subsequent pre-processing (DC padding, windowing, etc)
- The SEM is applied to the AIR in order to extract the first P dominant poles $\{s_p\}_{p=1,\dots,P}$ and the residues $\{\mathbf{R}_p(\hat{\mathbf{r}})\}_{p=1,\dots,P}$ through the Generalized Matrix-Pencil (GMP) algorithm.

[2] See chapter 3 for details
[3] See chapter 3

- The modal residues $\left\{\mathbf{R}_{nmp}^{TE,TM}\right\}_{n=1,\ldots,N,\,m=-n,\ldots,n,\,p=1,\ldots,P}$ are computed with the SMEM of the preceding residues, and depending on the desired accuracy, a truncation to order N is operated.

- The modeled ATF is reconstructed following the inverse procedure and the Total Mean Squared Error (TMSE) is examined.

This algorithm is depicted in (Fig. 5.1a). An alternative procedure is also shown (Fig. 5.1b), where the SMEM is performed before the SEM. It can be shown that the results are the same whatever the order, since both techniques are linear.

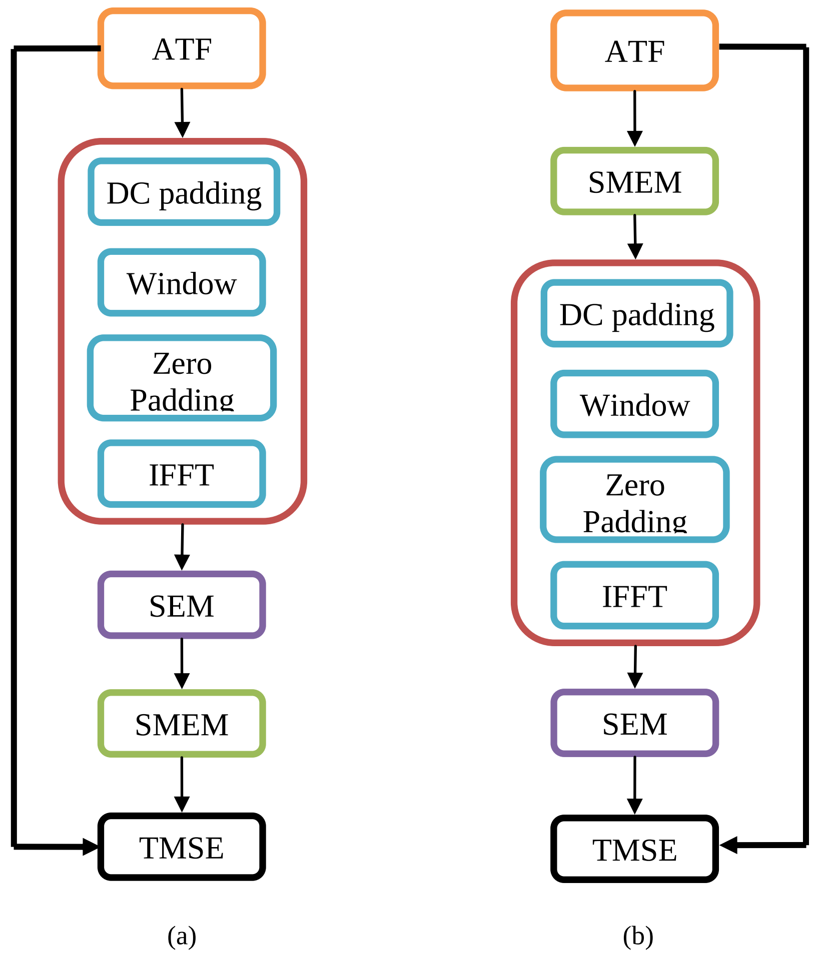

Fig. 5.1 Procedure adopted for ultra compressed modeling

5.3. Singularity Expansion Method (SEM)

The singularity expansion method is used to characterize the electromagnetic response — i.e. the diffraction and/or radiation — of structures (e.g., aircraft, antennas) in both the time and complex frequency domains. The SEM was first introduced by C. E. Baum and was inspired by typical transient responses of various complicated scatterers [91], [92]. The measured transient responses were usually a few cycles of damped sinusoids. One of the main applications of this method is the recognition of targets in the case of impulse radars. It is based on the expansion of the transient response on a set of damped sinusoids, whose counterpart in the Laplace domain is a rational function, specially characterized by its poles. These poles are the natural frequencies of the considered object i.e. frequencies for which the object can have a response in the excitation free regime. The poles can be either real or can appear as complex-conjugate pairs. It is important to stress that these poles are characteristic of the considered object, irrespective of the direction of observation. Moreover, it has been shown that for certain categories of objects, which are finite-size objects in free space and made up of passive materials (conductors and/or other media), the poles are the only singularities in the finite complex plane [93].

The SEM can be applied to a vast number of problems, from quantities bounded to the conductors (i.e. charge and currents densities) to diffracted fields (re-radiated in the case of scatterers and radiated in the case of antennas). In the literature, the method is mainly applied to diffracted fields but it has also been shown to be applicable to antenna radiation by C.E. Baum theoretically [91] and in practice [94].

The radiated field can be expanded over a series of rational fractions defined by their poles and residues [74]:

$$\mathbf{E}(s,\mathbf{r}) = w(s)\sum_{p}\frac{\mathbf{R}_p(\mathbf{r})}{s-s_p} + W(s,\mathbf{r}) \text{ ---(5.1)}$$

where w is a function representing the waveform directly related to the source (incident partial wave a_1). This expression is restricted to the most common cases, for which the poles are simple. In addition, the latter are independent of the direction of observation. Lastly, W is an entire function of s (containing none of the poles of the expansion in the finite s plane), which is generally not required for finite size conducting objects [91], as is the case for antennas in practice. Equation (5.1) is applicable to the near field as well as to the far field, but since the ATF is defined for the antenna's far field, we are interested by the latter. By linearity, the ATF can be written as [74]:

$$\mathcal{H}\left(s,\hat{\mathbf{r}}\right)=\sum_{p}\frac{\mathbf{R}_{p}\left(\hat{\mathbf{r}}\right)}{s-s_{p}} \tag{5.2}$$

The form of the residues is not unique (only the sum must be). However, it was shown that for perfectly conducting finite-sized bodies, a very simple entire function, representing a pure delay (e^{-st_0}) could be factored out, giving the simplified form:

$$\mathcal{H}\left(s,\hat{\mathbf{r}}\right)=e^{-st_0(\hat{\mathbf{r}})}\sum_{p}\frac{\mathbf{R}_{p}\left(\hat{\mathbf{r}}\right)}{s-s_{p}} \tag{5.3}$$

This is the expression in which the residues $\mathbf{R}_{\mathrm{p}}$ depend only on the direction of observation $\hat{\mathbf{r}}=\left(\theta,\varphi\right)$ and on the polarization, and are thus independent of the complex frequency. The expression of the AIR is deduced from (5.3) as:

$$\hbar\left(t,\hat{\mathbf{r}}\right)=\sum_{p}\mathbf{R}_{p}\left(\hat{\mathbf{r}}\right)e^{-s_p\left[t-t_0(\hat{\mathbf{r}})\right]} \tag{5.4}$$

In practice, the preceding sums are truncated in order to be able to process them numerically. Moreover, for real antennas, which are by nature band-limited, the number of poles is finite. In fact, including ideal antennas, the responses can be accurately represented by a limited number of dominant poles. Hence, equations (5.3) and (5.4) can be written as:

$$\mathcal{H}\left(s,\hat{\mathbf{r}}\right)=e^{-st_0(\hat{\mathbf{r}})}\sum_{p=1}^{P}\frac{\mathbf{R}_{p}\left(\hat{\mathbf{r}}\right)}{s-s_{p}} \tag{5.5}$$

$$\hbar\left(t,\hat{\mathbf{r}}\right)=\sum_{p=1}^{P}\mathbf{R}_{p}\left(\hat{\mathbf{r}}\right)e^{-s_p\left[t-t_0(\hat{\mathbf{r}})\right]} \tag{5.6}$$

The poles are sorted out in sums by ascending order of the resonance frequencies.

5.3.1. SEM algorithm

Many techniques have been proposed over the last few decades, ranging from polynomial methods based on Prony's method [98][99][100] to identification methods such as ARMA models [101][102]. These methods are satisfactory for high SNR, but are often prone to unacceptable inaccuracy in the presence of noise, i.e. at moderate SNR. The total least squares method has also been applied directly in the frequency domain. Unfortunately, it is also very sensitive to noise, particularly because of ill conditioning, and leads to erroneous results in practice. More sophisticated methods, based on the singular value decomposition (SVD) that performs a projection of the data on the signal subspace, are more promising [103]. In [104] and [105] the identification of the transfer function is directly carried out in the frequency domain. In practice, most often the frequency response is extracted from transmission measurements or from electromagnetic simulations. It is thus an interesting option since it avoids the calculation of an inverse Fourier transform.

An interesting alternative method is the "matrix-pencil" (MP) algorithm, which is applied in the time domain and therefore on the AIR. It is also known to be significantly more robust to noise than the conventional polynomial methods of identification. Moreover, the MP approach is a one-step process. The poles z_i, are found as the solution of a generalized eigenvalue problem. Hence, there is no practical limitation on the number of poles, (say P), which can be obtained by this method. In contrast, for a polynomial method it is difficult to find roots of a polynomial for, say, $P > 50$. The MP approach is also shown to be more computationally efficient than the “polynomial” methods [96].

In the following, a brief explanation of the MP method is provided.

5.3.1.1. Matrix-Pencil method

The matrix-pencil method was introduced by Sarkar and others [95], [96], [97]. They defined the noise affected data as:

$$y(t_k) = \sum_{p=1}^{P} R_p e^{s_p k \Delta t} \quad \text{---(5.7)}$$

where $k \in [0, N_{SEM}]$ (N_{SEM} is the number of data samples), $\boldsymbol{R}_p$ are the complex residues, s_p are the complex poles, and Δt is the sampling time. It is important to note that $z_p = e^{s_p \Delta t}$ are the poles on the z-plane.

It is possible to create a data matrix $[Y]$ for the N_{SEM} elements in terms of an (L + 1) × (L + 1) matrix where $L = N_{SEM}/2$:

$$[Y] = \begin{bmatrix} y(0) & y(1) & \cdots & y(L) \\ y(1) & y(2) & \cdots & y(L+1) \\ \vdots & \vdots & \vdots & \vdots \\ y(L) & y(L+1) & \cdots & y(2L) \end{bmatrix}_{(L+1)\times(L+1)} \quad \text{--(5.8)}$$

The singular value decomposition (SVD) of the matrix $[Y]$ can be written as:

$$[Y]=[U][\Sigma][V] \text{------------------------------------(5.9)}$$

A significant parameter, P, is chosen such that the singular values in Σ beyond P are small and can be approximated as zero. The value of *P* is typically selected by examining the ratio between the maximum singular value and all other singular values in the matrix:

$$\frac{\sigma_P}{\sigma_{\max}} \approx 10^{-n} \text{------------------------------------(5.10)}$$

where n is the number of significant decimal digits in the data.

Next, a reduced matrix $[V']$ is constructed by using only the rows corresponding to the P dominant singular values:

$$[V']=\begin{bmatrix} v_1 \\ v_2 \\ \vdots \\ v_P \end{bmatrix} \text{------------------------------------(5.11)}$$

The singular vectors that correspond to small singular values are discarded. Sub-matrices $[V_1]$ and $[V_2]$ are defined from $[V]$ by deleting the first and last column of $[V']$, respectively.

The problem then reduces to solving a left-hand eigenvalue problem given by:

$$v[V_2]=zv[V_1] \Rightarrow v[V_2][V_1]^H = zv[V_1][V_1]^H \text{------------------------(5.12)}$$

where symbol H refers to the Hermitian transpose. The eigenvalues *z* corresponds to the poles of the system in the *z*-plane. Once the reduction to P has been performed and the corresponding poles are obtained, the residues $\boldsymbol{R}_i$ are found as the least squares solution to:

$$\begin{bmatrix} y(0) \\ y(1) \\ \vdots \\ y(N_{SEM}-1) \end{bmatrix} = \begin{bmatrix} 1 & 1 & \cdots & 1 \\ z_1 & z_2 & \cdots & z_P \\ \vdots & \vdots & \vdots & \vdots \\ z_1^{N_{SEM}-1} & z_2^{N_{SEM}-1} & \cdots & z_P^{N_{SEM}-1} \end{bmatrix} \begin{bmatrix} R_1 \\ R_2 \\ \vdots \\ R_P \end{bmatrix} \text{----------------(5.13)}$$

Improvements are possible by deleting poles with low residue values and re-computing the residues using the retained poles.

5.3.2. Example

We here take an example of triangular monopole antenna, for which the AIR is calculated after applying a Blackman windowing without zero padding. The SEM on this response is applied with poles P = 16. The reconstructed impulse response resembles the original especially in the main peak. For GMP algorithm the data samples are taken to be N_{SEM} =100.

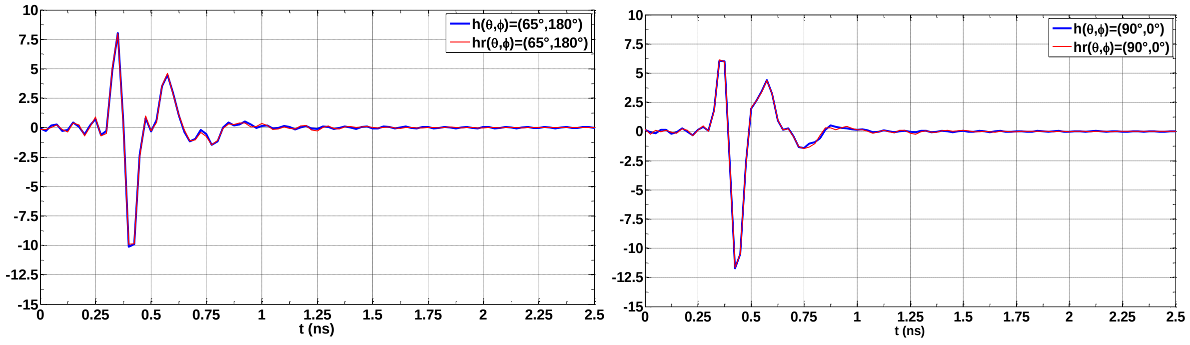

Fig. 5.2 Re-construction of impulse response *hr(t)* after the application of SEM with P=16 and N_{SEM} =100

5.4. Spherical mode expansion method (SMEM)

The expansion of the EM field onto a complete basis of spherical waves may take different forms. The most natural and simple, driving to the true spherical modal coefficients is based on the transverse magnetic (TM) and transverse electrical (TE) (with respect to radial vector **r**) modal expansion. In any coordinate system, the modal expansion principle is based on the solving of a scalar Helmholtz equation by separation of the variables (r,θ,φ) for each mode.

In spherical coordinates, for TM and TE modes, the magnetic and electric scalar potentials are respectively $\psi^a = A_r/r$ and $\psi^f = F_r/r$, **A** and **F** being respectively the magnetic and electric vector potentials. In this case, the field is given by [84]:

$$\mathbf{E} = -\nabla\times\mathbf{r}\psi^f + \frac{1}{j\omega\varepsilon}\nabla\times\nabla\times\mathbf{r}\psi^a \tag{5.14}$$

$$\mathbf{H} = -\nabla\times\mathbf{r}\psi^a + \frac{1}{j\omega\mu}\nabla\times\nabla\times\mathbf{r}\psi^f \tag{5.15}$$

The scalar potentials for each outward traveling mode taking the form:

$$\psi_{nm}^{a,f} = h_n^{(2)}(kr)Y_{nm}(\theta,\varphi) \tag{5.16}$$

where $h_n^{(2)}(kr)$ are the spherical Hankel functions of the second kind, Y_{nm} are the spherical harmonics and are defined as following:

$$Y_{nm}(\theta,\varphi) = P_n^m(\cos\theta)\cdot e^{jm\varphi} \text{---} (5.17)$$

where P_n^m are the associated Legendre functions. The electric field is given explicitly as:

$$E_\theta = \frac{-1}{r\sin\theta}\cdot\partial_\varphi F_r + \frac{1}{j\omega\varepsilon r}\partial_{r\theta}A_r \text{---} (5.18)$$

$$E_\varphi = \frac{1}{r}\cdot\partial_\theta F_r + \frac{1}{j\omega\varepsilon r\sin\theta}\partial_{r\varphi}A_r \text{---} (5.19)$$

With:

$$(A_r)_{nm},(F_r)_{nm} = \hat{H}_n^{(2)}(kr)Y_{nm}(\theta,\varphi) \text{---} (5.20)$$

where $\hat{H}_n^{(2)}(kr)$ are the spherical Hankel functions used by Schelkunoff [86] and can be defined as:

$$\hat{H}_n^{(2)}(kr) = kr\left[h_n^{(2)}(kr)\right] \text{---} (5.21)$$

5.4.1. Orthogonal basis

The relation (5.20) forms the set of solutions of the scalar Helmholtz equation (with the Somerfield radiation condition) in spherical coordinates. The aim is to build an orthogonal basis for the field and not for the vector potentials. A more general form of this solution is provided by forming a linear combination of elementary wave functions [84] and by linearity, the ATF can be consequently expanded on the same basis [87] as:

$$\mathcal{H}(f,\theta,\varphi) = \sum_{n=1}^{\infty}\sum_{m=-n}^{n}\left[H_{nm}^{(TM)}(f)\,\hat{\boldsymbol{\Psi}}_{nm}^{(TM)}(\theta,\varphi) + H_{nm}^{(TE)}(f)\,\hat{\boldsymbol{\Psi}}_{nm}^{(TE)}(\theta,\varphi)\right] \text{---} (5.22)$$

recalling that the asymptotic behaviour of the Schelkunoff functions is $\hat{H}_n^{(2)}(kr) \sim j^{n+1}e^{-jkr}$, and where the { $\hat{\boldsymbol{\Psi}}$ } series forms a complete orthonormal basis as:

$$\hat{\boldsymbol{\Psi}}_{nm}^{TM} = v_{nm}\left(\partial_\theta Y_{nm}\cdot\hat{\theta} + \frac{1}{\sin\theta}\partial_\varphi Y_{nm}\cdot\hat{\varphi}\right) \text{---} (5.23)$$

$$\hat{\boldsymbol{\Psi}}_{nm}^{TE} = v_{nm}\left(\frac{1}{\sin\theta}\partial_\varphi Y_{nm}\cdot\hat{\theta} - \partial_\theta Y_{nm}\cdot\hat{\varphi}\right) \text{---} (5.24)$$

The normalization coefficients $\{v_{nm}\}$ are computed [87][106] as:

$$v_{nm}=\left[\frac{2n+1}{4\pi n(n+1)}\cdot\frac{(n-m)!}{(n+m)!}\right]^{\frac{1}{2}} \text{------}(5.25)$$

Moreover, the partial derivatives of the spherical harmonics are given by:

$$\partial_\theta Y_{nm}(\theta,\varphi)=d_\theta P_n^m(\cos\theta)\cdot e^{jm\varphi} \text{------}(5.26)$$

$$\partial_\varphi Y_{nm}(\theta,\varphi)=jmP_n^m(\cos\theta)\cdot e^{jm\varphi} \text{------}(5.27)$$

One way to prove the orthogonality relationship of this functions set with the correct “scalar product”, and eventually to compute the normalization coefficients ν_{nm}, is to apply the Lorentz reciprocity theorem [84] (valid within a source-free enclosed volume), which is:

$$\oiint\left(\mathbf{E}^a\times\mathbf{H}^b-\mathbf{E}^b\times\mathbf{H}^a\right)\cdot dS=0 \text{------}(5.28)$$

For any two modes $\mathbf{\Psi}^a$ and $\mathbf{\Psi}^b$, also:

$$\left\langle\mathbf{\Psi}^a,\mathbf{\Psi}^{b*}\right\rangle=\oiint\mathbf{\Psi}^a\cdot\mathbf{\Psi}^{b*}d\Omega=\int_0^\pi\int_0^{2\pi}\mathbf{\Psi}^a\cdot\mathbf{\Psi}^{b*}\sin\theta d\theta d\varphi \text{------}(5.29)$$

This is the Hermitian inner product with the orthonormality condition (giving the ν_{nm}):

$$\left\langle\mathbf{\Psi}_{nm}^{TM},\mathbf{\Psi}_{nm}^{TM*}\right\rangle=\left\langle\mathbf{\Psi}_{nm}^{TE},\mathbf{\Psi}_{nm}^{TE*}\right\rangle=\delta_{np}\delta_{mq} \text{------}(5.30)$$

$$\left\langle\mathbf{\Psi}_{nm}^{TM},\mathbf{\Psi}_{pq}^{TE*}\right\rangle=0 \text{------}(5.31)$$

5.4.2. Computation of modal coefficients

The modal coefficients $\left\{H_{nm}^{TE}(f),H_{nm}^{TM}(f)\right\}$ are computed by finding the projection of ATF on the basis:

$$\begin{aligned}H_{nm}^{TM}(f)&=\left\langle\mathcal{H},\hat{\mathbf{\Psi}}_{nm}^{TM*}\right\rangle\\&=v_{nm}\int_0^\pi\int_0^{2\pi}\left[\sin\theta\frac{dP_n^m(\cos\theta)}{d\theta}\mathcal{H}_\theta-jmP_n^m(\cos\theta)\mathcal{H}_\varphi\right]e^{-jm\varphi}d\theta d\varphi\end{aligned} \text{------}(5.32)$$

$$\begin{aligned}H_{nm}^{TE}(f)&=\left\langle\mathcal{H},\hat{\mathbf{\Psi}}_{nm}^{TE*}\right\rangle\\&=v_{nm}\int_0^\pi\int_0^{2\pi}\left[jmP_n^m(\cos\theta)\mathcal{H}_\theta-\sin\theta\frac{dP_n^m(\cos\theta)}{d\theta}\mathcal{H}_\varphi\right]e^{-jm\varphi}d\theta d\varphi\end{aligned} \text{------}(5.33)$$

The AIR being real, the modal coefficients $\left\{H_{nm}^{TE}(f),H_{nm}^{TM}(f)\right\}$ satisfy a relationship similar to the Hermitian symmetry of the Fourier transform of real functions:

$$\left.\begin{array}{l} H_{nm}^{TE}\left(-f\right)=\left(-1\right)^{m}\left[H_{n,-m}^{TE}\left(f\right)\right]^{*} \\ H_{nm}^{TM}\left(-f\right)=\left(-1\right)^{m}\left[H_{n,-m}^{TM}\left(f\right)\right]^{*} \end{array}\right\} \tag{5.34}$$

5.4.3. A case of vertical polarization

In the particular case of "pure" linear polarization along $\hat{\boldsymbol{\theta}}$, (5.32) and (5.33) are reduced to:

$$H_{nm}^{TM,TE}\left(f\right)=\int_{0}^{\pi}\rho_{nm}^{TM,TE}\left(\theta\right)\tilde{\mathcal{H}}_{\theta}\left(f,\theta,m\right)d\theta \tag{5.35}$$

$$\rho_{nm}^{TM}\left(\theta\right)=v_{nm}\sin\theta\frac{dP_{n}^{m}\left(\cos\theta\right)}{d\theta} \tag{5.36}$$

$$\rho_{nm}^{TE}\left(\theta\right)=-jmv_{nm}P_{n}^{m}\left(\cos\theta\right) \tag{5.37}$$

$$\tilde{\mathcal{H}}_{\theta}\left(f,\theta,m\right)=\int_{0}^{2\pi}\mathcal{H}_{\theta}\left(f,\theta,\varphi\right)e^{-jm\varphi}d\varphi \tag{5.38}$$

which is actually the Fourier coefficient of $\mathcal{H}_{\theta}$ (φ), a function which must obviously be single-valued and consequently, 2π periodic in φ.

This last point is not only formal, not only because it shows that the calculation can be efficiently implemented with an FFT, but especially because it facilitates the interpretation of the mode order *m*, which is actually the Fourier conjugate variable of the azimuth φ, i.e. the "frequency" of the ATF variations with φ. In other words, we can anticipate that the number of m-modes (energy significant) should be low for omnidirectional or quasi-omnidirectional antennas. It is well-known that small size and/or low gain antennas present a small (total) number of modes.

The interpretation of the transform is comparable for mode degree n, although it is the Fourier-Legendre transform, which is in fact a Fourier transform in spherical coordinates which is involved — the two angles not playing symmetrical roles on the sphere. The degree *n*, conjugate variable of θ, therefore measures the frequency of the ATF variations in elevation.

5.4.4. Truncation and associated noise

In practice the summations are always truncated. The maximum value of n and m in (5.22) retained in the sums is denoted by *N* and *M*, respectively. For a truncation of degree N, the total number of modal coefficients is a priori given by [85]:

$$N_T = 2N(N+2) \text{---}(5.39)$$

In the specific case of pure linear polarization along $\hat{\boldsymbol{\theta}}$, $H_{n0}^{TE}(f) = 0$, so that N_T reduces to:

$$N_T = N(2N+3) \text{---}(5.40)$$

This truncation of modes degrees and orders (n, m) introduces computation errors, in addition to other sources of errors like measurement errors. Such errors stem for instance from the antenna imperfect alignment on the positioner, from cable effects and from an imperfect calibration. A general relation can be written as:

$$\mathcal{H} = \mathcal{H}_N + \Delta\mathcal{H}_N + \mathcal{N} \approx \mathcal{H}_N \text{---}(5.41)$$

$$\mathcal{H}_N(f,\theta,\varphi) = \sum_{n=1}^{N}\sum_{m=-n}^{n}\sum_{u=1}^{2} H_{nm}^{(u)}(f)\,\hat{\boldsymbol{\Psi}}_{nm}^{(u)}(\theta,\varphi) \text{---}(5.42)$$

$$\Delta\mathcal{H}_N(f,\theta,\varphi) = \sum_{n=N+1}^{\infty}\sum_{m=-n}^{n}\sum_{u=1}^{2} H_{nm}^{(u)}(f)\,\hat{\boldsymbol{\Psi}}_{nm}^{(u)}(\theta,\varphi) \text{-------------------------------------}(5.43)$$

where u={1, 2} = {TE, TM}, $\mathcal{N}$ denotes the noise and measurement errors. $\mathcal{H}_N$ represents the dominant (or powerful) modes and $\Delta\mathcal{H}_N$ is the rest of the modes. In practice the modeling is performed on $\mathcal{H}_N$ modes and the model error or modeling error is the combination of $\Delta\mathcal{H}_N$ and $\mathcal{N}$.

The number of dominant modes "N" is dependent on the minimal radius R_{min} of any circumscribing sphere enclosing the antenna (usually quoted as the minimal sphere) and on the wave number $k = 2\pi/\lambda$. It is shown in [85] that an approximate estimation can be expressed as:

$$N \approx \lfloor kR_{\min} \rfloor \text{--}(5.44)$$

A more precise estimate considering the relative error in decibel of the truncated power (P_{tr}) is given in [89]:

$$N \approx \left\lfloor kR_{\min} + 0.045\sqrt[3]{kR_{\min}}\,(-\Delta P_{tr}) \right\rfloor \text{---}(5.45)$$

The primary objective here is not a high accuracy but rather the order reduction by keeping only the dominant modes $\mathcal{H}_N$. In this case, the required total number of modes N_T is a function of the antenna size, the mean square error (MSE) and the existence or not of a structural symmetry (Sym) [87], [74], [106]:

$$N_T \approx f\left(kR_{\min}, MSE, Sym\right) \text{--} (5.46)$$

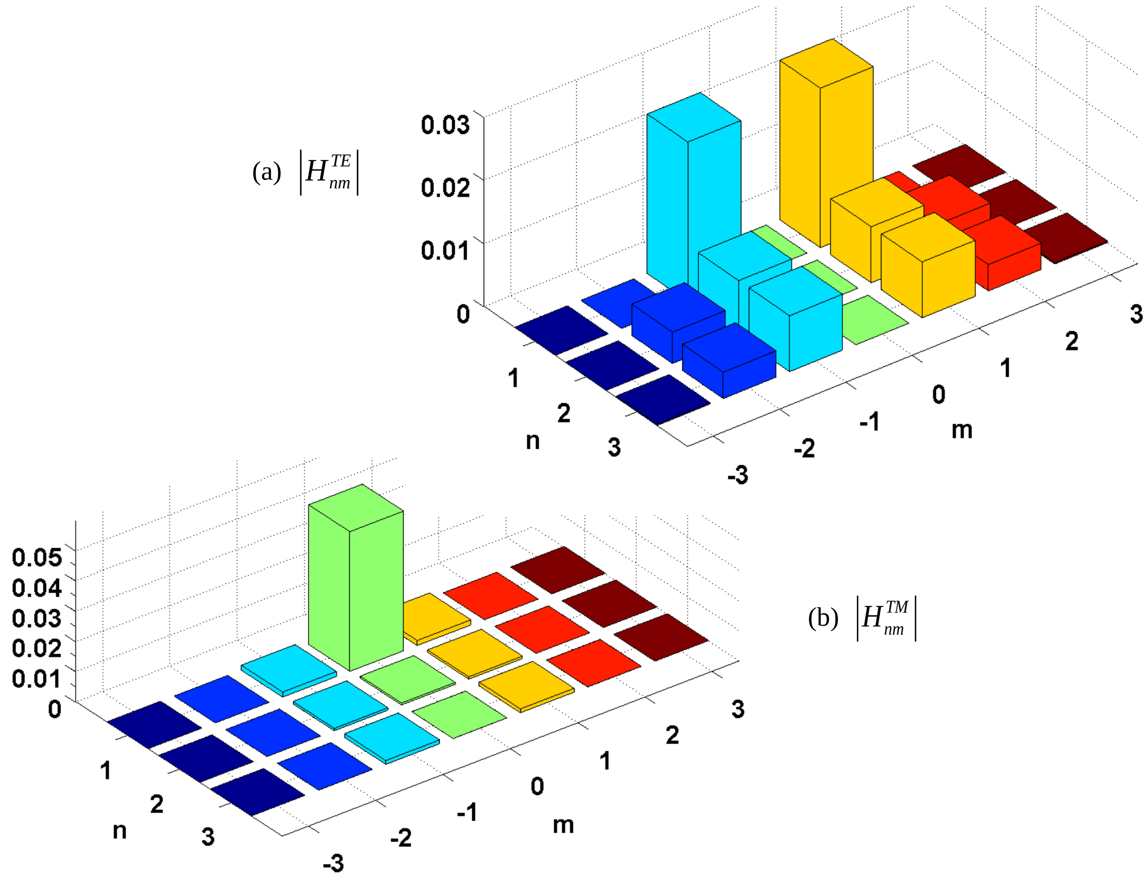

Fig. 5.3 Amplitude of TE and TM Modal Coefficients of triangular Monopole at 3 GHz with N=3.

5.4.5. Example

The triangular monopole's radiation pattern can be presented with ($N_f \times N_\theta \times N_\varphi$) = (81 × 37 × 72) = 215 784 complexes in the frequency band of [3−11] GHz. The realized gain at 3 GHz of this monopole is shown in Fig. 5.4a. Modal coefficients $H_{nm}^{TE,TM}$ with modes degree n and order m at 3 GHz are shown in Fig. 5.3.

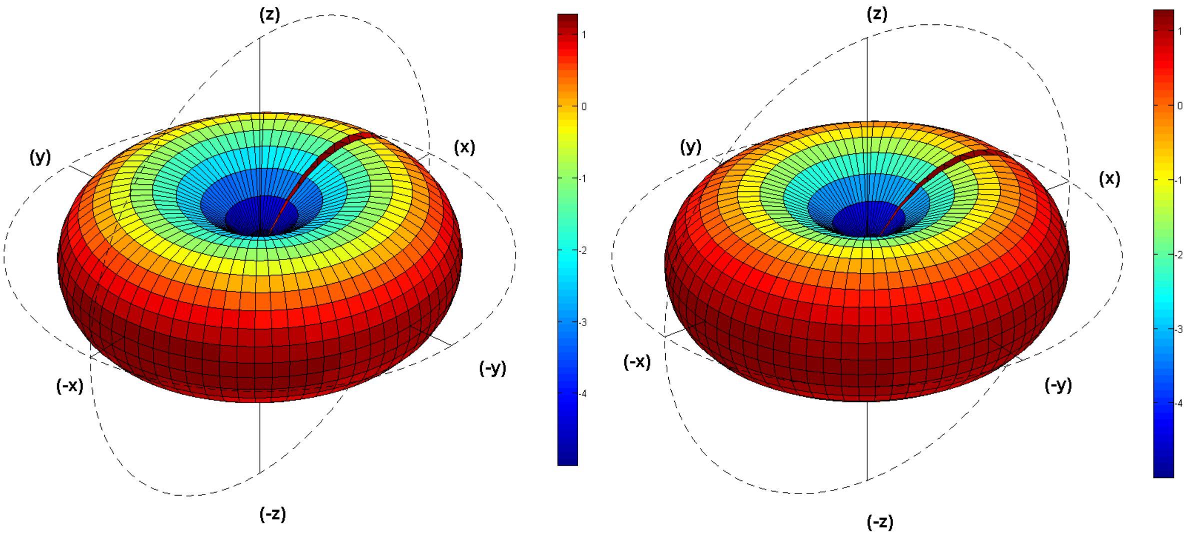

Original
(a)

Re-constructed
(b)

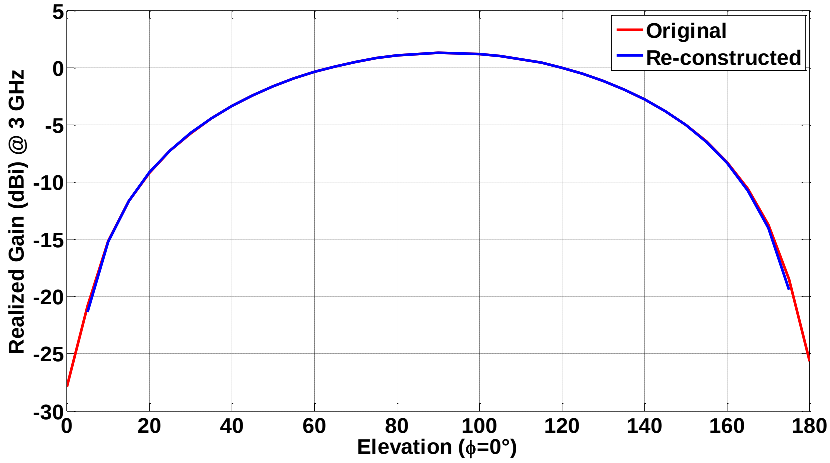

(c) Meridian cut

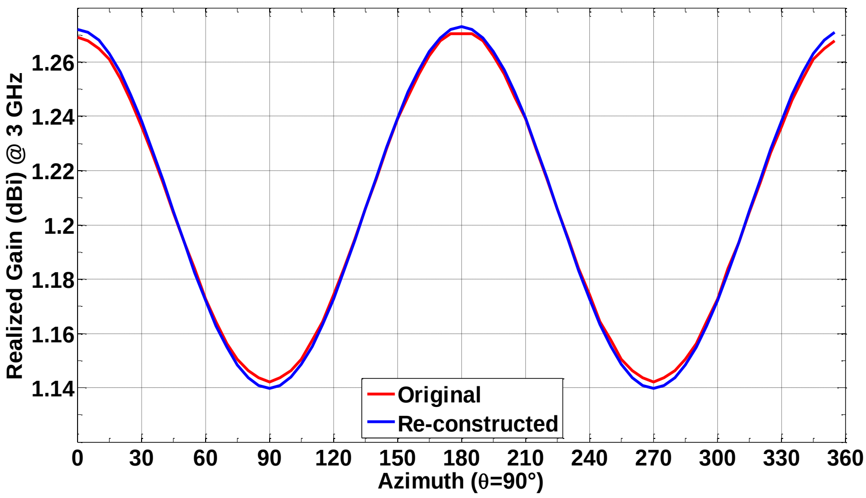

(d) Equatorial cut

Fig. 5.4 Triangular Monopole responses at 3GHz before and after the application of SMEM.

It is noted that the total number of modes N_T as given by (5.39) are 2[3(3+2)] = 30 complex numbers per frequency, resulting in 81 × 30 = 2430 complex numbers for the whole frequency band, i.e. a compression factor of 88.8 or 98.87 % compression. In addition, if the *x*O*z* plane symmetry is taken in to account, only half of the coefficients are required ($N_T = N(N + 2) = 15$).

The power captured by the modes is 96.4 % of the originally available power in the pattern. The 3.6 % loss is due to truncation. Using these computed modal coefficients, the pattern is reconstructed and a 3D reconstruction is shown in Fig. 5.4b, along with the comparison in meridian cut (Fig. 5.4c) and equatorial cut (Fig. 5.4d). A negligible difference between the two curves can be seen. In Fig. 5.4d, the y axis is zoomed in order to notice the difference.

5.5. Ultra Compressed Parametric Modeling

It has been shown in the previous sections that an antenna radiation pattern can be presented with a small numbers of parameters. The methods discussed above offer significant parameter compression at the cost of a few model errors. It has been shown in [87] that, by combining SEM and SMEM, ultra compression is achieved. Again, the objective is here the ultra compression rather than the accuracy, which in turn opens the route to statistical modeling.

According to the procedure defined in section 5.2, the SEM expansion is applied to the AIR. The reconstruction errors are observed in order to decide of the appropriate number of poles P, finally the SMEM is applied on the residues $\mathbf{R}_p$. Re-writing the ATF for both expansions:

$$\mathcal{H}(s,\theta,\varphi) = \sum_p \frac{\mathbf{R}_p(\theta,\varphi)}{s - s_p} = \sum_{n=1}^{\infty} \sum_{m=-n}^{n} \sum_{u=1}^{2} H_{nm}^{(u)}(s)\, \hat{\mathbf{\Psi}}_{nm}^{(u)}(\theta,\varphi) \text{ ----------------------------(5.47)}$$

The residues $\mathbf{R}_p$ can be expanded for each TM and TE modes as:

$$\mathbf{R}_p(\theta,\varphi) = \sum_{n=1}^{\infty} \sum_{m=-n}^{n} \sum_{u=1}^{2} R_{nmp}^{(u)} \hat{\mathbf{\Psi}}_{nm}^{(u)}(\theta,\varphi) \text{ ---(5.48)}$$

The modal residues $R_{nm}^{(u)}$ are the projection of residues on the basis,

$$R_{nmp}^{(u)} = \left\langle \mathbf{R}_p, \hat{\mathbf{\Psi}}_{nm}^{(u)^*} \right\rangle = \int_0^{\pi} \int_0^{2\pi} \mathbf{R}_p(\theta,\varphi) \cdot \hat{\mathbf{\Psi}}_{nm}^{(u)^*}(\theta,\varphi) \sin\theta d\theta d\varphi \text{ ----------------------------(5.49)}$$

Finally the antenna response can be expanded in the spectral domain as:

$$\mathcal{H}\left(s,\theta,\varphi\right) \cong \mathcal{H}_{N,P}\left(s,\theta,\varphi\right) = \sum_{p=1}^{P}\left[\sum_{n=1}^{\infty}\sum_{m=-n}^{n} R_{nmp}^{(u)}\hat{\mathbf{\Psi}}_{nm}^{(u)}\left(\theta,\varphi\right)\right]\cdot\left(s-s_p\right)^{-1} \text{-----------------}(5.50)$$

and in the time domain as:

$$\mathcal{h}\left(t,\theta,\varphi\right) \cong \mathcal{h}_{N,P}\left(t,\theta,\varphi\right) = \sum_{p=1}^{P}\left[\sum_{n=1}^{\infty}\sum_{m=-n}^{n} R_{nm}^{(u)}\hat{\mathbf{\Psi}}_{nm}^{(u)}\left(\theta,\varphi\right)\right]\cdot e^{s_p t} \text{----------------------------}(5.51)$$

The modal residues verify a general relationship similar to (5.34) for SMEM, since the AIR is real.

$$R_{nmp^*}^{(u)} = \left(-1\right)^{m}\left[R_{n,-m,p}^{(u)}\right]^{*} \text{--}(5.52)$$

where p^* is the index of the conjugate pole of the pole of index *p*.

The total number of complex parameters of the ultra compressed model can be estimated as:

$$N_T = \frac{P}{2} + N\left(N+2\right)P \text{--}(5.53)$$

where, *P* is dominant poles of SEM and *N* is the N^{th} order expansion of SMEM.

5.5.1. Example

An example of triangular planar balanced dipole (PBD) is taken. The antenna minimal sphere radius is set to 30 mm. The SEM is applied with *P* = 16 whereas the SMEM is computed with *N* = 6. The total number of complex parameters according to (5.53) is 776. The modal residues are $\{R_{nmp}\}$ for TM and TE modes are shown for the 1st pole (corresponding to f_1 = 2 GHz) in Fig. 5.5a and Fig. 5.5b respectively. The reconstructed realized gain (dBi) in the direction (θ, φ) = (90°, 0°) is shown in Fig. 5.5c. at higher frequencies a discrepancy can be seen which is due to the fact that the higher the frequency (or the pole index), the higher the required number of spherical modes.

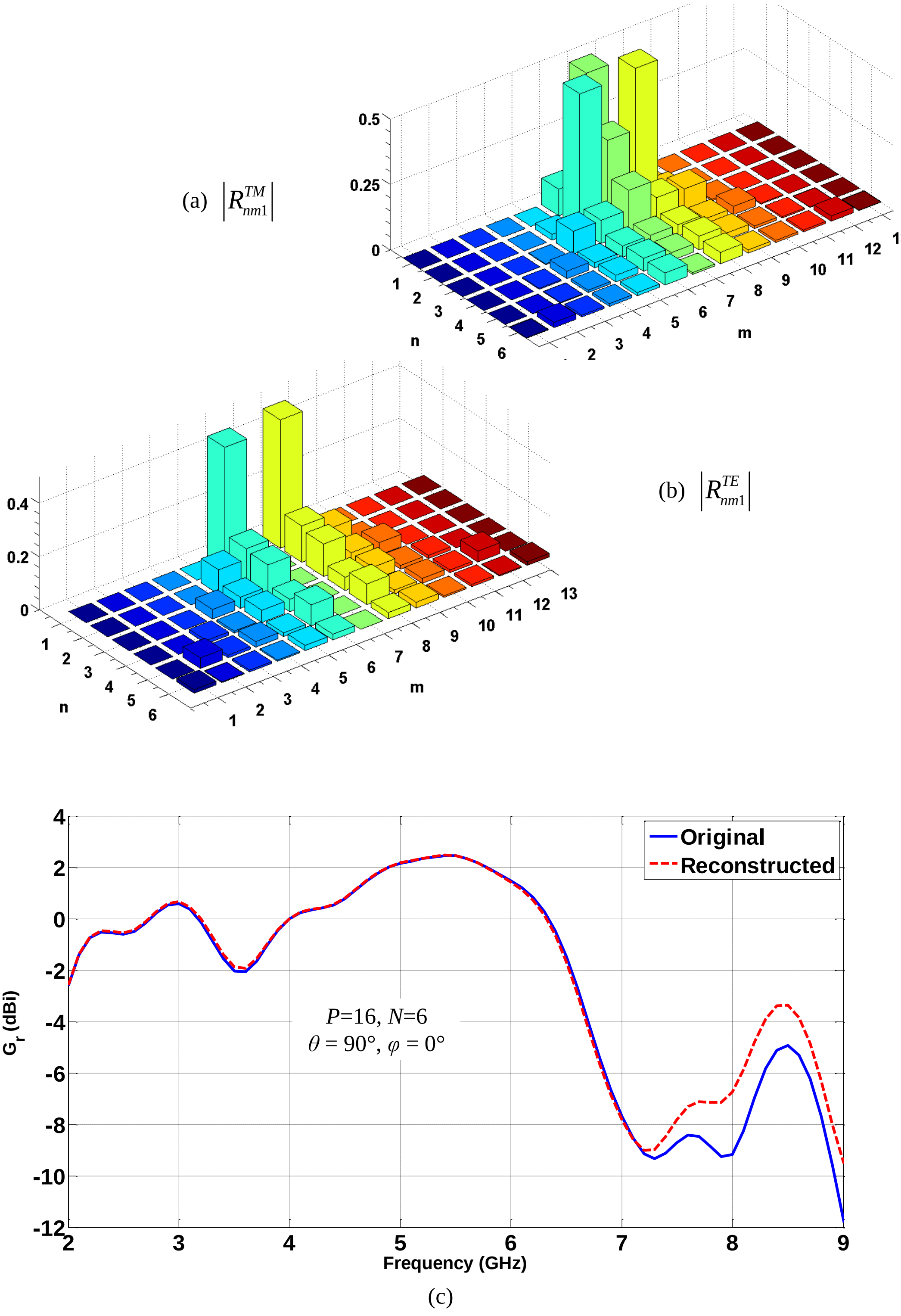

Fig. 5.5 Example of Triangular Planar Balanced Dipole (PBD) SEM SMEM combined model.

5.6. Conclusion

This chapter starts by explaining the procedure for ultra-compressed modeling technique. Two antenna synthesis techniques are discussed, first the singularity expansion method and its corresponding algorithm for calculation known as Generalized matrix pencil (GMP) algorithm, have been explained. Second, the Spherical mode expansion method (SMEM) has been explained. The combination of these two techniques is explained at the last part of the chapter.

It has been shown that through these techniques, the number of complex parameters that are needed to define the far field radiations pattern can be reduced by more than 98%.

Chapter 6

Ultra Compressed Statistical Modeling

6.1. Introduction

The ultra compressed modeling technique for antenna far field radiation pattern was discussed in the previous chapter. Here, the focus is the application of this technique on statistical modeling of the far field radiation pattern of an antenna design class.

It has been stressed that the radiation of a typical UWB antenna needed a huge number ($N_f \times N_\theta \times N_\varphi$) of complex parameters in order to be adequately represented. Obviously, the statistical modeling of so many parameters is impractical, if not impossible. The ultra compressed modeling method reduces this number to a quantity where the statistical modeling of radiation pattern is deemed possible.

As an example, a typical UWB antenna response can need a sampling in the angular domain of 37 elevation and 72 azimuth angles and in the frequency domain of 100 frequencies over 3-10 GHz, which corresponds to $N_f \times N_\theta \times N_\varphi$ = 266 400 parameters. If this antenna response is modeled with P = 12 poles and N = 4 modes, then according to equation (5.53) the total number of complex parameters is 6 + 4(4+2)12 = 294, which is a very much reduced quantity. The statistical modeling of

294 parameters is still demanding but may be feasible, which motivates the work presented here.

In this chapter, the general procedure of the statistical modeling of an ultra compressed parametric model of antenna far field radiation pattern is discussed. It is applied to a bicone, chosen as a rather extreme case of ultra data compression for an UWB antenna.

6.2. The procedure

The procedure for achieving ultra compression is illustrated in Fig. 6.1. It starts from the optimal design of the antenna class or subclass population and assumes the choice of the model parameters such as the required number of poles *P* and dominant modes *N*. Once decided, these parameters are fixed for the rest of the population.

The other parameters, for the singularity expansion method (SEM) can also be decided at this stage, such as a set of the number of direction (*DK*) on which residues are computed or the number of data samples in the impulse response (N_{SEM}), usually concerning the main beam response. The pencil parameter (*L*) is usually in the range of $N_{SEM}/3$ to $N_{SEM}/2$ [96].

The SEM is then applied to the (AIR) in order to calculate the poles s_p and the residues $\mathbf{R}_p$ of the categorized antenna realizations of the population. These selected antenna realizations can be rejected according to a criterion, for instance $|S_{11}| > -6$ dB or perhaps the *MME* < 75%, as discussed in chapter 4.

The SMEM computes the *N* dominant modes of the modal residues. At this stage, the ATF of each antenna realization is ultra-compressed. We can write the ATF $\mathcal{H}(s,\theta,\varphi)$ as:

$$\mathcal{H}_k\left(s,\theta,\varphi\right)=\sum_{p=1}^{P}\left[\sum_{n=1}^{\infty}\sum_{m=-n}^{n}\sum_{u=1}^{2}R_{nmp,k}^{(u)}\hat{\mathbf{\Psi}}_{nm}^{(u)}\left(\theta,\varphi\right)\right]\cdot\left(s-s_{p,k}\right)^{-1} \quad \text{----------------------(6.1)}$$

where, $k = 1\ldots\ldots K$, is the index of the antenna realization, for a population of size *K*.

Once the ultra compressed ATFs are calculated, the statistical analysis and thus the models of both the poles (the natural frequencies and damping factor) and the modal residues can be searched.

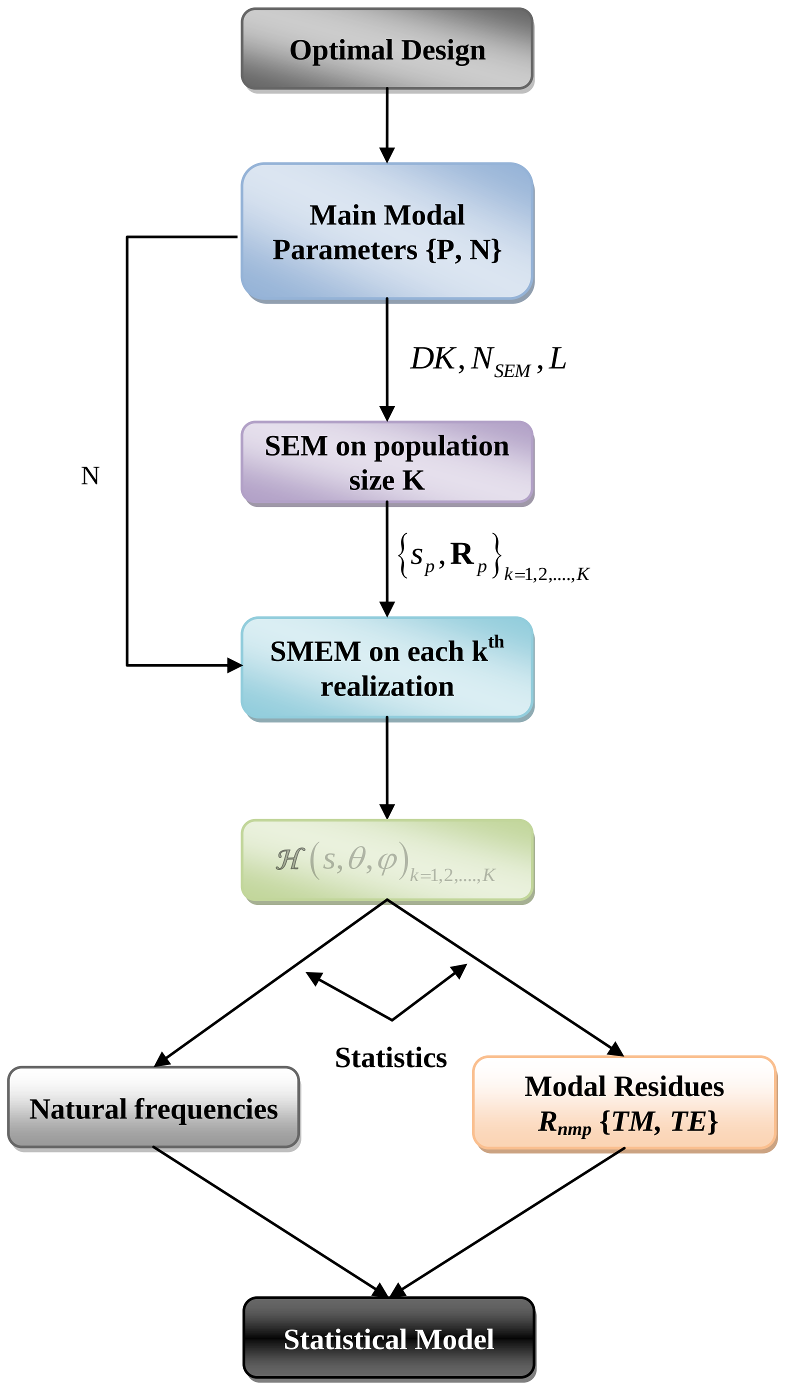

Fig. 6.1 Procedure for Ultra compressed Statistical Modeling

6.3. Parametric Model of the Biconical Antenna Class

In order to show the performance of the method, a population of 351 biconical antennas has been generated and simulated through CST MWS EM solver. Prior to the statistical modeling, 142 realizations have been selected, based on the criterion $|S_{11}| < 6$ dB using infinity norm over the bandwidth of 3 to 11 GHz.

.

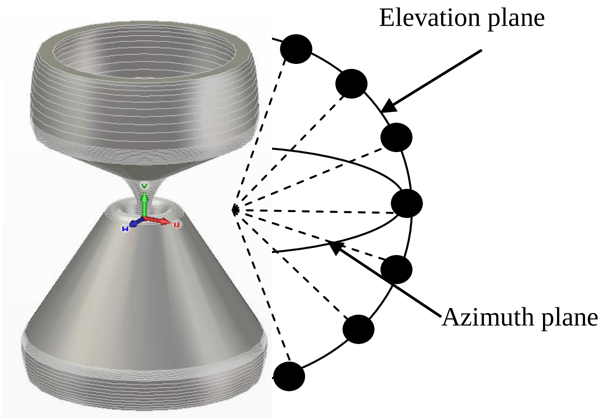

Fig. 6.2 Biconical antenna, Due to structural symmetry a single direction in azimuth plane and several directions in elevation plane are adequate to model the radiation pattern.

The optimal design of the population has a minimal sphere radius (R_{min}) of about 16mm. Hence, using the relation 5.45,

$$N \approx \left\lfloor kR_{\min} + 0.045\sqrt[3]{kR_{\min}}\left(-\Delta P_{tr}\right)\right\rfloor \text{ --(6.2)}$$

where, k is the wave number corresponding to the center frequency of operational bandwidth. The truncated power (P_{tr}) is the acceptable relative error in decibel, in this case chosen to be 30 dB. The N dominant modes are thus 4 and since in the population the maximum R_{min} is around 25mm, the dominant modes are fixed to N=5.

The required number of poles P can be decided by observing the decay of normalized singular values (with respect to the largest) of the optimal design as shown in Fig. 6.3. A slope break is observed at P = 14, which suggests that this zone of truncation offers a good trade-off between accuracy and compression. Therefore, P = 14 has been chose for the population.

The other (“free”) parameters of GMP-TLS algorithm are set as follows. The directions of observation, are chosen in the main beam (θ = {30,50,70, …..,150}) along any single meridian cut (e.g. φ = 0°). Directions outside this set of directions are not considered to be important, due to low radiated power close to the zenith. The number of time samples of the impulse response $\hbar$ (t) ("scanned" by the pencil of length L ~ 40) is taken as N_{SEM} = 100. The EM simulations are performed with 25 ps time steps, implying that 100 samples correspond to a time window of observation of 2.5 ns.

It is shown in Fig. 6.4 that these settings offer a performing model, with a reconstructed response close to the original, including in the ringing part (usually more difficult to represent than the main peak(s)).

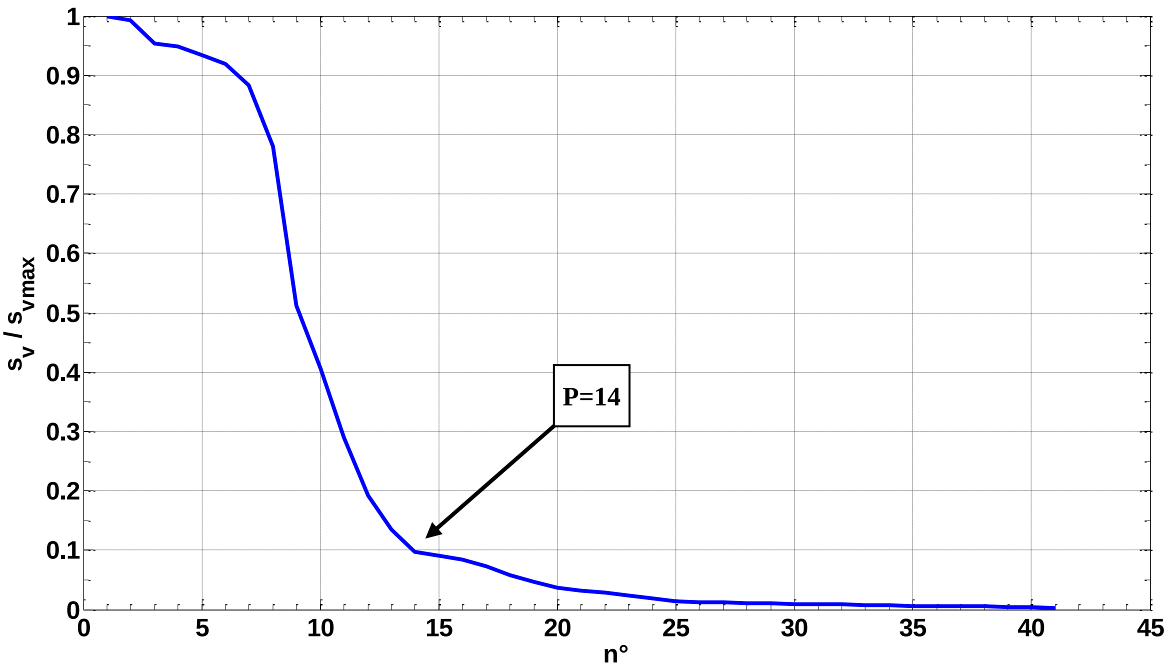

Fig. 6.3 Bicone optimal design: Normalized singular values of the generalized matrix pencil algorithm for SEM.

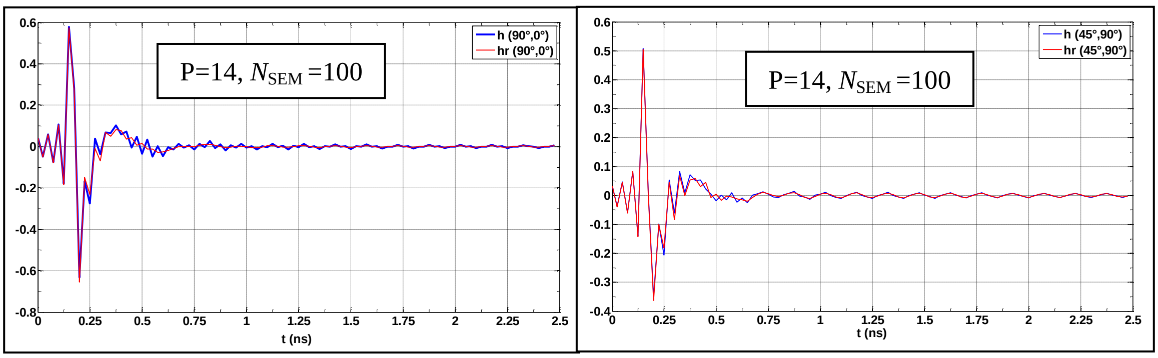

Fig. 6.4 Impulse response $\hbar(t)$ of the optimal bicone design and the reconstructed $\hbar_r(t)$ with SEM.

The summary of the initial parameters for the calculation of SEM and SMEM is given in the table below for the rest of the population:

Table 6. 1 Summary of Initial Parameters for the Bicone Class

	Parameter	Value
1	*P*	14
2	*N*	5
3	*DK*	$\Theta°$ = {30,50,70, …..,150} $\varphi°$ = 0°
4	N_{SEM}	100
5	*L*	40
6	*BW*	[3 11] GHz

6.3.1. Total number of Complex Parameters

The modal residues verify the following general relation

$$R^{(u)}_{nmp*} = (-1)^m \left[R^{(u)}_{n,-m,p} \right]^* \text{--} \quad (6.3)$$

where $p*$ is the index of the conjugate pole of index p. The modal residues require a total number of complex parameters as given in relation (5.53) and repeated here for convenience:

$$N_T = \frac{P}{2} + N(N+2)P \quad \text{---}(6.4)$$

Due to the omni-directionality, stemming from the rotational invariance, the field does not depend on the azimuth. This reduces the non zero spherical modes to the {TM_{n0}} with degree m = 0. Thus, (6.3) becomes

$$R^{(2)}_{n0p*} = R^{(2)\,*}_{n0p} \quad \text{--}(6.5)$$

This significantly reduces the number of model parameters to:

$$N_T = N(N+1)\frac{P}{2} \quad \text{---}(6.6)$$

The non zero modal residues being restricted to the $\{R^{(2)}_{n0p}\}$ set. For those reasons the bicone can be correctly represented over a bandwidth of [3-11] GHz with N = 5 and P = 14, leading to N_T = 210 complex parameters for the full UWB 3D far field model.

6.3.2. Statistical Modeling Results

In this section, our objective is to build a statistical model for the various parameters of the SEM/SMEM modeled antennas. This means that we wish to find a way to describe in the simplest possible way the variability of the antennas that are part of the investigated population. Building this model means to find a way to describe in a compact way the variation of each individual parameter, but also to take account of the fact that various parameters of the set may be inter-related in some way and not necessarily independent. This is clearly an important difficulty of the approach.

Let us first consider the natural frequencies and the damping factor. It is recalled that:

$$s_p = \sigma_p \pm j\omega_p = \sigma_p \pm j2\pi f_p \quad \text{--(6.7)}$$

$$\xi_p = \frac{-\sigma_p}{\left|s_p\right|} \quad \text{--(6.8)}$$

$$\cos\psi_p = \xi_p \quad \text{---(6.9)}$$

The scatter plot of (f_p, ξ_p) for the population is shown in Fig. 6.5. It depicts the variation of ξ_p with respect to the different natural frequencies f_p. It is noted that there is a strong variation of ξ_p in the first 2 poles and there is a dispersion of the poles in natural frequency. For example pole p = 3 is dispersed in this respect.

Another way to look at these variations is by calculating the angle ψ_p. This is shown in the Fig. 6.6. Here the variation is surely less, as compared to the case of ξ_p, thus it is perhaps better to model the angle ψ_p and f_p.

The cumulative distribution of f_p is given in Fig. 6.7, along with the Normal fit distribution, whereas the cumulative distribution of angle ψ_p is given in Fig. 6.8 with the Generalized Extreme Value (GEV) fit. The estimated first two moments for both f_p and angle ψ_p are given in Table 6.2. From these results, it can be stated that the natural frequencies of the biconical antenna class can be modeled with 7 × 4 = 28 parameters.

The mean values of the natural frequencies $<f_p>$ can be further modeled with a linear regression as shown in Fig. 6.9, reducing the number of parameters to only 2 (*af* and *bf*).

$$< f_p > = a_f\, p + b_f = 2.5p - 0.7 \quad \text{--(6.10)}$$

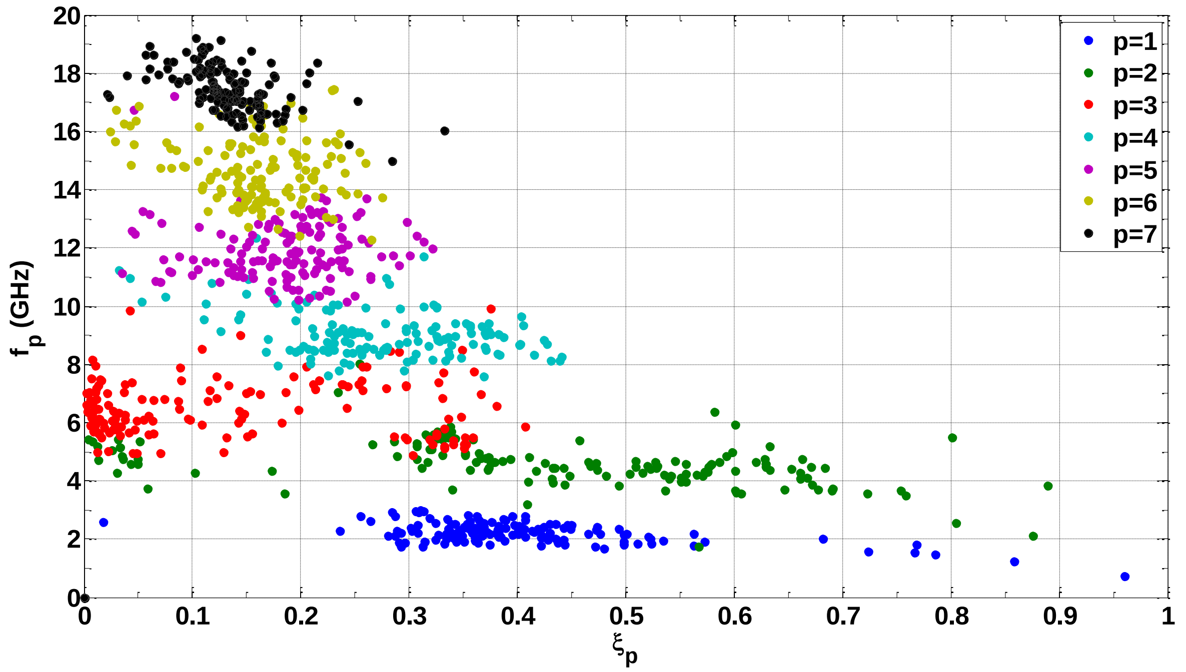

Fig. 6.5 scatter plot for the poles (ξ_p , f_p) representation.

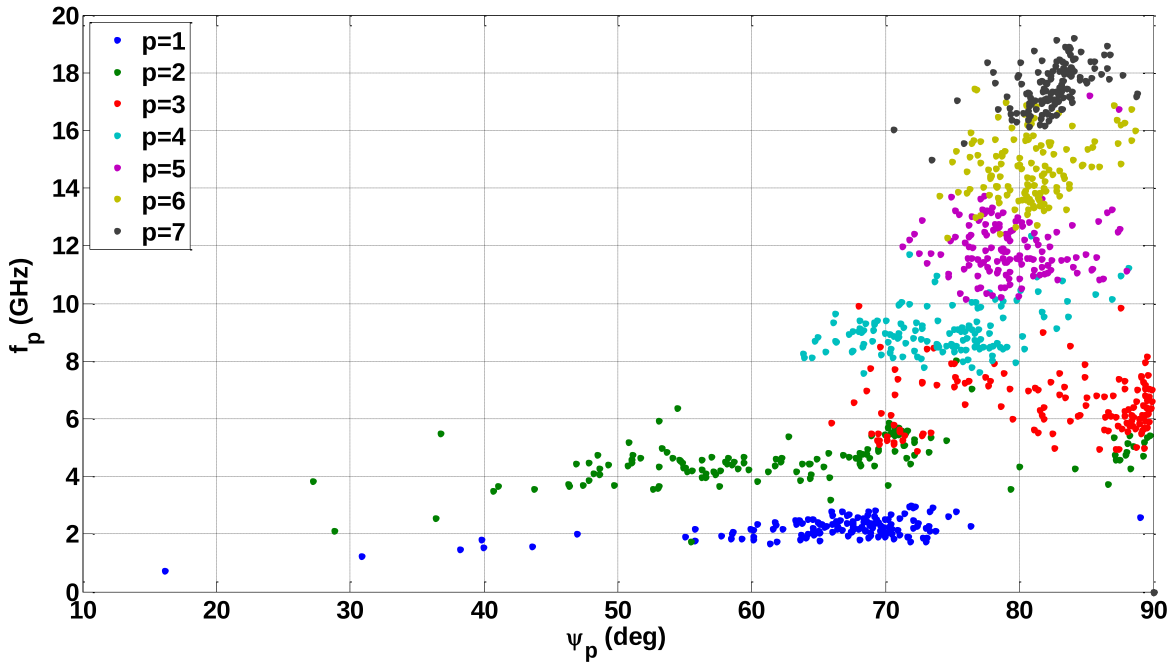

Fig. 6.6 scatter plot for the poles (ψ_p , f_p) representation.

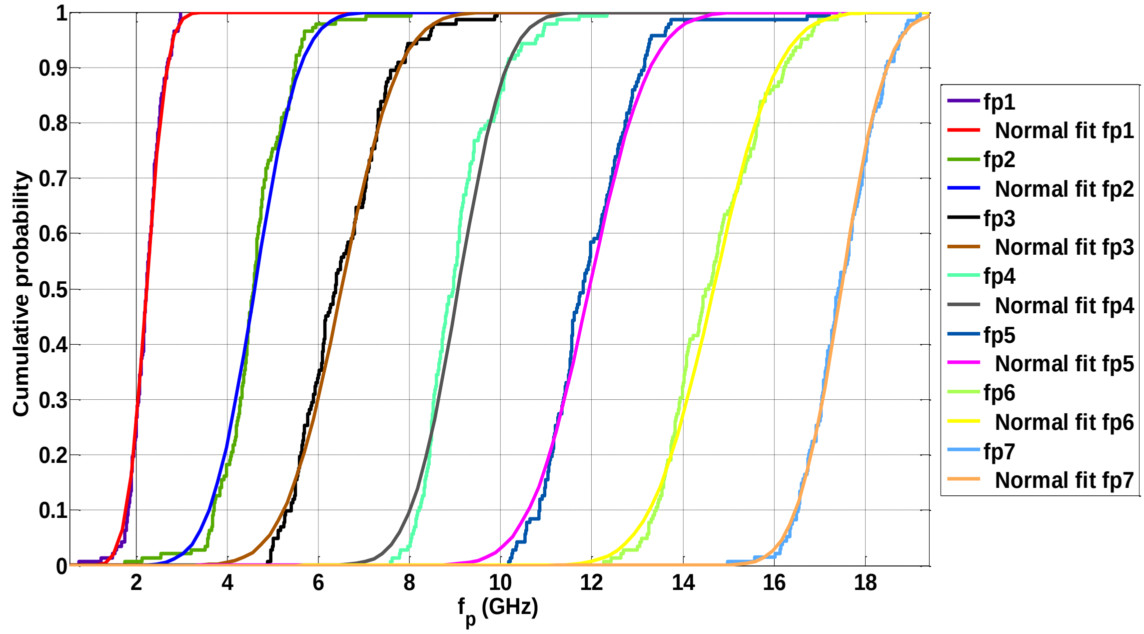

Fig. 6.7 Empirical CDF and Normal fit of the Natural Frequencies (f_p).

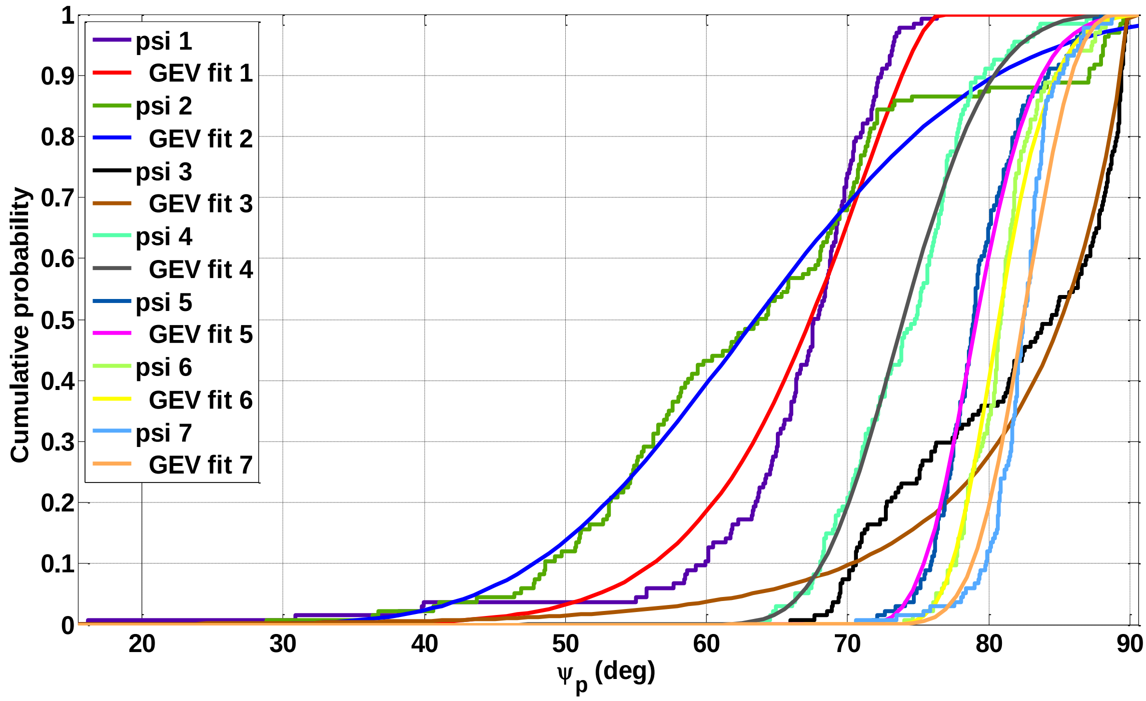

Fig. 6.8 Empirical CDF and GEV fit of the "pole angle" (ψ_p).

Table 6.2 Natural Frequencies: Estimated Parameters (Bicone Class)

Pole n°	Estimated Parameters			
	f_p (Normal)		ψ_p (GEV)	
	μ	σ	μ	σ
1	2.22206	0.351309	64.8667	7.7574
2	4.59341	0.779377	59.1449	12.3028
3	6.50535	0.989812	82.5425	8.63926
4	9.06691	0.829001	72.3616	4.53982
5	11.9441	1.04139	78.0802	2.97404
6	14.6718	1.10032	79.78	2.65836
7	17.4771	0.78141	81.5161	2.77488

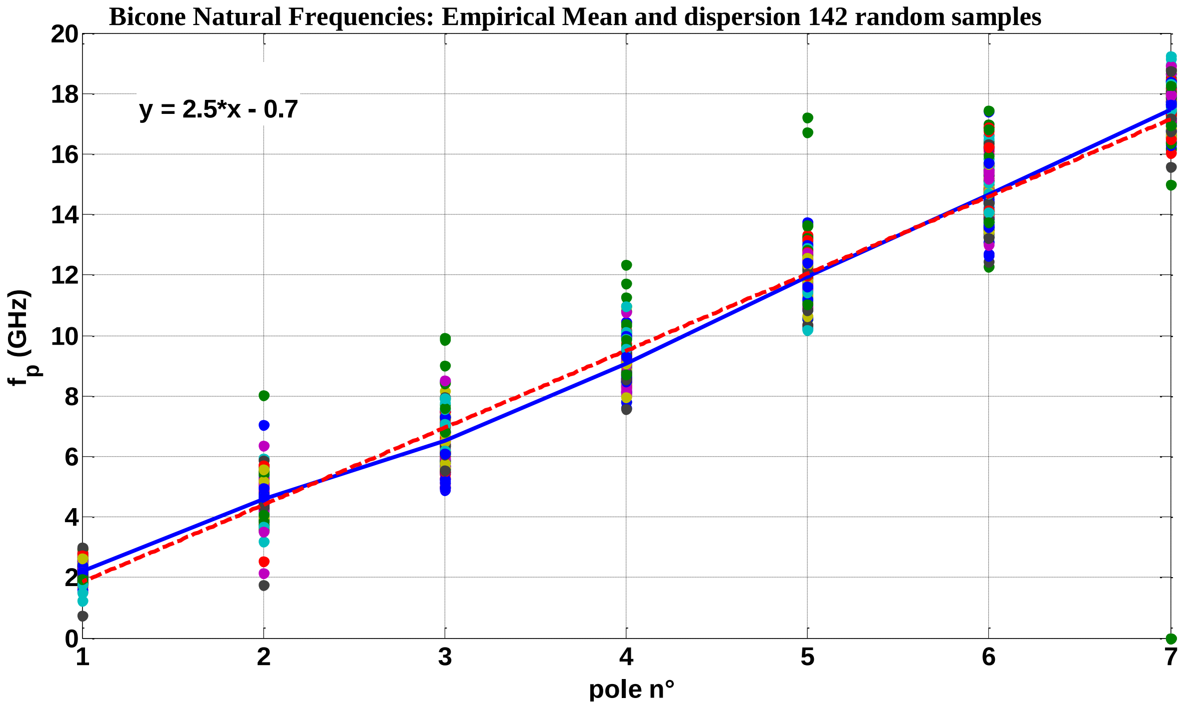

Fig. 6.9 Natural Frequencies (f_p) versus pole index and linear fit.

In order to appreciate the degree of inter relation between the various parameters of each individual antenna, we computed the covariance matrices of the f_p and ψ_p as shown in Table 6.3 and Table 6.4 respectively. Indeed, although the correlation is an imperfect measure of the dependence between random variables, it is a practical and useful way to get information on the relative behaviour of these variables.

Table 6.3 Covariance Matrix $\mathbf{C}_{f_p}$

0.1217	0.1629	-0.0539	-0.0516	0.0730	0.0817	-0.0246
0.1629	0.4886	-0.1070	0.0155	0.0940	0.1534	-0.0231
-0.0539	-0.1070	0.7776	0.4135	0.2343	0.4082	0.1793
-0.0516	0.0155	0.4135	0.5701	0.2422	0.3038	0.1247
0.0730	0.0940	0.2343	0.2422	0.7293	0.5296	0.2529
0.0817	0.1534	0.4082	0.3038	0.5296	1.0973	0.3523
-0.0246	-0.0231	0.1793	0.1247	0.2529	0.3523	0.6106

Table 6.4 Covariance Matrix $\mathbf{C}_{\psi_p}$

63.929	50.899	7.423	7.374	8.277	2.765	4.233
50.899	162.642	-39.900	34.506	19.758	13.203	4.384
7.423	-39.900	54.481	-17.390	-11.580	-1.621	3.902
7.374	34.506	-17.390	21.985	6.774	3.969	0.641
8.277	19.758	-11.580	6.774	10.732	0.418	-0.238
2.765	13.203	-1.621	3.969	0.418	8.300	0.501
4.233	4.384	3.902	0.641	-0.238	0.501	6.348

In practice an implementation of the model such as presented in Fig. 6.9 involves generating $P/2$ correlated normal values. This can be done from a normalized, uncorrelated, Gaussian vector **X,** and the Cholesky decomposition of the covariance matrix $\mathbf{C}_{f_p}$, and the means vector $\mathbf{M}_{f_p}$, as follows:

$$\mathbf{Y} = \mathbf{X} \cdot \mathrm{chol}\left(\mathbf{C}_{f_p}\right) + \mathbf{M}_{f_p} \quad \text{--}(6.11)$$

$\mathbf{M}_{f_p}$ and $\mathbf{C}_{f_p}$ have been given in Table 6.2 and Table 6.3 respectively. This regeneration of the poles natural frequencies have been shown in Fig. 6.10 and should be compared with Fig. 6.9.

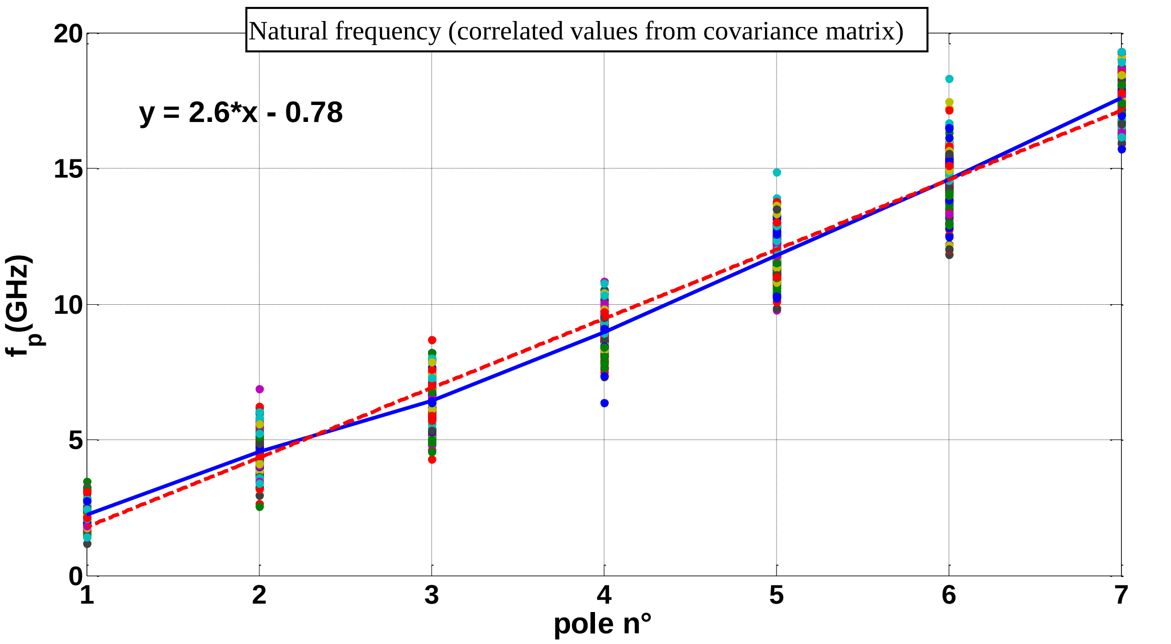

Fig. 6.10 Bicone : Randomly generated samples for f_p from covariance matrix C_p^f

Regarding the modal residues, the cumulative distribution of real and imaginary part of each modal residue $\{R_{n0p}\}$ for the TM mode is given in the subsequent part. First, we provide the distribution of real and imaginary of $\{R_{10p}\}$ along with the fit parameters, summarized in a table. In the same sequence, the rest of the modal residues $\{R_{20p}, R_{30p}, R_{40p}, R_{50p}\}$ are given.

At this stage, it is necessary to find the best fit distribution, able to quantitatively approach the "experimental" distribution as close as possible. It turns out that for all modal residues, the “t location–scale” is found to be the best fit according to maximum likelihood parameter.

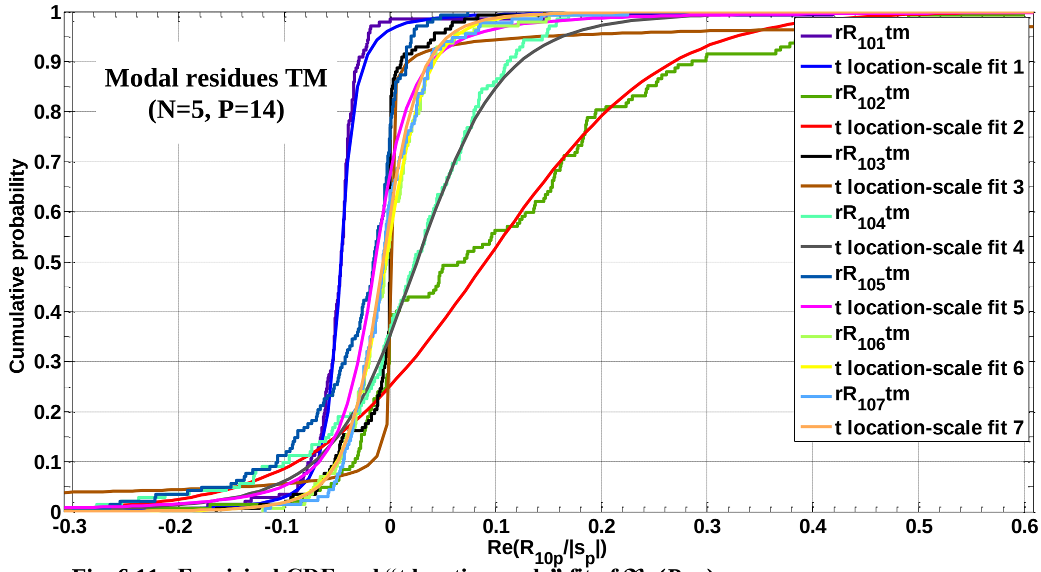

Fig. 6.11 Empirical CDF and "t location-scale" fit of $\mathfrak{Re}(R_{10p})$

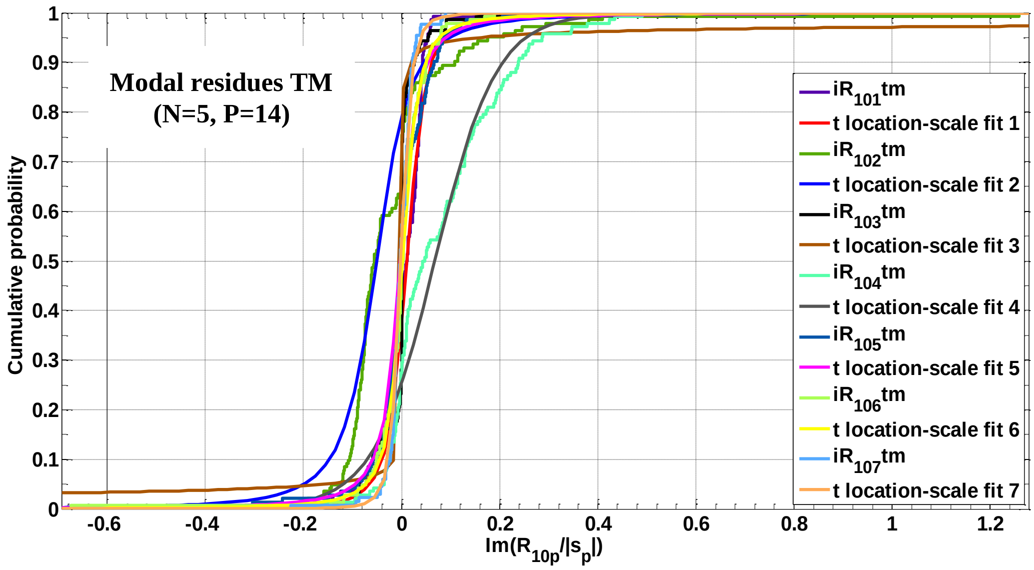

Fig. 6.12 Empirical CDF and "t location-scale" fit of $\mathfrak{Im}(R_{10p})$

Table 6.5 Estimated Parameters for Modal Residues R_{10p}TM (Bicone Class)

Pole n°	$\mathfrak{Re}$ (R_{10p}) (t location-scale)			$\mathfrak{Im}$ (R_{10p}) (Normal)		
	μ	σ	ν	μ	σ	ν
1	-0.0465	0.0105	1.5708	0.01066	0.02853	2.35
2	0.0905	0.13	9.6	-0.05091	0.05091	2.01
3	0.000157	0.000386	0.327	0.000161	0.000227	0.298
4	0.0255	0.062	3.53	0.068	0.0965	6.31
5	-0.01399	0.0253	1.596	-0.00266	0.0263	1.6
6	-0.00404	0.0294	3.47	0.00225	0.0223	1.687
7	-0.0066	0.0266	3.12	-0.00122	0.0151	2.6

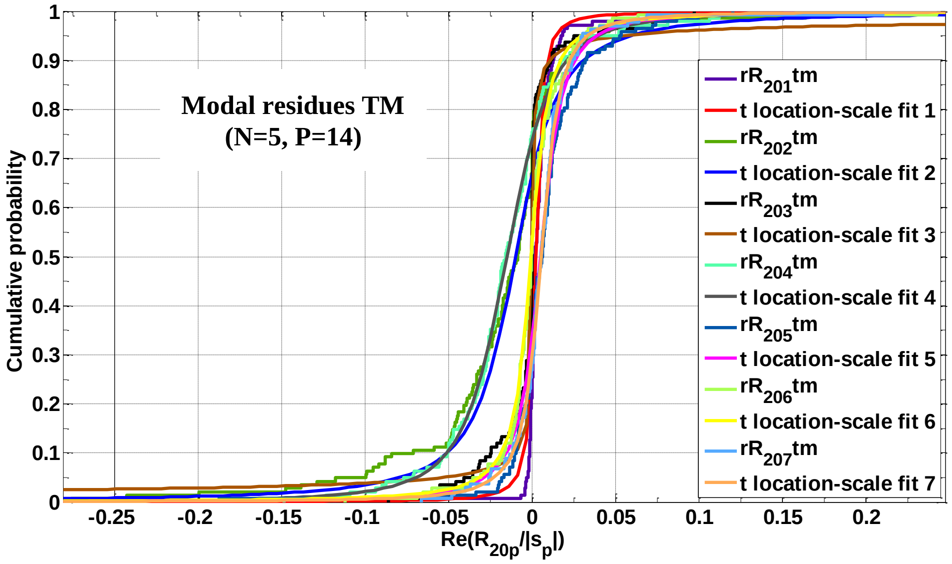

Fig. 6.13 Empirical CDF and “t location-scale” fit of $\mathfrak{Re}(R_{20p})$

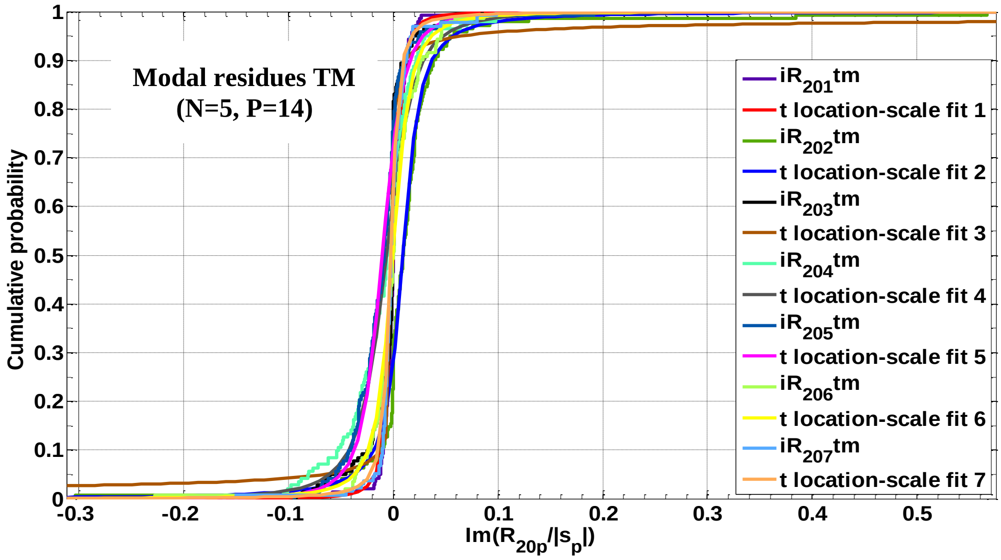

Fig. 6.14 Empirical CDF and “t location-scale” fit of $\mathfrak{Im}(R_{20p})$

Table 6.6 Estimated Parameters for Modal Residues R_{20p}TM (Bicone Class)

Pole n°	$\mathfrak{Re}$ (R_{20p}) (t location-scale)			$\mathfrak{Im}$ (R_{20p}) (Normal)		
	μ	σ	ν	μ	σ	ν
1	0.00214633	0.00306833	1.46434	0.000384389	0.00611425	2.08192
2	-0.00996263	0.0186394	1.49879	0.0093722	0.0123344	1.45501
3	0.000107165	0.000609779	0.42069	-0.00048047	0.000617685	0.405092
4	-0.0150173	0.01988	2.21249	-0.0065786	0.0198638	2.22894
5	0.0051196	0.00994134	1.66417	-0.0105931	0.015476	2.53716
6	-0.00068856	0.0076644	1.40311	-0.00036411	0.0123329	1.93763
7	0.00554253	0.00820745	1.64468	-0.00227872	0.00536487	1.51555

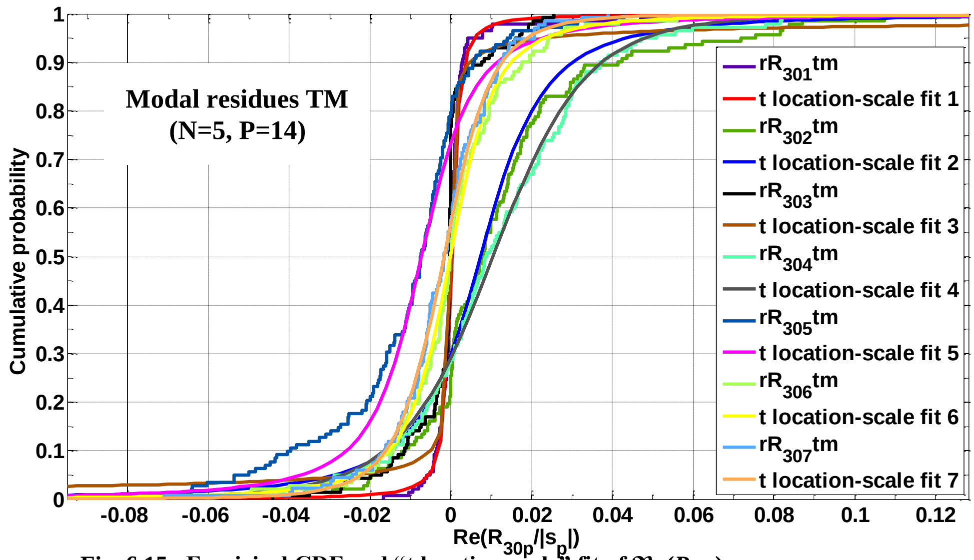

Fig. 6.15 Empirical CDF and "t location-scale" fit of $\mathfrak{Re}(R_{30p})$

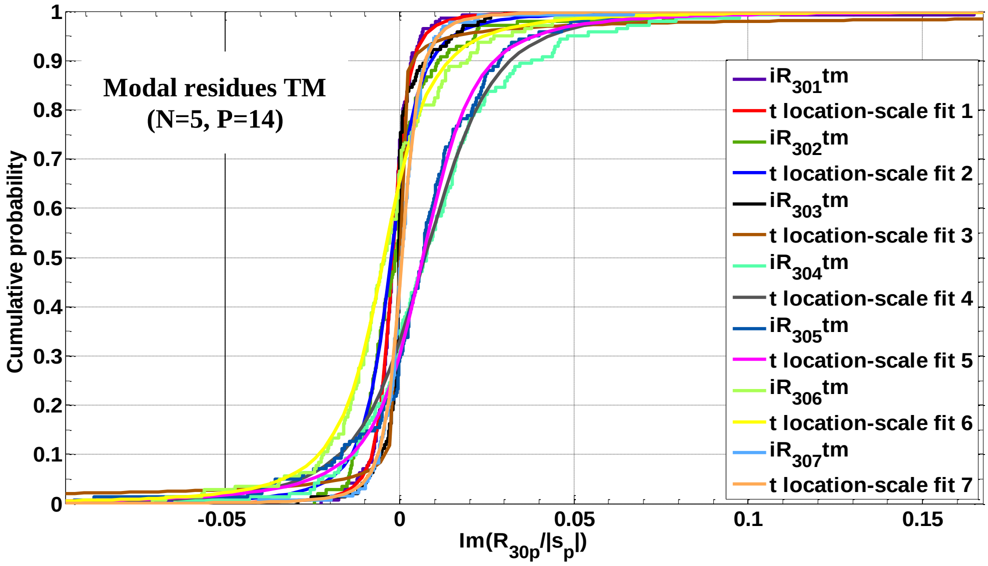

Fig. 6.16 Empirical CDF and "t location-scale" fit of $\mathfrak{Im}(R_{30p})$

Table 6.7 Estimated Parameters for Modal Residues R_{30p}TM (Bicone Class)

Pole n°	$\mathfrak{Re}$ (R_{30p}) (t location-scale)			$\mathfrak{Im}$ (R_{30p}) (Normal)		
	μ	σ	ν	μ	σ	ν
1	0.00016911	0.00137677	1.35725	-0.0019716	0.00314305	2.01203
2	0.00736074	0.0116368	1.83584	-0.00242872	0.0060816	2.02327
3	-0.00022328	0.000339207	0.443085	-0.00014390	0.000350029	0.487584
4	0.0104755	0.0176052	4.02217	0.00729218	0.0148153	2.86467
5	-0.00723808	0.00941803	1.79371	0.00673238	0.01092	1.98828
6	-0.00015324	0.00814066	2.04545	-0.00454025	0.00987527	1.99101
7	-0.001719	0.00894268	3.22804	0.000665355	0.00373477	2.18412

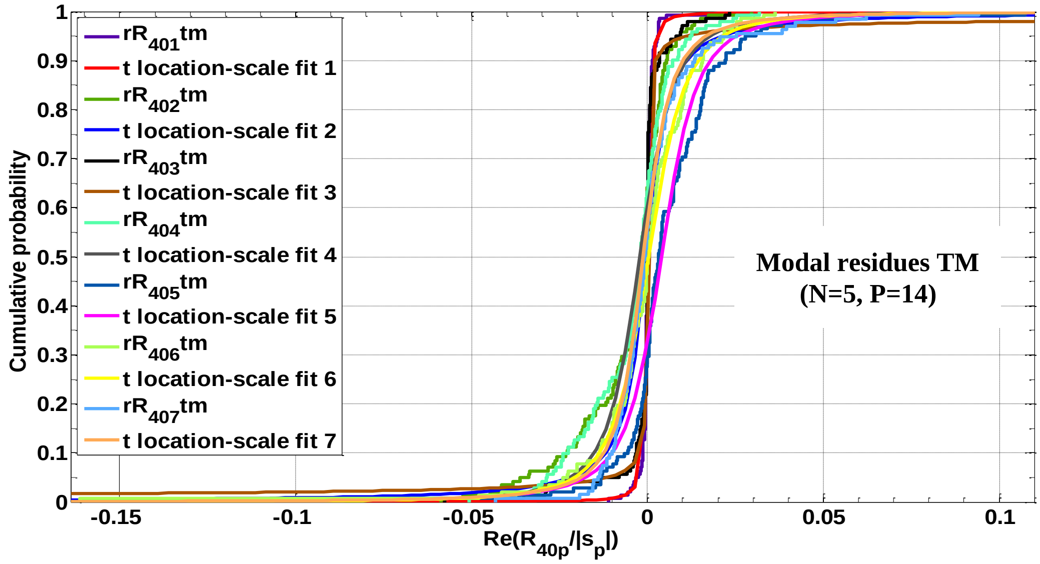

Fig. 6.17 Empirical CDF and "t location-scale" fit of $\mathfrak{Re}(R_{50p})$

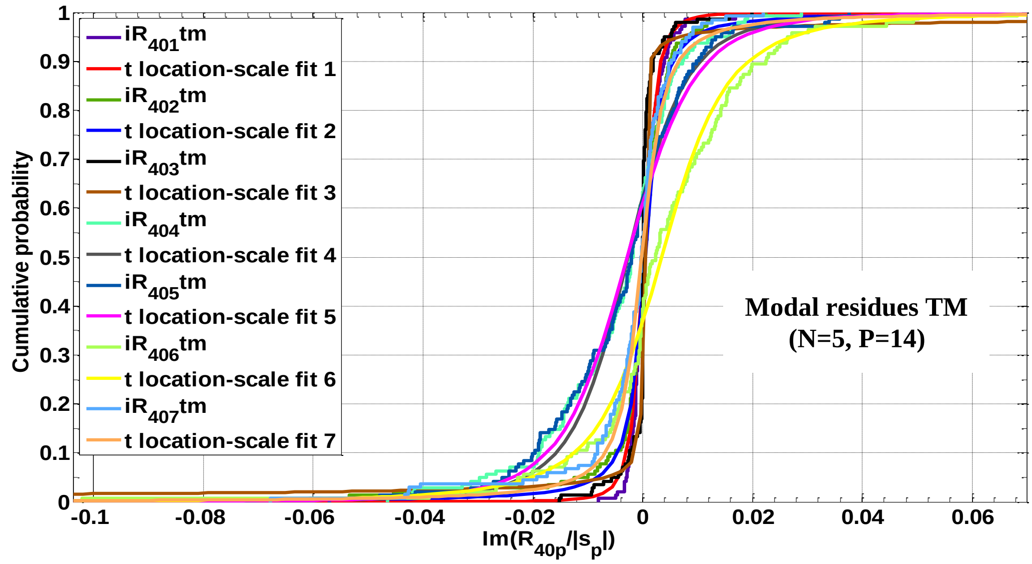

Fig. 6.18 Empirical CDF and "t location-scale" fit of $\mathfrak{Im}(R_{40p})$

Table 6.8 Estimated Parameters for Modal Residues R_{40p}TM (Bicone Class)

Pole n°	$\mathfrak{Re}$ (R_{40p}) (t location-scale)			$\mathfrak{Im}$ (R_{40p}) (Normal)		
	μ	σ	ν	μ	σ	ν
1	5.921e-005	0.00057984	1.34332	0.00021859	0.00169868	2.34656
2	-0.00037987	0.00431275	1.1675	0.000492064	0.0020864	1.33058
3	-2.68e-005	0.00011268	0.410022	5.773e-005	6.9587e-005	0.412937
4	-0.00207472	0.00707086	2.11324	-0.00264995	0.00798239	2.92751
5	0.00392681	0.00745575	2.03891	-0.00275352	0.00926805	3.33201
6	0.000341611	0.00775403	2.22439	0.0034168	0.00901638	2.3576
7	-0.00113729	0.00557201	1.7654	-0.00014289	0.00285558	1.36056

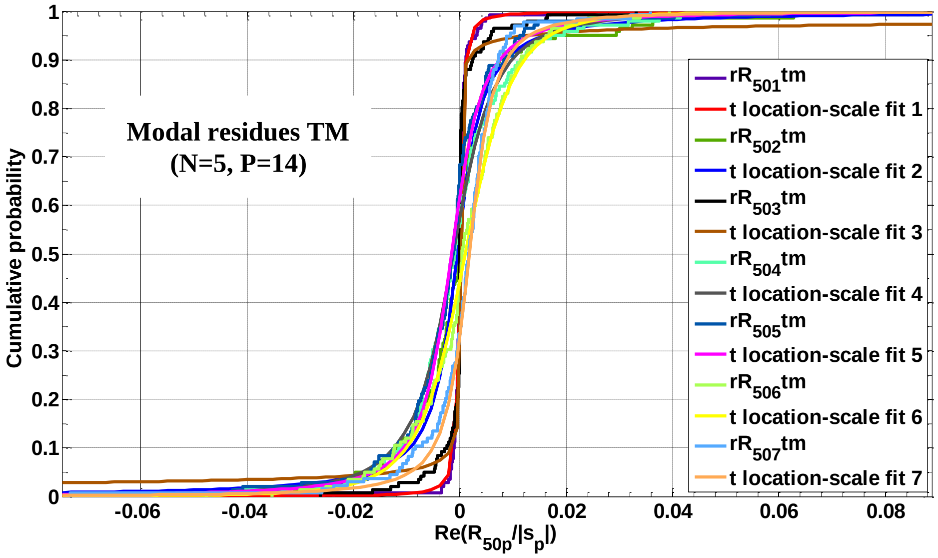

Fig. 6.19 Empirical CDF and "t location-scale" fit of $\mathfrak{Re}(R_{50p})$

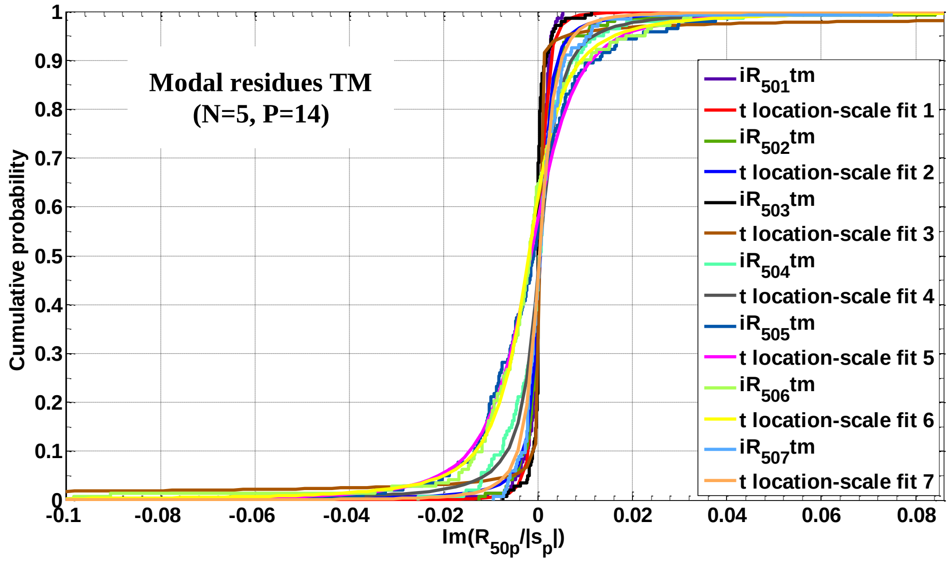

Fig. 6.20 Empirical CDF and "t location-scale" fit of $\mathfrak{Im}(R_{50p})$

Table 6.9 Estimated Parameters for Modal Residues R_{50p}TM (Bicone Class)

Pole n°	$\mathfrak{Re}(R_{50p})$ (t location-scale)			$\mathfrak{Im}(R_{50p})$ (Normal)		
	μ	σ	ν	μ	σ	ν
1	3.6826e-005	0.000489186	1.35893	0.000273686	0.00129811	2.28165
2	-0.00048879	0.00353548	1.22557	0.000464739	0.00157444	1.41144
3	5.2525e-006	3.2004e-005	0.323112	3.3998e-006	2.7842e-005	0.358561
4	-0.00127938	0.00582628	1.98028	0.00028803	0.00311659	1.50962
5	-0.00158193	0.00434169	1.65156	-0.0015840	0.00721329	2.27205
6	0.00102084	0.00672851	2.97443	-0.00203211	0.00547903	1.70546
7	0.00180742	0.00337843	1.6941	0.000273848	0.00246339	2.01053

6.4. Conclusion

In this chapter the procedure for ultra compressed statistical modeling for the antenna far field has been discussed. The number of required dominant poles P of the singularity expansion method (SEM) and the order N of the spherical mode expansion method (SMEM) has been chosen to be fixed, prior to applying the modeling procedure to the antenna population, as this reduces the time for data handling and this streamlines the subsequent statistical modeling.

The statistical modeling of a bicone antenna class has been presented. In this application example, the UWB response of the bicone was initially completely defined by 215 784 complex parameters, which after applying the ultra compression method has led to 210 complex parameters. Based on this intermediate result, we have further developed a simple statistical model able to adequately describe the variability of parameters over the population of antennas. It has been found that the natural frequencies of the bicone class were fairly well described by a normal distribution whereas the modal residues rather have a “t location-scale” distribution.

In general these models are used to generate $P/2$ correlated normal variables (for each pole pair). This can be done from a normalized uncorrelated, Gaussian vector, the covariance matrix, and the vector of means as given for f_p in Table 6.2. This regeneration of poles has been validated and demonstrated in Fig. 6.10. Once the poles and modal residues are known, the response can be regenerated easily. The validation of the regenerated response with respect to the initial distribution of the parameter space is the next logical step. For non Gaussian correlated variables, the same procedure should be applied, but prior to that a (non-linear) transformation from the considered distribution to a normal one should be performed. Once the normal correlated variables are generated, the inverse transformation should be used to obtain the final correlated variables following the considered distribution.

Summary and Conclusions

In any antenna design endeavor, the aim is to meet the application specific requirements (the input matching bandwidth, maximum gain and size). Unfortunately, this assiduous endeavor may take huge amounts of time even in the age of sophisticated EM solvers. One way to cope with this aforementioned time consumption issue is to have an approximate a priori knowledge about the final antenna design with respect to the initial requirements. This can be achieved by building the statistical models of the main characteristics of various antenna design classes (common or specific). In science, we have known for more than two centuries that phenomena that are difficult to predict from deterministic laws can be predicted, to a certain level of uncertainty, from the theory of probabilities. The statistical modeling of antennas is based on this very general recognition. Although it is very uncommon to use statistical and probabilistic methods in the field of antennas, there is no fundamental reason why it should be forbidden, or even uninteresting.

In this thesis we have focused on the statistical modeling of small UWB antennas. The work carried out provides answers to two main questions for the statistical antenna modeling: the generation of statistically adequate antenna data samples and the modeling of the main characteristics of an antenna population.

We have proposed a generic antenna design approach for UWB planar antennas as a tool to generate many antenna samples. The main features of this approach are its flexibility and versatility. Flexibility stems from the parametric nature of the underlying models, which allows to modify a design by small or wide parameter increments. The versatility is characterized by the wide variety of antenna shapes that can be designed (triangular, disc or staircase). Various planar monopoles and dipoles have been demonstrated as the possible outcomes of this approach.

All together five monopoles, triangular, staircase, crab-claw, disc and dual feed monopole designs have been presented, as derived from the generic design. In the case of dipoles, two planar balanced dipoles, namely triangular and disc planar balance dipole designs have also been described. All of these designs have been optimized —through evolutionary search algorithm— under stringent UWB criteria, which are compactness in size and input matching lower than −10 dB over the bandwidth of [3-11] GHz.

In order to demonstrate the capabilities of the method and further show its versatility, a compact multiband design has also been proposed in the same spirit as the generic design approach. It is able to operate in the three WiFi bands IEEE 802.11 'a/g/n' , 'b/g/n' and 'y'. Moreover, it has been demonstrated that the design had good in-band matching and out-of-band rejection.

The small volumic 3D Bicone design has also been demonstrated, after parameterizing its design and searching a compact optimized design through the genetic algorithm optimization technique.

We also have proposed a general method to create a statistical population of antennas, which takes into account the optimal design as generator design and creates a parameter space around the optimized values, for eventual population creation. Using this method, statistical populations of all the design mentioned above have been generated.

The statistical analysis has subsequently been performed for all the aforementioned monopoles, dipole and Bicone antennas over two output parameters, which are the antenna Mean Matching Efficiency (*MME*) and the maximum Mean Realized Gain (MRG_{max}). It has been observed that the Generalized Extreme value distribution was a suitable distribution in order to accurately model the MRG_{max} and *MME* of these designs.

An UWB Antenna radiation pattern is a combination of a huge number of complex parameters. Therefore, in order to model this pattern the number of complex coefficients had first to be reduced drastically. This has been done through a combination of the Singularity expansion method (SEM) and the spherical mode expansion method (SMEM), which is known to provide a strong reduction of this number. We have applied these ultra-compression techniques on the antenna statistical population, in order to model the radiation pattern representative of a class or subclass of antennas. For bicones, which possess the symmetry of revolution, a particularly small number of modeling parameters has been necessary for accurate modeling.

Finally, a statistical model of bicones has been proposed, involving 14 poles for the SEM, and a dominant order N = 5 for the SMEM. It has been observed that the natural frequencies of the model are normally distributed whereas the damping factors distribution can be modeled with generalized extreme value distribution. In addition, the modal residues could be reasonably well described by a "t location scale" distribution.

A model for pole natural frequencies f_p has been proposed and validated by regeneration of pole pairs. Once the poles and modal residues are known, the response can be regenerated easily. The validation of the regenerated response with respect to the initial distribution of the parameter space is the next logical step.

Perspective

The model for Gaussian correlated variables as pole natural frequencies can be validated as the available tools like decomposition of covariance matrix support Gaussian correlated variables. The non-Gaussian correlated variables such as the model for residues it is very complex and requires further study. One solution for latter could be the use of a non-linear transforms for the consider distribution to bring it to normal distribution. This requires study in the multivariate statistical modeling domain and hence left.

The relation between the effects of initial parametric modeling parameters is also very interesting as this study can better define the modeling parameters selection and hence the statistical model itself.

Relation of modeling parameters and initial geometric parameter space is also interesting as this study can be resulted in a priori knowledge of designing parameter space.

Publications

1. Muhammad Amir Yousuf & Christophe Roblin 2010. “Tri-Band Antenna for WLAN 802.11 ‘a/n’‘b/g/n’ and ‘y’ - A Planar Generic Antenna Design approach”, 5th European Conference on Antenna and Propagations EuCap2011.

2. Muhammad Amir Yousuf & Christophe Roblin 2009. “Analysis & Generation of Statistical Population of Planar UWB” antennas EuCAP 2010”, 4rth European Conference on Antenna and Propagations

3. Christophe Roblin and Muhammad Amir Yousuf 2009. “Statistical Models of wideband and UWB omnidirectional antennas based on parametric modeling” EuCAP2010, 4rth European Conference on Antenna & Propagation

4. Christophe Roblin & Muhammad Amir Yousuf 2009. A "Generic" Design of Planar UWB Antennas for Parametric or Statistical Analysis EuCAP 2009, 3rd European Conference on Antennas and Propagation.

References

[1]. "FCC News, Web page, New public safety application and broadband internet access among uses envisioned by FCC authorization of Ultra Wideband technology, Announcement of Commission Action." FCC (2002).

[2]. FCC, ‘‘Revision of Part 15 the Commission’s Rules Regarding Ultra-wideband Transmission Systems,’’ ET Docket, 2002.

[3]. R. A. Scholtz, "Multiple access with time-hopping impulse modulation", *Proc. MILCOM*, pp 447 - 450 , 1993.

[4]. Conroy, J.T.; LoCicero, J.L.; Ucci, D.R.; , "Communication techniques using monopulse waveforms," *Military Communications Conference Proceedings, 1999. MILCOM 1999. IEEE* , vol.2, no., pp.1181-1185 vol.2, 1999.

[5]. M. Ghavami, L. B. Michael, S. Haruyama, and R. Kohno, “A novel UWB pulse shape modulation system”, *Kluwer Wireless Personal Communications Journal*, vol 23:p 105–120, 2002.

[6]. H. Sheng, ‘‘Transceiver design and system optimization for Ultra-Wideband communications,’’ Ph.D. Dissertation, New Jersey Institute of Technology, Newark, May 2005.

[7]. Zhi Ning Chen; Xuan Hui Wu; Hui Feng Li; Ning Yang; Chia, M.Y.W.; , "Considerations for source pulses and antennas in UWB radio systems," Antennas and Propagation, IEEE Transactions on , vol.52, no.7, pp. 1739- 1748, July 2004.

[8]. Balanis C.A, “Antenna Theory, Analysis and Design”, chapter 2, 3rd Edition, WILIEY NEW YORK, 2007,

[9]. Schantz, H.G.; , "Dispersion and UWB antennas," Ultra Wideband Systems, 2004. Joint with Conference on Ultra wideband Systems and Technologies. Joint UWBST & IWUWBS. 2004 International Workshop on , vol., no., pp. 161- 165, 18-21 May 2004.

[10]. Schantz, H.G.; , "A brief history of UWB antennas," *Aerospace and Electronic Systems Magazine, IEEE* , vol.19, no.4, pp. 22- 26, April 2004

[11]. O. Lodge, “Electric Telegraphy,” U.S. Patent 609,154 (August 16, 1898).

[12]. Akdagli, A.; Ozdemir, C.; Yamacli, S. A Review of Recent Patents on Ultra Wide Band (UWB) Antennas. Recents Patents on Electrical Engineering, Vol. 1, No. 1, (January 2008) 8 (68-75), ISSN: 1874-4761.

[13]. Ammann, M.J. & Chen, Z.J. ,“A Wide Band Shorted Planar Monopole with Bevel. *IEEE Transactions on Antennas and Propagation*, Vol. 51, No. 4, April 2003

[14]. Kim, Y & Kwon, D.H., “CPW-Fed Planar Ultra Wideband Antenna Having a Frequency Band Notch Function”, *Electronics Letters*, Vol. 40, No. 7, April 2004.

[15]. Agrawal, P.; Kumar, G.; Ray & K.P., “New Wide-Band Monopole Antennas”, *Proceedings of IEEE International Symposium on Antennas and Propagation*, pp. 248-251, July 1997, IEEE,.

[16]. Huang, C.Y. & Hsia, W.C., “Planar Elliptical Antenna for Ultra wideband Communications”. *Electronics Letters*, Vol. 41, No. 6, March 2005.

[17]. Yi-Cheng Lin; Kuan-Jung Hung; , "Compact Ultra wideband Rectangular Aperture Antenna and Band-Notched Designs," *Antennas and Propagation, IEEE Transactions on* , vol.54, no.11, pp.3075-3081, Nov. 2006.

[18]. Ammann, M.J.; Zhi Ning Chen; , "Wideband monopole antennas for multi-band wireless systems," *Antennas and Propagation Magazine, IEEE* , vol.45, no.2, pp. 146- 150, April 2003.

[19]. Liang, J.; Chiau, C.C.; Chen, X.; Parini, C.G.; , "Printed circular disc monopole antenna for ultra-wideband applications," *Electronics Letters* , vol.40, no.20, pp. 1246- 1247, 30 Sept. 2004.

[20]. Shantz Hans, “The Art and Science of UWB Antennas”, ARTECH HOUSE, London, 2005.

[21]. I. Oppermann, "An overview of UWB activities within PULSERS," Presented in Ultra-Wideband in Singapore 2004.

[22]. http://www.antennamagus.com/

[23]. Ruze, J., “The effect of aperture errors on the antenna radiation pattern”, Suppl. al Nuovo Cimento, vol. 9, no. 3, p. 364, 1952.

[24]. Bailin, L.L., Ehrlich, M.J., “Factors affecting performance of linear arrays”, *Proc. IRE*, vol. 41, no.2, p. 235, 1953.

[25]. Gilbert, E.N., Morgan, S.P., “Optimum design of directive antenna arrays subject to random variations”, *Bell Syst. T.J.*, vol. 34, no. 3, p.637, 1955.

[26]. Cheng, D.K., “Effect of arbitrary phase errors on the gain and beamwidth characteristics of radiation patterns”, *IRE Trans.*, vol. AP-3, no. 3, P• 145, 1955.

[27]. Robieux, J., Influence de la précision de fabrication d'une antenne sur ses performances, Ann, *de Radio et électricité*, vol. 11, no. 43, p. 29, 1956.

[28]. Elliot, R.S., Mechanical and electrical tolerances for two-dimensional scanning antenna arrays, *IRE Trans.*, vol. AP-6, no. 1, p. 114, 1958.

[29]. Rondinelli, L.A., “Effects of random errors on the performance of antenna arrays of many elements”. *IRE Nat. Conv.Rec.*. vol. 7, Pt. 1, p. 174, 1959.

[30]. Bates, R.H.T., “Random errors in aperture distributions”, *IRE Trans.*, vol. AP-7, no. 4, p, 369, 1959.

[31]. Consortini, A., Ronchi, L., Scheggi, A.M., Di Francia, G,T., “Gain limit and tolerances of big reflector antennas”, *Alta Frequenza*, v. XXX,no. 3, p.232, 1961.

[32]. Consortini, A., Ronchi, L., Scheggi, A.M., Di Francia, G.T., “The influence of random errors on the gain of an array antenna”. *Alta Frequenza*, vol. XXXI, no. 8, p. 528, 1962.

[33]. Bracewell, R.N., “Tolerance theory of large antennas”, *IRE Trans.*, vol. AP-9, no. 1, p.49, 1961.

[34]. Ruze, J. “Anenna tolerance theory – a review”, Proc. IRE, vol.54, no. 4, p. 633, 1966.

[35]. SHIFRIN Y. S., “Statistical Antenna Theory”, The GOLEM PRESS, Boulder, Colorado, 1971.

[36]. C. Roblin, “A Preliminary Approach of the Statistical Modeling of Antennas for the UWB Communications”, *ICEAA-EESC '05*. Torino, Italy. 2005, 12-16 Sept.

[37]. Ch. Roblin, “Ultra compressed parametric modeling of UWB antenna measurements”, *EuCAP* 2006, Nice, 6-10 Nov. 2006

[38]. A. Sibille “Statistical antenna modeling”. 29th *URSI General Assembly*. Chicago, USA. 10-16 Aug.

[39]. Roblin Ch. and Yousuf A., “A Generic design of Planar UWB Antennas for Parametric Statistical Analysis,” EuCAP, Berlin, march 23–27, 2009.

[40]. Bories S., Roblin Ch. and Sibille A., “Dual strip-line fed metal sheet Monopoles for UWB Terminal Applications”, *ANTEM* 2005 Proc., St. Malô, France, pp. 142–143, june 2005.

[41]. Antonio-Daviu E., Cabedo_Fabrés M., Ferrando-Bataller M. and Valeiro_Nogueira A., “Wideband double-fed planar monopole antennas,” *Electronics Letters*, Vol. 39, No. 23, Nov. 2003.

[42]. Bories S., Ghannoum H. and Roblin Ch.. “Robust Planar Stripline Monopole for UWB Terminal Applications,” *Proc.* 2005 *IEEE International Conf. on Ultra-Wideband*, 2005.

[43]. Ghannoum H., Bories S., and D’Errico R., “Small-Size UWB Planar Antenna and its Behaviour in WBAN/WPAN Applications,” *IEE Symposium on Ultra Wideband Systems, Technologies, and Applications*, London, April 20, 2006.

[44]. Qiu, J., Du, Z., Lu, J and Gong, K “A case study to improve the impedance bandwidth of planar monopole” *Microwave and optical Technology Letters*, Vol. 452, No. 2, 124 – 126, 2005.

[45]. Schantz, H. G. and Fullerton, L, “The diamond dipole: A Gaussian impulse antenna”, *IEEE Antenna and Propagation Society International Symposium*, Vol. 4, p. 100 – 103, 2001.

[46]. Kerkhoff, A., Rogers, R. and Ling, H., “The use of genetic algorithm approach in the design of UWB antennas”, *IEEE Radio and Wireless Conference*, 93 – 96, 2001.

[47]. Agrawall, N. P., Kumar, G. and Ray, K. P. “Wide-band planar monopole antennas”, *IEEE transactions on Antennas and Propagation*, Vol. 46, No.2, pp. 294 – 295, 1998.

[48]. Honda, S., Ito M., Seki H., and Jingo Y., “A Disc Monopole Antenna with 1:8 Impedance Bandwidth and Omni-directional Radiation Pattern,” *Proc. ISAP, Sapporo,Japan*, 1992, pp. 1145-1148.

[49]. Hammoud, Poey P., and Colomel F., “Matching the Input Impedance of a Broadband Disc Monopole, ” *Electronics Letters*, Vol. 29, Feb. 1993, pp. 406-407.

[50]. Ray, K. P., Anob P. V., Kapur R., and Kumar G., “Broadband Planar Rectangular Monopole Antennas,” *Microwave Optical Tech. Letters*, Vol. 28, No. 1, 2001, pp. 55-59.

[51]. Ballantine, S.; , "High Quality Radio Broadcast Transmission and Reception," *Proceedings of the Institute of Radio Engineers* , vol.23, no.6, pp. 618- 652, June 1935.

[52]. Chang, D. C., Harrison C. W. Jr., and Aroson E. A., “Tubular Monopole of Arbitrary Dimensions: The Radiation Field,” *IEEE Trans. Antennas Propagation*, Vol. 17, May1969, pp. 534-540.

[53]. Naffall Herscovici and Christos Christodouloc , “Wideband monopole antennas for multi-band wireless systems” *IEEE Antennas and Propagation Magazine* , Vol. 45, No.2,April 2003.

[54]. Shun-Yun Lin; , "Multi-band planar monopole antenna for handset," *Antennas and Propagation Society International Symposium, 2003. IEEE* , vol.3, no., pp. 56- 59 vol.3, 22-27 June 2003.

[55]. Jen-Yea Jan; Liang-Chih Tseng; , "Planar monopole antennas for 2.4/5.2 GHz dual-band application," *Antennas and Propagation Society International Symposium, 2003. IEEE*, vol.4, no., pp. 158- 161 vol.4, 22-27 June 2003.

[56]. Kerkhoff, A.; Ling, H.; , "Design of a planar monopole antenna for use with ultra-wideband (UWB) having a band-notched characteristic," *Antennas and Propagation Society International Symposium, 2003. IEEE* , vol.1, no., pp. 830- 833 vol.1, 22-27 June 2003.

[57]. Ammann, M.J.; Zhi Ning Chen; , "A wide-band shorted planar monopole with bevel," *Antennas and Propagation, IEEE Transactions on* , vol.51, no.4, pp. 901- 903, April 2003.

[58]. Zhi Ning Chen; , "Impedance characteristics of planar bow-tie-like monopole antennas ," *Electronics Letters* , vol.36, no.13, pp.1100-1101, 22 Jun 2000.

[59]. Z. N. Chen, "Experimental on Input Impedance of Tilted Planar Monopole Antennas", *Microwave and Optical Technology Letters*, vol. 26, no. 3, pp.202 - 204 , 2000.

[60]. Lee, G.; Chiou, T.; Wong, K.; Wang, C.; , "Low-profile planar monopole antenna for GSM/DCS/PCS triple-band mobile phone," *Antennas and Propagation Society International Symposium, 2002. IEEE* , vol.3, no., pp. 26, 2002.

[61]. Chen, Z.N.; Ammann, M.J.; Chia, M.Y.W.; See, T.S.P.; , "Annular planar monopole antennas," *Microwaves, Antennas and Propagation, IEE Proceedings -* , vol.149, no.4, pp. 200- 203, Aug 2002.

[62]. Lee, E.; Hall, P.S.; Gardner, P.; , "Compact wideband planar monopole antenna," *Electronics Letters* , vol.35, no.25, pp.2157-2158, 9 Dec 1999.

[63]. Liu, W.-C.; , "Design of a CPW-fed notched planar monopole antenna for multiband operations using a genetic algorithm," *Microwaves, Antennas and Propagation, IEE Proceedings -* , vol.152, no.4, pp. 273- 277, 5 Aug. 2005

[64]. Kim, T.H.; Park, D.C.; , "CPW-fed compact monopole antenna for dual-band WLAN applications," *Electronics Letters* , vol.41, no.6, pp. 291- 293, 17 March 2005

[65]. Angelopoulos, E.S.; Stratakos, Y.E.; Kostaridis, A.I.; Kaklamani, D.I.; Uzunoglu, N.K.; , "Multiband miniature coplanar waveguide slot antennas for GSM-802.11b and 802.11b-802.11a wireless applications," *Wireless Communications and Networking, 2003. WCNC 2003. 2003 IEEE* , vol.1, no., pp.103-108 vol.1, 20-20 March 2003

[66]. Llorens, D.; Otero, P.; Camacho-Penalosa, C.; , "Dual-band, single CPW port, planar-slot antenna," *Antennas and Propagation, IEEE Transactions on* , vol.51, no.1, pp. 137-139, Jan 2003.

[67]. Chien-Wen Chiu; Yu-Jen Chi; , "Planar Hexa-Band Inverted-F Antenna for Portable Device Applications," *Antennas and Wireless Propagation Letters, IEEE* , vol.8, no., pp.1099-1102, 2009.

[68]. Tae-Hyun Kim; Dong-Chul Park; , "Compact dual-band antenna with double L-slits for WLAN operations," *Antennas and Wireless Propagation Letters, IEEE* , vol.4, no., pp. 249- 252, 2005.

[69]. McNamara, D.; Baker, D.; Botha, L.; , "Some design considerations for biconical antennas," *Antennas and Propagation Society International Symposium, 1984* , vol.22, no., pp. 173- 176, Jun 1984.

[70]. Schelkunoff, S.A. and Harald Friis, Antennas: Theory and Paractice, New York: John Wiley and sons, 1952, pp. 314-319.

[71]. Baum, Carl E., "Design of pulse radiating dipole antennas as Related to High-Frequency and Low-Frequency Limits", Sensor and simulation Note#69, January 13, 1969.

[72]. Baum, Carl E., "An equivalent charge method for defining geometries of dipole antennas", Sensor and simulation Note#72, January 24, 1969.

[73]. Roblin C., Bories S., and Sibille A., "Characterization tools of antennas in the Time Domain," IWUWBS, Oulu, June 2003

[74]. XAVIER BEGAUD, Ultra Wide Band antennas, Ch. 3, John Wiley & Sons, Inc., USA, 2011.

[75]. Johnson, J.M.; Rahmat-Samii, V.; , "Genetic algorithms in engineering electromagnetics," Antennas and Propagation Magazine, IEEE , vol.39, no.4, pp.7-21, Aug 1997

[76]. John, M.; Ammann, M.J.; , "Antenna Optimization With a Computationally Efficient Multiobjective Evolutionary Algorithm," *Antennas and Propagation, IEEE Transactions on* , vol.57, no.1, pp.260-263, Jan. 2009

[77]. W.-C. Liu, "Design of a CPW-fed notched planar monopole antenna for multiband operations using a genetic algorithm", *IEE Proc.-Microw. Antennas Propag.*, Vol. 152, No. 4, August 2005.

[78]. Kim, T.H.; Park, D.C.; , "CPW-fed compact monopole antenna for dual-band WLAN applications," *Electronics Letters* , vol.41, no.6, pp. 291- 293, 17 March 2005

[79]. Angelopoulos, E.S.; Stratakos, Y.E.; Kostaridis, A.I.; Kaklamani, D.I.; Uzunoglu, N.K.; , "Multiband miniature coplanar waveguide slot antennas for GSM-802.11b and 802.11b-802.11a wireless applications," *Wireless Communications and Networking, 2003. WCNC 2003. 2003 IEEE* , vol.1, no., pp.103-108 vol.1, 20-20 March 2003

[80]. Llorens, D.; Otero, P.; Camacho-Penalosa, C.; , "Dual-band, single CPW port, planar-slot antenna," *Antennas and Propagation, IEEE Transactions on* , vol.51, no.1, pp. 137-139, Jan 2003.

[81]. Chien-Jen Wang; Jin-Jei Lee; Rey-Bin Huang; , "Experimental studies of a miniaturized CPW-fed slot antenna with the dual-frequency operation," *Antennas and Wireless Propagation Letters, IEEE* , vol.2, no.1, pp.151-154, 2003.

[82]. Chien-Wen Chiu; Yu-Jen Chi; , "Planar Hexa-Band Inverted-F Antenna for Portable Device Applications," *Antennas and Wireless Propagation Letters, IEEE* , vol.8, no., pp.1099-1102, 2009.

[83]. Tae-Hyun Kim; Dong-Chul Park; , "Compact dual-band antenna with double L-slits for WLAN operations," *Antennas and Wireless Propagation Letters, IEEE* , vol.4, no., pp. 249- 252, 2005.

[84]. HARRINGTON R. F., Time-Harmonic Electro-magnetic Fields, McGraw-Hill, New York, USA, 1961.

[85]. HANSEN J.E. (Ed.), Spherical near-field antenna measurements, IEE Electromagnetic waves series 26, Peter Pregrinius, London, United Kingdom, 1988.

[86]. SCHELKUNOFF S.A., Electromagnetic waves, D. Van Nostrand Company, Reston, Virginia, USA, 1943.

[87]. ROBLIN C., Ultra compressed parametric modeling of UWB antenna measurements, EuCAP, Nice, 6-10 November 2006.

[88]. BELOUSOV, S. L., Tables of normalized associated Legendre polynomials, Pergamon Press, Oxford. 1962

[89]. JENSEN F., FRANDSEN A., On the number of modes in spherical wave expansions, AMTA, Stone Mountain Park, GA,USA, p. 489-494, October 2004

[90]. XAVIER BEGAUD, Ultra Wide Band antennas, Ch. 3, John Wiley & Sons, Inc., USA, 2011.

[91]. C. E. BAUM, On the singularity expansion method for the solution of electromagnetic interaction problems, Interaction Note 88, December 1971.

[92]. C. E. BAUM, The singularity expansion method, in Transient Electromagnetic Fields, Springer-Verlag, Berlin, pp. 129–179, 1976.

[93]. FELSEN L. B., Ed., “Transient Electromagnetic Fields” , in *Topics on Applied Physics*, Springer-Verlag, vol. 10, 1976.

[94]. LICUL S., DAVIS W.A., “Unified Frequency and Time Domain Antenna Modeling and Characterization”, *IEEE Trans. on Antennas and Propagation*, vol. 53, n° 9, September 2005, p. 2882-2888.

[95]. Y. Hua and T. K. Sarkar, “Generalized pencil-of-function method for extracting poles of an EM system from its transient response”, IEEE Trans. Antennas Propagation., Vol. 37, No. 2, pp.229–234, February 1989

[96]. T. K. Sarkar and O. Pereira, “Using the matrix pencil method to estimate the parameters of a sum of complex exponentials”, *IEEE Antennas Propagation. Mag*., Vol. 37, pp. 48–55, February1995.

[97]. Y. Hua and T. K. Sarkar, “Matrix pencil method for estimating parameters of exponentially damped/undamped sinusoids in noise”, *IEEE Trans. Acoustics Speech Signal Processing*, Vol. 38, pp. 814–824, May 1990.

[98]. R. Prony, Essai expérimental et analytique sur les lois de la dilatabilité de fluides élastiques et sur celles de la force expansive da la vapeur de l’alcool, a différentes températures, Paris J. l’Ecole Polytechnique, Vol. 1, No. 2, pp. 24–76, 1795.

[99]. VAN BLARICUM M.L., MITTRA R., “ A technique for Extracting the Poles and Residues of a System Directly from its Transient Response”, *IEEE Trans. on Antennas and Propagation*, vol. 23, n° 6, November 1975, p. 777-781.

[100]. M. L. Van Blaricum and R. Mittra, “Problems and solutions associated with Prony’s method for processing transient data”, *IEEE Trans. Antennas Propagation*, Vol. 26, pp. 174–182, January 1978.

[101]. ROBLIN C., SIBILLE A., “Antenna Effects and Modeling in UWB Impulse Radio, Ultra-Wideband Short-Pulse Electromagnetics”, UWB-SP 7, vol. 7, April 2007, p. 391-400.

[102]. ROBLIN C., BORIES S., SIBILLE A., LEPAGE A.-C., BEGAUD X., “Antenna Design, Analysis and Numerical Modeling for Impulse UWB”, *International Symposium on Wireless Personal Multimedia Communication*, WPMC 2004, Albano Terme, Italy, 12-15 September 2004.

[103]. KUMASERAN R., TUFTS D. W., “Estimating the Parameters of Exponentially Damped Sinusoids and Pole-Zero Modeling in Noise”, *IEEE Trans. on Acoustics, Speech, and Signal Processing*, vol. 30, n° 6, December 1982, p. 833-840.

[104]. KUMASERAN R., “Identification of Rational Transfer Function From Frequency Response Samples”, *IEEE Trans. on Aerospace and Electronic Systems*, vol. 26, n° 6, November 1990.

[105]. KUMASERAN R., “On a Frequency Domain Analog to Prony’s Method “, *IEEE Trans. on Acoustics*, Speech, and Signal Processing, vol. 38, n° 1, January 1990

[106]. ROBLIN C., “Ultra Compressed Parametric Modeling for symmetric or pseudo-symmetric UWB Antenna,” *ICUWB, Invited Papers on Ultra wideband Antennas*, Hannover (Ger.), Sept. 10-12, 2008.

Annex – A

A Goodness of fit Tests

A.1 Chi-Squared Test

The Chi-Squared test is used to determine if a sample comes from a population with a specific distribution. This test is applied to binned data, so the value of the test statistic depends on how the data is binned. It is noted that this test is available for continuous sample data only.

Although there is no optimal choice for the number of bins (k), there are several formulas which can be used to calculate this number based on the sample size (N). For example, the following empirical formula can be used:

$$k = 1 + \log_2 N \tag{7.1}$$

The data can be grouped into intervals of equal probability or equal width. The first approach is generally more acceptable since it handles peaked data much better. Each bin should contain at least 5 or more data points, so certain adjacent bins sometimes need to be joined together for this condition to be satisfied.

A.1.1 Definition

The Chi-Squared statistic is defined as

$$\chi^2 = \sum_{i=1}^{k} \frac{\left(O_i - E_i\right)^2}{E_i} \tag{7.2}$$

where, Oi is the observed frequency for bin i, and Ei is the expected frequency for bin i calculated by:

$$E_i = F(x_2) - F(x_1) \tag{7.3}$$

where F is the CDF of the probability distribution being tested, and x1, x2 are the limits for bin i.

A.1.2 Hypothesis Testing

The null and the alternative hypotheses are:

- H_0: the data follow the specified distribution;
- H_A: the data do not follow the specified distribution.

The hypothesis regarding the distributional form is rejected at the chosen significance level (α) if the test statistic is greater than the critical value defined as:

$$\chi^2_{1-\alpha,k-1} \tag{7.4}$$

meaning the Chi-Squared inverse CDF with k-1 degrees of freedom and a significance level of α. Though the number of degrees of freedom can be calculated as k-c-1 (where c is the number of estimated parameters), but commonly it is calculated as k-1 since this kind of test is least likely to reject the fit in error.

A.1.3 P-Value

The P-value, in contrast to fixed values, is calculated based on the test statistic, and denotes the threshold value of the significance level in the sense that the null hypothesis (H0) will be accepted for all values of α less than the P-value. For example, if P = 0.025, the null hypothesis will be accepted at all significance levels less than P (i.e. 0.01 and 0.02), and rejected at higher levels, including 0.05 and 0.1.

The P-value can be useful; in particular, when the null hypothesis is rejected at all predefined significance levels, and we need to know at which level it could be accepted.

A.2 Kolmogorov-Smirnov Test

This test is used to decide if a sample comes from a hypothesized continuous distribution. It is based on the empirical cumulative distribution function (ECDF). Assume that we have a random sample $x_1, \ldots, x_n$ from some distribution with CDF F(x). The empirical CDF is denoted by

$$F_n(x) = \frac{1}{n}\left[\text{Number of observations } \leq x\right] \tag{7.5}$$

A.2.1 Definition

The Kolmogorov-Smirnov statistic (D) is based on the largest vertical difference between the theoretical and the empirical cumulative distribution function:

$$D = \max_{1 \le i \le n} \left(F\left(x_i\right) - \frac{i-1}{n}, \frac{i}{n} - F\left(x_i\right) \right) \tag{7.6}$$

A.2.2 Hypothesis Testing

The null and the alternative hypotheses are:

- H_0: the data follow the specified distribution;
- H_A: the data do not follow the specified distribution.

The hypothesis regarding the distributional form is rejected at the chosen significance level (α) if the test statistic, D, is greater than the critical value obtained from a table. The fixed values of α (0.01, 0.05 etc.) are generally used to evaluate the null hypothesis (H_0) at various significance levels. A value of 0.05 is typically used for most applications, however, in some critical industries; a lower value may be applied.

The standard tables of critical values used for this test are only valid when testing whether a data set is from a completely specified distribution. If one or more distribution parameters are estimated, the results will be conservative: the actual significance level will be smaller than that given by the standard tables and the probability that the fit will be rejected in error will be lower

A.3 Anderson-Darling Test

The Anderson-Darling procedure is a general test to compare the fit of an observed cumulative distribution function to an expected cumulative distribution function. This test gives more weight to the tails than the Kolmogorov-Smirnov test.

A.3.1 Definition

The Anderson-Darling statistic (A^2) is defined as:

$$A^2 = -n - \frac{1}{n} \sum_{i=1}^{n} (2i-1) \cdot \left[\ln F\left(X_i\right) + \ln\left(1 - F\left(X_{n-i+1}\right)\right) \right] \tag{7.7}$$

A.3.2 Hypothesis Testing

The null and the alternative hypotheses are:

H_0: the data follow the specified distribution;

H_A: the data do not follow the specified distribution.

The hypothesis regarding the distributional form is rejected at the chosen significance level (α) if the test statistic, A^2, is greater than the critical value obtained from a table. The fixed values of α (0.01, 0.05 etc.) are generally used to evaluate the null hypothesis (H_0) at various significance levels. A value of 0.05 is typically used for most applications, however, in some critical industries; a lower value may be applied.

In general, critical values of the Anderson-Darling test statistic depend on the specific distribution being tested. However, tables of critical values for many distributions (except several the most widely used ones) are not easy to find.

The Anderson-Darling test uses the same critical values for all distributions. These values are calculated using the approximation formula, and depend on the sample size only. This kind of test (compared to the "original" A-D test) is less likely to reject the good fit, and can be successfully used to compare the goodness of fit of several fitted distributions.

A.4 Akaike information criterion (AIC)

The Akaike information criterion is a measure of the relative goodness of fit of a statistical model. It was developed by Hirotsugu Akaike, under the name of "an information criterion" (AIC), and was first published by Akaike in 1974. It is grounded in the concept of information entropy, in effect offering a relative measure of the information lost when a given model is used to describe reality. It can be said to describe the tradeoff between bias and variance in model construction, or loosely speaking between accuracy and complexity of the model.

A.4.1 General Case

In the general case, the AIC is

$$AIC = 2k - 2\ln(L) \tag{7.8}$$

where k is the number of parameters in the statistical model, and L is the maximized value of the likelihood function for the estimated model.

Given a set of candidate models for the data, the preferred model is the one with the minimum AIC value. Hence AIC not only rewards goodness of fit, but also includes a penalty that is an increasing function of the number of estimated parameters. This penalty discourages over fitting (increasing the number of free parameters in the model improves the goodness of the fit, regardless of the number of free parameters in the data-generating process).

A.4.2 AIC corrected (AICc)

AICc is AIC with a correction for finite sample sizes:

$$AICc = AIC + \frac{2k(k+1)}{n-k-1} \tag{7.9}$$

where k denotes the number of model parameters. Thus, AICc is AIC with a greater penalty for extra parameters. AICc is recommended over AIC, if n is small or k is large. Since AICc converges to AIC as n gets large, AICc generally should be employed regardless. Using AIC, instead of AICc, when n is not many times larger than k^2, increases the probability of selecting models that have too many parameters, i.e. of over-fitting.

Annex – B

Equation Chapter (Next) Section 1

B Statistical Distributions

B.1 Normal distribution

The normal distribution was first described by the French mathematician de Moivre in 1733. The development of the distribution is often ascribed to Gauss, who applied the theory to the movements of heavenly bodies. The normal distribution is the most commonly used distribution to model univariate data from a population or from an experiment. The probability density function of a normal random variable X with mean and standard deviation σ is given by:

$$f\left(x|\mu,\sigma\right)=\frac{1}{\sigma\sqrt{2\pi}}\exp\left[-\frac{(x-\mu)^2}{2\sigma^2}\right], \qquad -\infty<x<\infty,-\infty<\mu<\infty,\sigma>0 \tag{8.1}$$

This distribution is commonly denoted by $\mathcal{N}(\mu,\sigma^2)$. The cumulative distribution is given by:

$$F\left(x|\mu,\sigma\right)=\int_{-\infty}^{x} f\left(t|\mu,\sigma\right)dt \tag{8.2}$$

The normal random variable with mean□μ = 0 and standard deviation σ = 1 is called the standard normal random variable, and its CDF is denoted by $\Phi(z)$.

B.2 Weibull distribution

The Weibull variate is commonly used as a lifetime distribution in reliability applications. The two-parameter Weibull distribution can represent decreasing, constant, or increasing failure rates. These correspond to the three sections of the "bathtub curve" of reliability, referred to also as "burn-in," "random," and "wear out" phases of life. The bi-Weibull distribution can represent combinations of two such phases of life.

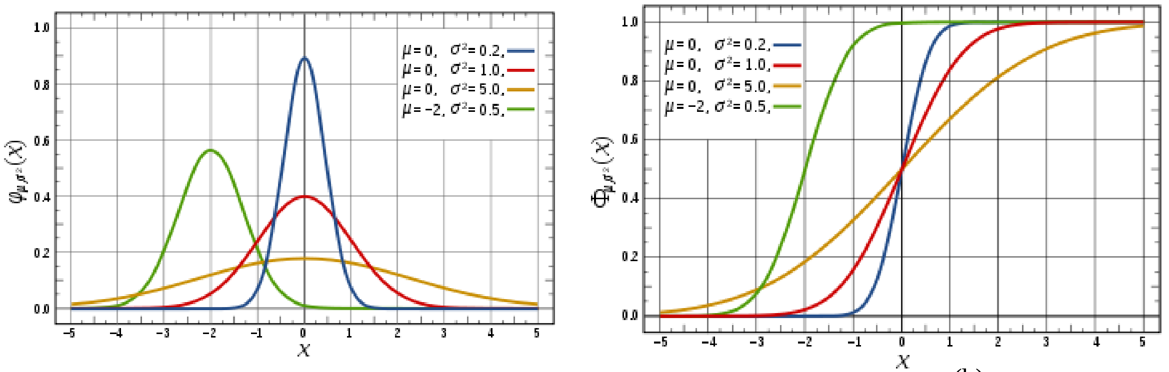

(a) (b)

Fig. A2.1 Normal (Gaussian) distribution (a) PDF (b) CDF

The probability function is defined as:

$$f(x) = \frac{\beta}{\eta}\left(\frac{x}{\eta}\right)^{\beta-1} \exp\left(-\left(\frac{x}{\eta}\right)^{\beta}\right) \tag{8.3}$$

Where, β > 0 and η > 0 are the continuous shape parameter and continuous scale parameter respectively. The cumulative distribution function is defined as:

$$F(x) = 1 - \exp\left(-\left(\frac{x}{\eta}\right)^{\beta}\right) \tag{8.4}$$

These distributions functions are shown in Fig. A2.2.

B.3 Beta distribution

The beta distribution is a family of continuous probability distributions defined on the interval [0, 1] parameterized by two positive shape parameters, typically denoted by α and β. The beta distribution can be suited to the statistical modeling of proportions in applications where values of proportions equal to 0 or 1 do not occur.

The probability density function of a beta random variable with shape parameters α and β is given by:

$$f(x|\alpha,\beta) = \frac{1}{B(\alpha,\beta)} x^{\alpha-1}(1-x)^{\beta-1}, \quad 0 < x < 1, \qquad \alpha > 0, \beta > 0 \tag{8.5}$$

Where the beta function B(α,β) = Γ(α)Γ(β)/Γ(α+β) and Γ is the gamma function. B, appears as a normalization constant to ensure that the total probability integrates to unity.

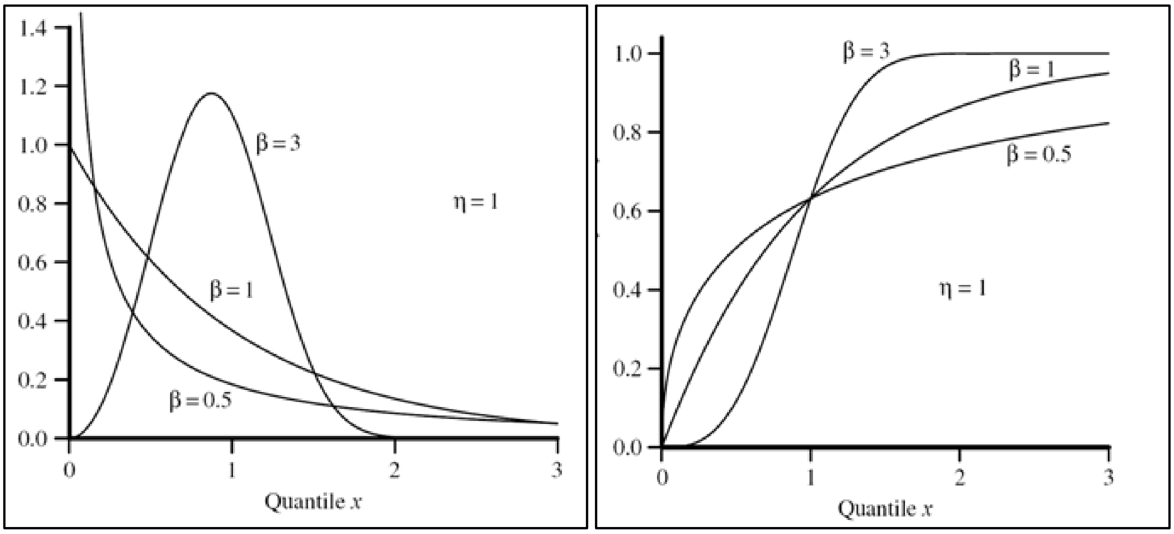

(a) (b)

Fig. A2.2 Weibull distribution, (a) PDF (b) CDF

The cumulative distribution function is

$$F\left(x|\alpha,\beta\right) = \frac{B_x\left(\alpha,\beta\right)}{B\left(\alpha,\beta\right)} = I_x\left(\alpha,\beta\right) \tag{8.6}$$

where $B_x(\alpha,\beta)$ is the incomplete beta function and $I_x(\alpha,\beta)$ is the regularized incomplete beta function.

B.4 Student’s t distribution

Student’s t-distribution (or simply the t-distribution) is a continuous probability distribution that arises when estimating the mean of a normally distributed population in situations where the sample size is small and population standard deviation is unknown. It plays a role in a number of widely-used statistical analyses, including the Student’s t-test for assessing the statistical significance of the difference between two sample means, the construction of confidence intervals for the difference between two population means, and in linear regression analysis. The Student’s t-distribution also arises in the Bayesian analysis of data from a normal family.

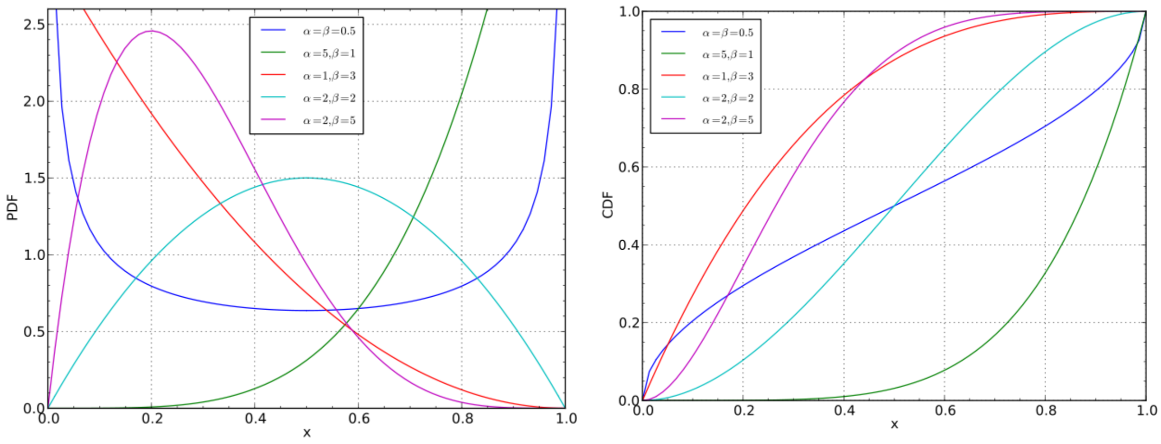

(a) (b)

Fig. A2. 3 Beta distribution, (a) PDF (b) CDF

The CDF and PDFs are defined as:

Distribution function

$$\begin{cases} \dfrac{1}{2} + \dfrac{1}{\pi}\tan^{-1}\left(\dfrac{x}{\nu^{1/2}}\right) \\ \quad +\dfrac{1}{\pi}\dfrac{x\nu^{1/2}}{\nu + x^2}\left[\displaystyle\sum_{j=0}^{(\nu-3)/2}\dfrac{a_j}{(1+x^2/\nu)^j}\right], & \nu \text{ odd} \\ \dfrac{1}{2} + \dfrac{x}{2(\nu+x^2)^{1/2}}\displaystyle\sum_{j=0}^{(\nu-2)/2}\dfrac{b_j}{\left(1+\dfrac{x^2}{\nu}\right)^j}, & \nu \text{ even} \\ \quad \text{where } a_j = [2j/(2j+1)]a_{j-1}, \quad a_0 = 1 \\ \qquad\qquad b_j = [(2j-1)/2j]b_{j-1}, \quad b_0 = 1 \end{cases}$$

Probability density function

$$\frac{\{\Gamma[(\nu+1)/2]\}}{(\pi\nu)^{1/2}\Gamma(\nu/2)[1+(x^2/\nu)]^{(\nu+1)/2}}$$

Where, ν is the degree of freedom and is a positive integer. The range of x is $-\infty < x < \infty$.

B.5 Generalized Extreme value (GEV) distribution

The generalized extreme value distribution is often used to model the smallest or largest value among a large set of independent, identically distributed random values representing measurements or observations.

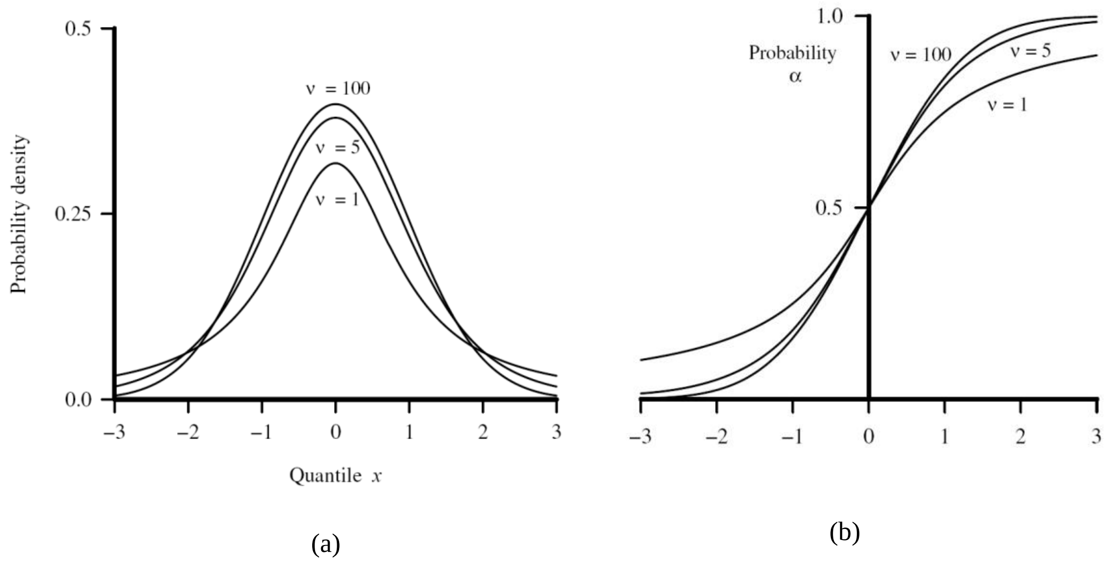

Fig. A2. 4 Student's t distribution, (a) PDF (b) CDF

The generalized extreme value combines three simpler distributions into a single form, allowing a continuous range of possible shapes that includes all three of the simpler distributions. we can use any one of those distributions to model a particular dataset of block maxima. The generalized extreme value distribution allows us to "let the data decide" which distribution is appropriate.

The three cases covered by the generalized extreme value distribution are often referred to as the Types I, II, and III. Each type corresponds to the limiting distribution of block maxima from a different class of underlying distributions. Distributions whose tails decrease exponentially, such as the normal, leads to the Type I. Distributions whose tails decrease as a polynomial, such as Student's **t**, lead to the Type II. Distributions whose tails are finite, such as the beta, lead to the Type III.

Types I, II, and III are sometimes also referred to as the Gumbel, Frechet, and Weibull types, though this terminology can be slightly confusing. The Type I (Gumbel) and Type III (Weibull) cases actually correspond to the mirror images of the usual Gumbel and Weibull distributions.

Three parameters k (continuous shape parameter), σ (continuous scale parameter) with σ >0 and μ (continuous location parameter) are used to model that distribution.

Domain

$$F(x)=\begin{cases}\exp\left(-(1+kz)^{-1/k}\right) & k\neq 0\\ \exp\left(-\exp(-z)\right) & k=0\end{cases} \tag{8.7}$$

Probability Density Function

$$\begin{aligned}&1+k\frac{(x-\mu)}{\sigma}>0 && \text{for} \quad k\neq 0\\ &-\infty<x<\infty && \text{for} \quad k=0\end{aligned} \tag{8.8}$$

Cumulative distribution Function

$$f(x)=\begin{cases}\dfrac{1}{\sigma}\exp\left(-(1+kz)^{-1/k}\right)(1+kz)^{-1-1/k} & k\neq 0\\ \dfrac{1}{\sigma}\exp\left(-z-\exp(-z)\right) & k=0\end{cases} \tag{8.9}$$

Where $z\equiv\dfrac{x-\mu}{\sigma}$

Annex – C

C Supported Programs

To support the work in this thesis several programs in matlab and in visual basic have been written, following are breif introduction to these programs.

C.1 MATLAB to CST control

The program overview has been demonstrated in Fig. C. 1. This program allows control of CST MWS software through the use of MATLAB scripting or functions.

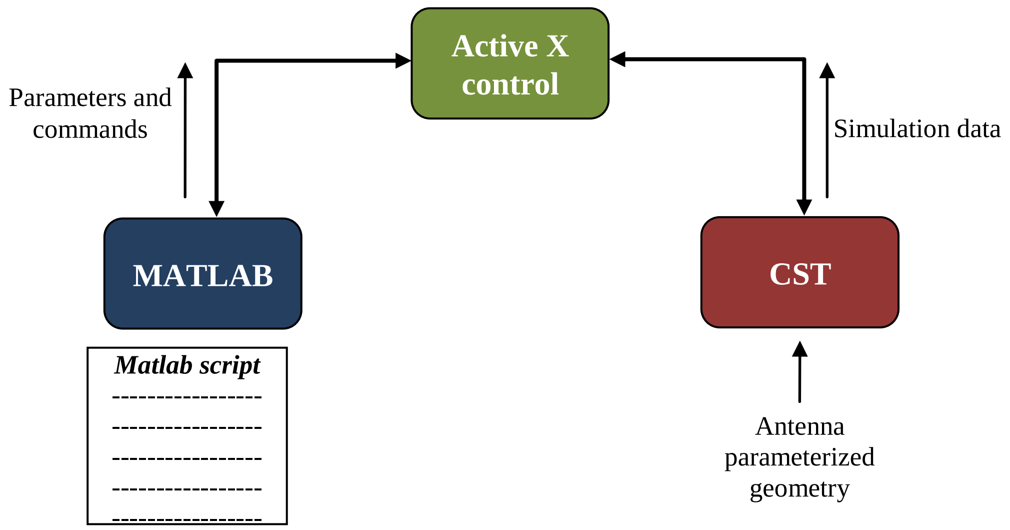

Fig. C. 1 MATLAB to CST control program structure

In the beginning, antenna geometry of the particular shape (triangular, step or disc) is fully parameterized in CST and saved in file. The program then launches the CST and load the desired design file. It then reads the parameters based on the design the specific set of parameters are chosen to be varied. Matlab then sent the values of the selected parameters and commands the CST to simulate. Once the simulation is done, the simulated data is then exported to back to Matlab. In the same manner many antenna samples can be simulated.

C.2 CST Data Export

One inconvenience with the previous program is the time that is required to transfer of data from CST to MATLAB.

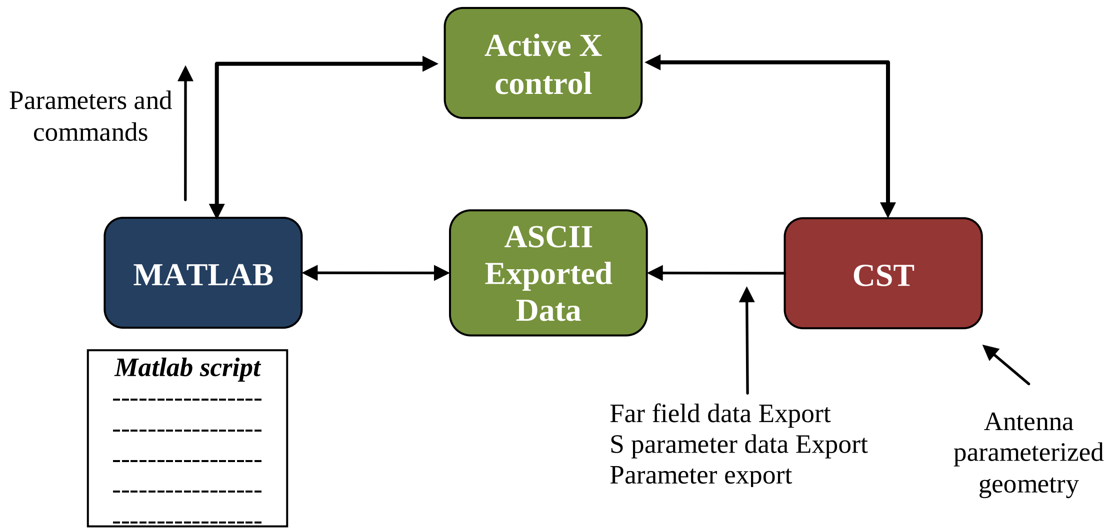

Fig. C.2 CST Data export and control program structure

In order to mitigate the time consumption problem the method of exporting the simulated data has been changed and all the related data in this program is exported in ASCII file format (Fig. C.2) and then MATLAB reads all these files. This certainly reduces the overall time.

To achieve this, at least three extra programs in visual basic has been developed and saved as Macros in CST. These are Far-field data export, S-parameter data export and geometrical parameter export.

MATLAB commands the CST to run these macros at the end of the simulation and once the data is exported MATLAB validates the data by counting the expected number of files. Reading these ASCII file into MATLAB is very less time consuming.

C.3 Optimization Cost functions

As discussed in the chapter 3 the cost function is the only link between the physical problem and the optimization algorithm and the problem with built-in CST goal/cost functions that they sometimes stuck with the deep resonances.

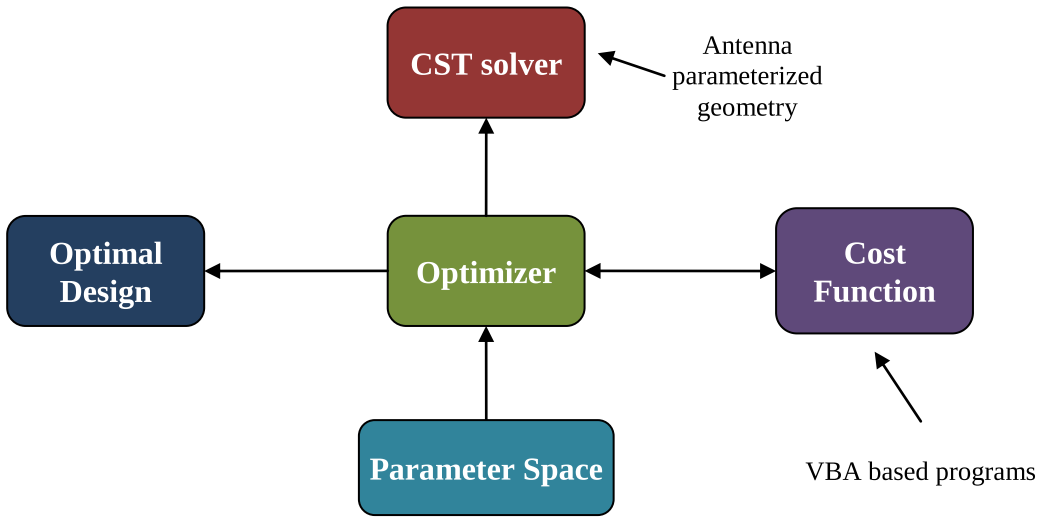

Fig. C.3 Optimizer block diagram with cost function role

We have written the cost functions in visual basic for application provided in CST to customize our desired response during the optimization. It is worth mentioning that these cost function can call MATLAB is required to solve the difficult mathematical computations if exists. This is especially true for Multiband antenna optimization.

In general, three main cost functions have been written, two for $|S_{11}|$ response of the UWB and multiband antenna — checking the in-band and out of band values of the $|S_{11}|$ response. Third was written for volume of the antennas.